Studies of Methods of Pre-launch Testing

of Satellite Radar Altimeters

by

Declan Vincent Sheehan

A thesis submitted to the University of London for the Degree of

Doctor of Philosophy in Electronic Engineering

Department of Electronic and Electrical Engineering

UNIVERSITY COLLEGE LONDON

January 1993

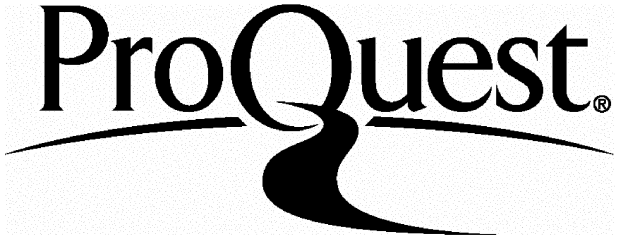

Abstract

The radar altimeter operating in a pulse-limited mode has been successful in charting the ocean surfaces of the Earth. The scientific community, in a drive to map rougher terrain, have adopted the same principle. However in order to overcome the problem of slope-induced error, the range window may be widened or narrowed in accordance with the surface roughness. The ERS-1 altimeter included a second range window for operation over ice, but which had to be controlled by macro-command from the ground. The Advanced Terrain-Tracking Altimeter is a prototype altimeter which has an on-board resolution-switching algorithm, allowing the range window to be changed appropriately.

This thesis focuses on methods of pre-launch testing of advanced radar altimeters. The early chapters review some of the calibration and testing methods used for the ERS-1 altimeter, presenting a critical assessment of some of the pre-launch methods. The testing procedure for the Adaptive Terrain-Tracking Altimeter is significantly more complex because of the extra resolution-switching algorithm, and a return signal simulator is identified as an essential element in testing the adaptive resolution prior to launch.

The core of the thesis therefore describes a novel method of return signal simulation in which sequences of realistic echoes, from all types of surface, are fed in real time to the prototype altimeter, at the appropriate resolution, with the appropriate fading characteristics, and at the appropriate instant in time. Such a simulator is feasible only if the simulated echo is modelled in the deramp domain (i.e range window space) rather than actual delay time. Then the Fourier Transforms of the echoes, rather than the echoes themselves, are calculated at the full pulse repetition frequency and are stored in a memory. The resolution may then be varied by altering the rate at which the echoes are read out of memory. A prototype Return Signal Simulator is built, tested and shown to be capable of testing the Adaptive Terrain-Tracking Altimeter.

A test philosophy is defined to assist the testing of the prototype altimeter, which will be undertaken by British Aerospace. A preliminary analysis, using a software implementation of the return signal simulator and realistic echoes, demonstrated that the Model Free Tracker has a superior tracking performance than the generally preferred Offset Centre Of Gravity tracking algorithm. However both algorithms suffer from problems, and these problems are identified.

Finally a new approach to the analysis of the effect of chirp phase errors is presented, which leads to a quantitative expression for the height error resulting from chirp phase distortion. Such an approach can be used to apply a correction to the height estimate, unlike previous approaches which could only be used to set a specification for altimeter design.

To my dear wife Yvonne,

whose love and understanding helped me complete this thesis

Acknowledgements

Many people have taken a keen interest in this research from the outset. First and foremost, I would like to express my gratitude to my supervisor, Dr. Hugh Griffiths, for his advice, guidance and technical suggestions throughout. He has always been prodigal of his assistance; in particular I am indebted to Hugh for the time he spent proof-reading my thesis, and I have respected his red pen. I thank Hugh also for his friendship.

Dr. Paul Brennan became involved towards the end of the project whilst Hugh was on sabbatical leave. Paul, whose technical competence is unrivalled, made a very significant contribution in the short time in which he was involved. I will always be grateful to Paul.

I would like to thank Professor K. Milne and Professor R. Benjamin for some stimulating discussions from which some valuable and important points emerged. Others I would like to mention include Dr. D.J. Wingham, who was responsible for the early development of the research, and Dr. Behruz Purseyyed, with whom I had many useful and enjoyable discussions during the early years of my research.

I am grateful to the British Embassy in Dublin for a two-year scholarship in the early part of my doctorate. I would also like to acknowledge the Royal Aerospace Establishment in Farnborough for supporting the early part of this and related work, and the European Space Agency for supporting the latter two years.

The technical construction and mechanical assembly of the prototype return signal simulator would not have been completed had it not been for the goodwill and efficiency of Wolfram Titze and Andrew Wilkinson who helped me greatly in my hour of need. For this I sincerely thank them.

From the other collaborating groups involved in the Breadboard Altimeter Test and Study, I would like to acknowledge John Bradford of the Rutherford Appleton Laboratory, Dick Durrant and Steve Parkes from British Aerospace, Filton and G. Franchin from Fabbrica Italiana Apparecchiature Radioelettriche S.p.A (FIAR).

Finally, I would like to thank my colleagues in the Antennas and Radar Group for their encouragement and friendship over the years. In this regard I will particularly remember Wolfram Titze, Tony Vernon and Brian Armstrong. For their part in creating a warm and friendly environment, I would like to thank Dr. Paul Brennan, Roni Eiges, James Garnett, Saeed Khosrowbeygi and Andrew Wilkinson.

Go n'eirí an bhothar leat

Originality is nothing but judicious imitation. The most original
writers borrowed from one another. The instruction
we find in books is like fire. We fetch it from our neighbours,
kindle it at home, communicate it to others, and it becomes the property of all.

Voltaire

Contents

Chapter 3 - Simulation of Altimeter Echoes

Chapter 4 - Prototype Return Signal Simulator Design and Analysis

Chapter 5 - Results Obtained from Testing the Altimeter

Chapter 6 - Analysis of Chirp Errors

Chapter 7 - Discussion of Results

List of Acronyms

AABB	Advanced Altimeter BreadBoard
AAFE	Advanced Applications Flight Experiment
AGC	Automatic Gain Control
APL	Applied Physics Laboratory
ATTA	Advanced Terrain-Tracking Altimeter
BAe	British Aerospace
DAC	Digital to Analogue Converter
DCG	Digital Chirp Generator
EOPAP	Earth and Ocean Physics Applications Program
EOS	Earth Observing System
ERS-1	European Remote Sensing Altimeter
FIAR	Fabbrica Italiana Apparecchiature Radioelettriche S.p.A.
FIFO	First In-First Out
FFT	Fast Fourier Transform
GLRS	Geodynamic Laser Ranging System
GPS	Global Positioning System
IF	Intermediate Frequency
LO	Local Oscillator
LPF	Low Pass Filter
MSSL	Mullard Space Science Laboratory
MFT	Model Free Tracker
NASA	National Aeronautical and Space Administration
OCOG	Offset Centre Of Gravity Tracker
PLL	Phase Locked Loop
PRF	Pulse Repetition Frequency
PROM	Programmable Read Only Memory
QA	Quality Assurance
RAL	Rutherford Appleton Laboratory
RAM	Random Access Memory
RSS	Return Signal Simulator
RF	Radio Frequency
SAW	Surface Acoustic Wave
SLR	Satellite Laser Ranging
SMLE	Sub-optimal Maximum Likelihood Estimator
SWH	Significant Waveheight
TWT	Travelling Wave Tube
UCL	University College London
VCO	Voltage Controlled Oscillator

List of Symbols

B	Chirp bandwidth (Hz)
D_{RA}	Altimeter range to the surface (m)
G	Antenna gain
I_m	Value of the in-phase version of signal at the m^{th} sampling point
L_a	Loss in the attenuator used for internal power calibration (dB)
L_{dcr}	Loss in the directional coupler in the receiver path (dB)
L_{dct}	Loss in the directional coupler in the transmit chain (dB)
L_r	Loss in the receiver path (dB)
L_t	Loss in the transmit chain (dB)
N	Number of samples in simulated echo
N_F	Number of filters (bins) in the range window
$N_{inflight}$	Number of pulses in flight
N_{let}	Percentage of time the return is maintained in the range window
N_{nzr}	Percentage of time the first non-zero return is not registered
N_{sat}	Percentage of time the return is tracked and unsaturated
N_{snr}	Percentage of time the signal to noise ratio is below a threshold
P_{COG}	Position of the centre of gravity in the OCOG algorithm
P_{oc}	Measured calibration signal power
P_{or}	Received power in the altimeter range window (W)
P'_{rc}	Calibration signal in the receiver (W)
P_r	Received power at the antenna (W)
P_t	Peak transmit power (W)
PRF	Pulse repetition frequency (Hz)
PRF_{max}	Maximum pulse repetition frequency (Hz)
Q_m	Value of the quadrature version of signal at m^{th} sampling point
Q_n	Percentage of time the return is tracked at the n^{th} resolution
S_{radial}	Satellite radial position (m)
T	Uncompressed pulse length (s)
T_c	Calibration 'equivalent' range (s)
T_L	Echo duration due to beam-limiting (s)

T_{radial}	Radial position of the Venice Tower (m)
T_s	Sampling interval (s)
W	Width of signal in OCOG algorithm
a_i	Amplitude weightings
b	Chirp modulation rate (Hz/s)
b_{RA}	Height bias of the radar altimeter
c	Speed of light (= 3.00×10^8)
d_{corr}	Decorrelation distance (m)
f	Frequency (Hz)
$\bar{f}$	Mean frequency (Hz)
f_{diff}	Frequency difference between the RSS and transmit chirp (Hz)
f_{mult}	Speed of the multipliers (Hz)
g	Receiver gain in altimeter after deramp
h	Height of satellite above the reference ellipsoid (m)
r	Radius of pulse-limited footprint (m), and radial vector to surface
t	Time coordinate (s)
t_h	Deramp trigger instant (s)
t_Δ	Time difference between received and deramp chirps (s)
t_{diff}	Time between actual and calibrated signal in 'in-orbit' calibration
t_o	Time of the first return
t_{pt}	Time delay to a point target (s)
t_r	Trigger instant of the RSS chirp (s)
tide	Tide gauge measurement in ERS-1 claibration scheme (m)
v	Speed of the satellite (m/s)
x	Along track coordinate (m)
y	Across track coordinate (m)
z	Radial coordinate (m)
s	Delay time variable (s)
α	α-β filter parameter
β	α-β filter parameter
δ_r	Range resolution (m)
ϕ_i	Weights used in power series approach to phase distortion (rad)
η	Resolution factor

λ	Wavelength of the RF carrier (m)
θ	Beamwidth of the antenna of the radar altimeter (°)
σ^o	Backscatter coeficient of the surface
σ_s	Sigma-s (significant waveheight / 4)
τ	Compressed pulse length, and resolution (s)
τ_i	Delay time to a facet on the surface
ω	Angular frequency space or 'deramp domain' (rad)
ω_o	Angular centre frequency of the chirp (rad)
ω_n	Angular frequency of the tone in the n^{th} resolution bin (rad)
ω_m	Angular frequency of Fourier series defining phase distortion
Δ_a	Time delay in the attenuator (s)
Δ_D	ERS-1 fixed time delay for transmit chain (s)
Δ_{fe1} Δ_{fe2}	Front end time delays (s)
$\Delta\phi_d(\ )$	Phase distortion of deramp chirp (rad)
$\Delta\phi_t(\ )$	Phase distortion of transmit chirp (rad)
Δ_{LO}	Timing delay in the deramp local oscillator (s)
Δ_{Tx1}	Time delay between transmit trigger and RSS chirp (s)
Δ_{Tx}	Timing delay in the transmit chain (s)
$\Delta_{\tau 2}$	RSS time delay (s)
ΔG	Change in gain (dB)
Δh	Height bias (m) or height difference
ΔR	Range window extent (m)
ΔT	Misalignment of deramp and returned chirp
A(t)	Quadratic phase function of chirp
$A_d(t)$	Amplitude distortion on the chirp
$b(\omega)$	Amplitude spectrum of signal in RSS at a coarser resolution
B(t,s)	Echo information
d(t)	Impulse response of the surface
$\delta(t)$	Dirac function
$\phi(t)$	Phase function (rad)

$\Phi(\omega)$	Spectrum of phase distortion
$f(\omega)$	Amplitude spectrum of the simulated echo
$f_a(\omega)$	Amplitude spectrum of the echo when observed in the altimeter
$F(t)$	Echo signal in time domain
$F_a(t)$	Echo signal in the time domain after deramp by the altimeter
$g(t)$	Simulated signal
$H(t)$	Gating signal whose width is equal to the pulse length
$I(t)$	In-phase component of the simulated baseband signal
$I_a(t)$	In-phase component of the signal in the altimeter
$n(\omega)$	Noise function
$P_1(\omega)$	Power spectrum in range window at a finer resolution
$P_2(\omega)$	Power spectrum in range window at a coarser resolution
$P_{FS}(\tau)$	Average flat surface impulse response (W)
$P_r(\tau)$	Average square law detected power from a rough surface (W)
$Q(t)$	Quadrature component of the simulated baseband signal
$Q_a(t)$	Quadrature component of the altimeter baseband signal
$q_s(t)$	Probability distribution of the heights of the scatterring facets
$R(\omega)$	Normalised Rayleigh fluctuations
$S_{LP}(\omega)$	Low pass anti-alias filter in altimeter
$s_r(t)$, $S_r(\omega)$	Point target response of radar
$S_1(\omega)$	Point target response modified by phase distortion
$U(t)$	Heaviside unit step function
$\otimes$	Convolution
$\|\|$	Modulus
$< >$	Expectation function
$\mathcal{F}$	Fourier Transform
Re	Real part of expression
Im	Imaginary part of expresion

List of Figures

Chapter 1

Introduction

Satellite-borne radar altimeters have been developed over the past few decades to make high-precision measurements of ocean surface elevation, as well as of waves, wind and swell. The precision achievable in height measurement is of the order of a few centimetres - a remarkable achievement from an altitude of several hundred kilometres.

Altimeters have also given limited coverage of non-ocean surfaces, permitting for example topographic maps of the Greenland and Antarctic ice sheets to be derived (Zwally et al., 1983). Such maps are of interest because they should permit estimation of changes in ice sheet mass balance, which are believed to be a sensitive indicator of the onset of climate change (Manabe and Stouffer, 1980). Other examples of the use of non-ocean altimeter data include studies of wetlands, lake levels and deserts (Rapley et al., 1987). However, since present altimeter designs have been designed principally for operation over oceans, their performance over non-ocean surfaces has generally not been optimum. Presently, there are many studies investigating more suitable instrumentation and measurement methods for topographic mapping (Rapley et al., 1990).

For all spaceborne instruments, thorough pre-launch testing and characterisation is essential. Such testing should ensure that the instrument meets its performance specification in engineering terms, as well as demonstrating proper extraction of geophysical parameters from the instrument data. The subject of this thesis is the pre-launch testing and simulation of advanced radar altimeter systems, and specifically of an altimeter with a capability of mapping topographic terrain.

1.1 HISTORICAL PERSPECTIVE

Satellite altimetry was proposed in 1966 as a means of refining the marine geoid. The Geodetic Satellite Office of NASA funded the resulting research programme into applicable measuring systems, which included a radar altimeter. The oceanographic community independently emphasised the importance of altimetry in measuring dynamics of the ocean surface. In 1969, a seminal meeting was convened at Williamstown,

Massachusetts, to study the application of space techniques to the terrestrial environment, and to determine the scientific value of such techniques. The study (Kuala, 1969) concluded that satellite altimetry could provide the measurement accuracies required by both the geodetic and oceanographic communities. The 1972 Earth and Ocean Physics Applications Program (EOPAP) subsequently called for the development of a 10-cm-accurate radar altimeter as one of the principal sensors to be carried by a remote sensing satellite.

The first NASA radar altimeter experiment was the S-193, deployed aboard the manned SKYLAB satellite in 1973. Its objective was to determine the feasibility of measuring the marine geoid, ocean wave height and wind speed (McGoogan et al., 1974). The altimeter demonstrated a height measurement precision of 1 m. More importantly, however, the altimeter provided a wealth of experimental data for the design of future satellite radar altimeters. The radar altimeter carried by the GEOS-C spacecraft, launched in April 1975, gave global coverage of the oceans, and achieved a height precision of about 60 cm, giving enhanced detail of the geoid over most of the ocean areas (Stanley, 1979).The next in the series, the SEASAT-A altimeter, was designed for a height precision of better than 10 cm (MacArthur, 1976). In order to bridge the gap between the performance of GEOS-C altimeter and the goals of the SEASAT-A altimeter, an airborne altimeter, the Advanced Applications Flights Experiment (AAFE), was commissioned to collect ground truth measurements in support of the SEASAT-A calibration and validation activities. The SEASAT satellite was launched in June 1978; the altimeter achieved the 10 cm height precision goal, and the data allowed considerable refinement of the marine geoid (Brown et al., 1983; Rapp, 1983). The success was short-lived, however, as a power supply fault terminated the operation of the satellite in October of the same year, but not before the mission had yielded a large amount of high quality data. In 1986 the GEOSAT-A satellite was launched, carrying an improved version of the SEASAT-A altimeter. The improvements included a longer-life, lower-power travelling wave tube amplifier for the transmitter, a longer uncompressed pulse length, and a lower receiver noise figure. The GEOSAT altimeter measurements helped to establish a global grid of high precision measurements (3.5 cm), that were used to further refine the geoid.

The present generation of satellite altimeters are very similar to those carried by SEASAT and GEOSAT, but include a number of further developments. A chart showing the development of altimetry is presented in figure 1.1-1. The TOPEX altimeter, launched in 1994, is designed to achieve a greater height precision using a higher pulse repetition frequency, a dual frequency implementation to provide a better ionospheric correction, and

by operating in a higher orbit to reduce the drag on the satellite, thus improving the satellite tracking. The French POSEIDON altimeter is carried on the same satellite, and uses an all-transistor transmitter, with potential benefits in reliability and lifetime. The first European remote sensing satellite, ERS-1, was launched in July 1991, and carries a dual mode radar altimeter. The primary mode has been optimised for operation over oceans, while the second mode is intended for tracking the ice covered regions of the Earth, by means of a wider range window and a tracking algorithm designed to cope with non-ocean waveform shapes. This is presently providing considerably better coverage of land and ice sheet surfaces than the SEASAT and GEOSAT altimeters.

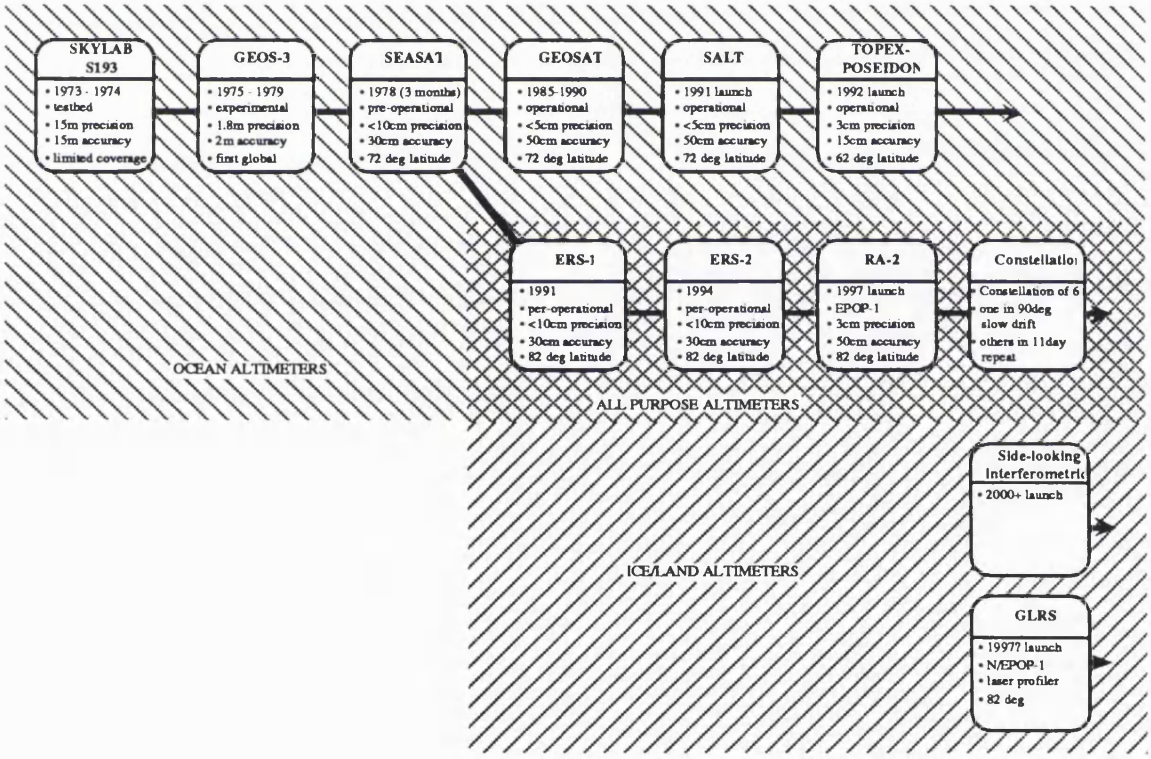

Figure 1.1-1. The development of altimeter instrumentation (Rapley et al., 1990).

Several studies have concluded that the conventional 'Seasat-like' altimeter is not optimum for topographic mapping (Rapley et al., 1985; Griffiths et al., 1985). This type of altimeter operates in the pulse limited mode (figure 1.1-2), with a relatively broad antenna beam and a short transmit pulse, and results in a pulse limited footprint rather smaller than the overall antenna footprint. The pulse-limited footprint is localised at nadir over a horizontal surface, thus the use of a broad antenna beam relaxes otherwise severe

requirements on antenna size and pointing. Over topographic surfaces, however, there is a slope-induced error, so the location of the point on the surface to which the range measurement is made is no longer at nadir (figure 1.1-3). This error can only be determined and corrected if the magnitude and direction of the slope are already known, which in general they will not be.

The other mode of operation - the so-called beam-limited mode - uses a narrow antenna beam to overcome the problems of slope-induced error, but requires an impractically-large antenna. Studies have been made of other methods of achieving high spatial resolution, but to date the pulse-limited approach has been universally adopted. The ERS-1 altimeter 'ice mode' achieves more robust tracking of non-ocean surfaces by reducing the pulse bandwidth by a factor of four. This increases the extent of the range window by the same factor, but equally degrades the height resolution. Ridley (1990) estimates that the ERS-1 altimeter will map over 50% of the Earth's non-ocean surface using the 'ice-mode'.

Taking the same principle further, an Advanced Terrain-Tracking Altimeter (ATTA) has been proposed, to gather data over all surface types (Andrewartha et al., 1988). On-board processing is required to adaptively select which of the five resolutions is appropriate for tracking the surface, and should allow the altimeter to map practically all of the Earth's surface to a resolution governed by the local surface roughness. The usefulness of this type of altimeter data is potentially enhanced by 'range migration' techniques (Wingham and Rapley, 1988), which should give spatial resolutions of the order of 500 m.

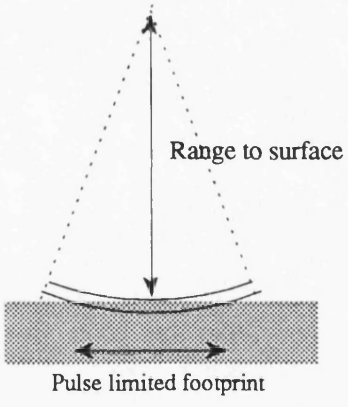

Figure 1.1-2. Pulse-limited operation over a flat surface.

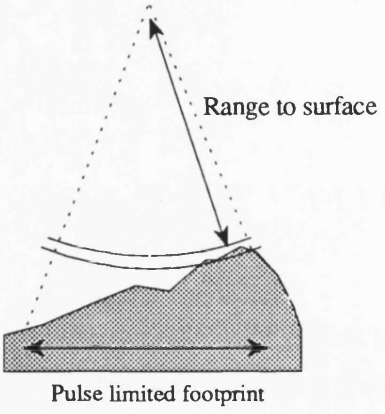

Figure 1.1-3. Pulse-limited operation over a rough surface.

A recent consultative meeting, organised by the European Space Agency, attempted to define the scientific requirements for future radar altimeters (Rapley et al, 1990), and examined some novel radar altimeter concepts as a means of fulfilling these requirements. The meeting considered instruments with improved range and spatial resolution, and techniques for increased spatial and temporal sampling frequency. One idea that aroused strong interest is that of a 'constellation' of small, dedicated, cheap altimeters (Chase and Mundt, 1989), and research is currently being undertaken by a number of institutions into the feasibility of this idea.

Laser altimetry, initially limited by the short lifetime and non-robustness of the laser, is slowly becoming a feasible alternative to microwave altimetry. NASA are developing the Geodynamic Laser Ranging System (GLRS) as one of the instruments residing on the Earth Observing System (Eos), a platform in a polar orbit at a height of 705 km. The GLRS is a combination of laser ranger and altimeter, and will be used for the precise measurement of the distance between strategically placed ground-based retro-reflectors, as well as the measurement of altimetric height dynamics (Dallas et al., 1991). If successfully developed and deployed, the GLRS will provide profile data of the Earth to a spatial resolution of 100 m and a height resolution of 1 m.

1.2 ERRORS IN ALTIMETER HEIGHT MEASUREMENT

Over the ocean, the altimeter measures the two-way propagation delay between the satellite orbit and the sea surface topography (see figure 1.2-1). The time variability of the sea surface topography can be averaged from repeat orbits. The mean sea surface then approximates to the geoid, except in regions of strong ocean currents and other quasi-permanent phenomena. The satellite orbit is not a useful datum with which to reference the geoid and sea surface topography; orbit errors occur due to perturbations in the Earth's gravity field and due to atmospheric drag on the satellite, and deviations can be as large as 10 km from the desired elliptical orbit. It is thus more appropriate to define the reference ellipsoid of the Earth, defined by the equatorial and polar radii of the Earth, as the reference for all measurements.

There are three major error components in the measured height. Firstly, there are errors in defining the satellite orbit with respect to the reference ellipsoid; secondly there are delays in the propagation of the pulse through the ionosphere and troposphere; and thirdly, there are errors associated with the instrument. The satellite orbit error can be reduced to less

than 100 cm using a suitable geopotential model of the Earth, aided by precise laser tracking of the satellite as it passes close to ground stations (Robinson, 1985). Propagation delays in the ionosphere and troposphere are also critical in determining the absolute accuracy of the height measurement, and they arise as a result of the difference in the value of the refractive index between these media and a vacuum. A number of models exist (Lorrell et al., 1982; Goldhirsh and Rowland, 1982) to account for these effects; however the residual error is nonetheless of the order of 3 cm for both the troposphere and the ionosphere.

Instrument errors determine the precision of the height measurement, and currently the achievable precision is about 10 cm. It is now possible to reduce the impact of the instrument error on the total error budget to the point where oceanographic effects such as geostrophic surface slopes as small as 1 in 10^5 (Challenor and Srokosz, 1990) can be observed.

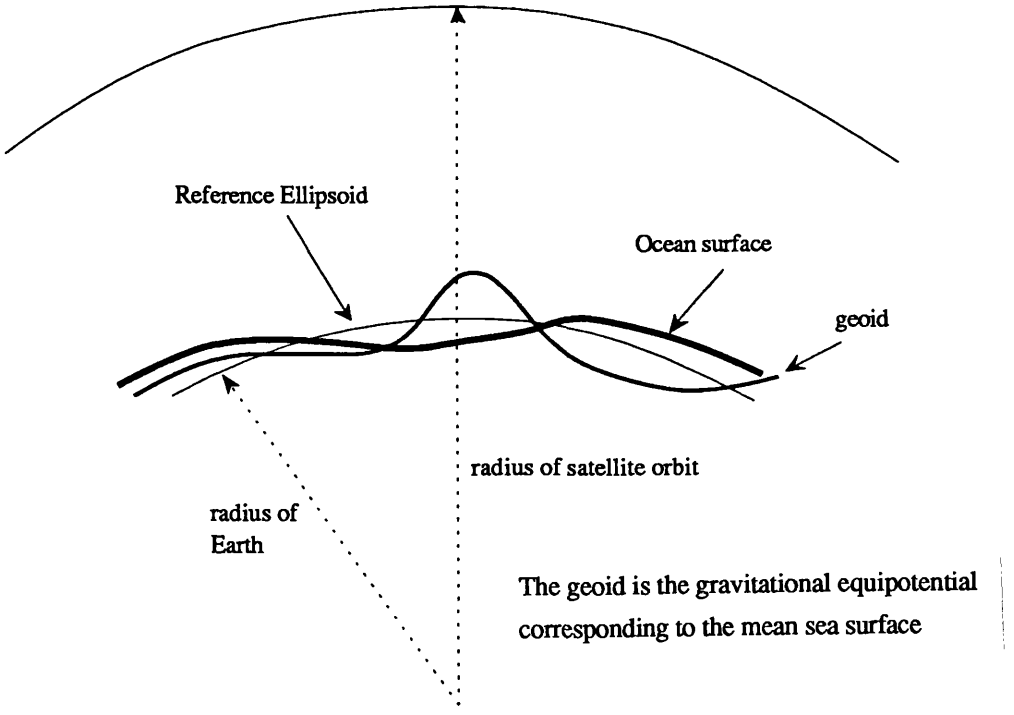

Figure 1.2-1. The geometry of the satellite measurement. The satellite orbit is tracked by ground stations that are referenced to the reference ellipsoid of the Earth. The altimeter makes a measurement from the satellite position in the orbit to the mean sea level. The geoid is also shown.

1.3 AIM OF THE RESEARCH

The overall objective of this research is to develop various methods of testing and analysis of the altimeter instrument. To date, most of the interest in radar altimetry has focussed on the returns from ocean surfaces, and researchers have been refining the models for the ocean return to include small geophysical perturbations. Two areas that have not received much interest are researched in this thesis, and these are:

> a method of testing the Adaptive Terrain-Tracking Altimeter prior to launch, and
> an analysis of the effect of instrument errors on the ocean return

Many methods of testing, including a return signal simulator, exist for ordinary uni-modal altimeters. The ATTA, however, requires a method of testing that will exercise the on-board resolution switching algorithm, and the tracking algorithms for terrain, which are different from the algorithms used for ocean surfaces. A return signal simulator that has an adaptive capability, and thus can change the resolution of the simulated echo easily, is the best means of testing the ATTA prior to launch. The development of an RSS that can provide the correct resolution echo is thus a major component of the work described in this thesis. The RSS then becomes the tool with which most of the pre-launch testing can be accomplished.

The second area covered in this thesis is an analysis of the effect of one of the instrument errors on the ocean return. Transmit and deramp chirp errors affect the measurement of height and significant waveheight made by the altimeter. The effect has been analysed by Brooks and Dooley (1975), Somma et al. (1981) and Francis (1982). However each approach requires numerous approximations, and all give different results. Thus it is difficult to be confident about the effect of chirp errors on the geophysical measurement. This thesis outlines the areas where these methods are lacking, and presents an alternative approach that is directly applicable to radar altimetry.

1.4 THESIS LAYOUT

An investigation of various methods of testing the Adaptive Terrain-Tracking Altimeter is carried out in chapter 2. A description of the altimeter is presented, and a comprehensive testing scheme is proposed. The distinction and connection between pre-launch and post-launch testing and calibration is made. The merits of Return Signal Simulation are outlined and the feasibility of using a Return Signal Simulator for calibration is discussed.

Chapter 3 discusses the simulation of altimeter echoes in considerable detail, and presents a very effective model for the return signal in a simple form. A novel method of changing the resolution of the simulated echo is then presented, and the results of a computer simulation are used to verify this method and many other ideas. The chapter finally considers some of the conventional methods of Return Signal Simulation, and underlines their unsuitability for adaptive testing.

Chapter 4 describes a prototype return signal simulator that was built specifically to test an adaptive terrain-tracking altimeter. An outline of the design requirements is presented, and a top-down design approach is presented. The hardware design is described briefly with more emphasis placed on the practical limitations of the simulator, and how these can be overcome. The realism of the simulated echoes is also discussed, and the implication of the sequence length on the simulation is discussed.

In chapter 5, the performance of the prototype RSS is analysed with respect to its capability of testing the advanced altimeter. A detailed analysis of the timing precision of the simulated echo is carried out. The analysis concludes that the RSS is capable of providing the timing stability for echo simulation. The dynamic range of a single echo and the range bin flatness are also measured, and the implication of the measurements on the simulation are analysed. Measurements of the RSS chirp are made, and the results are interpreted in the context of (a) how they affect the altimeter measurement and (b) the feasibility of this novel method of chirp generation. Finally, the chapter considers how the RSS can be used to test the advanced altimeter. Unfortunately, the prototype altimeter was not ready to be tested, and as a result a test philosophy is outlined. However a comparison of the performance of two different tracking algorithms using a number of the simulated echoes is performed at the end of the chapter.

In chapter 6 the effect of chirp phase and amplitude distortion is considered. The current approach, although not incorrect, is critically examined and found to be only useful for setting a specification on sidelobe level of an instrument point target response. However, in the context of corrections to the altimetric height measurement, it does not prove to be a useful method. An alternative method of analysis that is directly applicable to radar altimetry, and which does provide a correction factor, is presented.

In chapter 7, a summary of the work is presented, and the main achievements are outlined. An investigation of the altimeter performance using the RSS will be carried out by British Aerospace in the short term, and a suitable test philosophy is described. Although the research is specific to satellite pulse-limited altimeter, some other potential applications are suggested. Finally, the chapter lists the conclusions that have resulted from the research.

Chapter 2

Pre-Launch Testing of Altimeters

2.1 DESCRIPTION OF THE ADVANCED ALTIMETER

The basic principle of operation of present-generation geophysical radar altimeters is that of *full deramp*, illustrated in figure 2.1-1. A linear frequency-modulated pulse, or *chirp*, is transmitted towards the surface, and is returned to the altimeter after reflection from the facets that comprise the surface. On reception, the surface echo is mixed with a replica of the transmit chirp in a process known as *deramping*, mapping the range of each target into a corresponding frequency. The range information is therefore derived by performing a spectral analysis, using an FFT or digital filter. The resolution in the frequency domain is 1/T, and the corresponding delay time resolution is:

$$\tau = \frac{1}{bT} = \frac{T}{BT} \qquad (2.1\text{-}1)$$

where b is the rate of change of frequency modulation of the chirp:

$$b = \frac{df}{dt} = \frac{B}{T} \qquad (2.1\text{-}2)$$

The FFT output forms a range window of extent:

$$\Delta R = \frac{N_F}{T}\frac{T}{B}\frac{c}{2} = \frac{cN_F}{2B} \qquad (2.1\text{-}3)$$

The processing gain BT in eqn. 2.1-1 also constitutes the improvement in resolution of full deramp over a radar with an unmodulated pulse of the same duration.

Since the range resolution is inversely proportional to the chirp bandwidth, it is possible to change the range resolution simply by changing the chirp bandwidth, and all the sampling, filtering and baseband processing remain unchanged. This is the principle by which the ATTA is capable of reducing its range resolution over rougher surfaces. Over rough surfaces with greater range variability, the altimeter is able to maintain the radar echo within its range window more easily, giving more robust tracking of the echo.

Another advantage of reducing the resolution under such circumstances is the increase in the area of the pulse-limited footprint, which increases the signal-to-noise ratio of the echo. The upper limit to this improvement occurs when the return changes from being pulse-limited to beam-limited (see figure 2.1-2).

The altimeter tracks a surface by estimating the position of the leading edge of the echo, and controlling the instant at which the deramp chirp is triggered so as to maintain the leading edge of the echo in the centre of the range window. A block diagram of the ATTA is shown in figure 2.1-3. A fine height adjustment may be provided by means of a 'phase rotation' in the FFT coefficients. The height error is computed from an estimation or tracking algorithm. To avoid potential mistracking, the height error should be linearly proportional to the displacement of the echo from the centre of the range window, over the full extent of the range window, and should be independent of the shape of the echo (figure 2.1-4). The height error is filtered in a tracking loop before being used to update the instant at which the deramp chirp is triggered. The loop bandwidth is a compromise between tracking agility and reduction of height noise.

Proper estimation of the position of the echo leading edge depends on the model adopted for the echo shape. Picardi (Somma et al., 1982) developed the Sub-optimal Maximum Likelihood Estimation algorithm for the ERS-1 altimeter, to fit a simplified version of the Brown model of the ocean surface echo (Brown, 1977) to the waveform in the range window. This subsequently allows the three geophysical parameters - height, significant waveheight and backscatter coefficient - to be derived from the measured time delay, slope of leading edge and AGC value (signal strength) respectively.

Over non-ocean surface types it is difficult to fit a model to the return because of the diversity and rapid variation in the shape of surface echoes, as shown in figure 2.1-5. A common approach is to fit a model which is independent of the surface echo shape. An algorithm developed for the ERS-1 altimeter is the Offset Centre Of Gravity (OCOG) algorithm (Wingham, 1986). This estimates the position of the leading edge of the echo by first computing the position of centre of gravity of the echo, and then offsetting the track point by half the echo width (figure 2.1-6 and appendix A.6). Another algorithm based on the same principle is the Model Free Tracker (Levrini, 1990) which is claimed to have a superior performance.

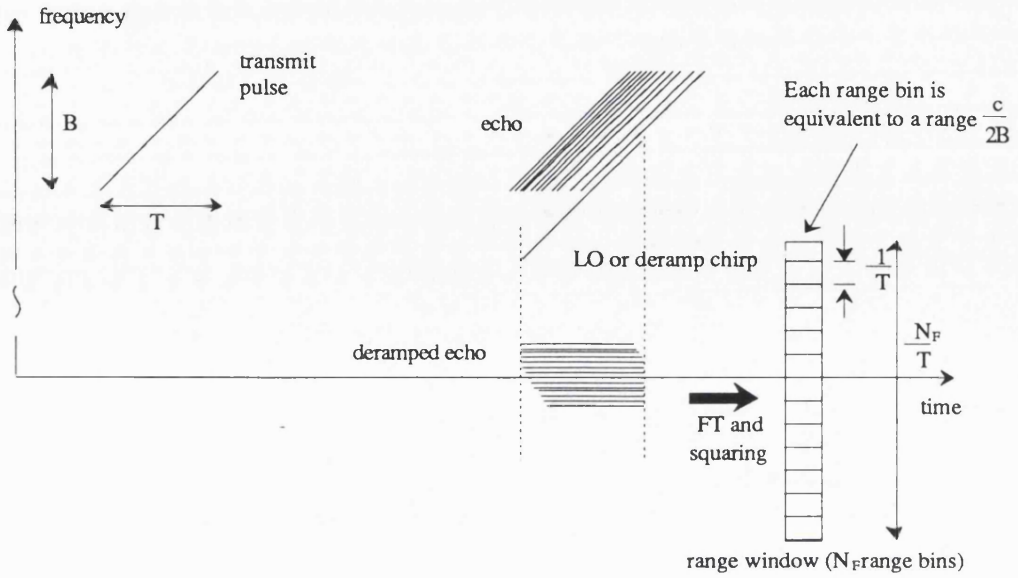

Figure 2.1-1. The full-deramp principle of operation of a radar altimeter. The spectral components of the baseband signal contain the timing of the echo.

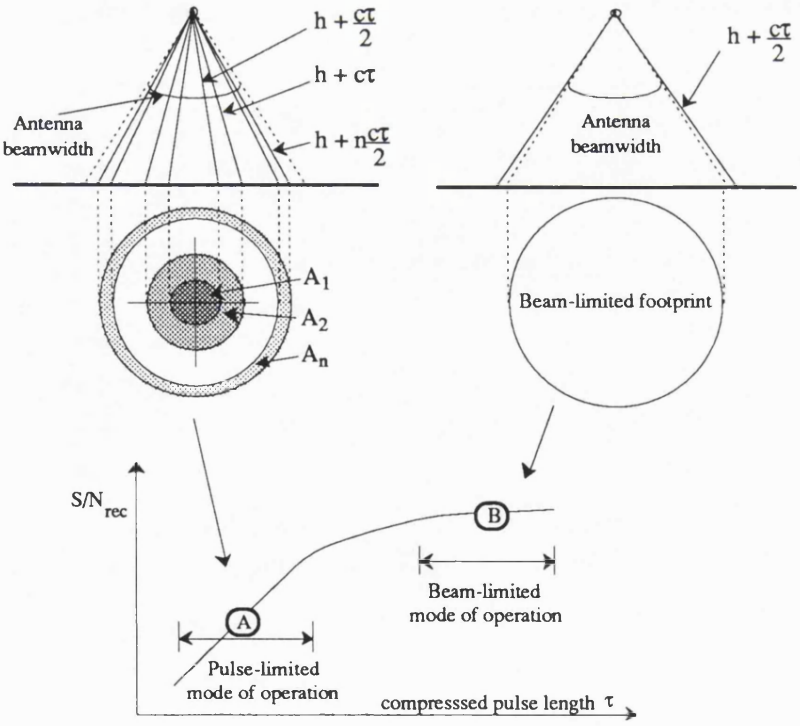

Figure 2.1-2. The pulse and beam-limited geometry of the satellite altimeter. The return becomes progressively more beam-limited, as the ramp rate is reduced.

The ATTA has an additional on-board algorithm to determine which chirp rate is appropriate for tracking the surface (Griffiths et al., 1987). It will reduce the chirp rate when the echo has drifted a certain distance from the centre of the range window (illustrated by the 'window switch' block in figure 2.1-3). Conversely, a similar criterion is applied to close the range window when appropriate, so that the echo is always tracked at the finest resolution consistent with maintaining track. An example of this principle is shown in figure 2.1-7.

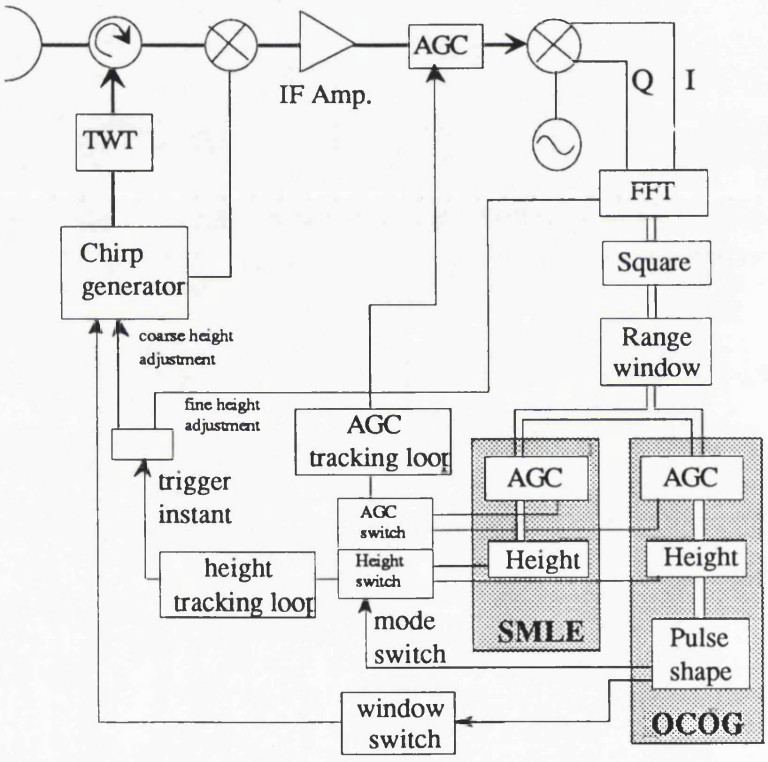

Figure 2.1-3. A block diagram of the Adaptive Terrain-Tracking Altimeter. The choice of tracking algorithm (SMLE or OCOG) is determined by the pulse shape. The window switch algorithm controls the bandwidth of the chirp (i.e. resolution of altimeter). The tracking loop smooths the height estimate. The most significant bits of the height word are used to position the deramp chirp and the least significant bits provide a fine adjustment at the FFT.

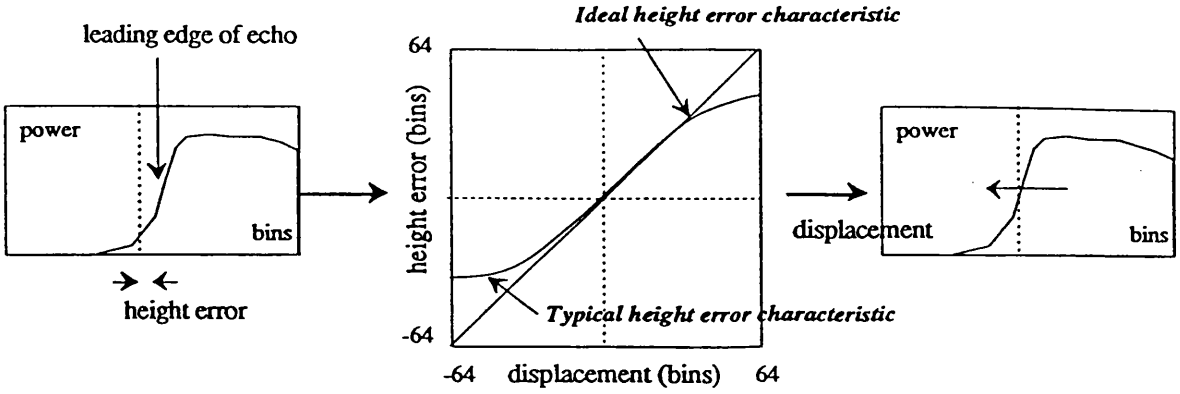

Figure 2.1-4. The ideal (linear with unity slope) and typical characteristic of the height error algorithm. The leading edge of the left hand echo is displaced from the centre of the range window. A height error is computed and is used to reposition the echo back to the centre of the range window.

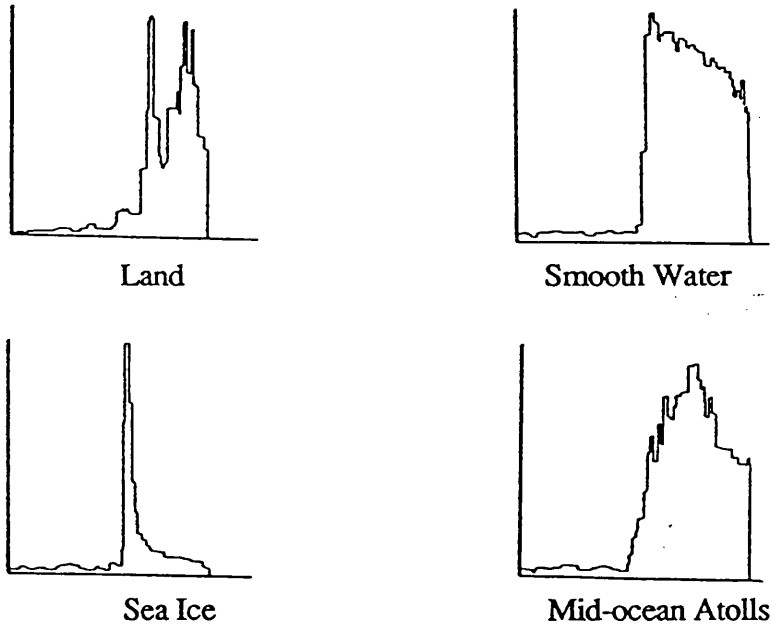

Figure 2.1-5. An example of four common types of radar altimeter echo (after Vass and Handoll, 1991).The echoes represent returns from land, smooth water, sea ice and mid-ocean atolls. The power of the echoes is plotted as a function of delay time.

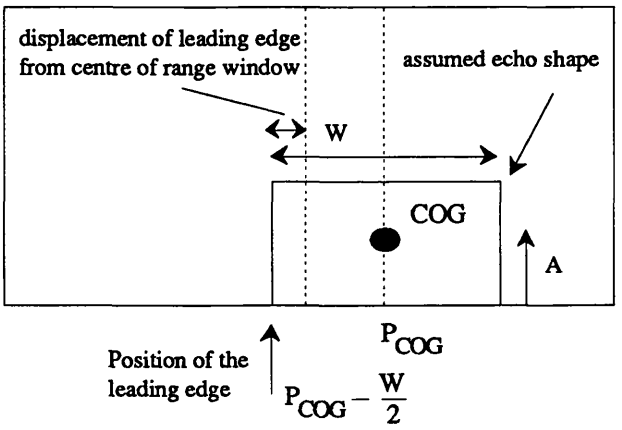

Figure 2.1-6. Approximating the position of the leading edge of the echo using a centre of gravity tracking algorithm. The position of the centre of gravity (COG) is first computed, and then offset by half the echo width.

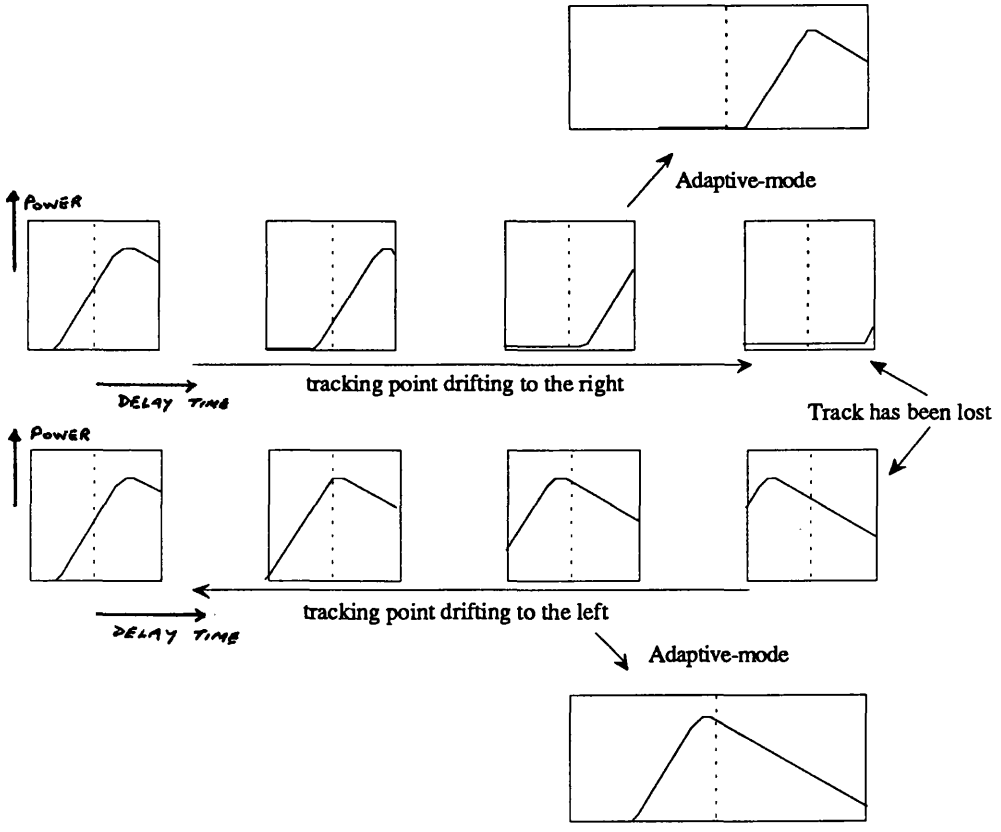

Figure 2.1-7. An example of the tracking point being lost, and the resulting switch to a coarser resolution in order to maintain track of the echo.

2.2 ALTIMETER TESTING

A suggested testing scheme for an altimeter is shown in figure 2.2-1. It is an 'end-to-end' scheme, and indicates the phases of testing and calibration necessary to produce useful geophysical data products.

The instrument design of ocean-dedicated altimeters is well established. The design of terrain-tracking altimeters is still at an early stage. In this regard, it is hoped that the ERS-1 altimeter will provide useful tracking information from its operation over the ice covered regions. Return signal simulation over simulated terrain is therefore necessary to confirm the feasibility of an instrument design and its tracking software. Levrini et al. (1990) have analysed the performance of a number of tracking algorithms using a software implementation of a return signal simulator and a terrain-tracking altimeter with adaptive resolution. This phase of testing is indicated by the oval box in the top right-hand corner of figure 2.2-1. A hardware implementation of a return signal simulator, on the other hand, will reveal a lot more information on the true performance of the prototype altimeter.

A number of instrument design changes were incorporated into the prototype ATTA, manufactured by British Aerospace (BAe). The SAW chirp expander has been replaced by a digital chirp generator, in order to obtain higher bandwidths, and more stability in the instant at which the chirp is triggered. The second major change is in the number of range bins that define the range window, which has been doubled to 128. A faster waveform processor has also been included to speed up the accumulation of echoes in the range window.

The latter phases of the testing scheme in figure 2.2-1 constitute the calibration of the instrument and subsequent corrections to the data product. Calibration is defined by Francis (1982) as '*the means by which the instrument measurements can be mapped into physical quantities, related to known standards*'. Overall calibration is considered in terms of engineering calibration and geophysical calibration. The former is a calibration of the altimeter raw data, and calibrates the measured time delay, and signal strength. The latter is a calibration of the data product. Calibration is performed after the launch, and the resulting corrections are applied to the altimeter raw data during ground processing of the radar echoes. A check that the data lies between acceptable limits and the resulting flagging of anomalous data is carried out on the ground, ensuring that the data product is validated.

Engineering calibration can be viewed in three different forms. Firstly, the engineering components of the altimeter are calibrated pre-launch. Secondly, an internal calibration of

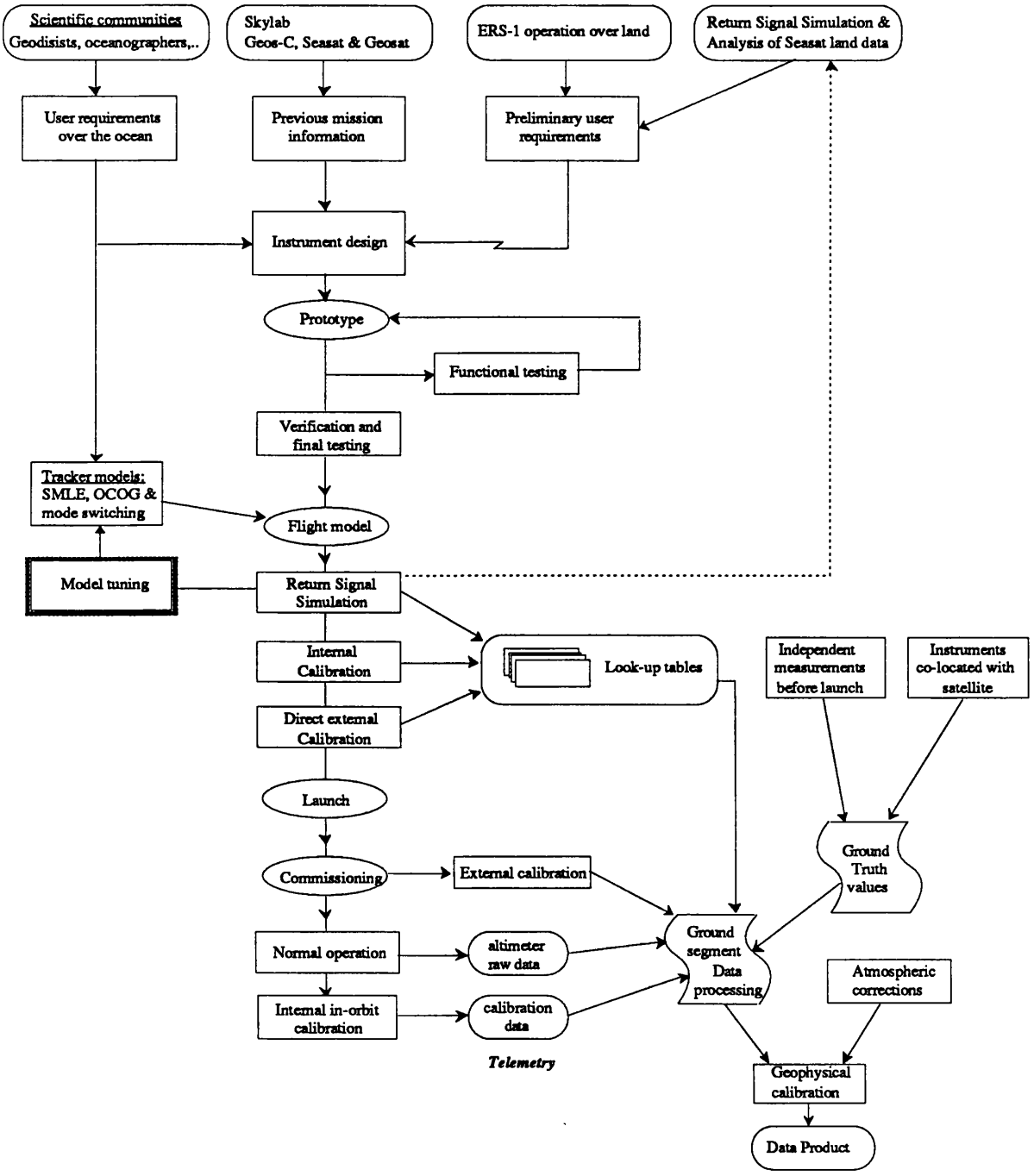

Figure 2.2-1. An overview of the calibration and testing envisaged for the Adaptive Terrain-Tracking Altimeter. This scheme illustrates the connection between the various pre-launch and post-launch calibration activities.

the engineering parameters is performed regularly during the operation of the altimeter (Francis et al., 1982). This results in corrections that are required to compensate for time-varying, and thermal-varying effects. Finally, an external calibration is performed during the commissioning of the altimeter to compare the altimeter-derived measurements with independently derived measurements. It includes all the engineering parameters, and is thus an absolute calibration (Francis and Duesmann, 1988). Many of the ERS-1 techniques discussed in §2.3 and §2.4 are directly applicable to the ATTA. As a result, only a brief critical assessment of these methods will be given at the end of this chapter.

Return Signal Simulation is also performed on the flight model in order to optimise the models used for estimating and tracking the echo waveforms, and to determine a realistic measure of the expected performance of the altimeter. The results of the return signal simulation then become a useful yardstick for analysing the in-flight performance of the altimeter, as it was for the SEASAT altimeter (Townsend, 1980). Over non-ocean surfaces, the user requirements are not as well defined as for ocean surfaces, and as a result the resolution switching algorithm, the tracking algorithms and the tracking time constants required for terrain tracking need to verified and optimised. Thus the return signal simulator is an essential element of pre-launch testing for the adaptive terrain-tracking altimeter.

2.2.1 Ocean Return Signal Simulators

A Return Signal Simulator is a device that returns an RF pulse, modulated by the realistic characteristics of the surface echo, in response to the transmit chirp trigger of the altimeter. This signal is delayed by the round trip propagation delay between the altimeter and the simulated surface, and should correctly represent information such as the echo shape, surface roughness, backscatter coefficient and statistical fading observed on a pulse-by pulse basis. A complete description of how these are modelled is presented in chapter 3.

Ocean return simulators have been used to characterise the SEASAT and ERS-1 altimeters. In each case, the RSS was able to measure the height precision, significant waveheight and backscatter coefficient precision of the altimeter. Figure 2.2-2 shows the measured and ideal height noise vs waveheight characteristic for a simulated ocean return using the RSS for the SEASAT altimeter. The difference in the curves indicated an additional noise contribution in the altimeter, either due to noise in the altimeter or noise passed to it from the RSS. MacArthur (1978) stated that the absence of an independent

method for accurately verifying the shape of the simulated return with a precision better than the altimeter itself, limits the ability of the RSS to calibrate waveheight. By using an RSS for the SEASAT altimeter, it also became clear that the interaction between the separate SAW chirp generator for the RSS and that for the deramp chirp introduced some spreading and raised the sidelobes in the point target response. This underlined the need to use the same chirp for both transmit and deramp.

The 10 cm height noise referred to in figure 2.2-2 is an accepted performance limit for the altimeter, which has been adopted for the ERS-1 altimeter (Levrini and Rubertone, 1984).

The same sort of testing was performed on the ERS-1 altimeter. However in addition, the RSS allowed the calibration of the gain step of the AGC used to control the amplification of the received echoes. Thus it played a principal rôle in determining the nominal value for the conversion of AGC to surface backscatter coefficient. Similarly, it enabled the measurement of the coefficients required to convert the on-board estimate of the leading edge slope of the echo into significant wave height (Cudlip et al., 1992). Clearly, as pointed out by both MacArthur and Cudlip, the usefulness of an RSS depends on how accurately it can represent the geophysical input parameters of the radar echo.

The pre-launch performance of the ERS-1 altimeter using an RSS to simulate an ocean surface is shown in figure 2.2-3(a) and (b). The height noise is shown as a function of σ_s (significant waveheight/4) and surface reflectivity (σ^o) in figure 2.2-3(a), and the σ_s noise is shown as a function of σ_s and surface reflectivity in figure 2.2-3(b) for both the active chain and the redundant chain of the altimeter. The height error is calculated over 50 pulses, and averaged using an α-β tracker. In all cases, the results are precise to 10 cm.

2.2.2 *Measures of altimeter performance over non-ocean surfaces*

To date, altimeters have only operated successfully over a limited amount of land, and this has generally been flat terrain. The ERS-1 altimeter has provided some coverage of the ice sheets and ice shelves of Antarctica; however it has provided no information on what resolution is required to track a particular terrain roughness, since a resolution change is controlled by macro-command from the ground, rather than by an intelligent on-board algorithm. Wingham (1987) has defined three preliminary requirements for operation over non-ocean surfaces, that should assist the design of tracking algorithms over such terrain, namely that: (1) the surface is tracked at all times; (2) the surface is tracked at the highest possible resolution; and (3) the receiver does not saturate.

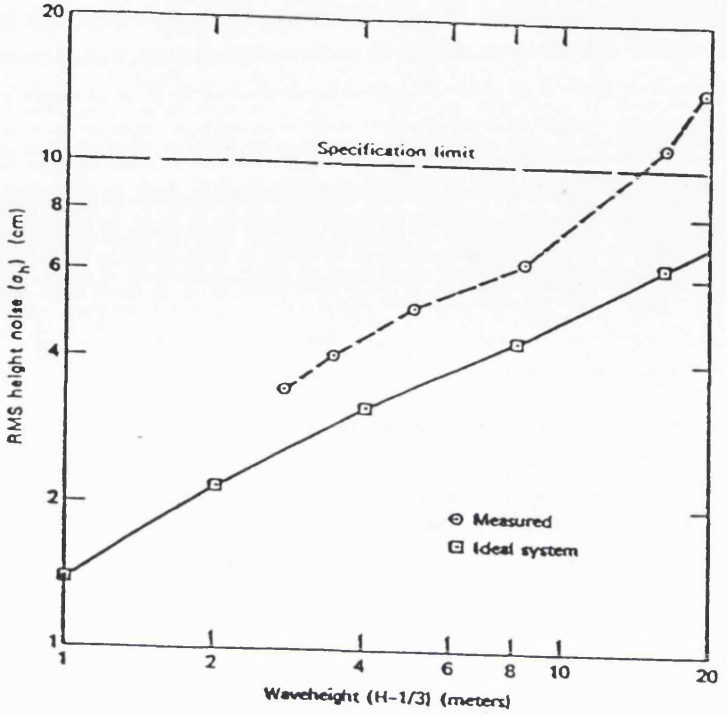

Figure 2.2-2 The pre-launch performance of the Seasat altimeter using an RSS (after MacArthur, 1978).

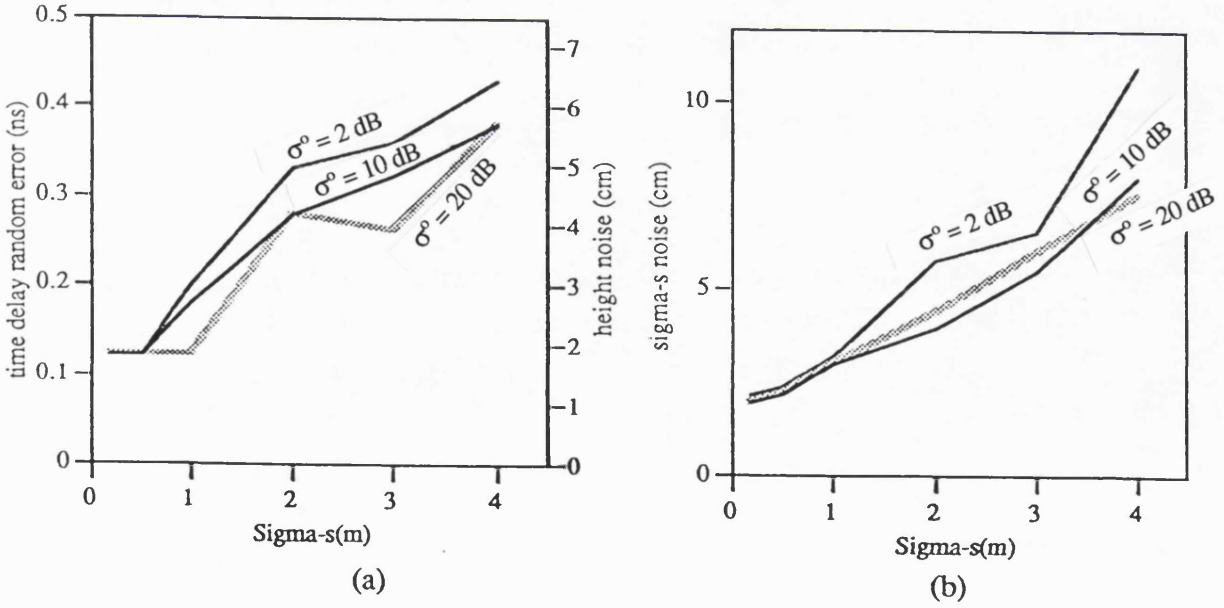

Figure 2.2-3 The pre-launch performance of the ERS-1 altimeter when an RSS is used to simulate an ocean surface (Francis, 1990). The delay and σ_s are plotted as a function of σ_s for three simulated values of backscatter coefficient.

The first and second requirement ensure that the echo leading edge is captured in the range window at the highest possible resolution each time. If necessary, the echoes can be retracked afterwards to compensate for potential mistracking. The third requirement will prevent the occurrence of pre- and post-cursors to the echo as a result of receiver saturation (Wingham and Rapley, 1987). The second requirement is the most interesting from the terrain-tracking point of view. Unless the correct criteria are used for changing resolution, there is the danger of losing track if too fine a resolution is used, or conversely the danger of not observing the interesting features at a fine enough resolution if too coarse a resolution is used. Figure 2.2-4 shows the performance of the ERS-1 altimeter using an RSS to simulate an ice surface. Shortly after the middle of the sequence, the range to the surface decreases by about 50 m; however the transition is tracked even though loss-of-track is indicated, thus indicating a non-optimum loss-of-track criterion. A number of such events have to be registered before the acquisition mode is entered.

Levrini et al. (1990) defined a criterion for a resolution change which increased the resolution if the range error, for four consecutive estimations, is smaller than a specified value, and degraded the resolution if the range error, for four consecutive estimations, is larger than a fixed threshold. If this criterion was applied to the ERS-1 altimeter, the tracker would have started oscillating between higher and lower resolutions for the sequence shown in figure 2.2-4. Oscillation also occurs because the SNR is often too low at the higher resolution to sustain track. An estimation of the noise floor, made in the early range bins of the altimeter, can therefore help to avoid this oscillatory behaviour.

Wingham has defined the following measures of performance for adaptive tracking of a rough surface:

N_{let} is the percentage of the time the return is maintained in the range window,
Q_n is the percentage of time the echo is tracked at the n^{th} resolution (n=1 is finest),
N_{sat} is the percentage of time the echo is tracked and not saturated,

(2.2-1)

Since these parameters are very much topography-dependent (Levrini et al., 1990), a parameter that is optimum for one surface may be far from optimum for another surface. For example it would be expected that Q_3 and Q_4 will be high for mountainous terrain whereas Q_1 and Q_2 will be higher for sea ice. However these measures are useful for comparing the performance of different tracking algorithms or for optimising tracking time constants over a particular surface type.

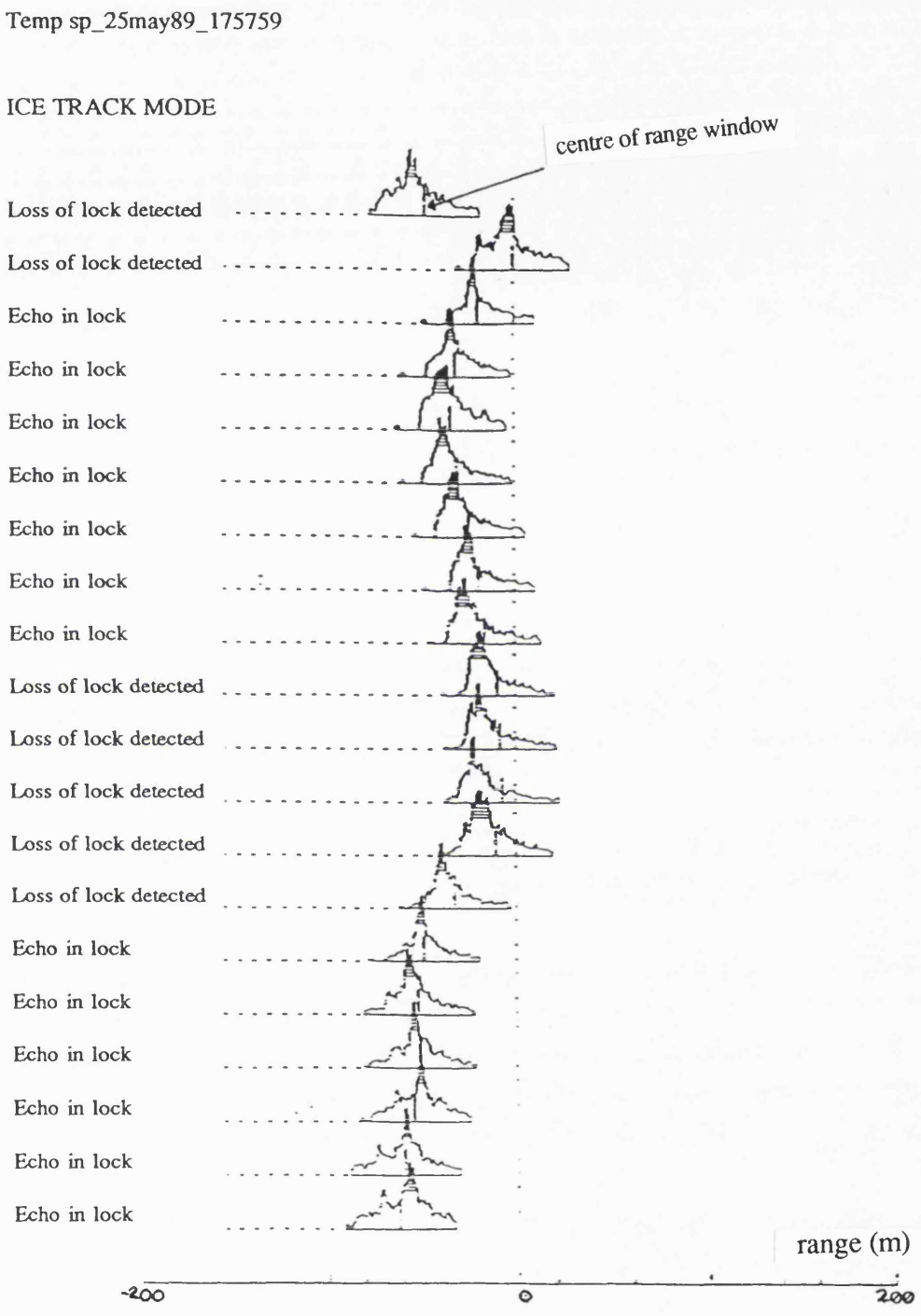

Figure 2.2-4 A series of echo waveforms from a single source packet (i.e. 1 s) over a simulated ice surface. There is a range discontinuity of approximately 50 m in the middle of the sequence. The echoes are tracked even though a loss of track is indicated.

The above measures of performance have been supplemented (Sheehan[55], 1992) to give additional information on how the echoes are tracked. These are:

N_{nzr} is the percentage of time that the first non-zero return is not registered,
N_{snr} is the percentage of time that the signal to noise ratio is below a defined threshold,
(2.2-2)

The former figure gives an estimate of the amount of time that the altimeter is making an incorrect estimate of the noise floor, since the altimeter will assume that signal in the early range bins is in fact noise. The latter gives an estimate of the time during which the altimeter is dangerously close to losing lock.

An RSS with an adaptive capability would be an invaluable method of providing echo waveforms from simulated terrain to the altimeter, thus allowing the altimeter to be tested with particular tracking algorithms and different time constants prior to launch. The RSS will also be able to quantify the height error that occurs as the resolution is changed (i.e. as the resolution is made coarser, the position of the centre of gravity in the COG tracking algorithms is biased because of the beam-limiting effect of the antenna beam).

2.2.3 Resumé of previous terrain-tracking studies

A comparison of different tracking algorithms under different noise conditions was carried out by Levrini et al. (1990). The performance of two different tracking algorithms, described in appendix A.6, was compared over seven different surface types. The yardsticks for comparison were (1) the linearity of the height error characteristic for different echoes, and (2) the parameters N_{let} and Q_1 defined in (2.2-1).

The study concluded that the Model Free Tracker (MFT) had a more linear height error characteristic to the OCOG over all surface types. The latter was shown to deteriorate for low signal to noise ratios, because the sensitivity of the position estimator to the average noise is quite bad as a result of the linear weighting with distance in the OCOG algorithm. However, it is nonetheless a robust algorithm as far as maintaining track of the surface is concerned. The former algorithm was also sensitive to the average noise floor since it would try to track the noise floor and never degrade resolution if the threshold level in the algorithm was set too low. Conversely, if the threshold is set too high, the tracker was shown to be too sensitive to the noise, and would degrade resolution unnecessarily.

However *a priori* knowledge of the noise in the altimeter meant that a suitable threshold could be found.

2.2.4 *Real time testing*

Up to now, the thesis has concentrated on the merits of supplying echoes to the altimeter. No mention has been made of the statistics of the echo. If an average echo is passed to the altimeter, then the dynamic range of the altimeter required to cope with exponential fading would not be adequately tested. The speed of processing and the accumulation time for the waveforms in the range window would also not be tested. Thus it is desirable to test the altimeter at the full pulse repetition frequency.

The pulse repetition frequency of the altimeter determines the real time requirement of the RSS. The maximum PRF is given by:

$$PRF_{max} = \frac{v}{d_{corr}} \qquad (2.2\text{-}3)$$

where v is the satellite velocity, and d_{corr} is the decorrelation distance defined by Walsh (1974):

$$d_{corr} = 0.305\frac{h\lambda}{r} \qquad (2.2\text{-}4)$$

where r is the radius of the altimeter footprint (typically 800 m), h is the altitude, and λ is the wavelength of the incident pulse.

Unfortunately, the decorrelation distance is the one parameter of the altimeter that the RSS cannot simulate since the decorrelation of the echo results from the change in signal phase due to the movement of the satellite itself between successive pulses. Thus it is necessary to assume that the PRF at which the altimeter operates is low enough to ensure echo decorrelation. For a wavelength of 2.2 cm, a satellite velocity of 7 km/s and a height of 800 km, the maximum PRF is 1043 Hz.

2.3 PRE-LAUNCH CALIBRATION ACTIVITIES

An absolute calibration of the engineering parameters is in principle possible prior to launch by flying the altimeter on an aircraft. However, the usefulness of this approach is in doubt because of the immense difference in operating conditions (e.g. antenna footprint area, platform velocity, and height). On the other hand, an effective internal calibration of the engineering parameters can be made prior to launch. In addition to the pre-launch calibration, it is also important to implement prior to launch the method of internal engineering calibration that will be used in orbit, in order to allow a comparison of the respective calibration data. The most important type of engineering calibration is the method in which a sample of the transmitter power is coupled back to the receiver, allowing both the internal time delays and gains to be calibrated.

The beam pattern and gain of the antenna is characterised in one of the conventional ways. Most large spacecraft antennas are sampled in the near-field, and the recorded information transformed to the far-field.

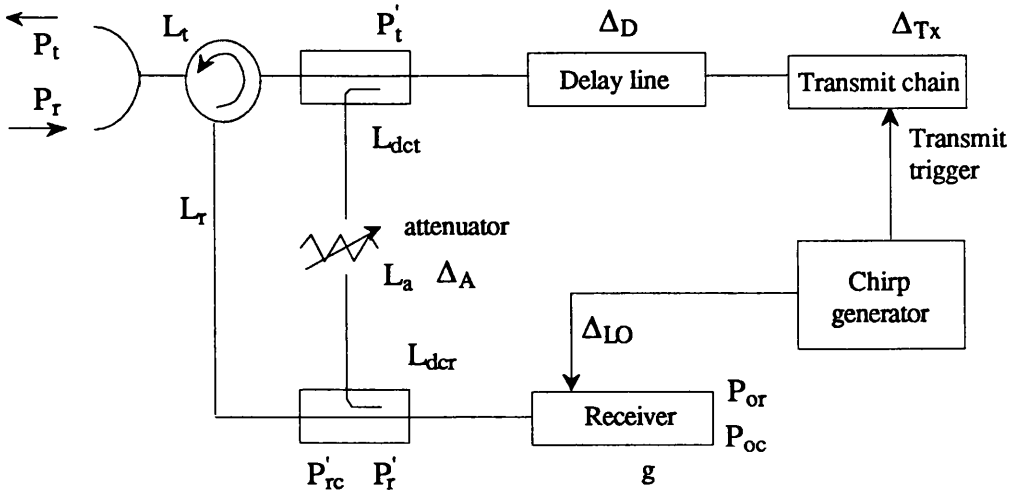

Figure 2.3-1. A block diagram of the internal engineering calibration method used in the ERS-1 altimeter. A chirped signal is coupled from the transmit chain to the receive chain. It is delayed and weighted by an attenuator, and subsequently deramped in the receiver. The receiver contains the deramp and baseband processing.

2.3.1 The ERS-1 internal calibration method

The ERS-1 altimeter employs an elegant method of in-orbit internal calibration (Francis, 1984, Somma et al, 1981), similar to the ratio method discussed by Ulaby et al. (1982).

Power level calibration

A sample of the transmitter power is coupled back to the receiver, producing a single chirp echo in the range window, equivalent to a point target. The block diagram of the coupled path, shown in figure 2.3-1, indicates how the receiver can be calibrated for both time delay and gain. From figure 2.3-1, the calibration signal in the receiver is:

$$P_{oc} = \frac{g\, L_t\, P_t}{L_{dct}\, L_a L_{dcr}} \qquad (2.3\text{-}1)$$

where g is the receiver gain, P_t is the transmit power, L_t, L_a, L_{dct} and L_{dcr} are the transmission line losses in the transmitter, attenuator and directional couplers respectively. The power recorded in the range window is related to the received power as follows:

$$P_{or} = \frac{gP_r}{L_r} \qquad (2.3\text{-}2)$$

where L_r is the transmission line loss in the receiver.

Thus the ratio of received power to transmit power, which is the radar cross section of a single point target, is calibrated by simply measuring the received and calibrated signal powers P_{or} and P_{oc} in the range window:

$$\frac{P_r}{P_t} = \frac{P_{or}}{P_{oc}} \frac{L_r L_t}{L_{dct} L_a L_{dcr}} \qquad (2.3\text{-}3)$$

During the calibration, an undesired signal is reflected from the antenna, and transmitted back to the receiver. For the ERS-1 altimeter, this signal has an isolation of 125 dB, whilst the useful calibration signal is attenuated by 100 dB. Thus thus the accuracy of this method, limited by the undesired signal, is approximately 0.015 dB. The attenuators have to be intrinsically stable with temperature over the operating life of the altimeter.

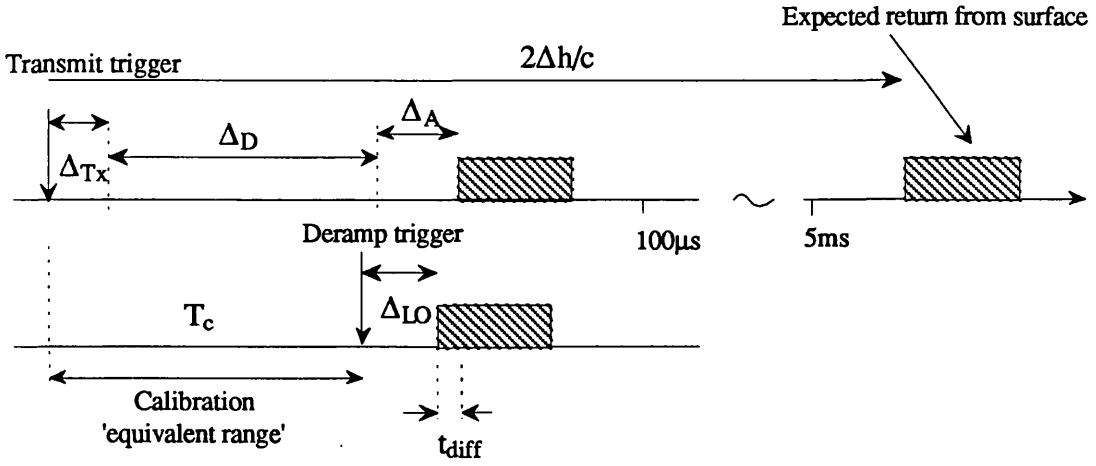

Figure 2.3-2. A timing diagram of the ERS-1 in-orbit calibration method (Francis, 1984). The calibration signal is delayed by the fixed delay Δ_D and the two parasitic delays Δ_A and Δ_{Tx}. The deramp chirp is triggered after a time T_c, but delayed additionally by the parasitic delay Δ_{LO}.

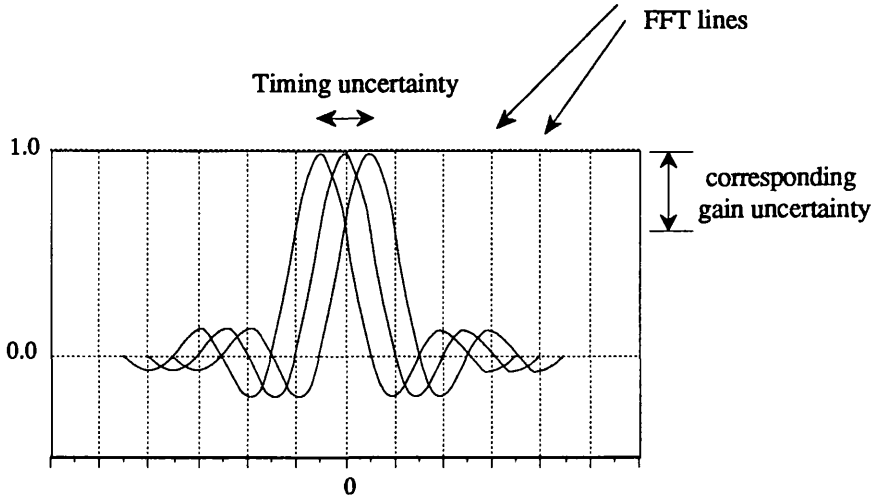

Figure 2.3-3. Examples of the uncertainty in the timing of a single point target. The error in the timing is ± half a range bin.

Internal time delay calibration

Calibration of the time delay is performed by using the deramp chirp instant as an internal reference or 'equivalent range' against which the unknown time delays in the altimeter can be calibrated (figure 2.3-2). In this scheme, it is important that the 'equivalent range' is greater than the chirp length so that the transmit chirp has ended before the deramp chirp is triggered (since only a single chirp generator is used). To achieve this the transmit chirp must be additionally delayed by Δ_D in order to align it with the deramp chirp. The time difference t_{diff} between the two pulses is measured, and is given by:

$$t_{diff} = \Delta_{Tx} + \Delta_D + \Delta_a - T_c - \Delta_{LO}, \qquad (2.3\text{-}4)$$

and the bias time $\Delta_{Tx} + \Delta_D - \Delta_{LO}$ to be calibrated is given by:

$$\Delta_{Tx} + \Delta_D - \Delta_{LO} = t_{diff} + T_c - \Delta_a. \qquad (2.3\text{-}5)$$

Thus if the delays Δ_D, Δ_{Tx}, Δ_{LO} are stationary between subsequent calibrations, then the quantity in (2.3-5) simply has to be subtracted from the time measured in the operational mode of the altimeter.

The correction factor in (2.3-5) calibrates the time delay to a precision defined by the resolution of the radar. The timing uncertainty in this quantity is illustrated in figure 2.3-3. To enhance the precision, an extended return, consisting of 50 shifted echoes, weighted according to the Brown model, is built up in the range window over the 50-pulse averaging period, as shown in figure 2.3-4. The weighting is achieved using a programmable attenuator in the coupled path, and the time displacement is achieved through a combination of coarse and fine tuning of the deramp chirp ('equivalent range'). By placing more than one echo in each range bin, it is possible to define a higher order approximation to the Brown return. The extended return is described by:

$$\sum_{k=1}^{50/N} \left(\sum_{i=1}^{N} a_i \mathrm{sinc}\left(\left(\omega - \omega_o + k\frac{2\pi}{T} \right) \frac{T}{2} + \left(i - \frac{N}{2} \right) \frac{\pi}{N} \right) \right) \qquad (2.3\text{-}6)$$

where a_i are the weighted coefficients used by the attenuator.

The primary advantage of this method is that it provides a convenient means of in-orbit calibration of delay, significant wave height and backscatter coefficient. It is, however, limited in a number of ways. Firstly, it is difficult to build wideband delay lines of adequate delay ($\geq \Delta_D$, typically 20 μs), and the stability with temperature of the delay line is difficult to guarantee even between calibration times, e.g. the ERS-1 altimeter needed a delay line in a temperature controlled oven to provide the required stability. Operation with longer chirps is likely to be a problem. The long delay line introduces a secondary effect: - additional phase distortion in the chirp waveform.

Secondly, the construction of the leading edge is a complicated process which may allow an accumulation of errors (particularly from non-linearities in the attenuator). The precision of the technique depends on the accuracy of the attenuator and its temperature stability.

Thirdly, the transmission delays in the front end are not included in the time delay calibration. The corresponding transmission line losses are indirectly included in the gain calibration since they have to be independently calibrated for use in eqn. 2.3-3. However, again no account is taken of their thermal stability. Finally, the timing is dependent on the stability of the altimeter clock, the ultimate and most stable internal reference.

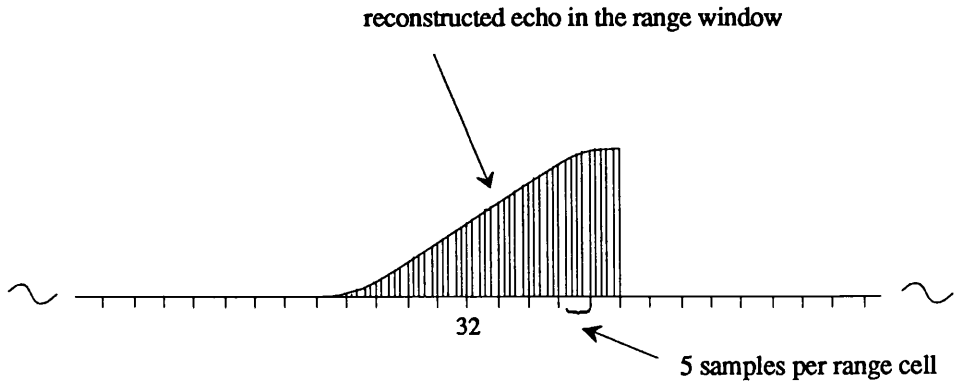

Figure 2.3-4. Improvement in the timing precision using a curve fitting technique. The echo leading edge is reconstructed using a number of individual point target responses.

2.3.2 *Pre-launch internal calibration using a precision RSS*

Internal time delay calibration

The form of internal calibration shown in figure 2.3-5 is based on a similar principle to that described in §2.3.1. The position of the deramp chirp becomes the 'calibration signal'. However, in this case, an RSS is triggered to generate a signal at the same instant as the transmit chirp, which externally links the transmitter and receiver. Thus, every delay in the altimeter with the exception of the antenna can be calibrated. The RSS generates a single chirp with respect to the transmit trigger after a delay time Δ_{Tx1}. This chirp, ideally a perfect replica of the transmit chirp, is delayed by an accurately known time $\Delta_{\tau 2}$ and passed to the altimeter where the time difference between it and the calibration chirp is measured. Referring to figure 2.3-5, the time difference t_{diff} is written as:

$$t_{diff} = \Delta_{Tx1} + \Delta_{fe1} + \Delta_{fe2} + \Delta_{\tau 2} - T_c - \Delta_{LO} \qquad (2.3\text{-}7)$$

where Δ_{fe1} and Δ_{fe2} are the front end delays, and T_c is the 'calibration' range. A second simultaneous measurement is required to account for the difference between the transmit chain delay and the external path delay to the RSS, which can be conveniently measured by observing the frequency difference f_{diff} between the two chirps on a suitably-calibrated spectrum analyser:

$$\Delta_{Tx1} - \Delta_{Tx} = \frac{f_{diff}}{b} \qquad (2.3\text{-}8)$$

Thus the bias time $\Delta_{Tx} + \Delta_{fe1} + \Delta_{fe2} - \Delta_{LO}$ to be calibrated is given by:

$$\Delta_{Tx} + \Delta_{fe1} + \Delta_{fe2} - \Delta_{LO} = T_c + t_{diff} - \Delta_{\tau 2} - \frac{f_{diff}}{b} \qquad (2.3\text{-}9)$$

This represents a calibration of the internal time delays of the altimeter. This calibration equation is limited by the accuracy of the RSS delay $\Delta_{\tau 2}$, which needs to be approximately an order of magnitude more stable than the precision required (i.e. it must be precise to the 1 cm or 67ps level). Since the transmit chain is disconnected, there is no requirement to delay the transmit chirp as in §2.3.1. Thus the delay $\Delta_{\tau 2}$ need not be as large as the altimeter delay in (2.3-5), affording the possibility of greater stability.

One reason why an RSS is unpopular for internal calibration is the fact that it fails to adequately model the distortion in the transmit chain. Phase errors on the transmit chirp can cause increased range sidelobes and introduce a range bias. Any manifestation of this effect is fully included in the method of in-orbit calibration, but is only indirectly included using a precision RSS. Figure 2.3-5 includes a comparison between the RSS chirp and transmit chirp in order to account for this effect. Figure 2.3-6 illustrates the corresponding timing diagram. The differential non-linearity between the RSS and transmit chirp sweeps can be treated as a jitter in the measurement which would be averaged over a longer observation period. This jitter is treated as a time-varying phase error when Fourier Transformed in the altimeter. If the phase distortion is expressed as:

$$\phi\left(\frac{t}{T}\right) = \phi_o + \phi_1\left(\frac{t}{T}\right) + \phi_2\left(\frac{t}{T}\right)^2 + ... \qquad (2.3\text{-}10)$$

then the mean frequency measured over the period T can be shown to be:

$$\bar{f} = \frac{1}{T}\sum_{i=1} \phi_i \qquad (2.3\text{-}11)$$

where the ϕ_i are the normalised coefficients in the definition of the phase distortion. It will be shown in §6.2 that this is identical to the frequency shift in the range window as a result of the same distortion.

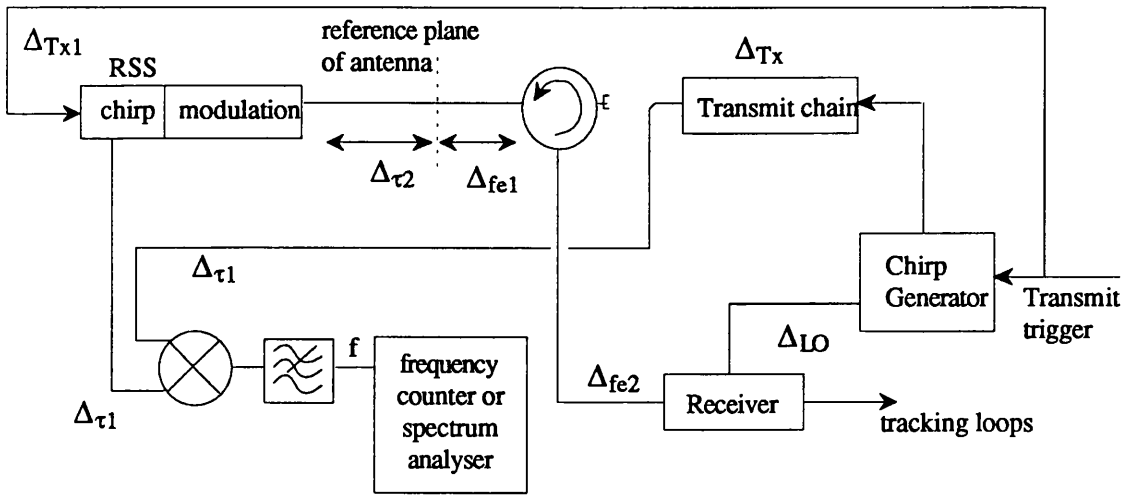

Figure 2.3-5. A form of internal pre-launch calibration using a precision RSS. In this method, the transmitter and receiver are externally linked to allow all the time delays in the systems to be calibrated.

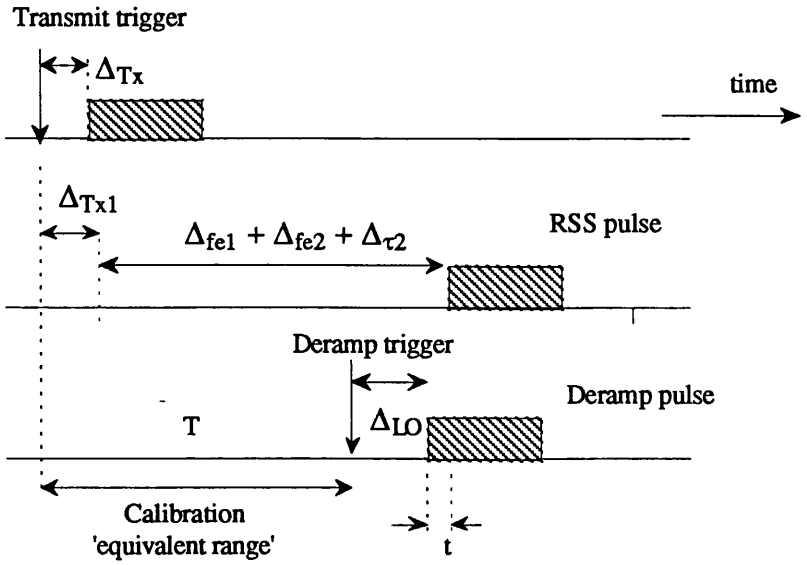

Figure 2.3-6. The timing diagram for the calibration method described in figure 2.3-5. The RSS chirp is triggered after a time ΔT_{x1}. The centre timing diagram shows how the RSS pulse is delayed by the front end of the altimeter. A deramp pulse provides the timing reference for the relative calibration.

Power level calibration

The basic RSS-altimeter set-up of figure 2.3-5 can be used to provide a relative gain calibration of the range window; however the RSS does not represent a useful means of internal backscatter coefficient calibration since its output power does not relate to the transmit power of the altimeter.

Significant waveheight calibration

Calibration of significant waveheight is a post-launch activity since it is a geophysical product. It is only possible post-launch to verify that the waveheight is proportional to the slope of the leading edge of an echo. The RSS however can be used to calibrate the slope of the leading edge. Such a calibration can be performed in two ways. Firstly, an echo of defined slope can be passed to the altimeter in one PRI. As we will see in chapter 3, this is prone to increasing the noise level on the calibration signal. Secondly, the echo can be built up over 50 PRIs by providing 50 point targets in successive range bins in a similar

manner to the signal shown in figure 2.3-4.

The leading edge slope is defined in the altimeter by the reciprocal of the width of the leading edge when the amplitude of the signal in the range window has been normalised to unity. Since the signal is normalised, there is no requirement on the absolute power value of the RSS output, but only on the linearity of the power over the dynamic range of the echo. The individual point target responses are weighted according to a Brown return.

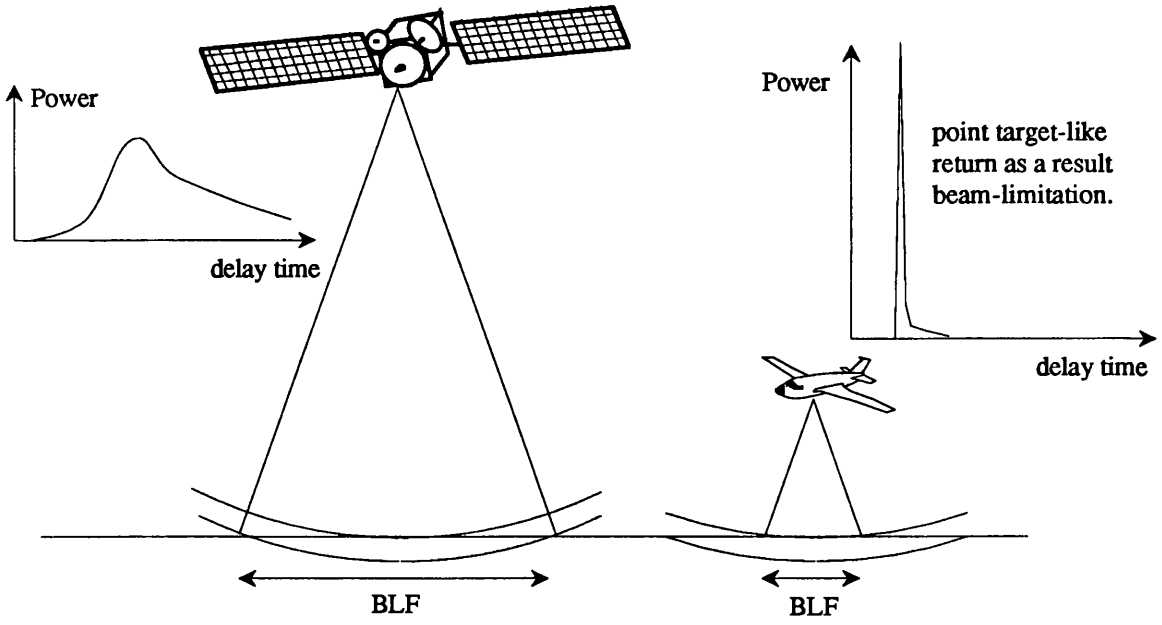

Figure 2.3-7. The operating conditions differ considerably when an altimeter designed for a satellite is flown on an aircraft. The satellite altimeter footprint is pulse-limited, thus the power is returned from a number of range bins for most surfaces. The footprint from an aircraft is much smaller as a result of the considerably reduced altitude. Thus the return is beam-limited in this case. In addition, the power returned is considerably higher.

2.3.3 *Pre-launch external calibration*

One method of performing external calibration prior to launch is to carry the altimeter on board an aircraft or balloon. For example, the NRL experimental radar altimeter flown on a C-54 aircraft (Walsh, 1974; Yaplee, 1972) was used to verify SKYLAB experimental data.

In operating an altimeter at a considerably lower altitude, some important differences must be noted. Firstly, from a satellite orbit, the illuminated footprint on the surface is pulse-limited. However, for an airborne altimeter, the footprint is beam-limited by virtue of the low altitude (figure 2.3-7). The spatial resolution is comparable to that of most satellite imaging radars, and as a result there may be a departure from Gaussian statistics used to define the surface echo. Secondly, the link budget changes dramatically. Although the backscatter is a property of the surface, its measurement is a function of the radar system. Thus if a comparison of the backscatter is to be made between an airborne and a satellite-borne altimeter, the only realistic scenario is a point target, e.g. a transponder. Francis[17] (1982) estimated that to avoid the beam-limiting effect, the beamwidth of the ERS-1 altimeter would have to be increased from 1.5° to 22.5° at an altitude of 3 km. However this level of change means that the small-angle approximation in the Brown model (eqn. 8: Brown, 1977) may no longer be valid. Thus, uncertainties always exist in either the engineering model or the models used to relate the engineering parameters to geophysical ones. In spite of these limitations, this type of testing may provide a useful source of ground truth or σ^o validation during post-launch commissioning.

2.4 POST-LAUNCH CALIBRATION

2.4.1 *External calibration of the engineering parameters*

External height calibration is usually achieved by comparing the height measurement made by the altimeter with an independent laser ranging to a defined point in the satellite trajectory. The defined point in the orbit corresponds to a particular point on the surface e.g. a laser on an island (the 'Bermuda' method) or an ice sheet. It is important that the altimeter is operating in a steady-state condition (e.g. over an ocean surface) at the instrumented point. Otherwise, as in the 'Bermuda' method, the altimeter data need to be retracked and interpolated in order to locate the instrumented point. The 'Venice Tower' method, used for the ERS-1 altimeter, is an improved technique (Francis and Duesmann,

1987; Francis and Duesmann, 1988) in which the satellite overflies a tower that is fixed to the sea bed in about 16m of water. As a result, the altimeter tracking loops are in a steady state as the altimeter overflies the calibration point.

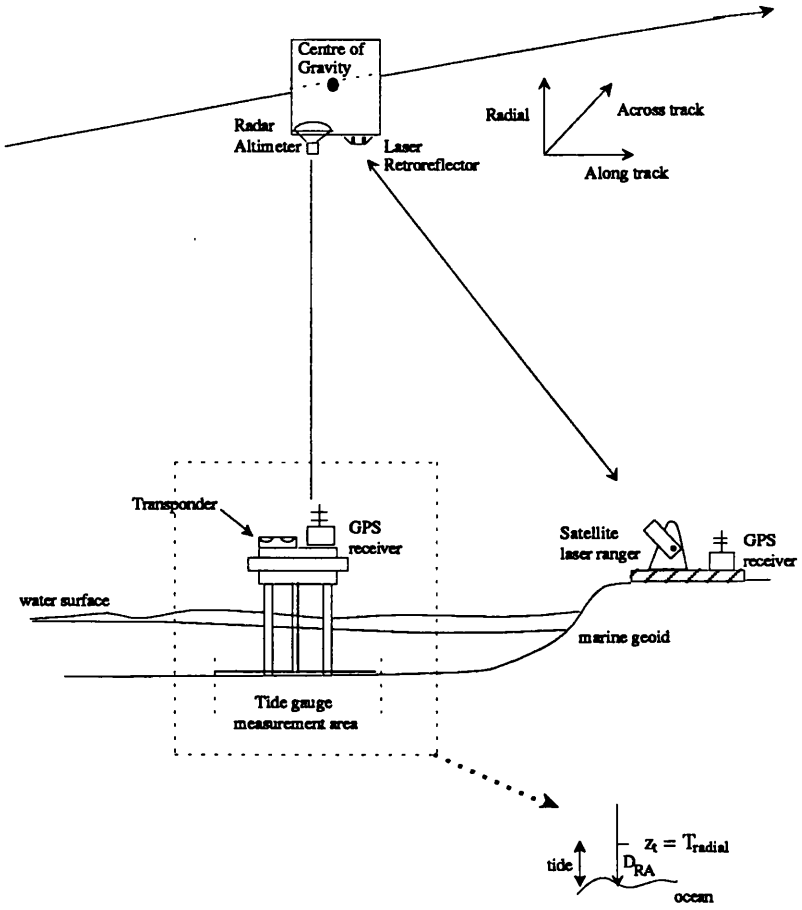

Figure 2.4-1. The 'Venice Tower' external height calibration method (Francis and Duesmann, 1987). The measured height is made to the water level. The satellite is positioned in the reference frame using a number of satellite laser ranging stations.

The angular tracking rate of a single laser may prevent continuous tracking of the satellite in the neighborhood of the measurement. Thus the 'Venice Tower' method employed a cluster of fixed and mobile Satellite laser Ranger (SLR) sites so that the satellite can be tracked simultaneously by up to five lasers, thus guaranteeing continuous tracking during the overpass. The geometry of the calibration scenario is shown in figure 2.4-1.

Moreover, the reliability of this technique is enhanced through the redundancy in the number of SLR stations, and because all fixed points (i.e. the tower and the SLR sites) in the measurement system are referenced directly via the Global Positioning System (GPS). Currently, GPS has a baseline accuracy of 1ppm (i.e. 1.6 cm for the shortest baseline of 16km). The radial position of the satellite is computed from at least 3 SLR ranging measurements. In the laser frame of reference, the following equation (inset of figure 2.4-1) (Francis and Duesmann, 1987) for the height bias can then be written:

$$b_{RA} = D_{RA} - \{S_{radial} - T_{radial} - tide\} \qquad (2.4\text{-}1)$$

where b_{RA} is the height bias of the radar altimeter, D_{RA} is the altimeter range to the water surface, S_{radial} is the satellite radial position in the laser frame, T_{radial} is the tower radial position in the laser frame and *tide* is the tide-gauge measurement from the tower reference point to the water surface.

In this calibration scheme, the emphasis is in mitigating the geophysical effects as much as possible, so that it could be considered an engineering rather than geophysical calibration. The low waveheight (approx. 0.5 m) in the region of Venice thus gives rise to minimal altimeter height noise Other geophysical effects such as tropospheric and ionospheric effects are impossible to minimise. In these cases, an upper bound to the error has been estimated. Francis has performed a detailed study of the effect of all the errors expected during the calibration campaign, and has shown that the bias errors in the calibration, which will be indistinguishable from the altimeter bias, will be about 3 cm. When the random component of the error is added to the bias, the total error can vary from 4.5 cm (summer) to 6 cm (winter).

2.4.2 *Geophysical calibration*

Geophysical calibration differs from engineering calibration in that it calibrates the data product rather than the instrument. The data products of the altimeter (height, significant waveheight and surface wind speed) are based on models that convert the engineering parameters into the relevant geophysical parameters. The method of engineering height calibration described in § 2.4 includes a constant term to allow for ionospheric and wet and dry tropospheric effects; however this does not account for variations in these corrections. These variations have been modelled (Bean and Dutton, 1966; Wrench, 1986) and are used to produce the geophysical height data product.

The significant waveheight may be validated by in-situ measurements using buoys and research vessels co-located with satellite observations. A large data base of measurements is needed to check and tune the models, and as a result careful planning must be undertaken to guarantee that the research vessels are correctly located. The backscatter coefficient may be calibrated by an overflight of a feature with a known backscatter coefficient, e.g a transponder, a sea surface, a desert region or even some areas of the polar ice cap. A slight variant of this type of calibration is a simultaneous satellite and aircraft overflight of the feature, thus reducing the uncertainty in the value of the reference backscatter coefficient.

2.5 Summary

This chapter summarises the testing schemes for the SEASAT and ERS-1 altimeters, and extends them to the Adaptive Terrain-Tracking Altimeter. The calibration procedures for the ERS-1 altimeter are analysed, and are shown to directly applicable to the ATTA. A precision return signal simulator is considered as a method of pre-launch delay time calibration.

The use of return signal simulators in the SEASAT and ERS-1 altimeters is reviewed. In each case the RSS was used for simulation of the geophysical parameters. Some results from the simulation of the ERS-1 ice-mode are also analysed. A return signal simulator is recommended as a means of testing the resolution changing and tracking algorithms of the ATTA. A study of resolution switching in 1990 made many useful conclusions regarding the performance of the tracking algorithms; however the number of non-ocean measures of performance limited the analysis. Two additional measures of performance over non-ocean surface have been proposed to facilitate future analysis.

It is believed much more could be learnt from a simulation of a prototype altimeter.

Chapter 3

Simulation of Altimeter Echoes

In this chapter, we continue with a study of some of the models used for generating altimeters echoes. In particular, we focus on a very general approach to echo modelling (Moore and Williams, 1957) and use this to develop an engineering model for the simulation of echo signals. At a number of points in the chapter, the link between the physical model and the engineering model will be shown. Finally, the chapter will discuss the generation of echoes with coarser resolutions, and a novel approach will be discussed.

3.1 SCATTERING MODELS

A rigorous formulation of the scattering problem (Berry, 1973) is required if the variation in surface elevation is comparable to the wavelength of the incident pulse and if the surface correlation length is of the order of the spatial resolution of the radar altimeter (Ulaby et al., 1982). Neither of these conditions are met for the pulse-limited altimeter, and thus it is possible to apply a simpler theory, based on geometric optics (Barrick, 1968), where the longer period variations of the surface are modelled and the finer detail (i.e. local roughness) is treated in a statistical manner.

The early work was pioneered by Moore and Williams, and later by Brown (1977). The former considered the surface as an ensemble of scatterers, i.e. facets with varying orientation, reflectivity and gain pattern. The underlying assumption was that the surface comprised a large number of such facets, and that the returns from each contributed more or less equally to the total scattered return. They developed an expression for the average returned power from a rough scattering surface at near-vertical incidence.

Brown extended their analysis to the return from a surface with backscatter coefficient σ^o, and described the mean power returned from an extended target as:

$$p_r(t,x) = \frac{P_t \lambda^2}{(4\pi)^3} \int_{-\infty}^{\infty} \int_{-\infty}^{\infty} G^2(\theta)\, \sigma^0(\phi)\, s(t - 2|r|/c)\, |r|^{-4} dS \qquad (3.1\text{-}1)$$

where t is the time from the instant of transmission, x is the location of the satellite in the along track direction, **r** is the vector joining a point on the surface to x, θ is the angle between the antenna boresight and the vector **r**, ϕ is the angle between the local surface and **r**, s(t) is the convolution of the compressed pulse shape with the local surface roughness, and σ^o is the surface backscatter coefficient.

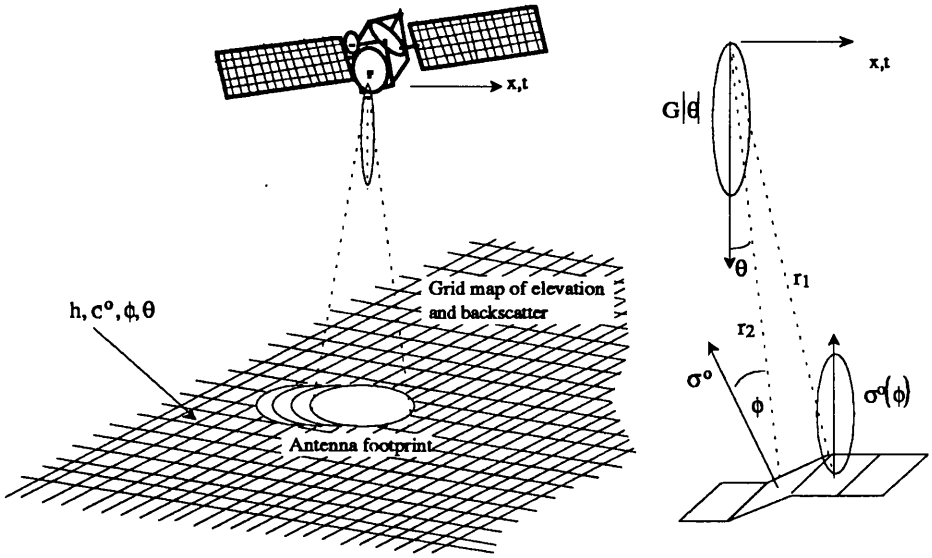

Figure 3.1-1. The grid map of elevation and backscatter coefficient, which forms the basis of the radar echo generator. The power returned from each facet is computed, and summed incoherently over all the facets in the altimeter footprint. The geometry for each facet is also shown.

Brown also showed that the above expression for the mean power could be expressed as a convolution of the transmitted power and a function which includes antenna pattern, ground properties and range to the surface. That is:

$$P_r(t) = P_{FS}(t) \otimes q_s(z) \otimes s_r(t) \qquad (3.1\text{-}2)$$

where $P_r(t)$ is the square law detected power from a rough surface, $P_{FS}(t)$ is the average flat surface impulse response, $q_s(z)$ is probability distribution of the heights of the scattering facets, and $s_r(t)$ is the radar system point target response. The Brown model simplifies (3.1.2) for the return power from an ocean surface by assuming that the height

PDF of the surface, the impulse response of the instrument and the antenna beam pattern can all be represented by Gaussian quantities. This results in a simple analytical expression which has proved to be a very successful model for the altimeter echo from the ocean.

Hayne (1980) and Srokosz (1986) have refined Brown's model for the ocean surface by considering a non-Gaussian (e.g. skewed) distribution for the height PDF in order to account for an observed bias in estimation of height. In a later chapter, we will account for the effect of a non-ideal instrument impulse response. It is nonetheless claimed (Rodriguez, 1988) that the model is not precise enough to define the altimeter data products to the required precision.

The return from a non-ocean surface is more difficult to quantify because of the non-uniformity of the statistics and because of the non-uniformity of the surface. The mean power can be computed from (3.1-1). A numerical computation of the mean power thus requires the backscatter coefficient and the convolution of the compressed pulse shape with the local surface roughness to be known at all points on the surface.

Wingham (1986) simplified the integral in (3.1-1) by assuming:

(a) that the surface comprised a matrix of facets, each of dimension 200 m x 200 m. Each facet has an associated area, elevation, orientation, backscatter coefficient and polar response.
(b) that the integral becomes an incoherent summation of the power from those facets lying within the footprint defined by the antenna beamwidth,
(c) that the power is summed by *binning* the power from each facet into a number of resolution cells depending on the maximum and minimum two way delay time to the facet.

The integration is then repeated for all the altimeter locations above the simulated terrain. Figure 3.1-1 illustrates the geometry of this model.

The above models define the power in each of the range bins of the altimeter; however none of the models express the echo in a form that is useful for return signal simulation. The following section will bridge the gap between these physical models and the engineering model required for simulation.

3.1.1 *The return signal scattered from a Poisson process*

Consider a surface comprising a large number of scattering facets. The echo contribution from each facet is a function of the two-way time delay between it and the satellite. Beckmann and Spizzichino (1964) have shown that the altimeter power spectrum will be exponentially-distributed irrespective of the process used to describe the scattering from a rough surface. Thus a Poisson process is sufficient, but more importantly is convenient, to describe the scattering from the surface. The advantage of the Poisson process is that the statistics are a function of time rather than amplitude. Thus it is inherently easier to study the effect of changing the resolution on both the physical and the engineering model.

The Poisson process will be defined as:

$$d(\tau) = \sum_{i=1}^{N} \delta(\tau-\tau_i) \qquad (3.1\text{-}3)$$

where τ_i is the two-way delay time to the i^{th} facet, τ is the time variable in the delay domain, δ is the Dirac impulse function, and $d(\tau)$ is the impulse response of the surface. Eqn. 3.1-3 is effectively a general expression for the impulse response of the surface. Equally, the process could have been described by a Gaussian process:

$$d(\tau) = \sum_{i=1}^{N} a_i \delta\left(\tau - t_o - i\frac{2\delta_r}{c}\right) \qquad (3.1\text{-}4)$$

where t_o is the time of the first return, δ_r is the range resolution, and a_i is the amplitude of the return in the i^{th} resolution cell. Each a_i is Gaussian random variate, as a result of the large number of independent scatterers contributing to the return in a single resolution cell (Central Limit Theorem). The relation between the two processes is shown in figure 3.1-6, and will be derived in §3.1.3. In the limit, when there is only one non-zero value of a_i, eqn. 3.1-4 represents perfect specular reflection.

For a pulse-limited altimeter with a beamwidth θ_B, the duration of the return depends on the slope of the surface, and the beamwidth of the antenna. Because of the two way attenuation in the antenna, the power of the echo is attenuated by 6 dB at an angle $\theta_B/2$ from nadir. Consider the nadir pointing beam in the geometry shown in figure 3.1-2. It can be shown that the duration of the return, corresponding to an antenna angle θ, is:

Footnote: The facet slope is included in eqn. (3.1-3) by varying the density of point target responses in the Poisson process in accordance with the strength of the return.

$$\tau_N - \tau_1 = N\delta_r = \frac{2}{c}\left(\frac{h}{\cos(\theta/2)} - h\right) \qquad (3.1.5)$$

Thus for an altitude h of 800 km, an antenna beamwidth of 1°, and a resolution cell δ_r of 3.125 ns, the duration of the echo from the leading edge to the point corresponding to the antenna beam width is typically 800 ns (i.e 265 range cells).

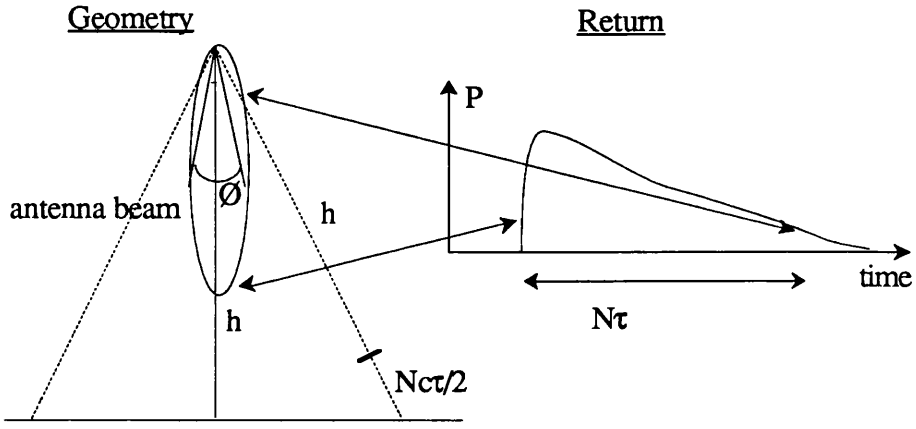

Figure 3.1-2. The duration of the return echo for an antenna beamwidth θ_B. The return (right) after time $N\tau$ is attenuated by the gain pattern of the antenna.

3.1.2 The scattered return from a surface

The scattered return g(t) is the convolution of the surface impulse response and the transmitted chirp:

$$g(t) = \cos\left(\omega_o t + 2\pi\frac{b}{2}t^2\right) \otimes d(t) \qquad (3.1\text{-}6)$$

where ω_o is the chirp centre frequency. It is assumed, for the moment, that the chirp is free of amplitude and phase errors. This will be treated separately in chapter 6. The form of (3.1-6) indicates that g(t) is the sum of a series of overlapping chirps, displaced in time.

Rewriting the convolution in its integral form:

$$g(t) = \int_{t_1}^{t_N} d(s)\cos\left[\omega_o(t-s) + 2\pi\frac{b}{2}(t-s)^2\right][U(t-s) - U(t-s-T)]\,ds \quad (3.1\text{-}7a)$$

where U(t) is the Heaviside unit step function and T is the chirp duration. Note that g(t) extends from t_1 to t_N+T. The argument of the cosine is a function of real physical time t, which varies over the chirp duration, and delay time s which varies over the maximum echo duration. Consider a change of variable given by $s_1 = s - t_r$, where $t_1 \le t_r \le t_N$. Then (3.1-7a) can be rewritten as:

$$g(t) = \int_{t_1 - t_r}^{t_N - t_r} d(s + t_r) \cos\left[\omega_o(t - t_r - s) + 2\pi \frac{b}{2}(t - t_r - s)^2\right][U(t - t_r - s) - U(t - t_r - s - T)]\, ds \qquad (3.1\text{-}7b)$$

The argument of (3.1-7b) can be written in the form A(t) - B(t, s) where:

$$A(t) = \omega_o(t - t_r) + \pi b\,(t - t_r)^2 \qquad t_1 \le t_r \le t_N \qquad (3.1\text{-}8)$$

and B(t,s) is the residual phase of the echo signal:

$$B(t,s) = \omega_o s - \pi b\, s^2 + 2\pi b s(t - t_r) \qquad (3.1\text{-}9)$$

A(t) represents the quadratic phase profile of a chirp that is triggered after a time t_r. The value of t_r will be determined later. Using the trignometric expansion:

$$\cos(A\text{-}B) = \cos A \cos B + \sin A \sin B, \qquad (3.1\text{-}10)$$

the scattered return g(t) can be expressed as:

$$g(t) = [I(t)\cos A(t) + Q(t)\sin A(t)].[U(t - t_1) - U(t - t_N - T)] \qquad (3.1\text{-}11)$$

where:

$$I(t) = \int_{t_1 - t_r}^{t_N - t_r} d(s + t_r) \cos B(t, s)[U(t - t_r - s) - U(t - t_r - s - T)]\, ds \qquad (3.1\text{-}12)$$

and Q(t), the quadrature component of I(t) is given by:

$$Q(t) = \int_{t_1 - t_r}^{t_N - t_r} d(s + t_r) \sin B(t, s)[U(t - t_r - s) - U(t - t_r - s - T)]\, ds \qquad (3.1\text{-}13)$$

So:

$$I(t) + jQ(t) = \int_{t_1 - t_r}^{t_N - t_r} d(s + t_r)\, e^{j(\omega_o s - \pi b s^2 - 2\pi b s t_r)} [U(t - t_r - s) - U(t - t_r - s - T)]\, e^{j2\pi b s t}\, ds \qquad (3.1\text{-}14)$$

The integrand of (3.1-14) can be divided into four terms. The term d(s) defines the density of facets on the surface. The quadratic phase term describes the phase variation from each facet as a result of the chirping. The staggered Heaviside functions model the true time modulation of the echo; however the echo timing has been transformed to the frequency domain, and is contained in the $e^{j2\pi bts}$ term. Figure 3.1-3 illustrates the echo signal described by (3.1-14). Eqn.(3.1-14) simplifies to a Fourier Transform if we assume that the chirps start and end at the same time as each other, i.e. we assume that the Heaviside function U(t - s) can be replaced by U(t). This assumption is justified by the fact that the delay due to surface roughness varies typically from 0.8 μs (ocean) to 5 μs (terrain), and that the chirp length is of the order of 20 - 300μs. The implications of not modelling the true time modulation will be discussed more fully in §3.1.4.

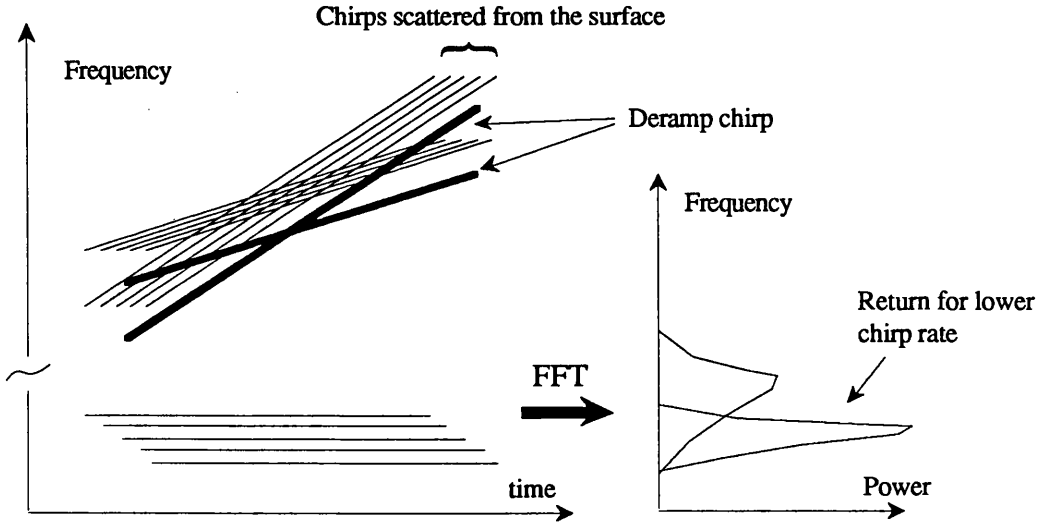

Figure 3.1-3. The series of overlapping chirps and the the corresponding power in the range window after deramp for two different ramp rates. The heavy line in the frequency-time diagram represents the deramp chirp. This is mixed with the scattered return from the surface, producing the baseband signal, shown in the lower section of the frequency-time diagram.

The equivalent frequency variation is given by the argument of the second exponential term of eqn. 3.1-14 (cf. Francis et al (1982) and see figure 3.1-4), and is:

$$\omega = 2\pi bs \tag{3.1-15}$$

Let us define a quantity $f(\omega)$ such that:

$$f(\omega) = d(s + t_r)\, e^{j(\omega_o s - \pi b s^2)} \tag{3.1-16}$$

Now, (3.1-14) reduces to a Fourier Transform relationship, and

$$I(t) + jQ(t) = \frac{1}{2\pi b} \int_{2\pi b(t_1 - t_r)}^{2\pi b(t_N - t_r)} f(\omega) e^{j\omega t}\, d\omega\, [U(t - t_r) - U(t - t_r - T)] \;=\; F(t) \tag{3.1-17}$$

The function $f(\omega)$ is band-limited as a result of the antenna beam-limiting. The function $f(\omega)$ is bounded by:

$$[\pi b(t_1 - t_r),\ \pi b(t_N - t_r)] \tag{3.1-18}$$

where $t_N - t_1$ is the duration of the echo. Eqn. (3-1-17) shows that the in-phase and quadrature components can be obtained from the echo spectrum using the inverse Fourier Transform. This is the basis behind the RSSs for the ERS-1 altimeter and the Advanced Terrain-Tracking Altimeter.

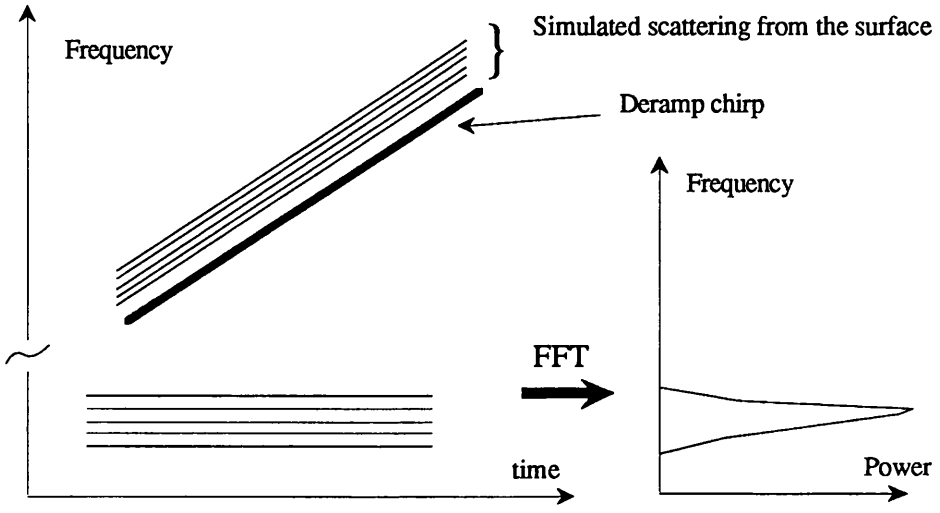

Figure 3.1-4. An approach to echo simulation in which the delay variation is modelled an equivalent frequency. The chirp ramp rate must be known *a priori* in order to transform the time delay variation into a frequency variation.

Finally, a convenient model for the simulated signal can be derived from (3.1-11) if the delay time dependency of the Heaviside functions is neglected:

$$g(t) = [I(t)\cos(\omega_o(t - t_r) + \pi b(t - t_r)^2) + Q(t)\sin(\omega_o(t - t_r) + \pi b(t - t_r)^2)] \quad (3.1\text{-}19)$$

Eqn.(3.1-19) represents a single sideband modulation of the baseband form of the echo signal onto a replica of the transmit chirp, that is triggered after a time t_r. The baseband echo, given by (3.1-17), can be computed from the echo spectrum using an inverse FFT. A block diagram of this return signal simulator is illustrated in figure 3.1-5. The dotted boxes shown in the figure denotes the generation of the baseband echo, which can be done on-line or off-line.

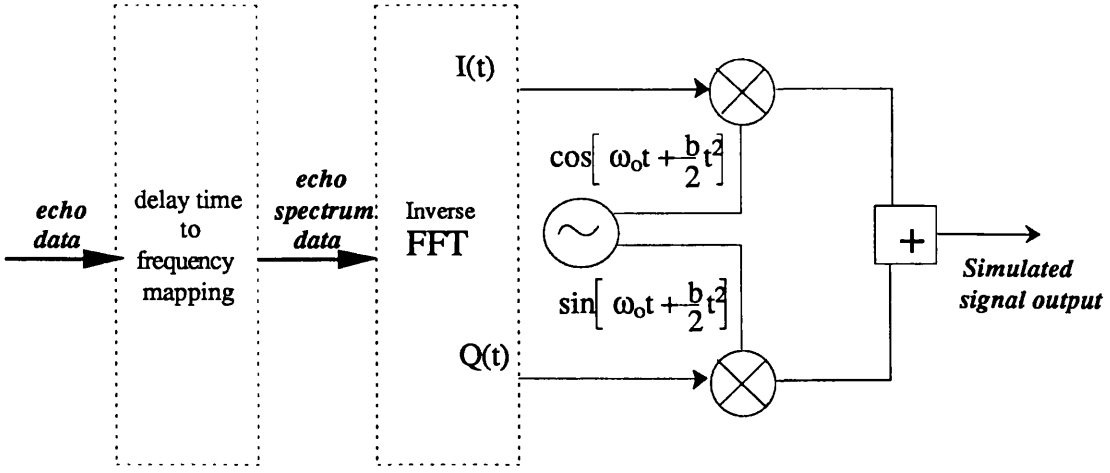

Figure 3.1-5. The mathematical representation of the RSS. The dotted boxes show the baseband signal at intermediate stages. This computation, which can be done off-line, has previously been performed on-line. In the latter case, the right most dotted box would refer to an echo store.

3.1.3 *Relation between the facet model and the Poisson process*

The analysis up to now has not considered the fact that the signal F(t) is time limited, as shown by the Heaviside functions in (3.1-17). Thus the definition of the quantity f(ω) in (3.1-15) needs to be refined. If we take the inverse Fourier Transform of each side of (3.1-17) we observe that f(ω) is correctly expressed as:

$$f(\omega) = d(s + t_r)\, e^{j(\omega_o s - \pi b s^2)} \otimes \frac{\sin(\omega T/2)}{\omega/2} \quad (3.1\text{-}20)$$

The width of the sinc function term is equal to a resolution cell. Thus when it is convolved with the Poisson process, the density of impulses is translated to an amplitude value. The relation between the two processes will now be derived. Figure 3.1-6 illustrates the relation between the two processes. The conjugate form of (3.1-20) is:

$$f^*(\omega) = d(s + t_r)\, e^{-j(\omega_o s - \pi b s^2)} \otimes \frac{\sin(\omega T/2)}{\omega/2}. \qquad (3.1\text{-}21)$$

and the power spectrum is:

$$|f(\omega)|^2 = f(\omega)\, f^*(\omega) \qquad (3.1\text{-}22)$$

From (3.1-21) and (3.1-22):

$$|f(\omega)|^2 = \int_{-\infty}^{\infty} \int_{-\infty}^{\infty} d\left(\frac{\omega_1}{2\pi b} + t_r\right) d\left(\frac{\omega_2}{2\pi b} + t_r\right) \exp\left(j\phi(\omega_1,\omega_2)\right) \frac{\sin(\omega-\omega_1)T/2}{(\omega-\omega_1)} \cdot \frac{\sin(\omega-\omega_2)T/2}{(\omega-\omega_2)}\, d\omega_1 d\omega_2 \qquad (3.1\text{-}23)$$

where

$$\phi(\omega_1,\omega_2) = \omega_o\left(\frac{\omega_1}{2\pi b} - \frac{\omega_2}{2\pi b}\right) + \pi b\left(\left(\frac{\omega_1}{2\pi b}\right)^2 - \left(\frac{\omega_1}{2\pi b}\right)^2\right) \qquad (3.1\text{-}24)$$

The expectation value of the power spectrum is:

$$\langle |f(\omega)|^2 \rangle = \int_{-\infty}^{\infty} \int_{-\infty}^{\infty} \left\langle d\left(\frac{\omega_1}{2\pi b} + t_r\right) d\left(\frac{\omega_2}{2\pi b} + t_r\right) \exp\left(j\phi(\omega_1,\omega_2)\right) \right\rangle \frac{\sin(\omega-\omega_1)T/2}{(\omega-\omega_1)} \cdot \frac{\sin(\omega-\omega_2)T/2}{(\omega-\omega_2)}\, d\omega_1 d\omega_2 \qquad (3.1\text{-}25)$$

which can be rewritten as:

$$\langle |f(\omega)|^2 \rangle = \int_{-\infty}^{\infty} \int_{-\infty}^{\infty} \left\langle d\left(\frac{\omega_1}{2\pi b} + t_r\right) d\left(\frac{\omega_2}{2\pi b} + t_r\right) \right\rangle \left\langle \exp\left(j\phi(\omega_1,\omega_2)\right) \right\rangle \frac{\sin(\omega-\omega_1)T/2}{(\omega-\omega_1)} \cdot \frac{\sin(\omega-\omega_2)T/2}{(\omega-\omega_2)}\, d\omega_1 d\omega_2 \qquad (3.1\text{-}26)$$

The expectation value of the integrand of (3.1-26) is defined as follows (Papoulis, 1970):

$$\left\langle d\left(\frac{\omega_1}{2\pi b}\right) d\left(\frac{\omega_2}{2\pi b}\right)\right\rangle = \left\langle d\left(\frac{\omega_1}{2\pi b}\right)\right\rangle \delta\left(\frac{\omega_1}{2\pi b} - \frac{\omega_2}{2\pi b}\right) + \left\langle d\left(\frac{\omega_1}{2\pi b}\right)\right\rangle \left\langle d\left(\frac{\omega_2}{2\pi b}\right)\right\rangle \qquad (3.1\text{-}27)$$

$$\left\langle \exp[\, j\phi(\omega_1, \omega_1)]\right\rangle = 0 \qquad \omega_1 \neq \omega_2 \qquad (3.1\text{-}28)$$

If (3.1-27) and (3.1-28) are substituted into (3.1-26), the double integral reduces to a single one, and the expression can be solved analytically, giving:

$$\langle |f(\omega)|^2 \rangle = \left\langle d\left(\frac{\omega}{2\pi b} + t_r\right)\right\rangle \otimes \frac{\sin^2(\omega T/2)}{(\omega/2)^2}. \qquad (3.1\text{-}29)$$

This represents the value of the power spectrum in each resolution cell, and will now form a basis for us to consider various methods of signal simulation.

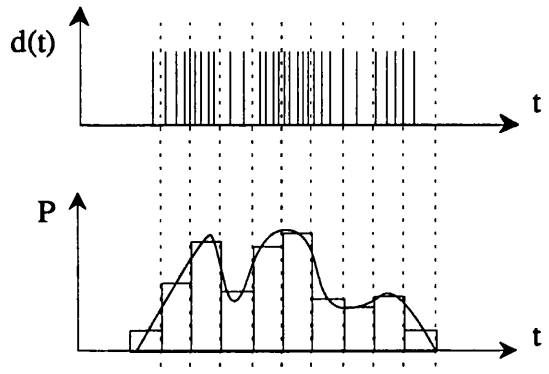

Figure 3.1-6. The scattering process represented as a series of Poisson impulses. The power in each resolution cell is computed by convolving the surface impulse response with the sinc squared function shown in (3.1-29).

3.1.4 Timing of the simulated echo

The timing of the simulated echo is provided by the instant at which the RSS chirp is triggered, and by the frequency of the components in the baseband signal. It is apparent from (3.1.8) and (3.1-18) that there is a certain amount of freedom in specifying the timing of the simulated echo. The only constraint is that the time of the RSS chirp t_r must be constrained to $t_1 \leq t_r \leq t_N$ as specified by (3.1-8). The resulting echo spectrum after transformation to the frequency domain is then bounded by $[\pi b(t_1 - t_r), \pi b(t_N - t_r)]$. Clearly, the optimum choice for the value of t_r is:

$$t_r = \frac{t_1 + t_N}{2} \qquad (3.1\text{-}30)$$

since the echo spectrum is then symmetrically disposed about zero frequency, thus reducing the sampling frequency required to digitally synthesise this spectrum. The timing of the simulated echo is illustrated in figure 3.1-7. Appendix 1 provides a mathematical derivation for the echo timing.

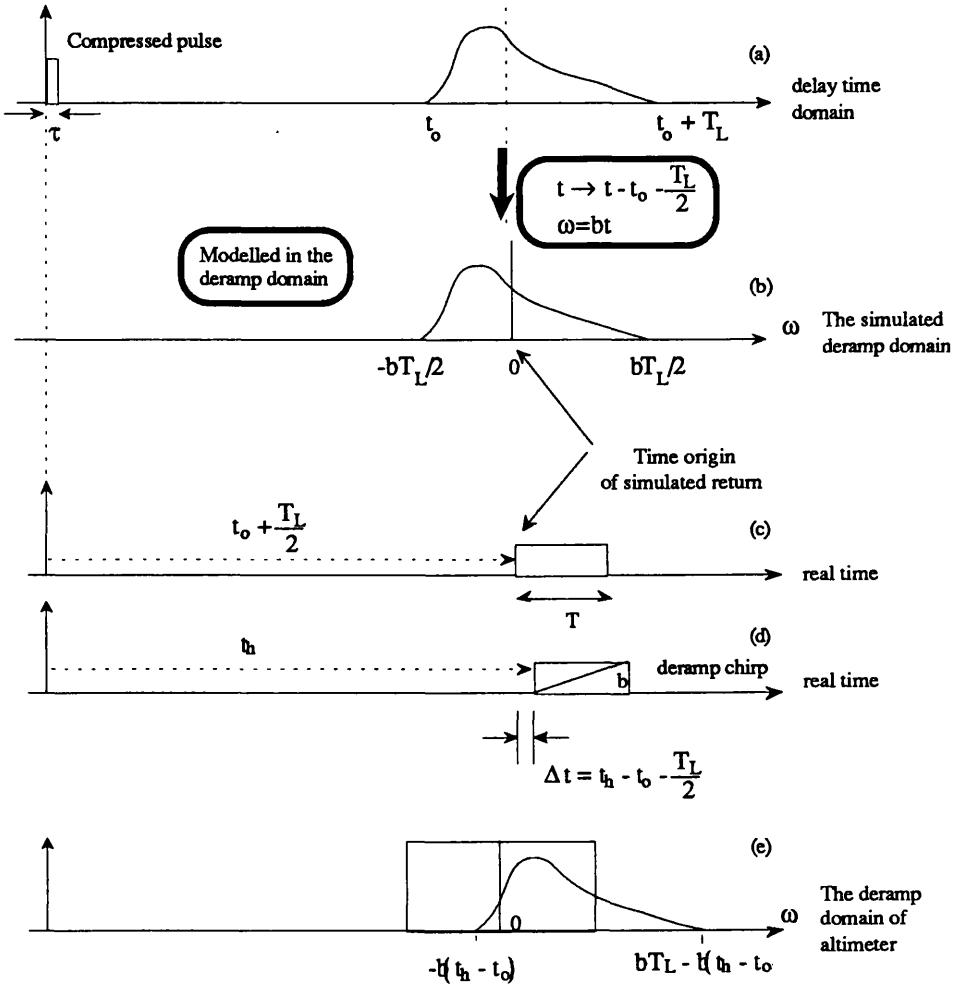

Figure 3.1-7. The timing of the simulated echo: (a) shows the timing of the echo in the delay time domain, referenced to the compressed pulse length; (b) illustrates the spectrum of the baseband form of the echo after the time-frequency transformation; (c) indicates the time origin of the RSS signal, and (d) shows the relative positon of the deramp chirp; and finally (e) illustrates how the echo is tracked in the range window.

3.1.5 Timing errors as a result of the simulation

There is a small error that results from neglecting the delay time dependency of the Heaviside function in §3.1.2. This section will analyse the effect of such an error.

If the signal in the altimeter is tracked at the centre or close to the centre of the range window, then the echo components at the centre of the range window have length T after deramp, as illustrated in figure 3.1-8. The components further away from the leading edge have a decreasing length, prior to the FFT in the altimeter. Thus the signal amplitudes in the range window are affected by the quantity ΔG:

$$\Delta G = 20\log_{10}\frac{T - \Delta T}{T} \qquad (3.1\text{-}31)$$

where ΔT is the misalignment of the echo component with the deramp chirp. The error depends on the slope of the leading edge, and is insignificant for high values of slope. For example, if the leading edge is 16 range bins wide, then the change in amplitude is equal to 0.01 dB at ± 8 range bins from the centre. This is shown in figure 3.1-8, and will give rise to a very small timing error aswell as an error in the estimation of the leading edge slope. This variation in overlap does not occur with the simulated signal. The magnitude of the amplitude error is typically less than 0.01 dB; thus, neglecting to model the true time modulation will not affect the accuracy of the simulated signal.

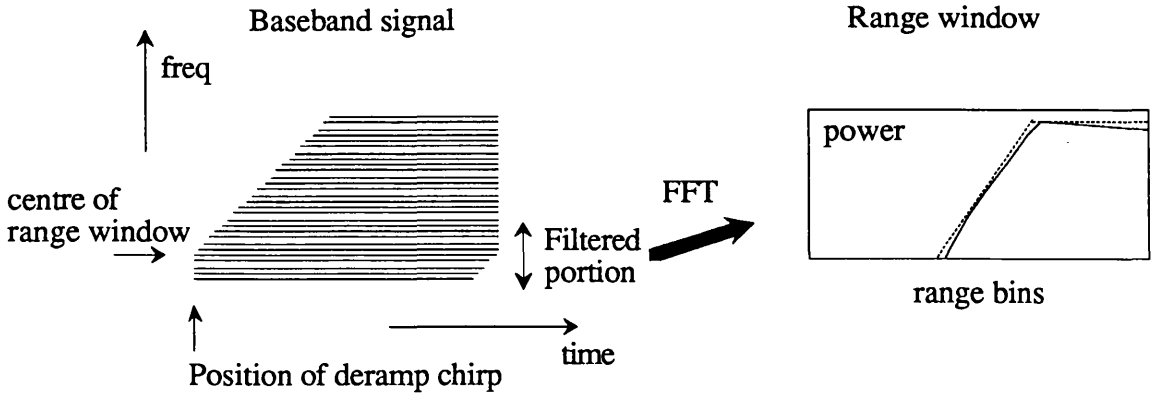

Figure 3.1-8. The signal in the altimeter before and after the FFT. The error in the shape of the echo in the range window as a result of the true time modulation is shown by the dotted line, but the magnitude of the error is exaggerated.

3.2 ADAPTIVE RESOLUTION

For the methods of return signal simulation discussed so far, the bandwidth of the simulated signal is equal to the delay variation multiplied by the ramp rate of the chirp. If the ramp rate of the chirp is reduced, i.e to degrade the resolution, then the spectrum of the simulated signal must be made narrower by the same quantity. There are two different ways in which a coarser echo can be generated. Firstly, the signal in the range window could be re-computed for a different resolution, and secondly the RSS baseband signal could be spectrally compressed by the appropriate factor (Sheehan et al., 1991).

3.2.1 Adaptive resolution using a number of different data sets

The first method is computationally expensive, and rather inelegant. In this scheme, a set of coefficients is stored for each resolution, and these become the inputs to the inverse FFT, which may be performed on- or off-line. However, the main requirement is that as many different data sets are needed as resolutions to be modelled. Since the frequency resolution (1/T) in the range window is independent of the resolution, the length of the time domain signal is, as expected, equal to the chirp length T for all resolutions.

3.2.2 Adaptive resolution by spectrally compressing

The second method can be associated with the Fourier Transform identity of (3.1-17), and is based on expanding the time axis of the RSS input signal to achieve an equivalent compression of the echo spectrum, thereby simulating a change to a coarser resolution. If the RSS baseband signal F(t), whose spectrum f(ω) is defined by the Fourier Transform in (3.1-17), is scaled in time, then the spectrum of the resulting signal is given by:

$$\int F(\eta t)e^{-j\omega t}\,dt = \frac{1}{\eta} f\left(\frac{\omega}{\eta}\right) \qquad (0 < \eta \leq 1) \qquad (3.2\text{-}1)$$

If the entire echo duration is modelled, then it is possible (Sheehan et al., 1991) to generate a coarser resolution echo from the finest resolution by selecting the appropriately sampled subset of data. In the arguments that follow, we will refer to a resolution reduction by a factor η; however this means that the range resolution cell is increased by $1/\eta$.

Implicit in the above argument is a data reduction, illustrated in figure 3.2-1. The time axis of the RSS input is scaled by $1/\eta$, so that its duration becomes T/η, extending beyond the chirp (length T). As a result, a proportion k of the echo is not modulated onto the chirp, where:

$$k = \frac{1/\eta - 1}{1/\eta} = 1 - \eta$$

Thus, for a resolution change by a factor of 4, only 1/4 of the echo data is modulated onto the chirp.

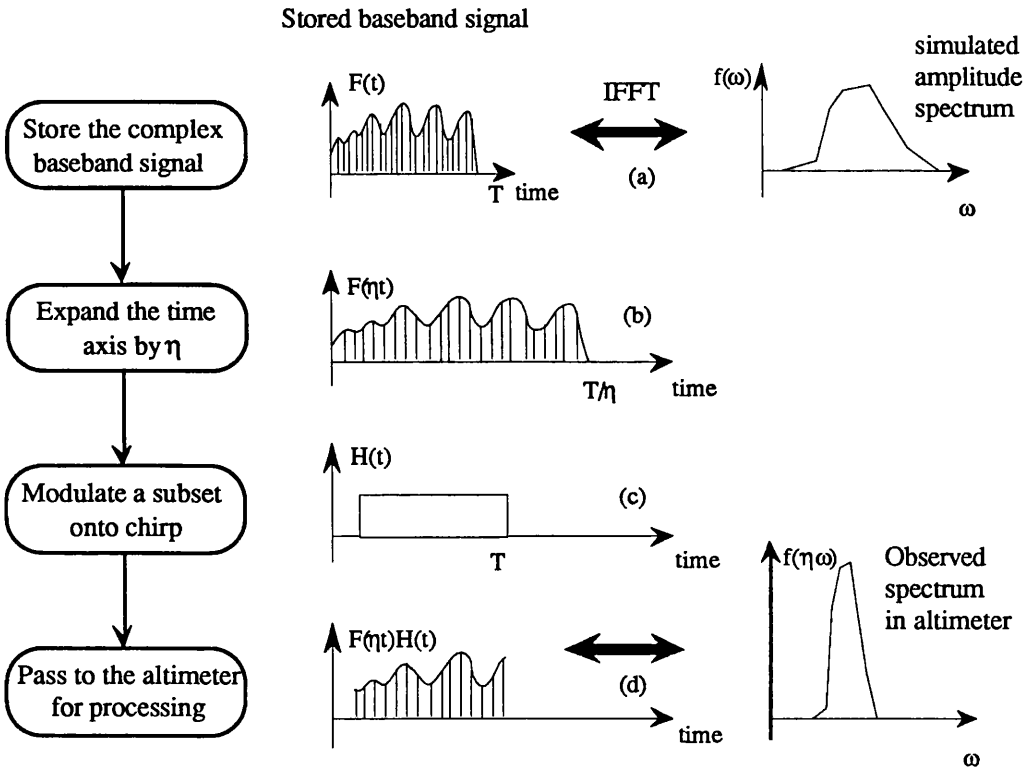

Figure 3.2-1. The proposed method for generating the echoes at a coarser resolution.

(a) the baseband signal F(t) is computed from the spectrum f(ω),

(b) F(t) is expanded by $1/\eta$ to effect a change in resolution by η,

(c) F(ηt) is gated by the signal H(t) which defines the chirp duration, and

(d) the filtered signal is representative of the coarsely resolved echo when it is deramped and processed in the altimeter.

The above argument is not rigorous enough to allow us to determine the shape and peak power of the coarsely-resolved echo spectrum. The signal g(t) at a coarser resolution is:

$$g(t) = \left[I(\eta t+t_o)\cos(\omega_o t + \pi bt^2) + Q(\eta t+t_o)\sin(\omega_o t + \pi bt^2)\right] . [U(t) - U(t - T)] \tag{3.2-2}$$

The time is referenced to the position of the RSS chirp, as indicated by the bracket of Heaviside functions, and t_o is the time misalignment between the origin of the baseband modulation and the RSS chirp. In figure 3.2-1, it is necessary that $t_o \geq 0$ so that data are modulated onto the entire chirp. Moreover, when $\eta = 1$, then t_o must be zero.

The simulated return is passed to the altimeter where it is deramped by a chirp of the same slope, and subsequently Fourier Transformed to give the signal in the range window. The power spectra for the two resolutions corresponding to $\eta=1$ and $\eta<1$ are derived in appendix A.1, and are given as follows:

$$P_1(\omega) = \left| f(\omega) \otimes \frac{\sin(\omega T/2)}{\omega} \right|^2 \qquad \eta = 1 \tag{3.2-3}$$

$$P_2(\omega) = \left| b(\omega) \otimes \frac{\sin(\omega T/2)}{\omega} \right|^2 \qquad \eta < 1 \tag{3.2-4}$$

where:

$$b(\omega) = \int_0^T [I(\eta t) + jQ(\eta t)]\,[U(t).U(T-t)]\, e^{-j\omega t}\, dt \tag{3.2-5}$$

The squared sinc function is the impulse response of the altimeter. By comparing (3.2-3) to (3.2-4), one can see that the impulse response is the same in both, and as a result it does not de-resolve the echo. De-resolving in the altimeter is effected by the reduction in chirp ramp rate and, in the RSS it is accounted for by the difference in the parameters $a(\omega)$ and $b(\omega)$. Eqn.'s (3.2-3) and (3.2-4) are not yet in a form to allow a meaningful comparison between the power spectra, $P_1(\omega)$ and $P_2(\omega)$, at the two different resolutions. This comparison must be done on an average basis since the echoes are stochastic.

Footnote: De-resolving means reducing the resolution

Comparison of the simulated power spectra at the two resolutions

For stationary statistics, it is assumed the decorrelation of the echo ensures that the signal power is uniformly distributed over time, and this will be proven in §3.2.1. As a result, the position of the gating function shown in figure 3.2-1 is arbitrary, meaning that any contiguous subset of length T of the 'stretched' waveform data can be used to generate the coarser resolution.

The initial stage of this comparison computes the total power in the echo at the two resolutions. The total power in the subset of the echo can be written as:

$$<\int_0^T [F(\eta t)]^2\, dt> = \eta <\int_0^{T/\eta} [F(t)]^2\, dt> \qquad t \in [0,T],\ \eta \leq 1 \qquad (3.2\text{-}6)$$

Applying Parseval's theorem to (3.2-6), and substituting (3.2-5), the following identity can then be made:

$$<\int_{-\infty}^{\infty} |b(\omega)|^2 d\omega > = \eta <\int_{-\infty}^{\infty} \left|\frac{1}{\eta} f\left(\frac{\omega}{\eta}\right)\right|^2 d\omega > \qquad (3.2\text{-}7)$$

In the analysis thus far, the windowing effect of the anti-aliasing filters just prior to digitisation of the altimeter echo has not been considered. Eqn. (3.2-7) demonstrates that the power in the echo is scaled by a factor η commensurate with the resolution change. This is not true for non-stationary statistics. These will be treated in a simulation in the following section since it is difficult to analyse.

The shape of the echo signal is independent of the position of the windowing function because of the uniform distribution of its power over time. As a result, we can infer that the truncation does not affect the signal shape, giving:

$$\langle |b(\omega)|^2 \rangle = \frac{1}{\eta}\left\langle \left| f\left(\frac{\omega}{\eta}\right)\right|^2 \right\rangle \qquad (3.2\text{-}8)$$

Thus the simulated signal power at a coarser resolution is given as:

$$P_2(\omega) = \langle |b(\omega)|^2 \rangle = \frac{1}{\eta}\left\langle \left| f\left(\frac{\omega}{\eta}\right)\right|^2 \right\rangle \qquad (3.2\text{-}9)$$

The signal in the range window is given by:

$$P_2(\omega) = \frac{1}{\eta}\left\langle \left| f\left(\frac{\omega}{\eta}\right)\right|^2 \right\rangle S_{LP}(\omega) \qquad (3.2\text{-}10)$$

where $S_{LP}(\omega)$ is the the frequency response of the anti-aliasing low pass filter.

This analysis shows that if the resolution is degraded by a factor of 4, then the spectrum of the simulated echo is compressed by 4 and the peak power is increased by a factor of 4. In practice, this is exactly what happens. Thus this method of generating a coarser resolution is ideally suited for use with an adaptive resolution altimeter.

3.2.3 Properties of the RSS simulated echo signal

A real echo from a surface has stationary statistics. However, the altimeter square-law detects the signal and does not process the phase of the echo. This section determines whether it is actually necessary to reproduce the correct phase statistics of the echo.

Non-stationary statistics in the simulated echo

Suppose the phase of the echo is not uniformly distributed, but is constant. Thus:

$$f(\omega) = \sqrt{P_r(\omega)}\, R(\omega) \qquad (3.2\text{-}11)$$

where $P_r(\omega)$ is the average power spectrum of the echo, and $R(\omega)$ are the normalised (to unity) Rayleigh fluctuations of the amplitude spectrum. This can be rewritten as:

$$f(\omega) = \sqrt{P_r(\omega)} + n(\omega) \qquad (3.2\text{-}12)$$

with the noise component $n(\omega)$ given by:

$$n(\omega) = \sqrt{P_r(\omega)}\,.\,[R(\omega) - 1] \qquad (3.2\text{-}13)$$

The multiplicative noise of (3.2-11) can be treated in an additive fashion. The baseband RSS signal is the inverse Fourier Transform of (3.2-12), and is of the following form:

$$F(t) = \mathcal{F}^{-1}\left\{\sqrt{P_r(\omega)}\right\} + \mathcal{F}^{-1}\{n(\omega)\} \qquad (3.2\text{-}14)$$

and $\mathcal{F}^{-1}$ is the inverse Fourier Transform operator. Thus if we consider an echo from a distributed target in the frequency domain, modelled without its random phase spectrum, then most of the energy is localised in only a few time samples of F(t). A small additive noise component is superimposed onto this signal.

In order to demonstrate this effect the echo spectrum shown in figure 3.2-2 was used as an example. The RSS baseband signal F(t), given by (3.2-14), is shown in figure 3.2-3 when $R(\omega) = 1$. The additive noise is shown in figure 3.2-4 for $R(\omega) \neq 1$. The dynamic range of this signal is very large because of the localised energy. Two important points must be noted. Firstly, the quantisation error is quite severe since the majority of the low-energy signal can be defined using only about 6 quantisation levels. Secondly, the reconstructed echo spectrum at a coarser resolution will suffer severely from windowing the signal F(t). An example of the distortion due to the windowing is shown in §3.3.2.

Two examples of such a signal are a point-target calibration signal with a deterministic amplitude, or a stationary signal modelled without the uniformly-distributed phase spectrum.

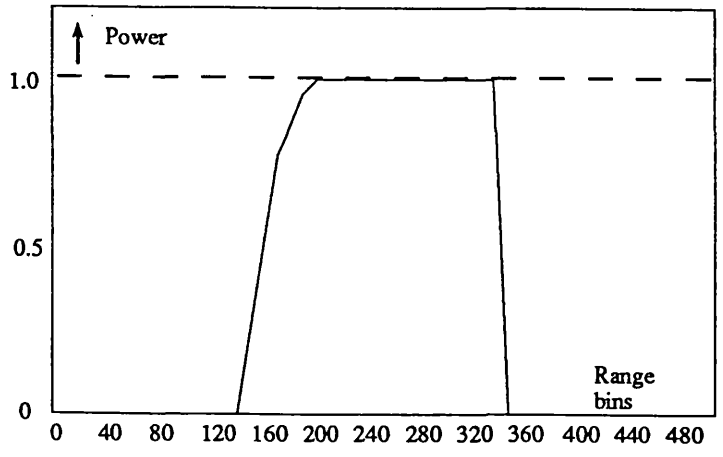

Figure 3.2-2. The mean power spectrum of a simulated echo signal. The echo is modelled over 512 range bins, of which 220 are non-zero.

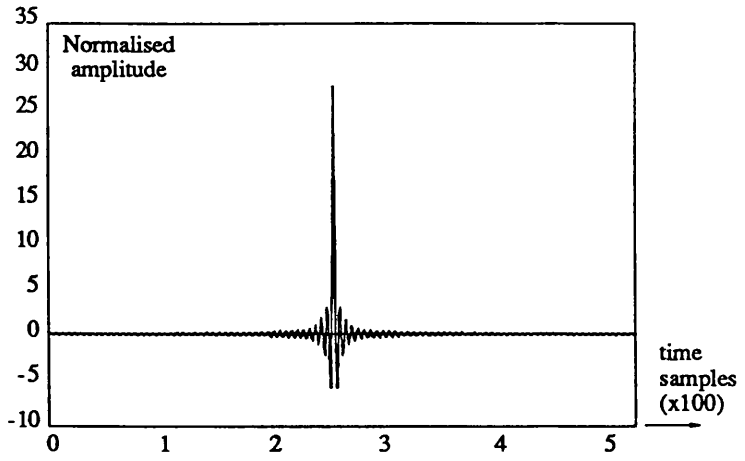

Figure 3.2-3. The inverse Fourier Transform of the mean echo of figure 3.2-2. This represents the baseband signal modulated onto the regenerated transmit chirp in the absence of a uniformly-distributed random phase spectrum.

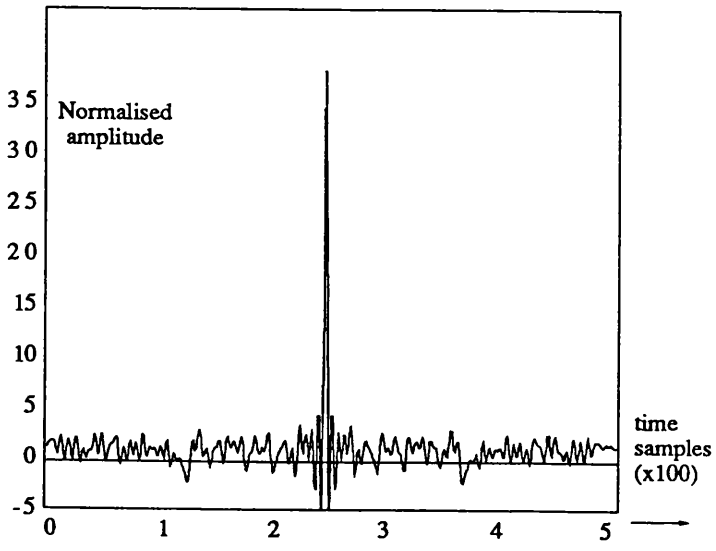

Figure 3.2-4. The inverse Fourier Transform of the spectrum resulting from a Rayleigh-distributed amplitude in each of the resolution cells of the mean spectrum illustrated in figure 3.2-2.

Stationary statistics in the simulated echo

The simulated echo spectrum is given by:

$$f(\omega) = \sqrt{P_r(\omega)}R(\omega) \, . \, e^{j\phi(\omega)} \qquad (3.2\text{-}15)$$

where $\phi(\omega)$ is a uniform distributed phase spectrum. The corresponding RSS input in the time domain is then given by:

$$F(t) = \mathcal{F}^{-1}\left[\sqrt{P_r(\omega)}R(\omega)\right] \otimes \mathcal{F}^{-1}\left[e^{j\phi(\omega)}\right] . \qquad (3.2\text{-}16)$$

In this case, the random phase cannot be considered in an additive sense since it is the argument of the complex exponential function. The transition from additive to multiplicative noise can be observed by increasing the phase variation of $\phi(\omega)$ from zero and using the small angle approximation in the Taylor expansion for $e^{j\phi(\omega)}$. The convolution in (3.2-16) effectively spreads the signal uniformly over the chirp length if $\phi(\omega)$ varies over $[-\pi,\pi]$. Figure 3.2-5 illustrates the in-phase component of the RSS signal F(t) for this case. Two important points should be noted. Firstly, the signal energy is more evenly spread over the chirp length. Secondly, the signal amplitude is more evenly distributed over its dynamic range, thus reducing the quantisation error.

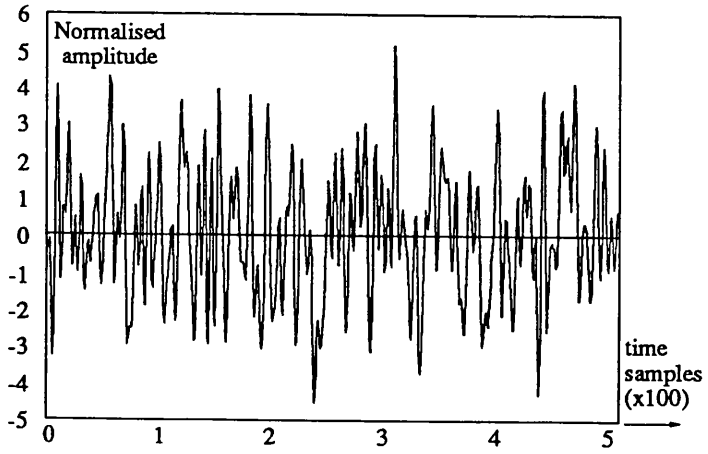

Figure 3.2-5. The in phase component of the RSS baseband signal when a uniform random phase is applied to the mean spectrum illustrated in figure 3.2-2.

Figure 3.2-6 shows the distribution of the signal power for the running average of length T/4 across the chirp length T. It is apparent that the signal power is distributed uniformly across the chirp length. The small variation in the distribution results from performing a running average on a stationary signal. This variation would be reduced if we averaged over a number of stationary signals. Thus the time origin of the subset of data used to generate a coarser resolution is arbitrary if the echo spectrum at the finest resolution is assumed to have stationary statistics.

Consider the case when $R(\omega) = 1$. This is typical of a calibration signal. A corollary of the second point is that calibration waveforms will be less affected by quantisation errors if the model includes a uniformly distributed phase spectrum, i.e

$$f(\omega) = \sqrt{P_r(\omega)} \cdot e^{j\phi(\omega)} \qquad (3.2\text{-}17)$$

The in-phase and quadrature components are spread out in time, as illustrated by figure 3.2-5. The spectra will recombine to give a deterministic signal as long as the Hilbert transform relationship between the two components of the RSS input signal is maintained.

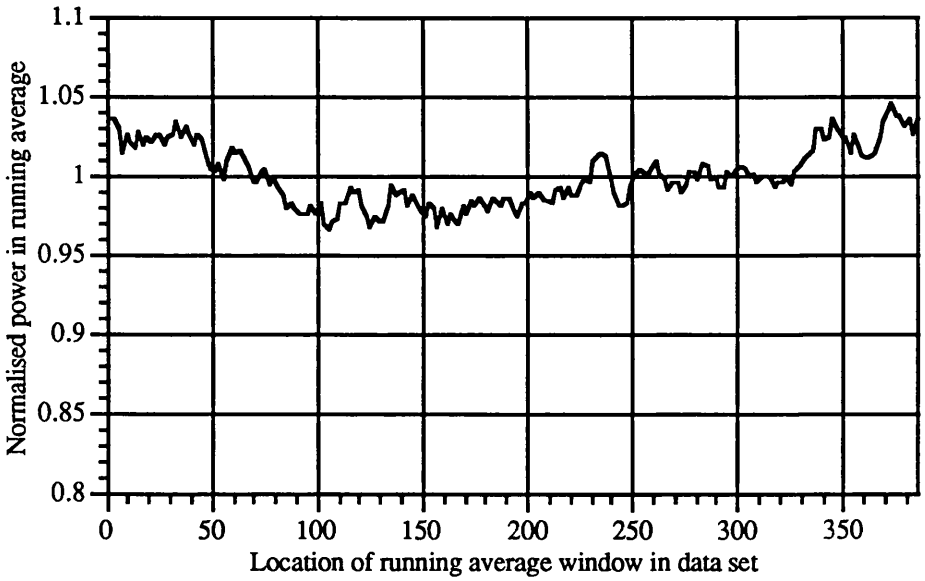

Figure 3.2-6 Distribution of power as a function of a running average window equal to 1/4 of the chirp length. The chirp length is modelled using 512 samples, and the running average window averages 128 contiguous samples.

3.2.4 Effect of using an FFT rather than an FT

In both a practical RSS and a software implementation, it is computationally more efficient to use an FFT or a DFT rather than the continuous FT. Two important side effects of using a discrete approach are now discussed. Consider the echo spectrum as a continuous Fourier Transform:

$$f(\omega) = \int_{-\infty}^{\infty} F(t)\, e^{-j\omega t} dt \qquad (3.2\text{-}18)$$

If this signal is digitised, then:

$$f(\omega_k) = \sum_m F(t_m)\, e^{-j\omega_k t_m} \Delta t \qquad (3.2\text{-}19)$$

where $\omega_k = \frac{2\pi k}{T}$, $t_m = \frac{mT}{N} = mT_s$, and T_s is the sampling interval.

The first effect relates to a resolution-dependent gain change in the simulated echo that arises as a result of the difference between the sampled spectrum in (3.2-19) and the conventional implementation of the FFT, which does not include the Δt factor. Thus the FFT will not take into account the $1/\eta^2$ ($\eta \leq 1$) increase in amplitude by simply stretching the signal in time, as indicated by (3.2-4). Thus a practical realisation of the RSS must compensate for this by adding additional gain:

$$G = 20\log_{10}\frac{1}{\eta} \qquad (3.2\text{-}20)$$

The second effect relates to the relative size of the truncation window shown in figure 3.2-1 with respect to the data set when there is a periodic component in the echo. The following expression for $\widetilde{F}(t)$, shown in (3.2-21) and derived in appendix A.2, represents a function that samples F(t) at t = 0, T_s, $2T_s$, ... , $(N-1)T_s$, and then repeats periodically outside this interval with period T.

$$\widetilde{F}(t) = T \sum_{p=-\infty}^{\infty} \left[\sum_{n=0}^{N-1} F(nT_s)\delta(t - nT_s - pT) \right] \qquad (3.2\text{-}21)$$

The windowing interval T is the chirp length. The choice of this interval must be long

enough to preserve all important features of $F(\omega)$, determined by the frequency resolution. The wrong choice of interval (Fante, 1988) can also lead to completely erroneous results if F(t) is a periodic function or has a periodic component. This is particularly important when the echo consists of a specular return that occupies a single range bin.

From (3.2-21), it can be seen that the windowing interval T must be chosen to be an integral multiple of the signal period if the signal $\widetilde{F}(t)$ is to look like F(t). This is always the case for the finest resolution since a specular return in the n^{th} range bin will produce a signal with period T/n. Consider using (3.2-21) to analyse a specular return generated at a coarser resolution using the method in §3.2.2. The windowing interval must be replaced by ηT, N must be replaced by ηN, and $\widetilde{F}(t)$ represents the sampled signal at a coarser resolution. Obviously the windowing interval ηT may not be a multiple of the signal period, and thus the signal $\widetilde{F}(t)$ will not look anything like the $F(\eta t)$. In order to guarantee that the signal $\widetilde{F}(t)$ does resemble $F(\eta t)$ it is necessary to ensure that the windowing interval ηT is an integral multiple of signal periods of F(t). That is:

$$\eta T = mT_o \qquad (3.2\text{-}22)$$

where T_o is the signal period at the finest resolution. This implies that the signal period at the finest resolution must be restricted to ηN values if a specular return is to be generated at a resolution $1/\eta$ times coarser using this method. The condition in (3.2-22) is modified, if k-1 resolutions are to be generated, as follows:

$$\eta^{k-1} T = mT_o \qquad (3.2\text{-}23)$$

If the condition in (3.2-22) is not met, the energy will none the less be predominantly at a frequency η/T_o; there will however be considerable smearing of the energy into adjacent range bins.

3.2.5 Possible resolution changes

The number of coarse resolutions that can be generated from a signal comprising N resolution cells is N-1. The coarsest resolution must have at least two samples to satisfy the Nyquist criterion. The possible changes are given as:

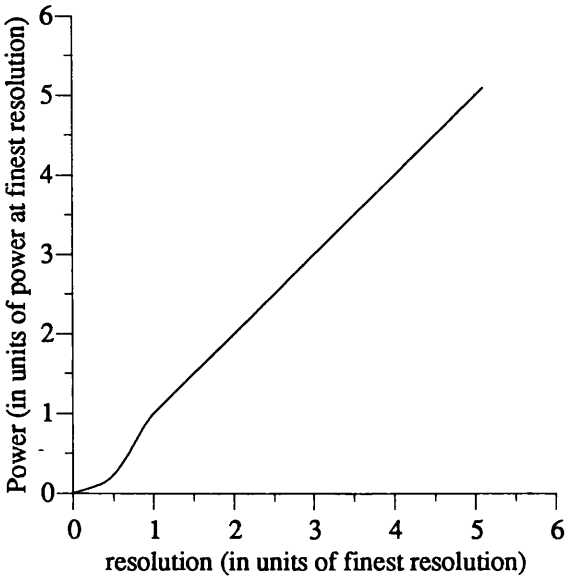

Figure 3.2-7. The power of the simulated echo as a function of the range resolution. The power is proportional to the range resolution for $1/\eta \geq 1$ (i.e. coarse resolutions). However for $1/\eta < 1$, the power decays according to a square law.

$$\eta = \frac{k}{N} \qquad k \leq N \tag{3.2-25}$$

where k is the number of samples modulated onto the chirp. For resolution changes by a factor η, according to (3.2-21), the power of the simulated echo varies according to $1/\eta$. For $\eta > 1$, the simulated baseband signal is shorter than the chirp; the chirp has been truncated to a duration T/η. The range window spectrum in the altimeter then becomes:

$$\int_0^{T/\eta} F(\eta t) e^{-j\delta t} e^{-j\omega t}\, dt \tag{3.2-26}$$

where δ is a frequency parameter dependent on how the echo is tracked by the altimeter. The amplitude spectrum in the range window can be shown to be:

$$\frac{1}{\eta} f(\eta\omega - \delta) \tag{3.2-27}$$

and the power is given as:

$$P(\omega) = \frac{1}{\eta^2} |f(\eta\omega - \delta)|^2 \qquad \eta > 1 \qquad (3.2\text{-}28)$$

$\eta > 1$ represents the condition where we are attempting to generate an echo that has a finer resolution from the stored echo. The range resolution of the simulated echo has been increased; however it is lost in the altimeter because the smaller chirp overlap (for $\eta > 1$) would de-resolve the echo. Figure 3.2-6 illustrates the peak power of the simulated echo as a function of the range resolution.

3.3 SOFTWARE RETURN SIGNAL SIMULATION

A software model of the Return Signal Simulation was implemented in order to verify the principle and to simulate the effect of changing a number of the parameters. The model is outlined in the following section. §3.3.2 simulates a resolution change, and §3.3.3 considers the signal to noise ratio of an echo generated with a coarser resolution.

3.3.1 Software model of the RSS

A block diagram of the software representation is shown in figure 3.3.1. The model is divided into three parts: respectively, the RSS, the RF interface and the digital processing in the altimeter.

The RSS

In this section of the model, the echo spectrum is defined by the user. The echo is defined over 512 range bins. In each of the non-zero range bins, a fading function is applied to both amplitude and phase. As shown in figure 3.3-1, the user may define Exponential, Gamma or no power fading, and either a uniformly distributed phase or a constant phase. The inverse FFT of this signal is taken. The user has the option of misaligning the baseband echo information with respect to the chirp carrier in order to simulate hardware filter delays. In this case, a number of samples at the end of the baseband echo are set to zero. Finally, a proportion of the baseband echo is selected in order to simulate a resolution change. This is the simulated RSS output.

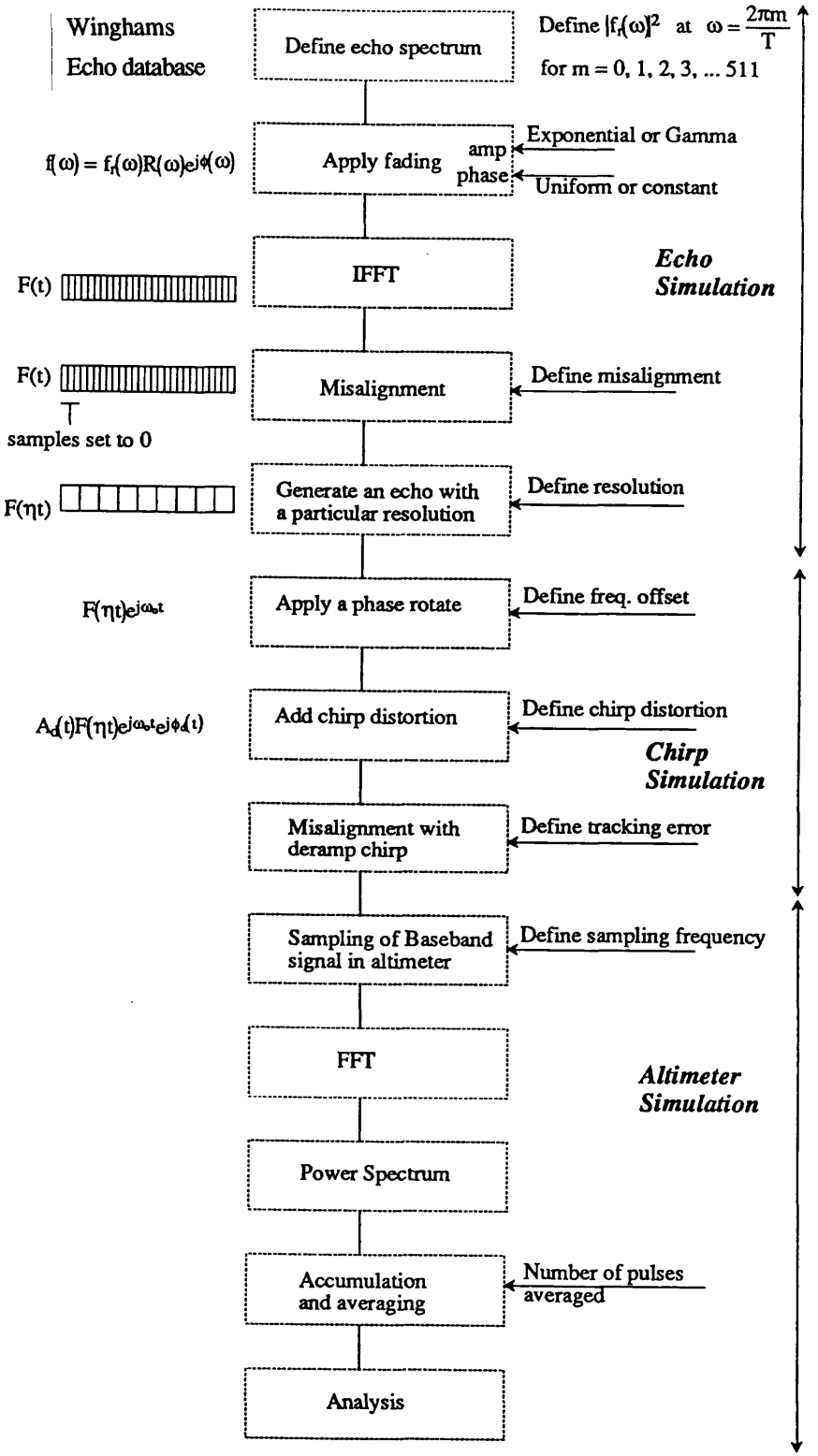

Figure 3.3-1 The software model of the RSS and altimeter. Three different sections of the model are isolated: (a) the echo generation; (b) the simulation of the upconversion in the RSS and the downconversion in the altimeter; and (c) the simulation of the baseband processing in the altimeter.

RF part

The RF part of the model simulates the effect of RF up/down conversion onto a chirp. Three effects are simulated: firstly, the frequency difference between the RSS chirp and the deramp chirp is applied by means of a phase rotate to the baseband signal, as shown in figure 3.3-1; secondly, the effect of phase and amplitude distortion resulting from the non-ideal RSS and deramp chirps is applied; and thirdly, the effect of a misalignment between the RSS and deramp chirps is modelled by setting the pertinent samples to zero.

The amplitude distortion is applied by weighting the RSS signal with a particular distortion profile, and the phase distortion is applied by multiplying the baseband signal with the function $\exp[j\phi(t)]$ where $\phi(t)$ is the phase distortion difference between the two functions. The form of the distortion functions will be given in §6.

The altimeter

The altimeter performs many of the functions of the RSS in reverse. It initially takes the FFT of the received baseband signal, then forms the power spectrum. A number of the echo spectra are accumulated and averaged. The resulting spectra is output into a data file ready for analysis.

The analysis section will be discussed along with the results. Appendix A.1 outlines the equations at each point in the model.

3.3.2 Simulation of a resolution change

This section simulates a resolution change. The reduction in resolution will be a factor of 4 in each case. The mean echo power spectrum used in the simulation is shown in figure 3.2-2. Exponential power fading and a uniform phase distribution were applied to each of the range bins of the simulated spectrum.

The misalignment and distortion options of the model defined in §3.3.1 are not used in this analysis. The required subset of data at the coarser resolution is represented by any contiguous set of 128 samples of the RSS input signal. For the first coarse resolution, the time axis of this signal is expanded by a factor of $1/\eta$ (= 4) such that the sample spacing becomes T/128. Figure 3.3-2 shows the in-phase component of the first 128 samples of the RSS baseband signal, when it is expanded to occupy a time span T.

A single echo generated by this technique is illustrated in figure 3.3-3. Figure 3.3-4 illustrates the mean echo computed from an average of 500 individual pulses. The mean power spectrum at the finest resolution has been plotted over the echo at the coarser resolution, but with its frequency axis scaled. It can be seen that the echo shape has been preserved through the generation process described in §3.3.2. A small deviation exists on the leading edge due to coarser sampling. In addition the spectrum is compressed by $1/\eta$ and the power is scaled by $1/\eta$. A secondary effect is also observed in figure 3.3-4; a small pre- and post-cursor exist around the de-resolved echo, arising from the data set truncation.

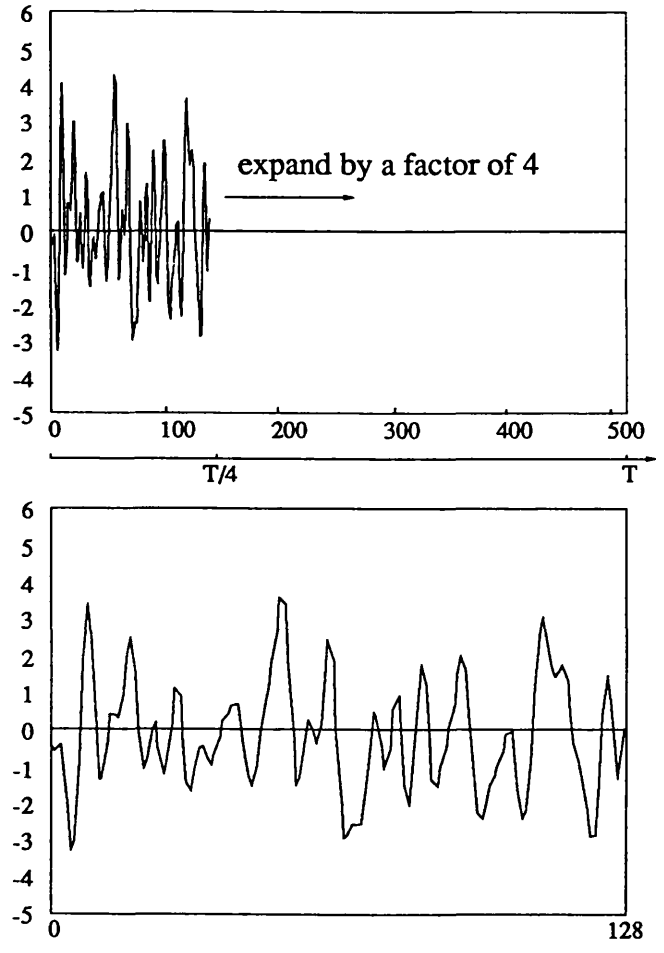

Figure 3.3-2. Generation of the in-phase component of an echo at a coarse resolution. It is shown in figure 3.3-1 to be generated from the fine resolution signal by stretching the time axis by a factor of 4 and windowing the first 25 %.

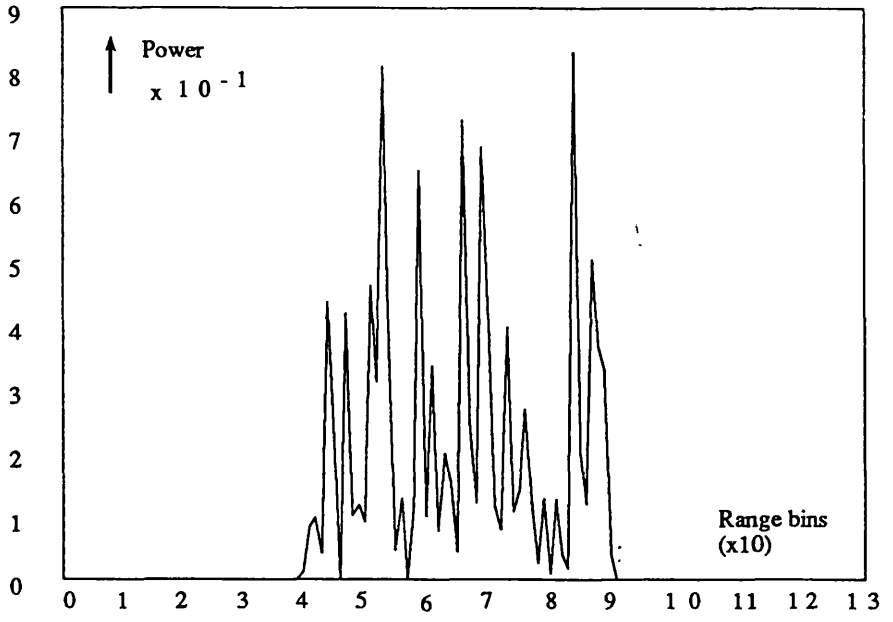

Figure 3.3-3. The spectrum of a single echo at a coarser resolution generated using the method proposed in figure 3.3-5. The typical fluctuations associated with exponential fading are clearly visible.

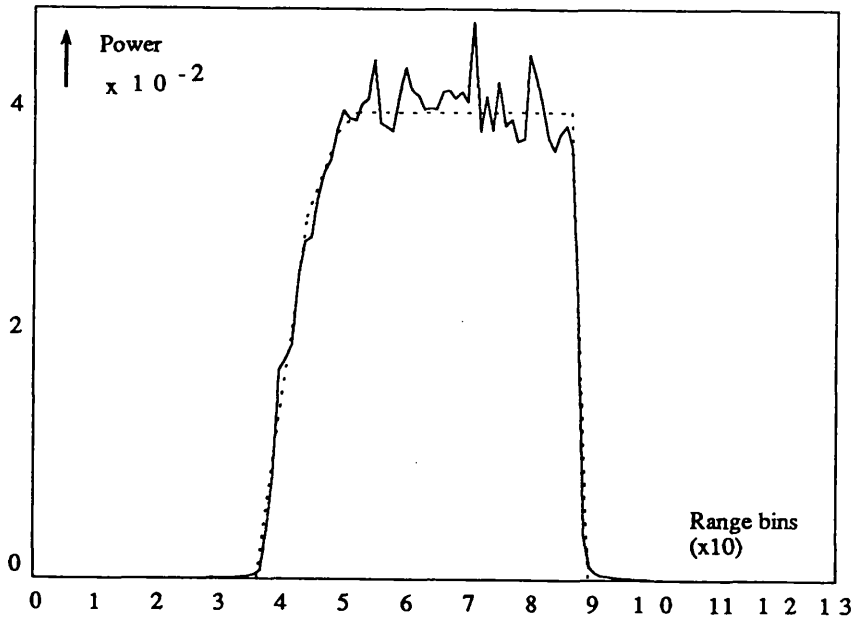

Figure 3.3-4. The echo spectrum afer 500-pulse averaging at the coarser resolution, and the mean echo spectrum (shown in dotted line).

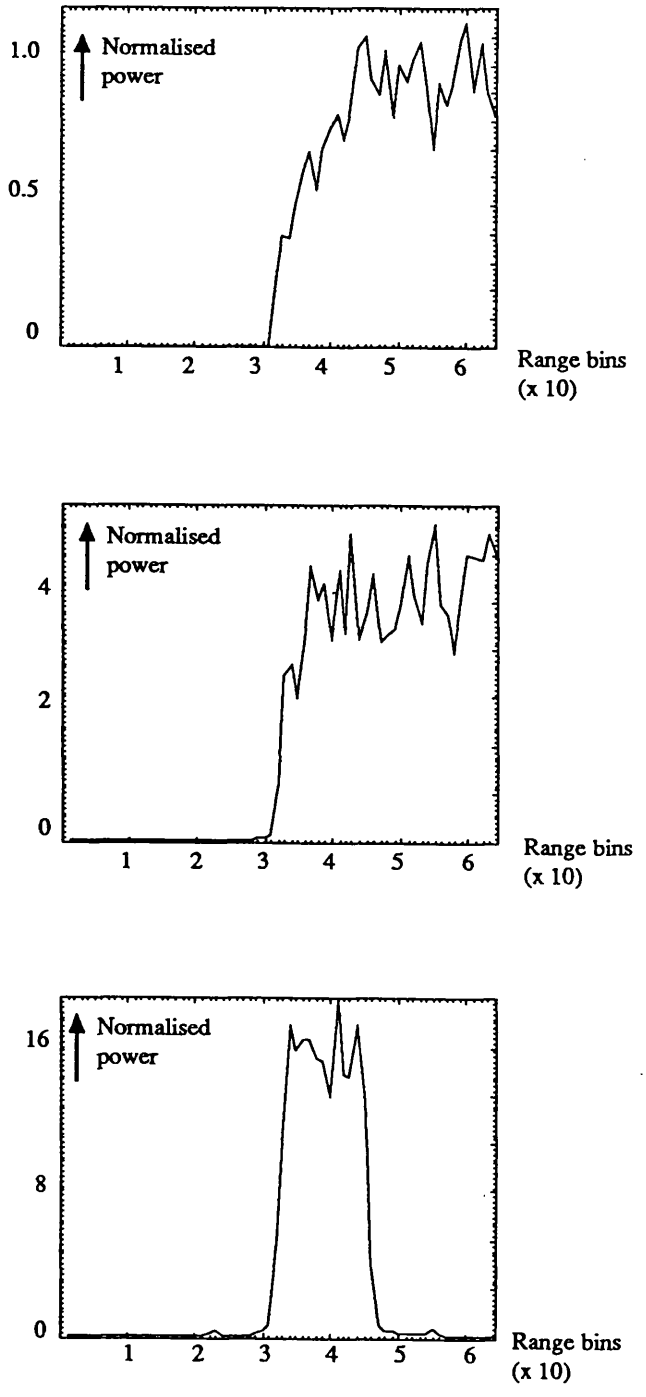

Figure 3.3-5. The echoes at the 1st, 2nd and 3rd resolutions respectively, generated from the echo at the finest resolution, and filtered by the anti-alias filter in the altimeter. The resolution is progressively reduced by 0.25.

Figure 3.3-5 illustrates the signal at the first, second and third resolutions when the anti aliasing filter of the altimeter is fixed at 64 range bins. In this case the FFT length of the data in the altimeter is fixed, and the RSS baseband signal passed to the altimeter must be sampled (interpolated). The echo is positioned in the same range bin each time i.e. the change in resolution does not introduce a timing error, it merely changes the timing resolution.

The pre-cursor and post-cursor are evident if the same procedure is applied to the echo in figure 3.2-2 without the uniformly distributed phase spectrum in each range bin, i.e. the in-phase component has the form of (3.2-12) or (3.2-13). If we again consider a change in the resolution by a factor of 4, the power in the range window is illustrated by figure 3.3-6. Considerable spillover has taken place as a result of the abrupt truncation of the signal data set. Moreover, the shape of the signal is dependent on the position of the gating signal.

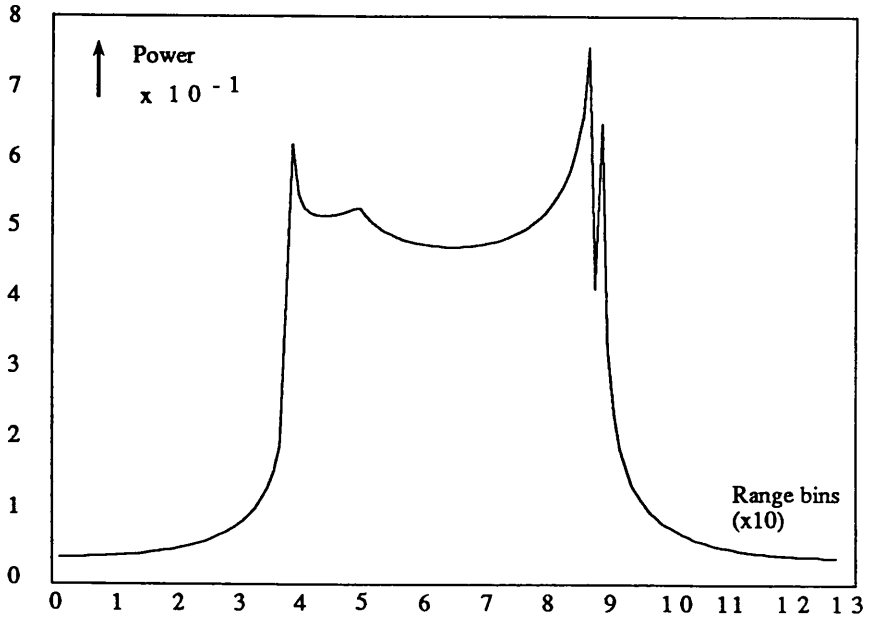

Figure 3.3-6. The detected echo power spectrum when the statistics of the simulated spectrum are non-stationary. In this case the portion of the signal modulated onto the chirp is extremely critical.

3.3.3 Signal to noise considerations

In the previous section, we observed a small pre- and post cursor around the de-resolved echo as a result of truncating the data set. This is merely a consequence of windowing the data set which has the effect of smearing energy in the range window, producing ripples around the echo. The smearing is reduced for signals having stationary statistics because much of the ripple is averaged out. Another way of considering it is that the echo information is approximately uniformly distributed over time, as seen from §3.2.3. As a result, the sampled data set of length ηT ($\eta \leq 1$) contains on average 100η % of the echo data.

The ripple level or residual multiplicative noise was computed for an echo spectrum having stationary statistics at a number of different resolutions. The noise level was observed to be independent of the echo resolution. However since the peak signal is reduced every time a resolution change occurs, the effective signal to noise ratio is therefore reduced by η each time. A plot of the relative noise level as a function of resolution is shown in figure 3.3-7. The noise level at the finest resolution ($\eta = 1$) is only limited by the round-off noise in the computer, since the entire data set of the FFT is used to reconstruct the spectrum.

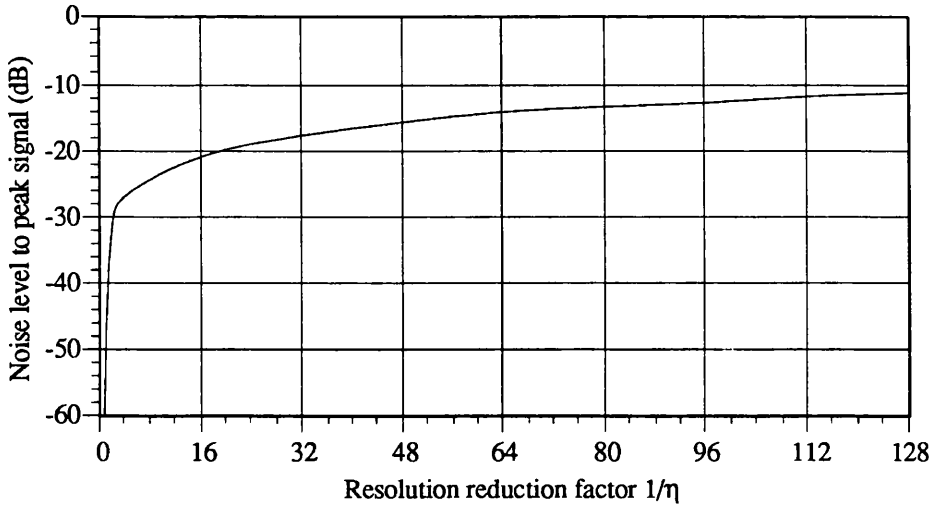

Figure 3.3-7. The noise level relative to the peak signal power in the echo spectrum for a number of resolutions. The relative level of the noise floor increases by approximately 3 dB per octave reduction in resolution.

The bandwidth of the echo spectrum determines how much power is leaked into the range bins around the echo. The bandwidth of the echo used to generate the noise level in figure 3.3-7 was 220 range bins and 512 range bins were used to calculate the FFT. Figure 3.3-8 shows the dependence of the relative noise level at the second resolution on the echo bandwidth. The worst case signal to noise ratio at the second resolution is 30 dB and occurs for large echo bandwidths. Therefore the plot of noise to signal level as a function of resolution represents a worst case limit for signals generated using the method described in §3.2.1.

The signal to noise ratio at very coarse resolutions (i.e. $1/\eta > 128$) is of the order of 10 dB which is none the less still high enough for the altimeter to track the surface (Somma et al., 1980; p178).

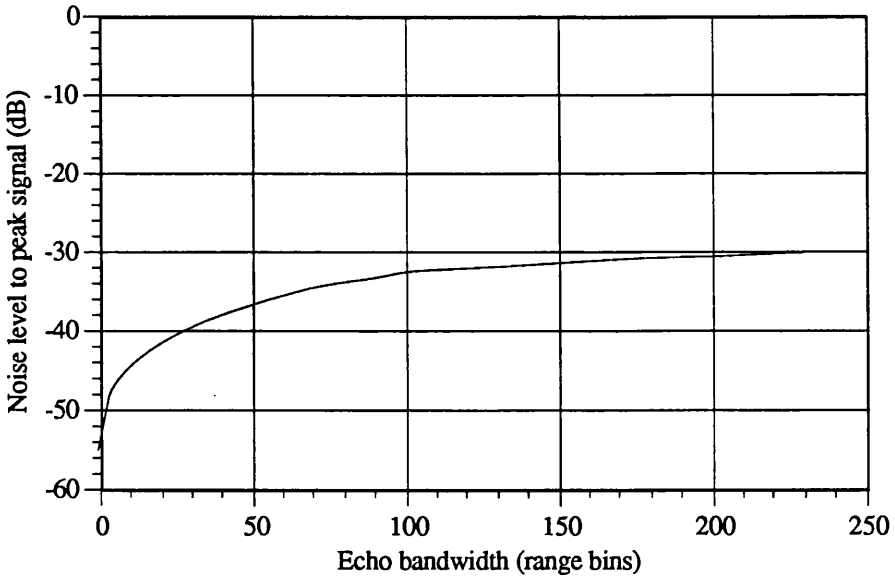

Figure 3.3-8 The mean noise level relative to the peak echo power at the second resolution.

3.4 OTHER FORMS OF RETURN SIGNAL SIMULATION

There are three different categories of return signal simulation. Each of the categories will be analysed in turn.

3.4.1 *Methods using an inverse Fourier Transform*

There are two other variants of the method of return signal simulation based on the inverse Fourier Transform - the method used for testing the ERS-1 altimeter (Francis, 1982) and a method which requires as many data sets as there are resolutions. This method is discussed and compared with the proposed technique in §3.4.1.2.

3.4.1.1 RSS for the ERS-1 altimeter

The return signal is spectrally band-limited to N resolution cells of the altimeter, i.e. to a bandwidth B where:

$$B = \frac{N}{T} \tag{3.4-1}$$

The in-phase and quadrature channels, referred to in figure 3.1-5, are digitally synthesised, and are given by (Francis, 1982):

$$I(mT_s) = \sum_{n=-N/2}^{N/2-1} a_n \cos(\omega_n m T_s + \varphi_n) \tag{3.4-2}$$

and:

$$Q(mT_s) = \sum_{n=-N/2}^{N/2-1} a_n \sin(\omega_n m T_s + \varphi_n) \tag{3.4-3}$$

where a_n and ϕ_n are the amplitude and phase of the signal in the n^{th} resolution bin of the altimeter, in the presence of fading. These fading quantities relate to a discrete form of $f(\omega)$ in (3.1-17):

$$a_n = |f(\omega_n)| \tag{3.4-4}$$

$$\phi_n = \tan^{-1}\frac{\mathrm{Im}\{f(\omega_n)\}}{\mathrm{Re}\{f(\omega_n)\}} \qquad (3.4\text{-}5)$$

$$\omega_n = n\frac{2\pi}{T} \qquad (3.4\text{-}6)$$

By setting:

$$T_s = \frac{T}{N}, \qquad (3.4\text{-}7)$$

eqn.s (3.4-2) and (3.4-3) become:

$$I_m + jQ_m = \sum_{n=-N/2}^{N/2-1} \left(a_n e^{j\phi_n}\right) e^{j2\pi nm} \qquad (3.4\text{-}8)$$

The implementation of the RSS for the ERS-1 altimeter is shown in figure 3.4-1. The critical element of this scheme is the multiplier that forms the product of the amplitude a_n and the value from the sine or cosine PROM. Since the return signal is sampled at the Nyquist rate, N samples are required per tone and thus N^2 multiplications are required to synthesise the return signal. The time samples are accumulated in a summing RAM, and converted to analogue form. The subsequent modulation is as depicted in figure 3.1-5.

The RSS for the ERS-1 altimeter has the same interface to the RF part, and therefore could use the proposed technique for generating a coarser resolution. However, since the bulk of the computational effort is performed on-line, the hardware is substantially more complex. In addition, the method is limited by the speed of the multipliers, which is given by:

$$f_{mult} = N^2 PRF \qquad (3.4\text{-}9)$$

The square law dependency of the multiplier rate on the number of resolution cells restricts the extent of the echo that can be modelled in real time. Figure 3.4-2 shows the dependency as a function of N and PRF. For example, the multiplier speed would need to be at least 60MHz if 256 resolution cells were to be modelled at a PRF of 1 kHz. Observing that the echo duration:

$$T_L = N\tau, \qquad (3.4\text{-}10)$$

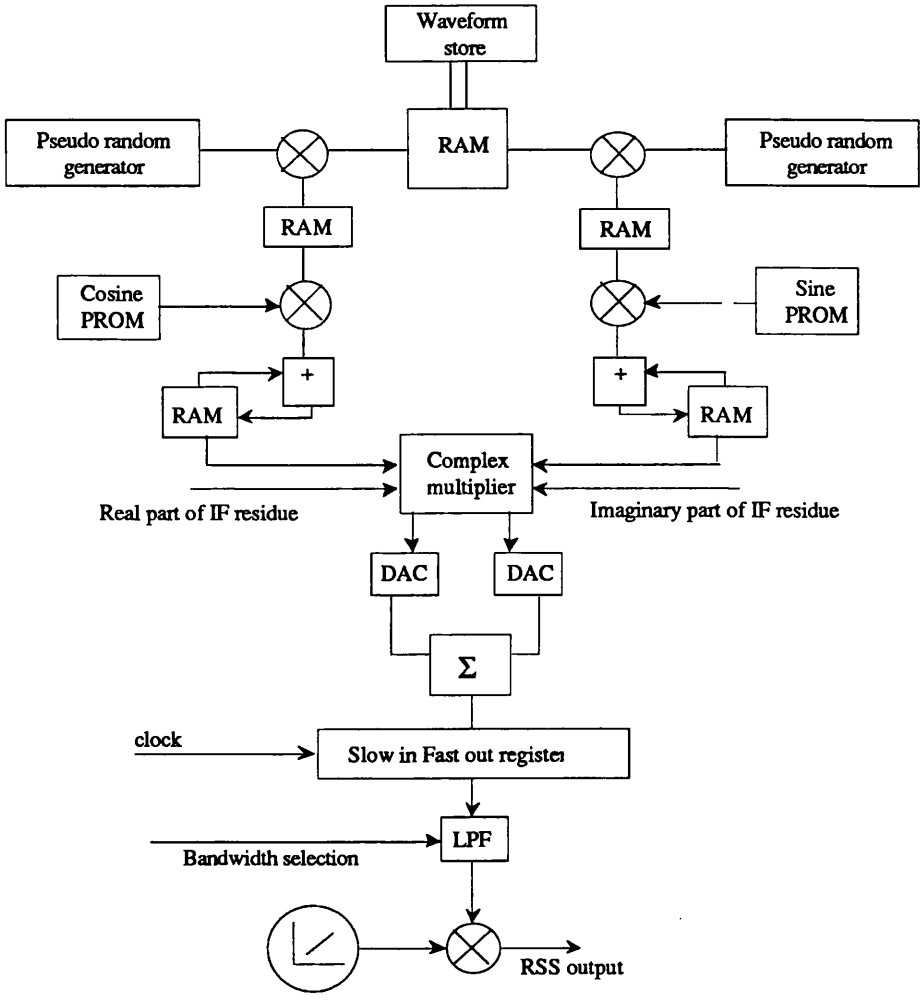

Figure 3.4-1. The generation of the in phase and quadrature channels for the RSS used in the testing of the ERS-1 altimeter (after Francis, 1982). The DFT is computed on-line by the combination of multiplier and summing RAM. The diagram has also been modified to include a filter bandwidth selection for adaptive resolution.

then by manipulating (3.4-10) and (3.2-9), the maximum echo duration that can be modelled is:

$$T_L \leq \tau \sqrt{\frac{f_{mult}}{PRF}} \qquad (3.4\text{-}11)$$

This constraint is made more severe if there is a desire to operate the altimeter with a finer

resolution, or if there is a need to model a longer echo duration. Both of these features are required by the ATTA. The inability of the RSS for the ERS-1 altimeter to properly model the entire echo duration corresponding to rough topographic terrain is its primary weakness.

The proposed RSS does not have this limitation; however it is limited by the access time of the Slow in Fast out register. With typical access speeds of 30 MHz, the number of samples that can be clocked out in 20 μs (i.e. and modulated onto the chirp) is 600. Naturally, for longer chirp lengths, the number of resolution cells that can be modelled is proportionally increased.

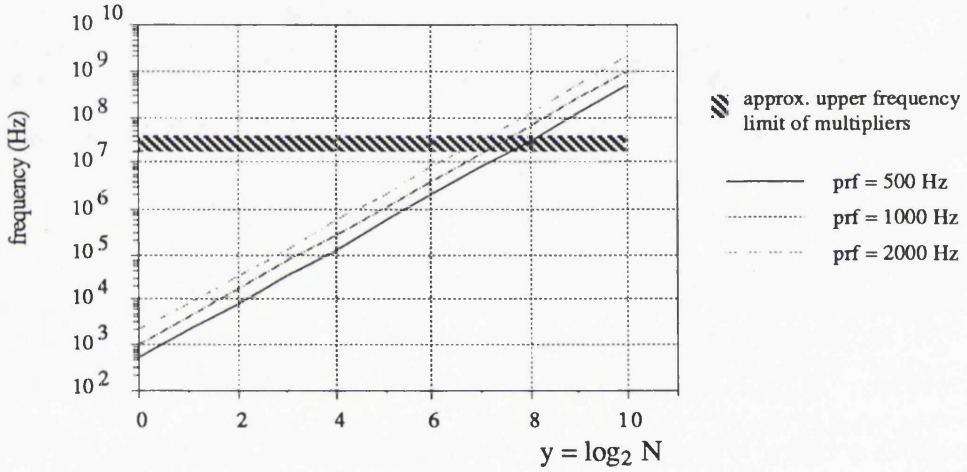

Figure 3.4-2. The dependency of the number of resolution cells on the multiplier speed and pulse repetition frequency in the RSS for the ERS-1 altimeter. The number of resolutions cells N is plotted as the index y, where $N = 2^y$.

3.4.1.2 RSS with separate data sets for each resolution

The method of return signal simulation that utilises N different data sets for N resolutions does have one advantage that offsets the N-fold increase in the digital hardware complexity. That is, if the number of samples, and hence sampling frequency, is the same for each resolution, then only one anti-aliasing filter is required, and it will suffice for each of the resolutions. Essentially, the coarser resolutions are progressively oversampled by a factor of 4.

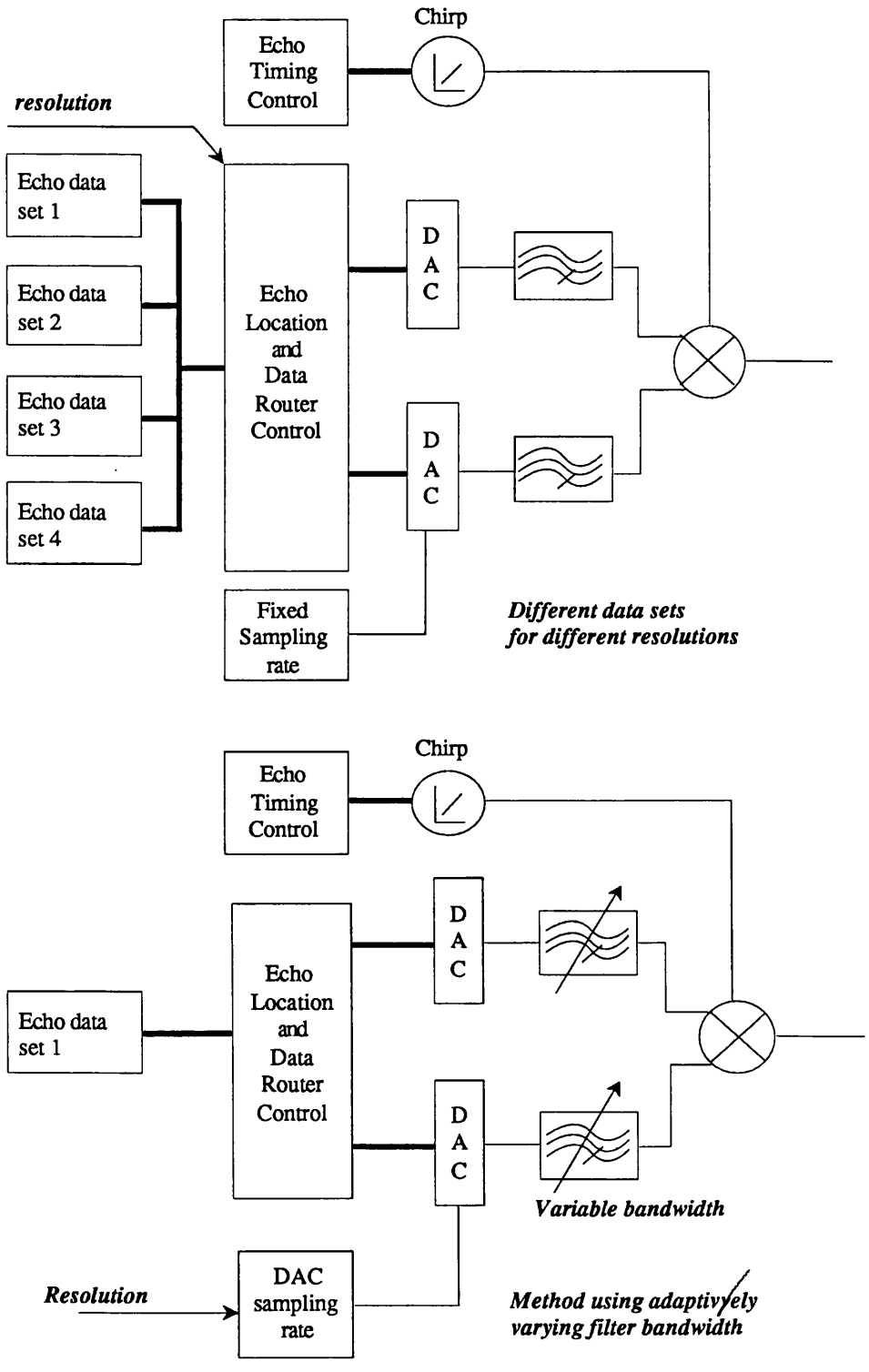

Figure 3.4-3. The two RSS designs that give suitable adaptive resolution operation. The first one requires more N different data sets for N resolutions; the latter requires N anti-alias filters for N resolutions.

The proposed RSS cannot include this over sampling since the data set, and thus sampling frequency, is reduced by a factor of 4 each time the resolution is made coarser. Thus N different anti-aliasing filters are required for N different resolutions. Moreover, the group delay through the filters is a function of the cut-off frequency, and thus the group delay increases proportionally as the resolution is made coarser. If no compensation was made for the group delay, the baseband signal would be progressively misaligned with respect to the chirp as the resolution was made coarser. The misalignment of the echo signal is not critical since the timing of the simulated echo is contained in the spectral components of the baseband signal, and the timing instant of the chirp. The secondary effects of such a misalignment are analysed in §4.

Figure 3.4-3 illustrates a block diagram of the two RSS methods discussed. The principal difference between the two methods is the N-fold increase in echo data, which even for a single resolution is immense.

3.4.2 Convolver

The SAW convolver is based on a parametric interaction that takes place in a medium when the power level is such that the medium becomes non-linear (Quate and Thompson, 1970). Thus if two waves are oppositely directed, a beat frequency is generated that is equal to the sum of the two frequencies of the two input waves. In addition, if the waves are respectively modulated by signals F(t) and G(t), then the output is modulated by a signal that is the convolution of F(t) and G(t). A diagram of this process is shown in figure 3.4-4.

This principal can be used in an RSS to directly perform the convolution in (3.1-6), i.e. the two input signals are the chirp and the surface impulse response respectively. A time compression, by a factor of two, also occurs at the output because the relative velocity of the two signals is twice that of each of them. As a consequence, the bandwidth and centre frequency of the output are doubled. The two input signals must therefore be appropriately scaled so that the output has the correct bandwidth and duration. The bandwidth of the surface impulse response is determined by the required delay time resolution of the return, and thus is of the order of the chirp bandwidth (B).

The synthesis of an ocean return signal at the appropriate delay time resolution would require a Nyquist rate of at least twice the bandwidth B, i.e. a 1.2 GHz sampling

frequency would be required to generate the ocean return signal to a resolution of 0.25m. Francis et al. (1980) devised a complicated solution to ease the generation of this signal, introducing parallel processing as a means of reducing the high sampling frequency. Figure 3.4-5 shows how the samples of the signal would be arranged to allow a reduction in the sample rate by a factor of N (=3). The delay line spacing is equal to the clock period 1/(2B), and the N channels are clocked successively by a reduced clock rate (2B/N). The outputs are combined in a delay line, up-converted to IF and fed into one input of the convolver. The clock frequency has effectively been reduced by a factor N at the expense of an N-fold increase in the circuit complexity.

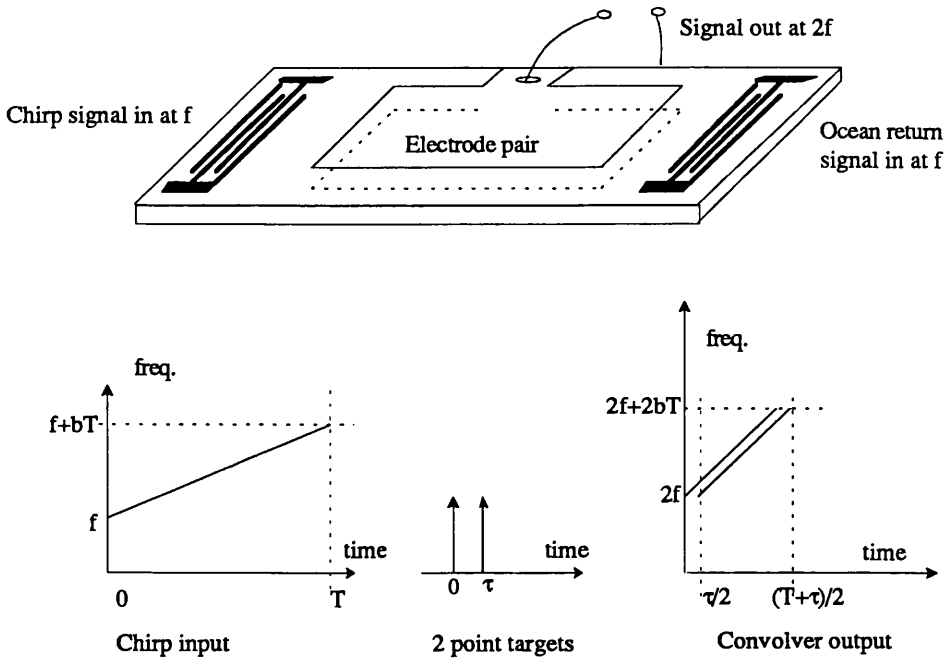

Figure 3.4-4. The operation of a typical convolver. The output of the convolver is shown graphically in frequency-time for two simulated point targets.

The maximum achievable bandwidth of a SAW convolver is approximately 500 MHz, which limits the maximum resolution of the simulated return. The bandwidth of the convolved output could be increased by frequency multiplication; however intermodulation products would degrade the fidelity of the simulated return. In addition, this approach does not offer much flexibility in changing the bandwidth (and hence resolution) of the simulated return. Each of the PROMs of figure 3.4-5 would need to be reprogrammed to contain the new amplitude values, and a scaled clock frequency would be needed to generate the sampling frequency for the new delay time resolution.

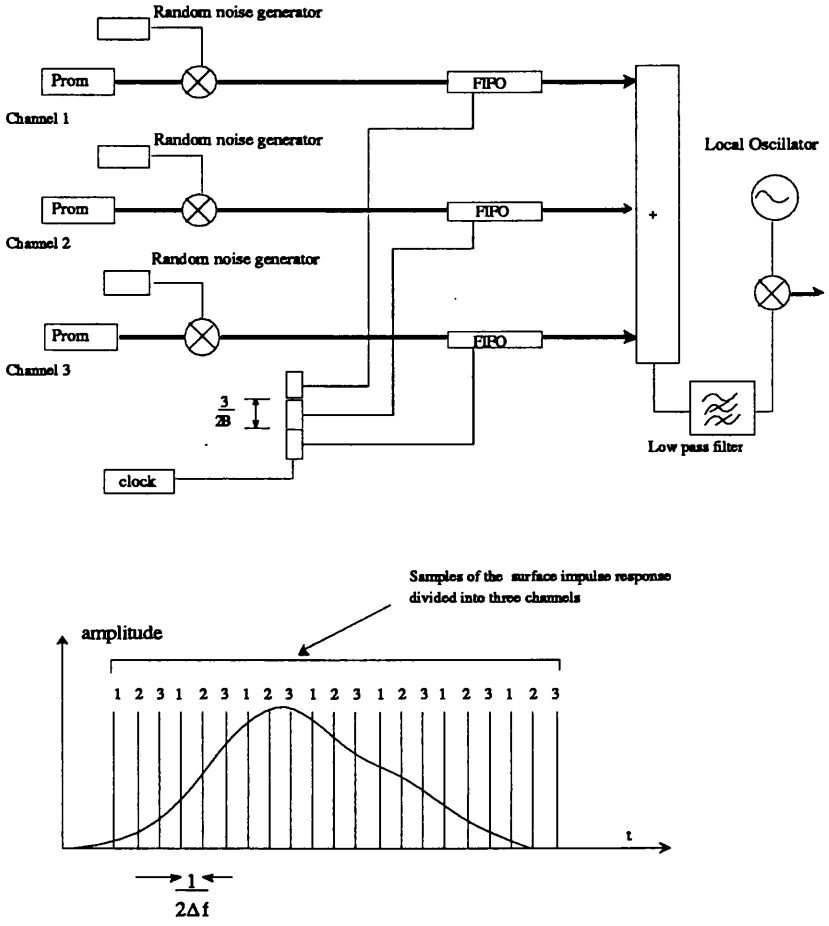

Figure 3.4-5. A method of generating the baseband echo signal using parallel processing. The samples are interleaved, fed into three parallel FIFOs which are strobed successively. The outputs are combined in a delay line [taken from Francis (1982) and adapted].

3.4.3 Series of overlapping chirps

This method of return signal simulation, shown in figure 3.4-6, models the range window of the altimeter in the delay time domain. The resolution cell is represented by the spacing of the delay elements, and thus the number of delay elements physically models the extent of the return. At each delay line tap, the signal is weighted according to the net reflectivity associated with that cell, and the various contributions are summed using a power combiner or another tapped delay line. The principal advantage of this technique is that it simulates the true time modulation of the return. The quadrature channel in figure 3.4-6 also allows the phase of the signal to be correctly reproduced The phase distribution of

each cell is modelled by generating a random phase value (ϕ_i for the i^{th} cell) for each cell. Then, by weighting the i^{th} I and Q channels by $A_i\cos(\phi_i)$ and $A_i\sin(\phi_i)$ respectively, the combined signals will exhibit the required random phase variation from cell to cell, according to eqn.'s 3.1-7 and 3.1-8 respectively.

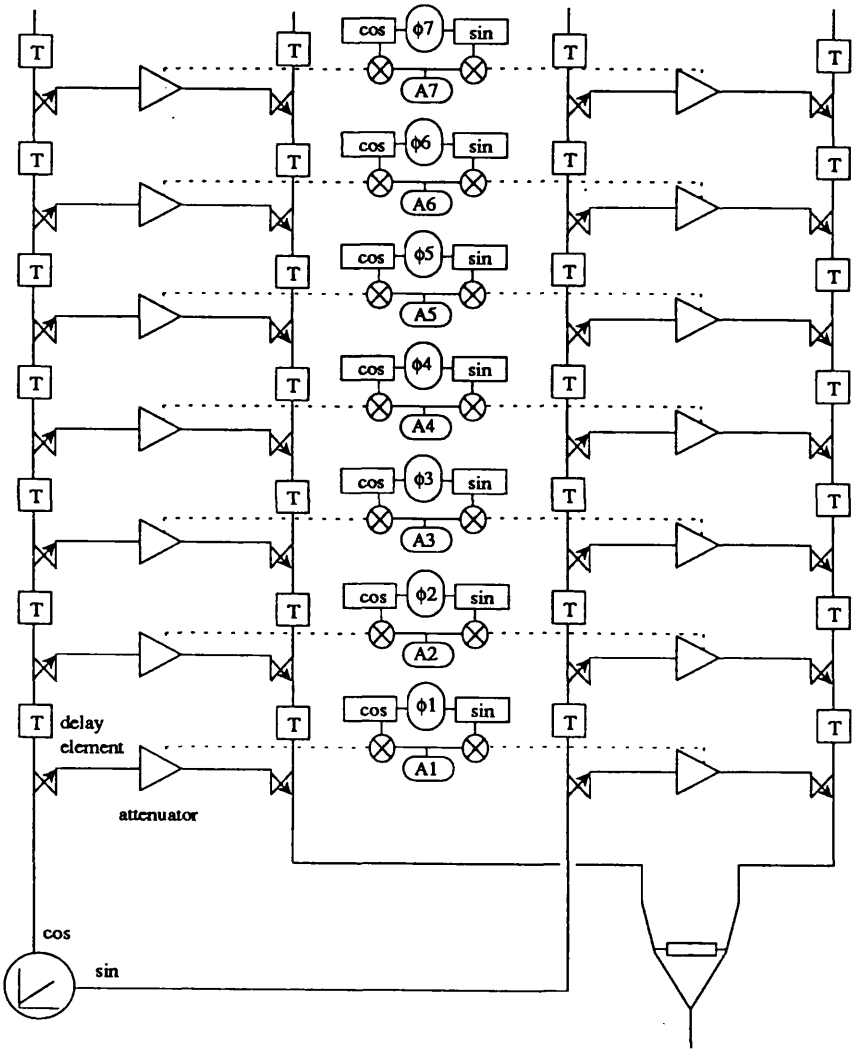

Figure 3.4-6. A method of return signal simulation based on delaying a chirp in a tapped delay line, and attenuating the signal in each tap. The phase of the signal is also modelled in each resolution cell by the parameter ϕ_i.

3.5 Summary

We can summarise this chapter with the following statements.

The scattered signal from a rough surface was defined in a form that allows substantial simplifications to be made, thus yielding a convenient expression for the return signal.

The analysis relating the facet model to the poisson process is very useful and will be used later to quantify the effect of phase and amplitude errors.

The timing of the simulated signal is achieved through timing a chirp in physical time, and through considering the residual timing in the frequency domain. It was shown that there was no loss of precision in timing the echo in this way.

The expression for the return signal is particularly suited to generating a more coarsely resolved echo from an existing echo. This would therefore allow the echo to be derived from the finest resolution echo in real time. This approach is only applicable when the echo signal is statistically stationary.

A comparison of this method with other forms of return signal simulation was undertaken, and concluded that this is the one form of simulation that is least affected by extremely high sampling rates and/or extreme circuit complexity.

Chapter 4

Prototype Return Signal Simulator Design and Analysis

4.1 OUTLINE OF THE DESIGN REQUIREMENTS

The three principal requirements of an RSS are to correctly reproduce the echo timing and dynamic range, and to operate at the full pulse repetition frequency. The timing and signal dynamic range requirements of an RSS can be derived by requiring that the specification for the RSS is approximately an order of magnitude more precise than that of the altimeter, if it is to be used successfully to test the altimeter. The requirements of the altimeter, and the suggested requirements of the RSS are listed in table 4.1-1.

A prototype altimeter breadboard was constructed by the Space Systems Division of BAe, and the main operational parameters of this altimeter are listed in table 4.1-2.

Parameter	Altimeter requirement	Suggested RSS requirement
Timing precision	670 ps (10 cm)	67 ps (1 cm)
PRF	0.5 kHz to 2.0 kHz	0.5 kHz to 2.0 kHz
Minimum S/N	- 4 dB	- 4 dB
Maximum S/N	20 dB	20 dB

Table 4.1-1 Altimeter and RSS requirements

Parameter	Altimeter specification
Chirp bandwidths	320 MHz, 80 MHz, 20 MHz, 5 MHz, 1.25 MHz
PRF	0.5 kHz to 2.0 kHz
Number of pulses averaged	50
Tracking and estimation algorithms	SMLE (ocean), OCOG (land)
Pulse lengths	19.2 μs, 102.4 μs and 300.8 μs

Table 4.1-2 Operational parameters of the altimeter

4.2 OUTLINE OF THE DESIGN

The PRF requirement determines how quickly the RSS must operate. The following operations must be performed within a single pulse repetition interval:

- determination of the resolution used by the altimeter,
- setting the timing of the echo by triggering the chirp at the correct instant,
- setting the gain of the echo,
- setting the resolution of the echo, and
- reconstructing the echo at the correct resolution.

If these operations are accomplished successfully, then the RSS will provide realistic echoes in real time with the correct resolution, and at the correct instant in time. Each of these operations will each be discussed in the following sections.

4.2.1 Basic solution - the DRAM memory

The design of the RSS is inherently limited by the conflicting requirements to perform all the operations within a particular time interval, and to maximise the number of range bins that constitute the echo signal within that time. The latter requirement is formidable if real time operation at a relatively high PRF is to be achieved. A sensible design philosophy will separate the two requirements. This can be achieved by using a second processor dedicated to handling the immense quantity of echo samples. Three different approaches were considered.

Approach 1

The echo store would be RAM-based and resident in the RSS computer. Thus in every PRI (i.e. 1 ms) the samples of a single echo would need to be transferred through the computer interface. At a maximum interface speed of approximately 1 MHz, the maximum number of samples that could be handled is 500. However, the primary address space (i.e. fast addressing) is typically limited to 64 kbytes (16-bit addressing); thus this would limit the echo sequence to 64 PRIs. Extended addressing is twice as slow, thus echoes over a long sequence would have at most 250 resolution cells. The above calculations assume that the processor is dedicated to transferring data. However, in practice it must also set the timing, gain and resolution of the echo.

Approach 2

The echo store is the hard disc, and the echoes are transferred directly from the hard disc to the RSS hardware in each PRI. The principal limitation is the hard disc access time. A hard disc sector typically contains 13 kbytes of data, and the seek time of the sector is approximately 23 ms. Thus if the hard disc could be driven such that it was continuously seeking a sector and passing data, it would only be capable of a transfer rate of 0.5 Mbytes/s. Thus a maximum echo duration of 250 resolution cells is possible.

Approach 3

The echo store would be RAM-based, but not resident in the RSS computer. In this configuration, there is no interface limitation, and the transfer rate is only limited by the RAM access time, which is typically 100 ns. Thus transfer rates of 5 to 10 MHz are possible. There is also no limitation on the size of RAM that can be accessed. The only limitation is the amount of time required to pass data from the permanent data base to this temporary RSS echo store.

The last approach is the one adopted since it offers the most flexibility and the highest data rates.

4.2.2 Timing considerations

The RSS timing is critically dependent on the timing of the chirp, whereas it is not so dependent on the instant at which the baseband signal is triggered with respect to the chirp (see §4.2.5). Since the simulated altitude is approximately 800 km, the two way time delay corresponds typically to 5 pulses in flight (i.e. for a PRF of 1 kHz); thus the RSS must delay the processing of the simulated signal by 5 PRIs. The timing is therefore derived from the nearest preceding transmit trigger instant, rather than the one 5 pulses back. The instant at which the echo is timed with respect to the start of the transmit chirp (defined in §3.1.4) is given as:

$$t = t_o + \frac{T_L}{2} \qquad (4.2\text{-}1)$$

where t_o is the time at which the first return occurs, and T_L is the duration of the echo. The processing delay is:

$$N_1 = \text{integer}\left[\left(t_o + \frac{T_L}{2}\right).PRF\right] \qquad (4.2\text{-}2)$$

The timing relative to the nearest transmit instant is defined in multiples of a stable clock period and the residual time, less than the clock period, is implemented as a fine frequency offset to the start frequency of the chirp. The number of clock periods is given as:

$$N_2 = \text{integer}\left[\frac{t_o + \frac{T_L}{2} - \frac{N_1}{PRF} - C_1}{\tau}\right] \qquad (4.2\text{-}3)$$

C_1 accounts for extraneous transmission delays (e.g. the group delay in the filter of the upconversion unit), and N_2 is the number of clock periods. The residual fine frequency shift is:

$$\Delta f = b\left[t_o + \frac{T_L}{2} - \frac{N_1}{PRF} - C_1 - N_2\tau\right] \qquad (4.2\text{-}4)$$

The digital chirp generator developed by BAe (Durrant and Richards, 1990) can be programmed to output a chirp after a certain number of clock pulses given by (4.2-3). The start frequency of the chirp can also be programmed to include the offset given by (4.2-4).

The timing precision is governed by the smallest frequency increment that can be produced by the chirp generator. The frequency is specified to 24 bit resolution; thus if the input clock is 40 MHz, the smallest frequency unit is 2.38 Hz. This corresponds to a timing precision of 15 ps for a chirp of duration 102.4 μs and bandwidth 320 MHz.

The digital chirp generator, described in §4.3.1, outputs a gate pulse which is used to synchronise the baseband modulation to the start of the chirp. However, due to the group delay of the filters, the baseband modulation is delayed progressively more and more as the resolution is made coarser. In order to compensate for this delay, the gate used to synchronise the baseband signal to the chirp signal must be triggered a time $\Delta t_i - \Delta t_c$ before the chirp is triggered (where Δt_i is the delay through the anti-alias filter for the i^{th} resolution, and Δt_c is the chirp delay through the upconversion unit). If the same prototype filter is used for each of the anti-alias filters, then:

$$\Delta t_i = 4\Delta t_{i-1} = ... = 4^{i-1}\Delta t_1 \qquad (4.2\text{-}5)$$

Figure 4.2-1 shows two means of compensating for the group delay difference between the anti-alias filters. Figure 4.2-1(a) requires two variable delays to be programmed according to the resolution. It is possible to realise both delays using programmable counters. Figure 4.2-1(b) achieves the same result using numerous fixed delays. It will be shown in §4.2.5 that since the timing information of the baseband echo is contained in the

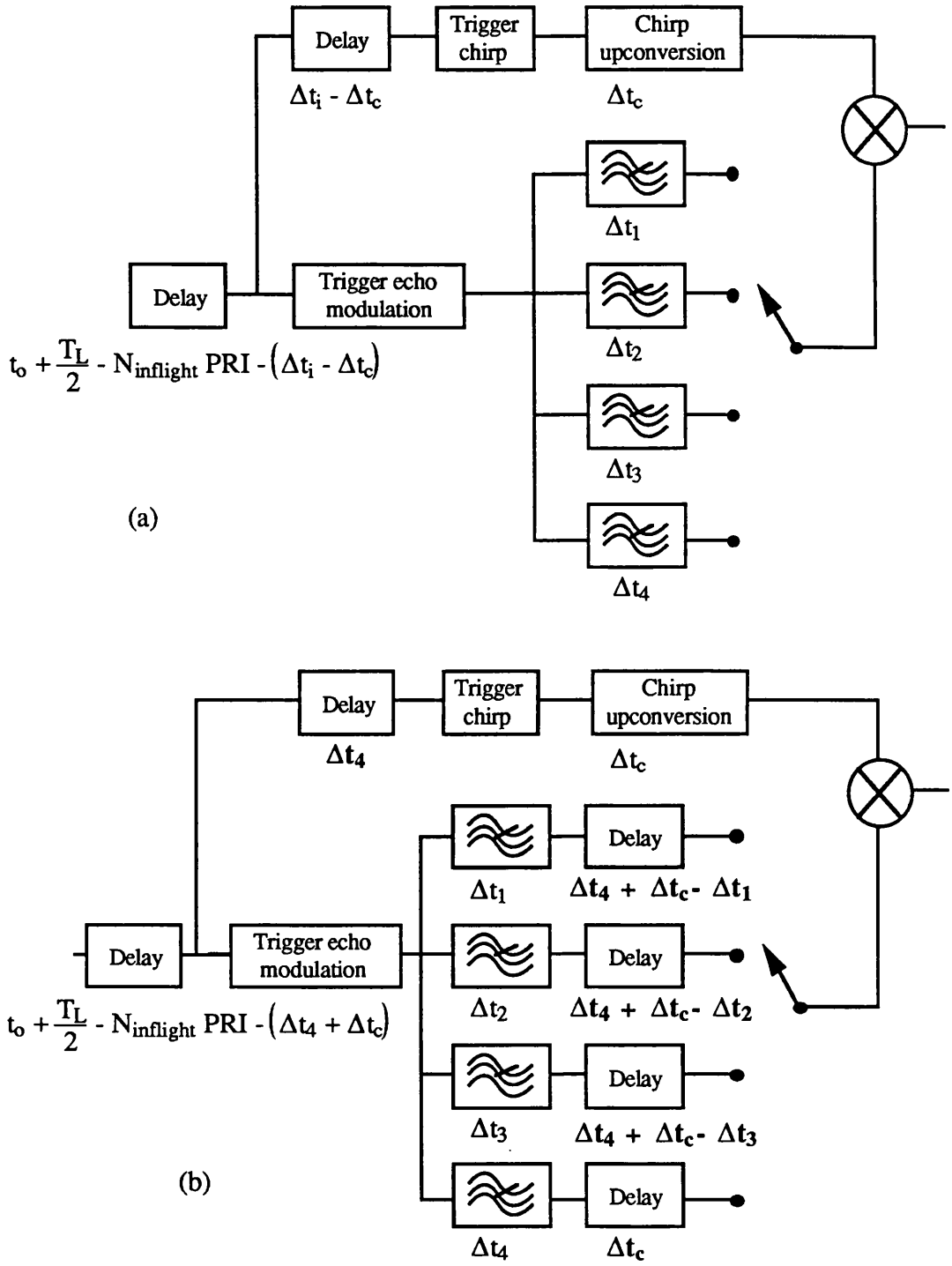

Figure 4.2-1(a) Group delay compensation using two variable time delays. This solution is, in principle, feasible

Figure 4.2-1(b) Group delay compensation using six fixed time delays. The realisation of the delays in this configuration presents a serious problem.

frequencies of the signal components rather than their phases, such a misalignment is not important. The main effect of such a misalignment is a decrease in the signal to noise ratio of the signal in the range window. If the latter effect is deemed to be a problem at the coarse resolutions, appendix A.3 outlines how a suitable trigger for the modulation can be output before the chirp is generated, as in figure 4.2-1(a).

4.2.3 Chirp considerations

The interaction of the transmit pulse with the surface characteristics give rise to the radar return signal. Thus any distortion on the transmit pulse will be observed as a form of distortion on the returned signal. There are two ways in which the characteristics of the transmit chirp can be included in the simulation.

The first method is to regenerate the characteristics of the transmit chirp. This requires measuring the difference between the transmit chirp and the chirp that will be used in the simulation, and subsequently superimposing this difference onto the RSS chirp. Figure 4.2-2 shows that the difference between the two chirps can be measured by mixing the two chirps and digitising the resulting baseband signal. Such a technique is only applicable for a single resolution. The second method is to use the transmit chirp as the RSS chirp and to trigger it at the appropriate instant. In this case, the data bus to the transmit chirp generator would need to be controlled from the RSS computer rather than from the altimeter computer. This is the best way of including the transmit chirp in the simulation. However it also involves complicated changes to the altimeter hardware. Since the altimeter is a prototype and has been developed only for use in conjunction with an RSS, the transmit chain of the altimeter was not developed; thus the latter option is not a possibility. Thus the chirp distortion is not modelled in the RSS prototype. Chapter 6 presents a novel analysis of chirp distortion that precisely quantifies the magnitude of the height error as a result of the distortion.

Apart from modelling distortion, a second consideration is the generation of the RSS chirp. There are three possibilities. Firstly, as mentioned above, the transmit chirp could be used. However, in addition to modifying the timing of the transmit chirp, the resolution (ramp rate) needs to to be delayed by the processing delay in (4.2-2). Secondly, the deramp chirp could be used. This would not require any modifications to the ramp rate since the ramp rate of the deramp chirp is delayed by the processing delay with respect to the transmit chirp. In fact, the deramp chirp is ideally aligned with the simulated return,

and thus the residual timing difference should be small. This difference could be incorporated by offsetting the simulated signal by the appropriate frequency. In this case, the delay-to-frequency transformation of the chirp would not be properly exercised. Thirdly, a separate chirp generator could be used, offering more flexibility with regard to the timing of the echo and changing resolution.

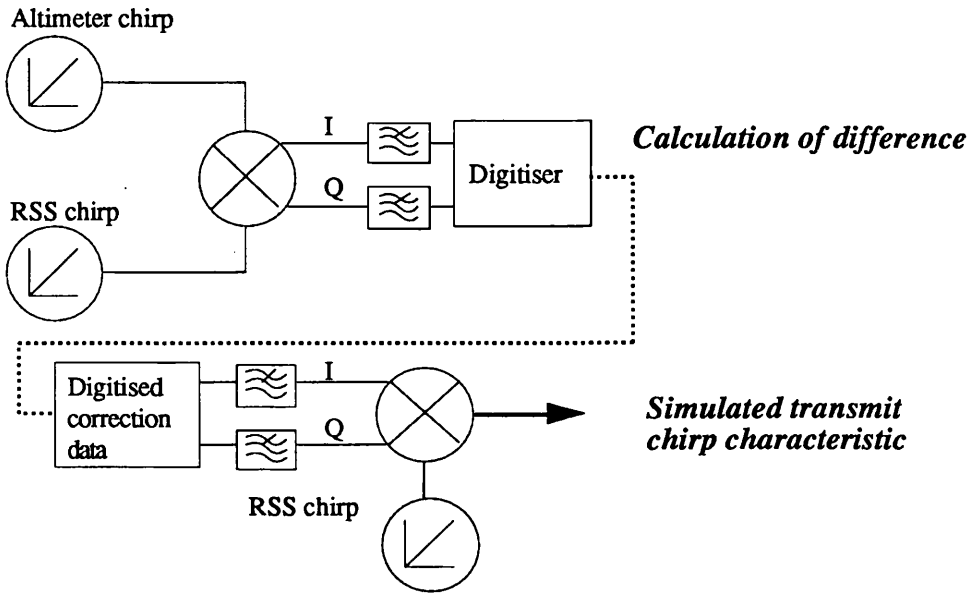

Figure 4.2-2 A method of regenerating the amplitude and phase characteristic of the transmit chirp. The transmit chirp is mixed with the RSS chirp, the baseband signal is digitised and becomes a correction to the RSS chirp for the simulation.

4.2.4 Echo duration

The number of resolution cells required to model an echo of duration T_L is given by:

$$N = bT_LT \qquad (4.2\text{-}6)$$

Typically, for a chirp bandwidth of 320 MHz, and extended return of duration 5 μs, the echo comprises 1600 range bins. The number of resolution cells that can be modelled depends on:

- technological constraints of the digital hardware, and
- anti-alias filter requirements.

The former limits the number of resolution cells (hence samples) that can be handled by the RSS hardware. The optimum access speed for memory devices is typically 30 MHz. Thus the maximum number of samples that can be accessed during the shortest chirp length (19.2 μs) is 576, unless parallel processing is used. The number of samples is rounded down to the nearest multiple of 2, to facilitate the FFT processing, and is thus restricted to 512. For the 102.4 μs pulse length, the number of resolution cells could be as large as 3000. The latter requirement determines the number of non-zero resolution cells, once a particular number of zero-padded cells have been allocated to obtain the desired degree of oversampling, which will be defined in §4.3.5. Figure 4.2-3 illustrates both of these constraints for an echo comprising a total of N resolution cells. The echo is band-limited to [-N/2T, +N/2T], and the sample spacing in the time domain is T/N.

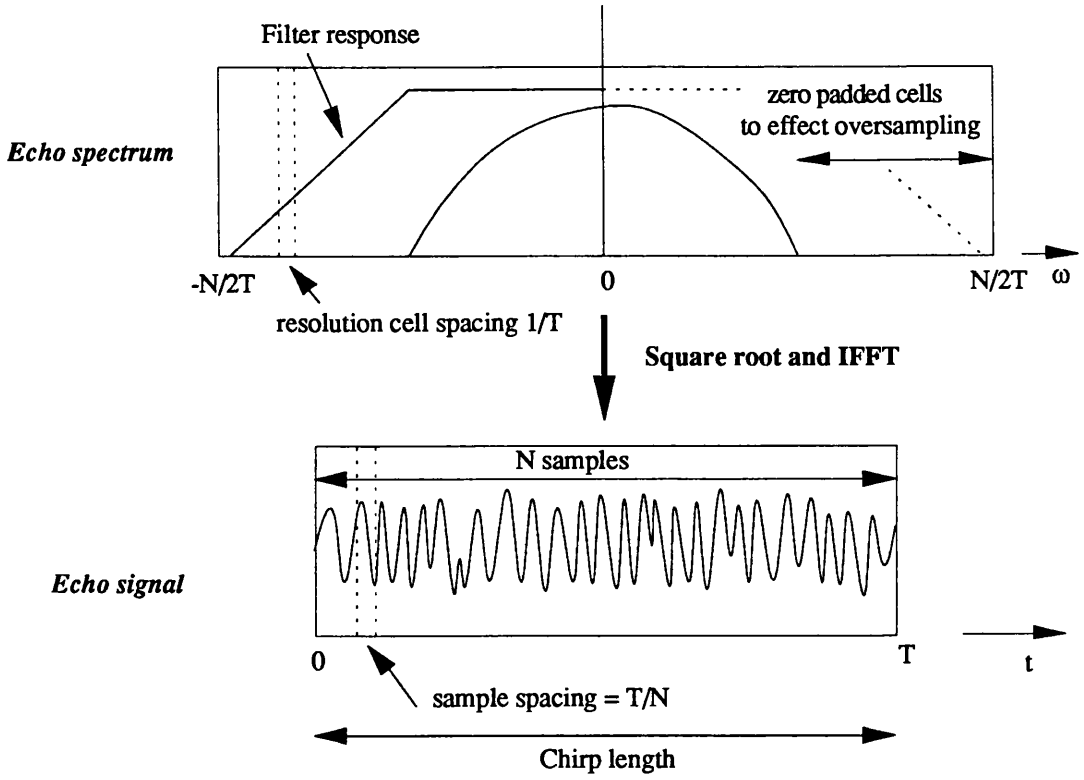

Figure 4.2-3 The simulated echo is shown in both the time and frequency domains. The bandwidth of the echo determines the sample spacing in the time domain. The two constraints are (i) the requirement to oversample the echo, and (ii) the requirement to optimise the duration of the echo, i.e. number of samples.

The cutoff frequency of the anti-alias filter at the finest resolution is:

$$f_c = \frac{\xi N}{2T} \qquad (4.2\text{-}7)$$

where $\xi \leq 1$ represents a degree of oversampling. It will be shown in §4.3.5 that $\xi = 1/2$ is a suitable figure. The technology limits the number of resolution cells to 512, and the requirement to oversample therefore restricts the echo duration to 256 cells.

4.2.5 Sensitivity of echo timing to baseband signal misalignment

As discussed in section 4.2.2, the timing of the baseband echo is contained in the frequencies of the signal components. In the following analysis, the software model of the RSS, defined in §3.3, is used to determine the sensitivity of the echo timing to misalignments between the baseband echo and the RSS chirp. The RSS baseband signals were formed from (3.1-17) by assuming that the echo power spectrum, shown in figure 4.2-4(a), is exponentially distributed. A misalignment is simulated by excluding samples that do not overlap with the RSS chirp, and adding zeros at the other end. The echo spectrum in the range window is formed for both the 1st and 2nd resolutions, and 100 single pulse spectra are averaged. The leading edge of the echo is curve-fitted with a 1st order polynomial, and then the variance of the noise power is computed over the leading edge of the echo. Finally, the timing jitter is related to the noise power by the slope of the leading edge at the half power point.

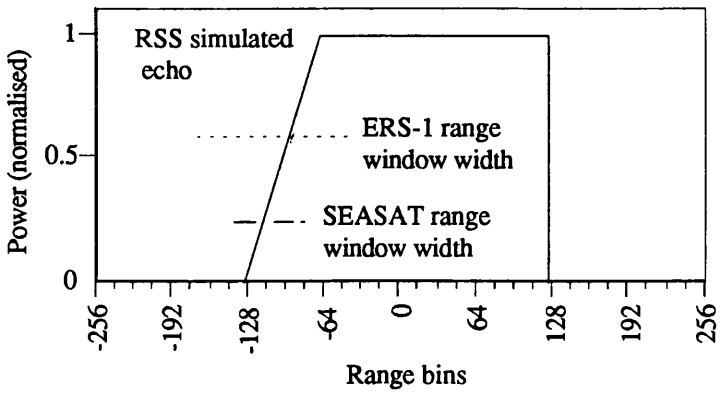

Figure 4.2-4(a) The echo spectrum used in the analysis to determine the sensitivity of the echo timing to a misalignment between the baseband echo and the RSS chirp.

Figure 4.2-4(b) shows the standard deviation of the leading edge noise power as a function of timing misalignment and of resolution. The standard deviation for zero misalignment and the 1st resolutions is 0.053 units, which is close to the expected value of 0.05 ($0.5/\sqrt{100}$) for 100 pulse averaging at the half power point of the leading edge. The standard deviation of the noise power increases as the misalignment increases for both resolutions. Thus the timing jitter, which is proportional to the standard deviation of the noise power (MacArthur, 1978), increases accordingly.

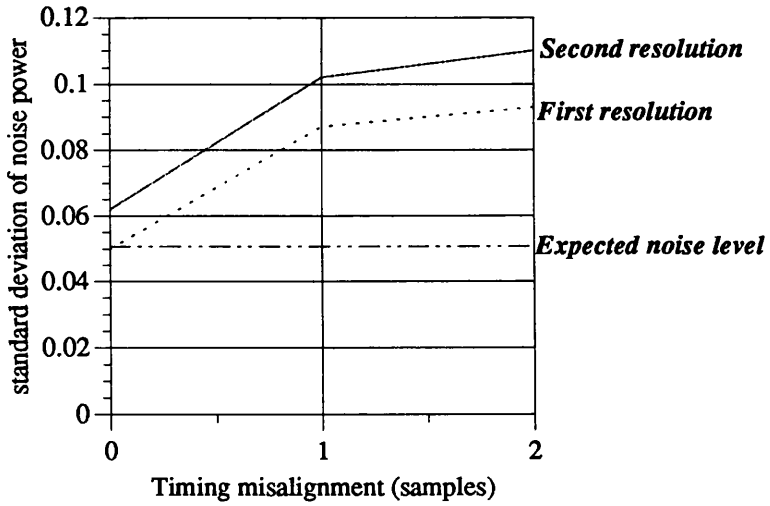

Figure 4.2-4(b) The level of height noise on the leading edge of the echo after 100 pulse averaging as a function of timing misalignment.

Figure 4.2-4(c) shows the equivalent height noise (in range bins at the 100 pulse rate) for two different echoes - of leading edge widths 16 and 64 range bins respectively - at both the first and second resolutions. The jitter is approximately four range bins for the echo of width 64 bins, and is approximately 1 range bin for the echo of width 16 bins. Obviously, the height noise decreases with increasing slope of leading edge. For typical chirp bandwidths of 320 MHz, and 1000 pulse averaging, a misalignment of 2 samples for an echo of leading edge width 16 bins will increase the height noise from 5 cm to 10 cm.

The percentage misalignment due to the group delay is given as:

$$\frac{T_g}{T} \qquad (4.2\text{-}8)$$

where T_g is the group delay of the anti-alias filter. The group delay can be written in terms of the normalised filter group delay T_n; thus the percentage misalignment is:

$$\frac{1}{T}\left(\frac{T_n 4T}{2\pi N}\right) \cong \frac{2}{N} \qquad \text{for } T_n = 6. \qquad (4.2\text{-}9)$$

Thus for a normalised group delay of 6 secs, the misalignment is approximately 2 samples out of N. Such a misalignment can be tolerated if the maximum width of the leading edge of the echo is restricted to approximately 16 range bins.

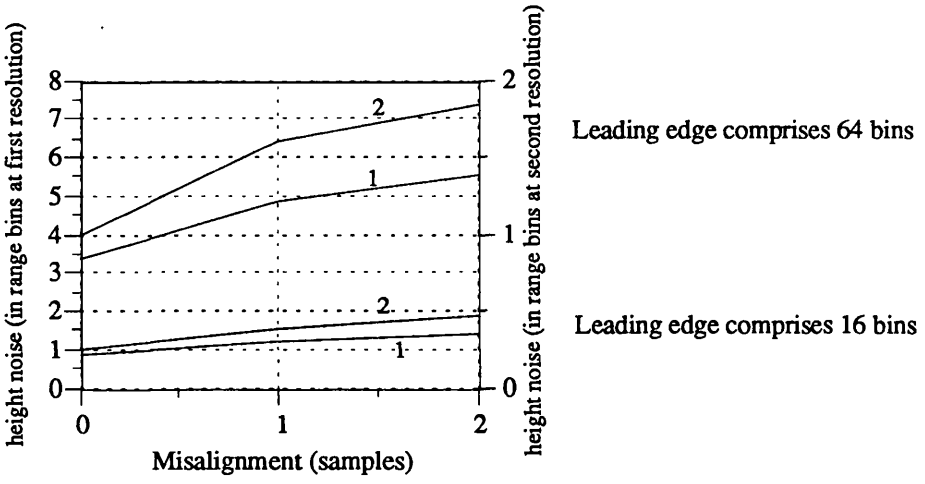

Figure 4.2-4(c) The timing jitter for two different echo spectra, and for two resolutions.

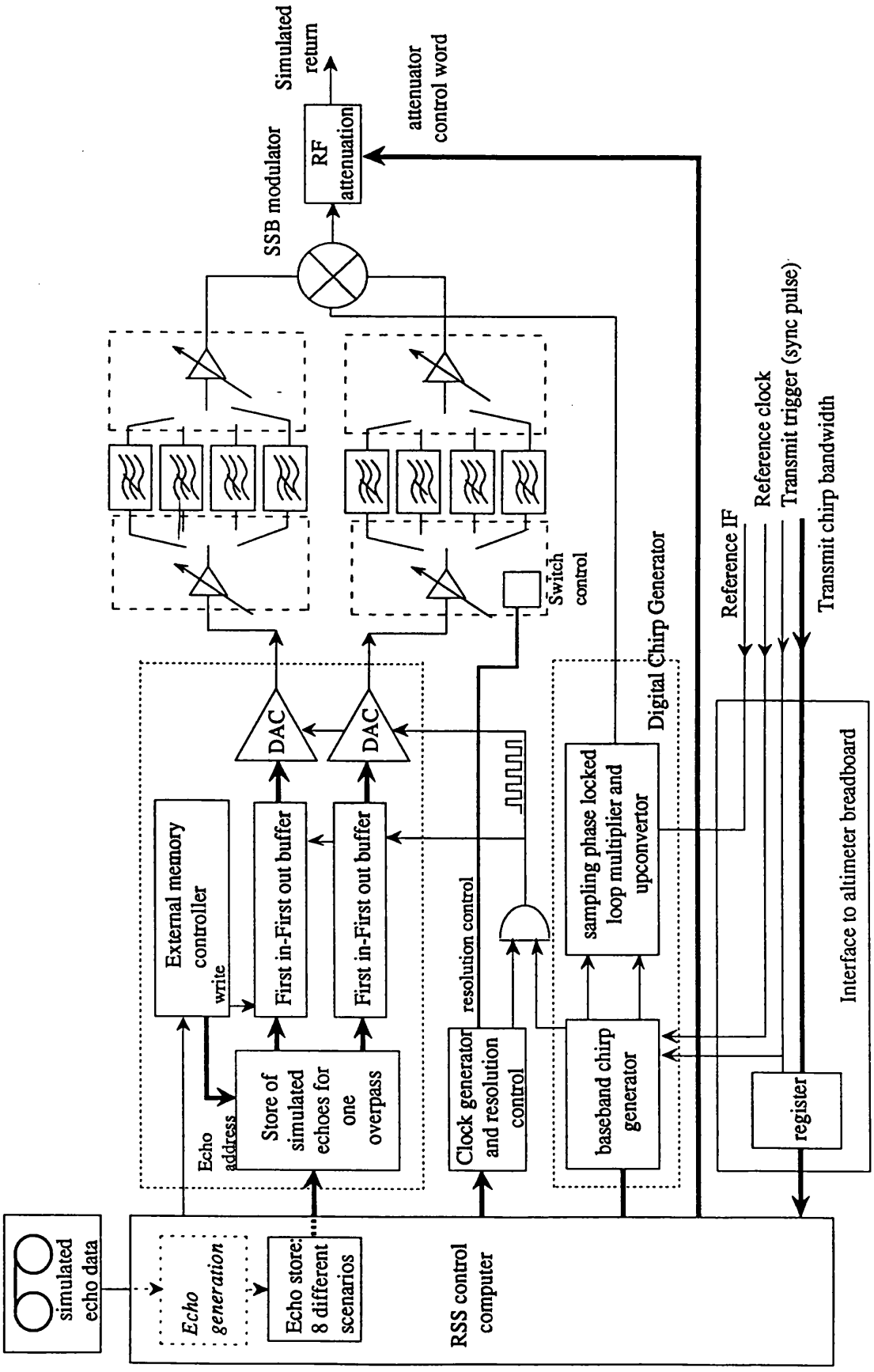

Figure 4.3-1 A block diagram of the prototype Return Signal Simulator.

4.3 PROTOTYPE CIRCUIT DESIGN

A block diagram of the return signal simulator is shown in figure 4.3-1. It consists of 7 basic parts: a computer to control all the RSS operations, a chirp generator, a memory and control unit, a clock frequency generator, a filter switching network, an upconversion and attenuation unit, and an interface to the altimeter. The functions of each of the above units will be discussed in the following sections. A more detailed description of the RSS hardware is available in Sheehan[53] (1992).

4.3.1 Digital Chirp Generator

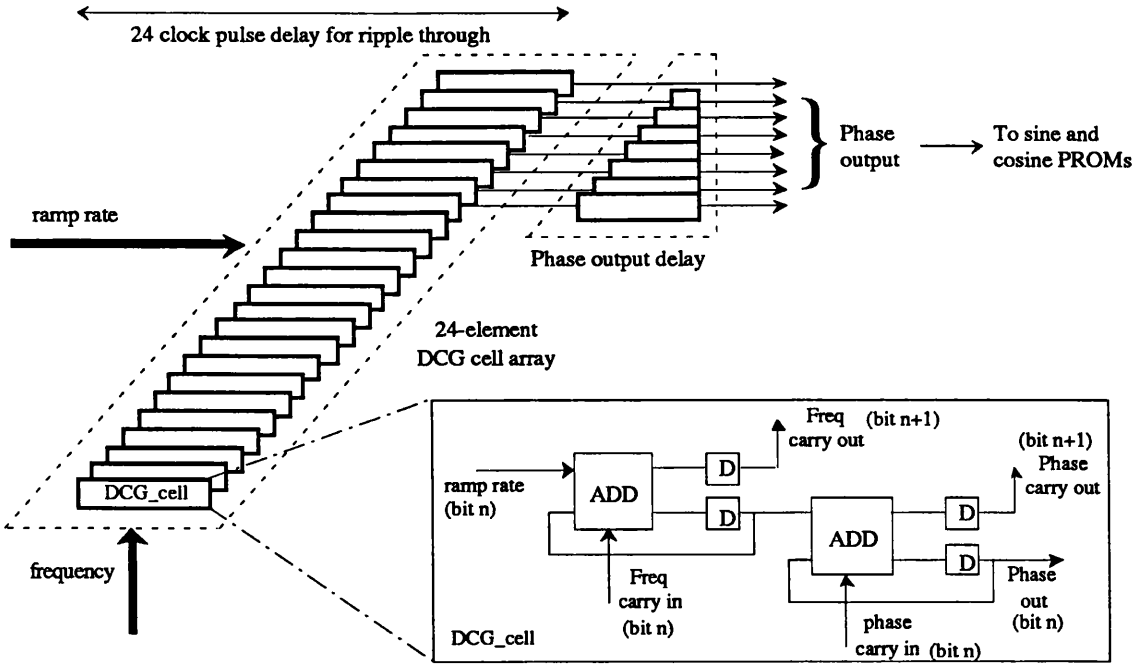

Figure 4.3-2. A block diagram of the digital chirp generator (after Parkes et al., 1991). The accumulators, marked 'ADD' are clocked at 40 MHz, and integrate the ramp rate twice to produce a phase output.

The architecture of the baseband part of the chirp generator is shown in figure 4.3-2. It comprises 24 individual cells. Each cell consists of a single bit frequency accumulator followed by a single bit phase accumulator. The first accumulator integrates the ramp rate, whilst the second integrates the frequency output from the first accumulator, yielding a phase bit. The frequency carry in provides a means of specifying the start frequency of the

chirp. After 24 clock cycles, the loaded ramp rate will have rippled through the system and the phase output is available at the most significant eight bits. These phase bits need to be incrementally delayed to compensate for the systolic pipeline delay shown, before they can subsequently be used to drive sine and cosine PROMs and digital to analogue converters.

The digital chirp generator is synchronised to an external trigger representing the transmit instant. After a programmed delay, given by (4.2-3), a chirp is output. The envelope of the chirp is also output in the form of a logic signal, and is used as a gate to modulate the baseband signal onto the chirp. In this way it is possible to synchronise the start of the modulation with the start of the chirp.

The outputs of the digital chirp generator are 50Ω matched and have voltage levels of ±0.5V. A description of how the chirp generator operates in conjunction with the RSS is given in appendix A.3.

4.3.2 Memory and Control Unit

The reconstruction of the echo from its samples is controlled by the memory and control unit. Every PRI, 1 kbyte of data, corresponding to the sampled I and Q components of a single echo, is transferred to the FIFOs. The FIFO acts as a buffer between the asynchronous operation of the DRAMs, and the modulation onto the chirp which is synchronous with the system clock. The data is passed through digital to analogue converters and modulated onto the chirp when the envelope of the chirp gates a clock of the required sampling frequency. A block diagram of the DRAM memory and control unit is shown in figure 4.3-3.

Every PRI the RSS computer sends an instruction to transfer data from the DRAMs to the FIFOs. This sets a flip flop which enables a PROM to increment a counter through all the DRAM addresses of the samples of a single echo. For each address, the PROM produces the control pulses that enable the data to be transferred from the DRAM and into the FIFO. After all the echo samples for a single echo are transferred, the PROM produces a pulse that resets the flip flop. The whole process is repeated for the next echo whose echo samples are adjacent to the previous echo.

The location of the echo samples is determined by a 24 bit counter. With N= 512 samples per echo, the DRAMs can hold up to 16384 echoes. For a PRF of 1 kHz, this

corresponds to just over 16 seconds of simulated terrain. The 24 bit counters can be set to point to any echo in the sequence, and at any time in the sequence. Thus it is possible for the sequence to recirculate on itself to give the effect of continuous operation.

The second mode of operation passes data to the DRAMs from the RSS computer. The data is initially passed to the FIFOs which act as a buffer. Once the samples of a single echo have been passed asynchronously to the FIFO, they are passed to the DRAMs in a single burst, in the manner described above. The filling up of the DRAMs takes approximately 2 hours. Thus the above configuration speeds up the RSS by a factor of 450. The two other modes of operation, the DRAM configure and refresh, are discussed in appendix A.4.

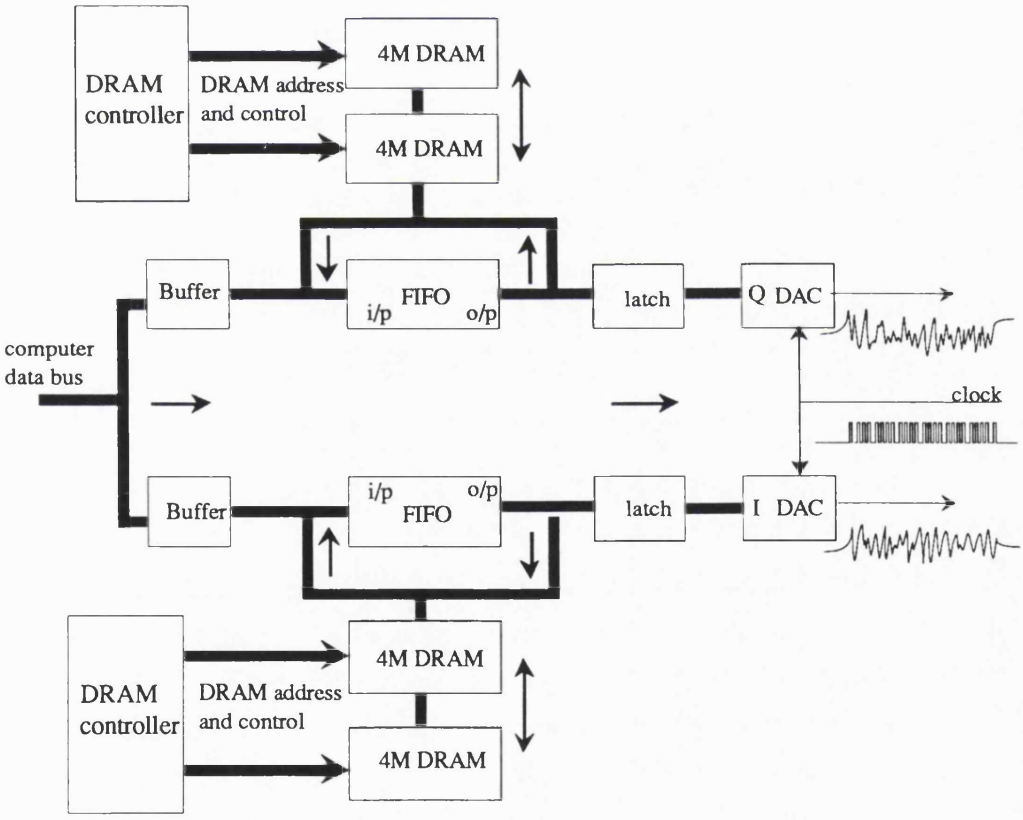

Figure 4.3-3. A block diagram of the memory and control Unit. The flow of data between the DRAMs and the FIFOs is indicated by the arrows. The same DRAM controller (shown twice in the diagram for convenience) controls the DRAMs in both the in-phase and quadrature channels.

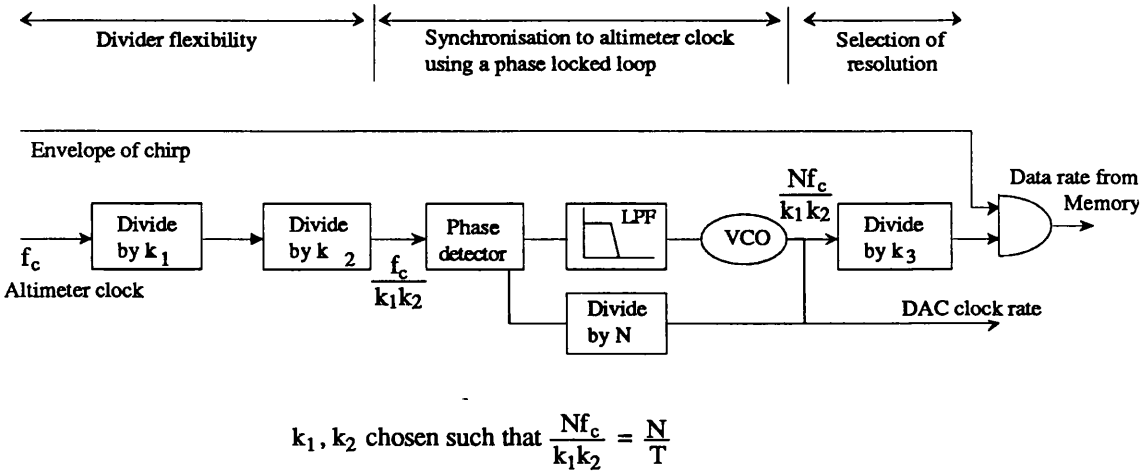

Figure 4.3-4. A block diagram of the frequency synthesiser. The resolution is controlled by programming the value of k_3 in eqn. (4.3-1).

4.3.3 The Frequency Synthesiser

The sampling frequency of the DACs is defined by the number of samples to be modulated divided by the chirp length:

$$f_s = \frac{Nk_3}{T} \qquad (4.3\text{-}1)$$

where k_3 = 1, 1/4, 1/16, 1/64, 1/256 depending on the resolution.

A phase locked loop multiplier was the only means of obtaining the multiplication by N in (4.3-1). In this case, the reference frequency must be a multiple of 1/T, where T is the chirp length. Thus the reference frequency varies from 3 kHz for T = 300 μs to 50 kHz for T = 20 μs. In order to reduce the reference level sidebands, a second order loop filter was required with a loop bandwidth of 40 Hz. The settling time of the loop is the inverse of the loop bandwidth (Gardner, 1979), and is thus of the order of 25 ms (i.e. 25 PRIs). Thus it is not possible to vary the multiplication ratio or the reference frequency in real time. However it is possible to set up the PLL prior to real time operation with the correct sampling frequency for the finest resolution.

The sampling frequency for a coarser resolution can be derived by dividing the PLL output by the appropriate factor of 4 ($1/k_3$). A programmable divider can be used since it

has a switching time of the order of 1 μs. The reference frequency is derived from the stable system clock, in the manner shown in figure 4.3-4. The output of the frequency synthesiser is gated by the envelope of the transmit chirp (of duration T) so that only k_3N clock pulses strobe the DAC as shown in figure 4.3-3.

4.3.4 The Chirp Upconversion Unit

The upconversion unit, designed by FIAR (Franchin et al., 1989), upconverts the ± 8 MHz baseband chirp to 685 ± 8 MHz, and then provides x 20 frequency multiplication using a x 10 phase locked loop followed by a frequency doubler. The single sideband modulator and upconverter are shown in figure 4.3-5.

The operation of the upconversion unit is critically dependent on the suppression of the unwanted components in the single sideband modulator, and the natural loop frequency of the phase locked loop. The former guarantees a clean reference frequency for the phase locked loop, avoiding the possibility of the PLL locking on to the spurii rather than the wanted component. The latter determines how the loop will respond to the maximum ramp rate of the input chirp.

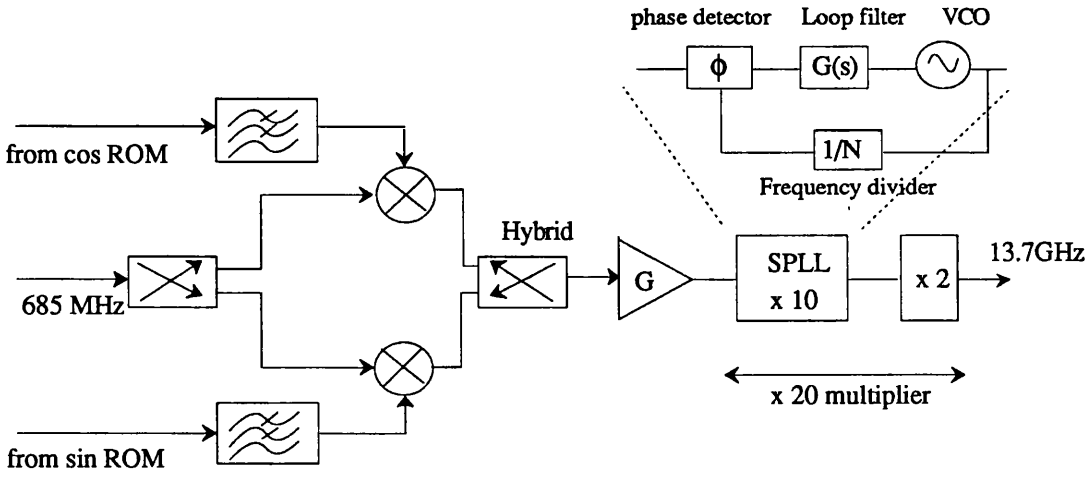

Figure 4.3-5. A block diagram of the FIAR modulator and upconversion unit. The baseband components of the chirp from the digital chirp generator are modulated onto a 685 MHz carrier, and subsequently amplified and multiplied by 20 to Ku-band.

The following stability analysis considers the response of a ramping frequency input to a second order loop with bandwidth ω_n. The loop transfer function is (Gardner, 1979):

$$\frac{\phi_o}{N\phi_{in}} = \frac{2\zeta\omega_n s + \omega_n^2}{s^2 + 2\zeta\omega_n s + \omega_n^2} \qquad (4.3\text{-}2)$$

The error in the loop is given as:

$$\phi_e(s) = \phi_{in}(s)\frac{s^2}{s^2 + 2\zeta\omega_n s + \omega_n^2} \qquad (4.3\text{-}3)$$

For a ramp input of bandwidth Δf, the Laplace transform of $\phi(t)$ is:

$$\phi_{in}(s) = \frac{\Delta f}{T}\frac{1}{s^3} \qquad (4.3\text{-}4)$$

The error in time can then be determined from the final value theorem:

$$\mathrm{Lim}_{t\to\infty}\ \phi_e(t) = \mathrm{Lim}_{s\to 0}\ s\phi_e(s) \qquad (4.3\text{-}5)$$

Substituting (4.3-3) and (4.3-4) into (4.3-5) gives:

$$\phi_e(t) = \frac{\Delta f}{T}\cdot\frac{1}{\omega_n^2} \qquad (4.3\text{-}6)$$

This is the phase error that occurs in the phase detector as a result of the input chirped signal. The loop will lose lock if this phase variation exceeds the allowable swing in the detector. For the loop natural frequency of 0.3 MHz (Franchin et al., 1989), a chirp length of 19.2 μs and a sweep bandwidth of 16 MHz, the maximum phase error at the detector output will be 0.23 rads. This is well within the linear range of the detector (approximately ± 1 rad), as shown in figure 4.3-6. From (4.3-6) and with f_n = 0.3 MHz, it seems that chirp bandwidths in excess of 600 MHz can be comfortably generated.

The transient response of the upconversion unit just after it starts chirping and just after it finishes chirping is likely to be poor because the the loop filter is only first order, and thus will not have the capacity to respond to abrupt changes. The response is non-linear and thus is difficult to predict; however it will cause a phase error at the start of the chirp. Figure 4.3-7 shows an example of the phase distortion that could occur as a result of the upconversion. The effect of such distortion is analysed in greater detail in §6.

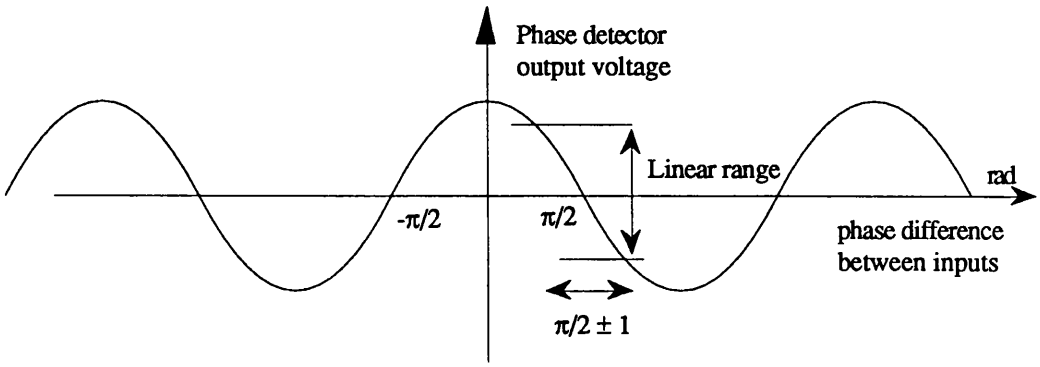

Figure 4.3-6 The response of a phase detector when both inputs are sinusoids.

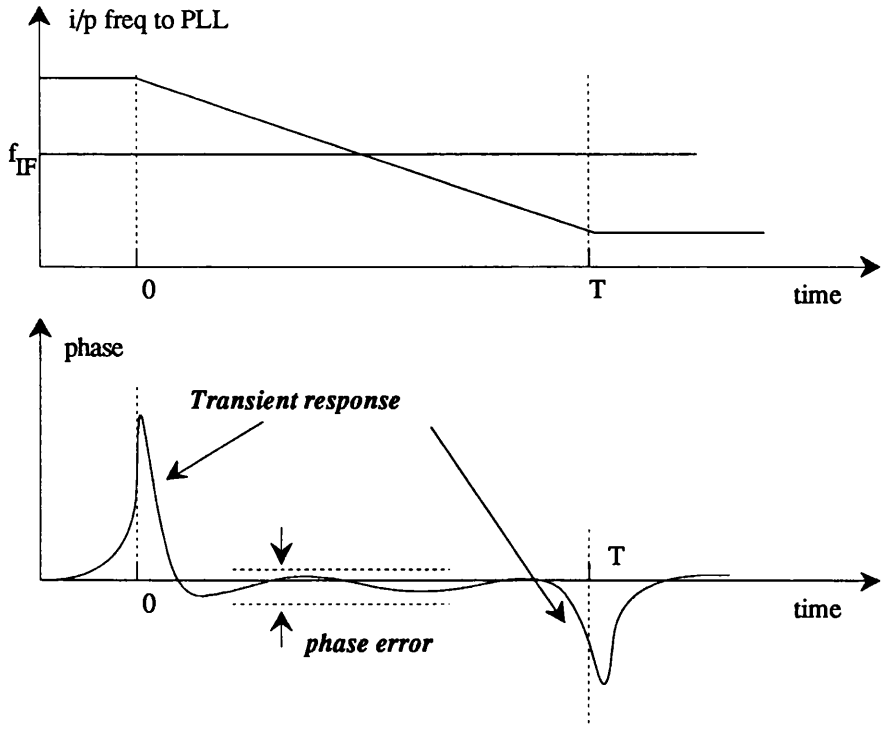

Figure 4.3-7 The chirp phase distortion resulting from the upconversion unit. The plot shows the transient phase response of the PLL to a change from CW to chirp input. The phase error at the centre of the band should be zero since a second order PLL is capable of tracking a chirped input.

4.3.5 The Anti-Alias Filters and Switching Networks

The group delay variation within the passband of the anti-alias filters introduces distortion into the simulated echo spectrum. Different frequency components of the echo will be shifted by varying amounts depending on the group delay characteristic of the filter with frequency. The time shift that a particular frequency component undergoes becomes a frequency shift after up/down conversion onto the RSS and deramp chirps. In effect, each range bin is itself additionally range shifted by an amount depending on the group delay variation. In order for the range shift to be less than a range bin, it is necessary to restrict the group delay variation within the filters to less than the reciprocal of the chirp bandwidth. For a chirp bandwidth of 320 MHz, the tolerable group delay variation is ± 3.125 ns at the finest resolution. Naturally, it is easier to meet this group delay specification for shorter uncompressed pulse lengths since the anti-alias filter has a wider bandwidth (cf. (4.2-6)).

The severe group delay requirement meant that we were limited to one of the filters from the family of linear phase filters. As a result the insertion loss roll-off into the stopband is relatively slow. Thus the alias component of the echo is not as well attenuated unless the guard band is made larger, as illustrated in figure 4.3-8. This restricts the effective echo duration to approx. N/2 (ξ =1/2) where N is the number of resolution cells i.e. the number of padded zeroes is N/2. The cutoff frequency of the filter is given by:

$$f_c = \frac{f_s}{4} \qquad (4.3\text{-}7)$$

For a 7th order linear phase filter the attenuation at the lowest frequency of the aliased component is - 32 dB; the sinx/x frequency response of the DACs contribute another - 10 dB to the attenuation at this point. §4.4.1 describes a method of compensating for the insertion loss variation of the filters.

A block diagram of the switching networks is shown in figure A.4-6 of appendix A.4. The appropriate anti-alias filter is selected by a set of ganged switches. The amplifiers shown in the figure A.4-7 enable the DC offsets to be nulled and the gains of the in-phase and quadrature channels to be equalised so that the level of the unwanted sideband and carrier can be suppressed in the SSB modulator. The combined isolation of both switches will suppress the breakthrough of signals at the wrong resolution by up to 100 dB.

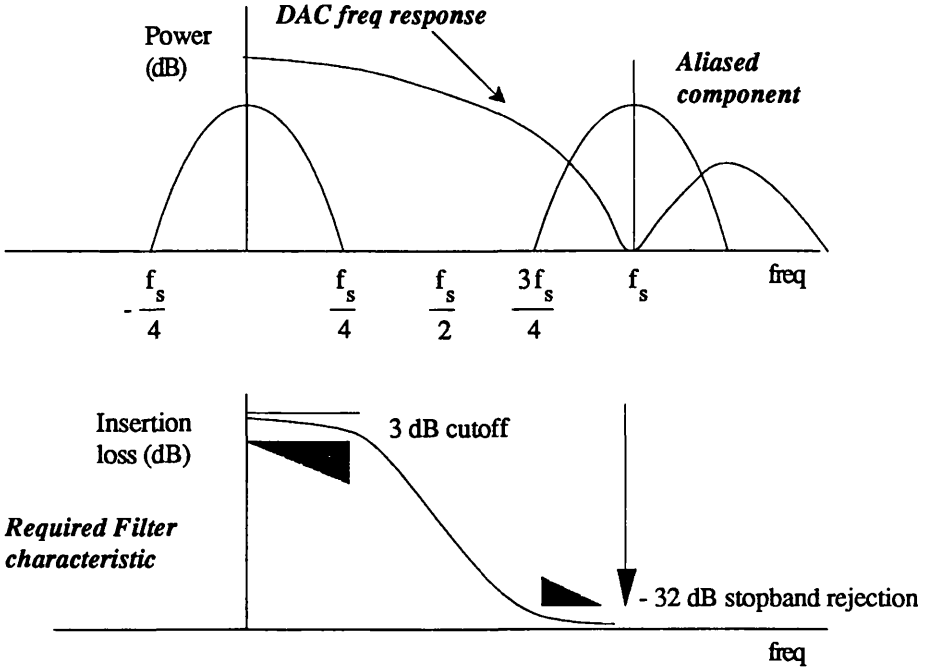

Figure 4.3-8 The stopband requirement of the anti-alias filters. The upper graph shows the attenuation contributed by the frequency response of the DACs. The lower shows the extra attenuation required to eliminate alias components.

4.3.6 The RF front end

The principal element of the RF front end is the single sideband modulator (shown in figure 3.1-5 and 4.3-1). The amplifier and attenuator shown in figure 4.3-9 condition the input and output of the SSB modulator. A 7 dB amplifier boosts the chirp output power from 0 dBm to 7 dBm, the drive level for the SSB modulator. The buffer amplifiers in the switching networks shown in figure A.4-5 are varied to set the I and Q channel power level at 2.5 dBm.

The output of the SSB modulator is reduced by the conversion loss of the mixer (approx. 8 dB), and subsequently by the insertion loss of the attenuator. The insertion loss for zero attenuation is - 4dB. Thus the maximum output power of the RSS is - 10 dBm. The range of the attenuator must at least equal the expected dynamic range of the echoes over all surface types, which is 55 dB. It is shown in § 4.5.3 that this is the approximate power window of an echo when the antenna is not used to interface the RSS to the altimeter. The

gain of the echoes for a sequence is scaled so that they fit into this range. The attenuator also changes the gain of an echo by 12 dB each time a resolution (by a factor of 4) occurs. Thus the overall range of the attenuator should be equal to the change in gain resulting from a resolution change and the dynamic range of the echoes. The range of the attenuator is 60 dB. This figure is justified in §4.5.3.

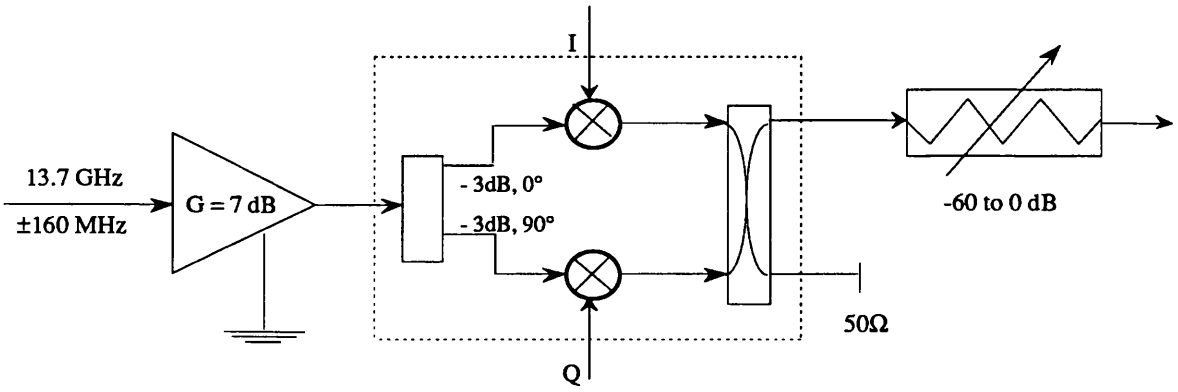

Figure 4.3-9 A block diagram of the RF front end.

4.3.7 Interface to the chirp generator

The function of this board is to read the ramp rate information from the altimeter bread-board, every PRI, and to interface to the RSS digital chirp generator. It allows all of the following operations:

- detection of the altimeter transmit instant,
- reading the altimeter transmit chirp ramp rate every PRI,
- programming the RSS chirp generator with the required timing, frequency and ramp rate information.

The interface from the RSS computer to this board is via a bi-directional parallel port. The speed of the port is 67 kHz which is fast enough to transmit the 20 bytes of information to the RSS chirp generator and to read the three ramp rate bytes from the altimeter within a single PRI. The data required to generate a chirp is described in appendix A.3. The first operation in each PRI is to monitor the altimeter transmit instant. The computer will monitor the port until the trigger is detected, and this becomes a rough timing reference for the RSS computer with which to coordinate all the data processing in a PRI. For the precise chirp timing, the altimeter transmit instant is routed directly to the RSS chirp generator.

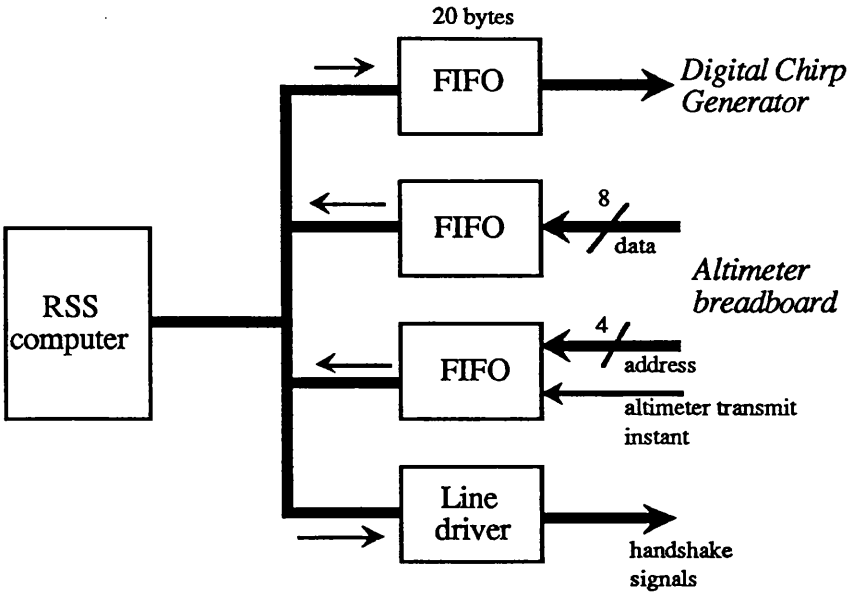

Figure 4.3-10 A block diagram of the interface to the altimeter breadboard and to the digital chirp generator.

4.3.8 RSS control computer

The RSS computer controls the sequence of operations described in the previous seven sections. The computer is an IBM PS/2 and the software is written in C language in order to optimise the speed of the processing. A detailed description of the RSS control software is provided by Sheehan[54] (1992). The RSS computer operates as a slave to the altimeter computer, being controlled via the serial port and performing the following operations when requested.

Reset: The reset operation computes all the parameters required for a simulation, e.g. the location of the first echo, the chirp parameters, the resolution of the echo, and the pulse length. The hardware is configured so that it is ready to accept data or to operate in real time.

Simulation setup: The echo data corresponding to a simulation is transferred from the hard disc of the RSS computer to the DRAMs. The timing information in (4.2-3) and (4.2-4) is also computed so that the data are processed in integer form during the simulation, thus being computationally more efficient. The required attenuation of the echo is also computed at this point. Thus the time and gain words are contained in an array in the RSS

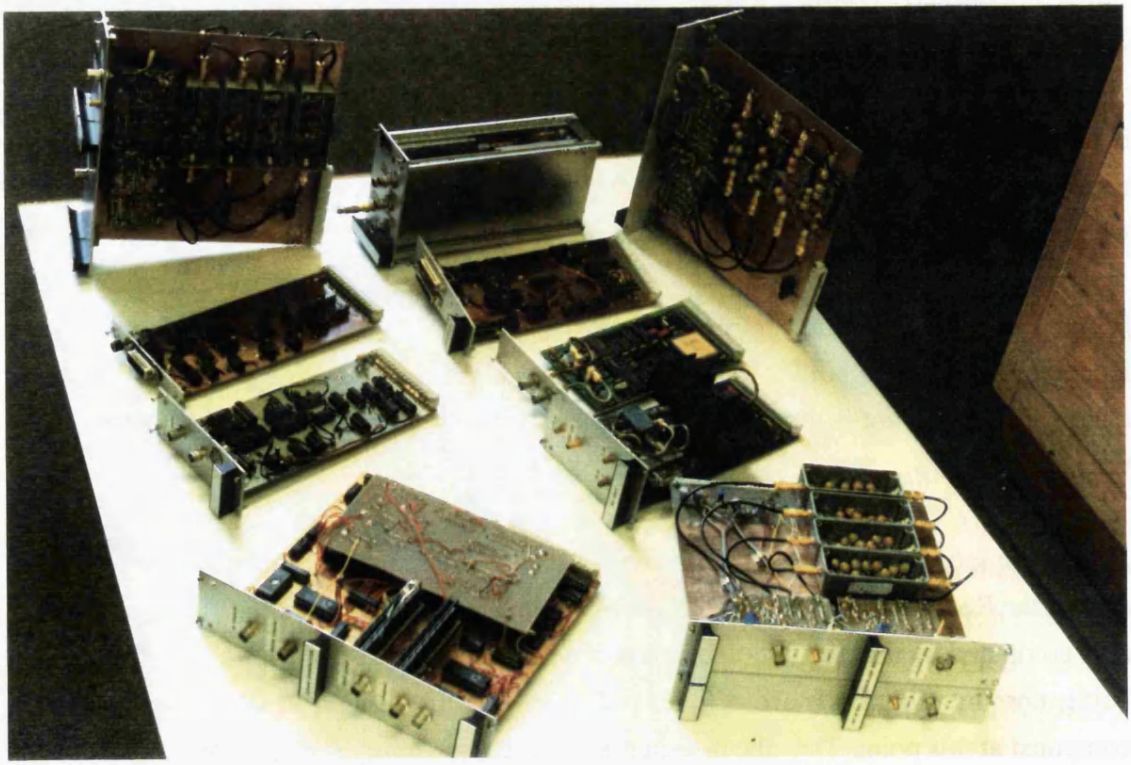

Figure 4.3-11.A photograph of the RSS
The combined RSS apparatus and test set up (top) and individual boards (bottom)

RAM, as shown in appendix A.5, and the echo samples are contained in a contiguous section of DRAM.

Start Simulation: Figure A.5-3 of appendix A.5 shows the operations that have to be performed in real time in order to simulate an echo with the correct shape, correct power level, correct resolution and correct timing. The correct shape is guaranteed by ensuring that all the echo samples are ready in the FIFOs, and that the correct DAC sampling frequency has been chosen before the chirp occurs. The correct power level is achieved by setting the attenuator on a PRI basis, and the correct timing is achieved by passing the ramp rate, frequency and time information to the digital chirp generator before the altimeter transmit trigger, to which the echo is referenced, occurs. A summary of the commands required are given in appendix A.5.

A picture of the RSS and circuit boards is shown in figure 4.3-11.

4.4 COMPENSATION FACTORS

4.4.1 Filter distortion

The amplitude of the signal emerging from the DAC and the filters is distorted by the insertion loss roll-off of the filter, and the frequency response of the DACs. The frequency response of the DACs arises from the sample-and-hold action of the DACs, and is:

$$IL_{dac}(f/f_s) = \left[\frac{\sin\left(\pi \frac{f}{f_s}\right)}{\pi \frac{f}{f_s}} \right]^2 \qquad (4.4\text{-}1)$$

If the insertion loss of the filters is given by $IL_{fil}(f/f_c)$, then the total distortion function is the product of $IL_{dac}(f/f_s)$ and $IL_{fil}(f/f_c)$. The individual insertion loss functions are shown in figure 4.3-8. The required pre-distortion function over the passband of the filter, i.e. duration of the echo, is shown in figure 4.4-1. The pre-distortion function is therefore given by:

$$P_d(f/f_c) = \frac{1}{IL_{dac}(f/f_s).\ IL_{fil}(f/f_c)} \qquad (4.4\text{-}2)$$

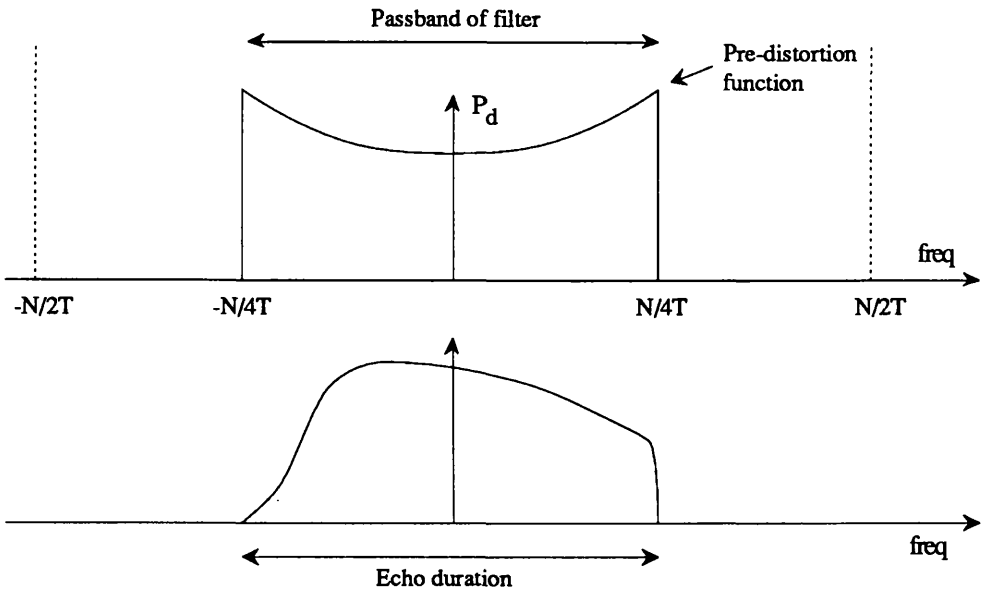

Figure 4.4-1 The pre-distortion function required to compensate for the insertion loss of the filter and the frequency response of the DACs.

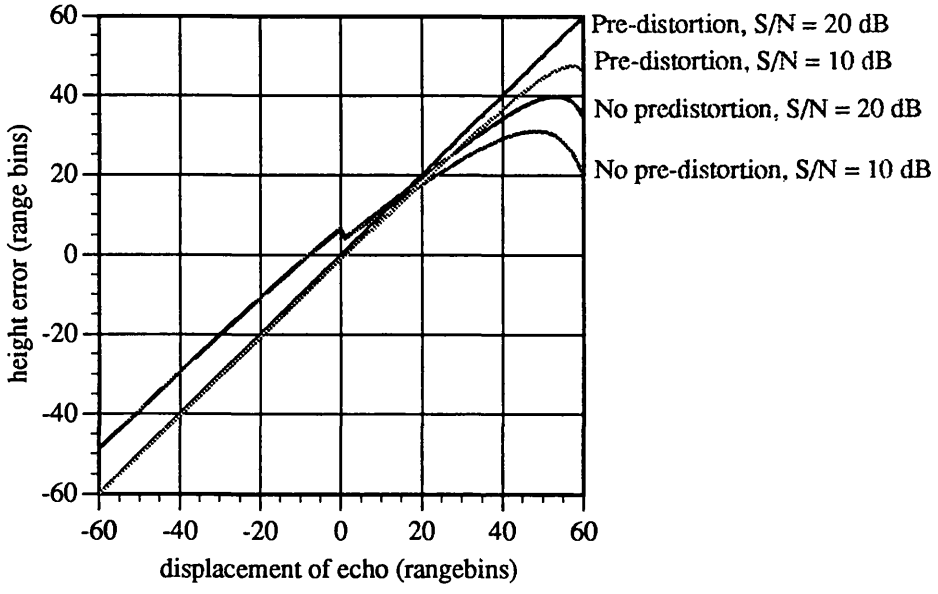

Figure 4.4-2 The height error characteristic computed for a rectangular echo waveform with and without pre-distortion.

For a coarser resolution, the echo is compressed by a factor η, the sampling rate is reduced by η, and the bandwidth of the low pass filter is compressed by η. Thus (4.4-2) represents a normalised distortion function, and is applicable to all the resolutions if all the filters are based on the same prototype filter.

The effect of the filter distortion on the height error characteristic of the OCOG tracking algorithm is illustrated in figure 4.4-2. The characteristic refers to a rectangular echo with and without pre-distortion. The attenuation of the leading edge of the echo distorts the rectangular echo and effectively shift the centre of gravity towards the later range bins (i.e. positive height error). Clearly, the height error characteristic depends on the echo shape; however figure 4.4-2 indicates that the effect of filter distortion is to bias the echo by approximately 4 to 5 range bins for small displacements of the echo from the centre of the range window.

4.4.2 Maximum number of resolutions

As the resolution is made coarser by this technique, the baseband signal and the RSS chirp are progressively misaligned because of the increasing group delays of the anti-alias filters at the coarser resolutions. In practice the maximum coarsest resolution is defined by the point that the group delay exceeds the chirp length, i.e. the baseband information and chirp do not overlap. This condition is defined by:

$$T_g \leq T \tag{4.4-3}$$

where T_g is the group delay. If T_n is the normalised group delay for the prototype filter, then by substituting (4.3-7) and (4.3-1) into (4.4-3) we get:

$$\eta = \left(\frac{1}{4}\right)^i \geq \frac{4T_n}{2\pi N} \qquad i = 0,\ 1,\ 2,\ 3\ \ldots\ldots \tag{4.4-4}$$

Thus for a typical normalised group delay of 4 s and N = 512, then the minimum value of η is 0.005, i.e. the resolution can be degraded by a factor of no more than 200. For the fifth resolution of this RSS, the baseband signal will not overlap with the chirp if a filter is used to eliminate the alias components.

The echo at the fifth resolution is a special case if there are 256 range bins in the simulated echo spectrum, and if the resolution is degraded by a factor of 4 for each change. In this

case the echo at the coarser resolution consists of a single range bin, as illustrated in figure 4.4-3. The nulls of the sinc function due to the sampling occur at the aliased components. Now, since the echo consists of a single range bin, the aliased component is heavily attenuated. Assuming that the energy is uniformly distributed across a range bin, then the total energy in the first aliased range bin is:

$$\int_{3\pi/4}^{5\pi/4} \left[\frac{\sin x}{x}\right]^2 dx = -23 \text{ dB} \qquad (4.4\text{-}5)$$

The power in the wanted component is given by:

$$\int_{-\pi/4}^{\pi/4} \left[\frac{\sin x}{x}\right]^2 dx = +3 \text{ dB} \qquad (4.4\text{-}6)$$

Thus the total suppression of the first aliased component is - 26 dB. Thus, if the echo at the finest resolution consists of 256 range cells, there is no need for an anti-alias filter at the fifth resolution since the sinc function provides sufficient attenuation.

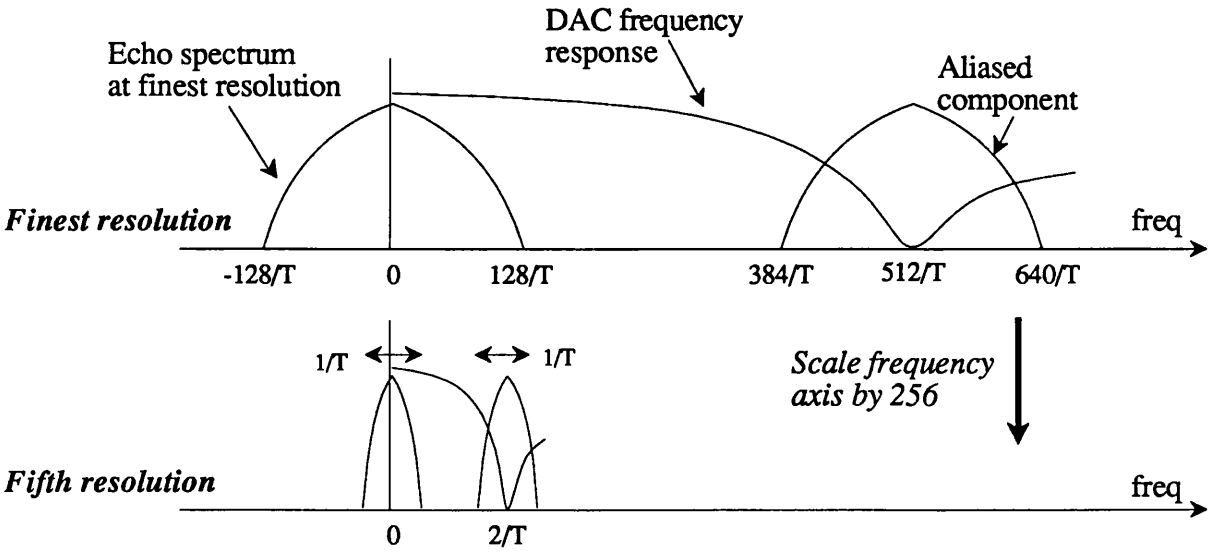

Figure 4.4-3 The echo spectrum at the fifth resolution consists of a single range bin if the echo at the finest resolution comprises 256 range bins. In this case, the aliased components are almost eliminated by the nulls of the sinc function.

4.4.3 *Effects at coarser resolutions*

There are three ways in which the gain will vary as the resolution is changed.

Firstly, a misalignment between the RSS chirp and the baseband echo echo signal shortens the duration of the simulated signal by an amount ΔT. When this signal is deramped in the radar altimeter, the point target response is broadened by:

$$\left(\frac{\Delta T}{T - \Delta T}\right)\frac{1}{T} \tag{4.4-7}$$

Thus if the misalignment is T/3 (i.e. for the fourth resolution, and a normalised group delay of 4 s) then the resolution is further reduced by half a resolution cell. A second implication is that the amplitude of altimeter impulse response is reduced by:

$$20\log_{10}\left(\frac{T - \Delta T}{T}\right) \tag{4.4-8}$$

It is not possible to compensate for the broadening of the point target response; however it is possible to compensate for the gain variation that results from the misalignment if the group delay of the anti-alias filters is accurately determined.

Secondly, there is a gain variation $\Delta G_{1\text{-}i}$ between each channel of the switching network and the finest resolution channel. Thirdly, the gain change as a result of a change to a coarser resolution is approximately 6 dB; however the change that needs to be implemented is 12 dB because of an extra 6 dB resulting from the realisation of an FT as an FFT. It is shown in chapter 3 that the gain change due to the beam-limiting of the return is accounted for in the model. Thus the gain compensation for the i^{th} resolution is given as:

$$G_i = \Delta G_{1\text{-}i} + 20\log\left(\frac{T - \Delta T}{T}\right) + 20\log\left(\frac{1}{\eta}\right) \tag{4.4-9}$$

where $1/\eta$ is the degradation in resolution and $\Delta G_{1\text{-}1} = 0$.

4.5 DEFINITION OF ECHO SEQUENCES

4.5.1 Types of scenario

The size of the data file required to define a scenario of the form shown in figure 3.1-1 is immense if the height, backscatter coefficient and other surface parameters are to be specified in 2 dimensions. In order to reduce the size of the data file required, each scenario is assumed to be uniform and homogeneous in the across track direction, thus allowing the replication of a two-dimensional profile across track to form a three-dimensional geometry. In this simplified approach, the maximum rate of change of the surface parameters always occurs in the along track direction. It is thus much simpler to identify the features to which the altimeter responds. Homogeneity in the across track direction is not necessarily a limitation, because in practice many features of interest are homogeneous in one direction, e.g. a cliff top perpendicular to the altimeter track, open ocean, an ice edge or a lake.

The length of the simulated sequences should correspond to a minimum of several times the time constants of the altimeter tracking loops, which will each be of the order of 0.5 s. Thus for simple simulated scenarios, only a short track of simulated echoes is required, e.g. a step change in elevation might only require a 5 second track. More complicated surfaces will demand multiple resolution changes, so a maximum sequence length of 20 s is provided. To give continuous operation such a surface can be repeatedly traversed, to and fro, in the manner described in §4.2.2.

Six different scenarios representing a wide variety of surface types were constructed by Wingham, and the echo power profiles were generated using the Brown integral in (3.1-1) at the Mullard Space Science Laboratory. These waveforms were used for the current research. In order to regenerate the surface elevation profile, we had to perform open loop tracking of the echoes using a simple tracking algorithm. Closed loop tracking (e.g as in the altimeter) provide some *a priori* knowledge of the surface height from the previous echo, and thus would give an unrealistically smooth profile. Open loop tracking of the waveforms, although prone to losing track more easily, will give an unbiased estimate of the height at each sampling point. By tracking the echoes without a range window, there is no danger of losing track.

This simple tracking algorithm works by searching through the range bins for the peak power of the profile. Then it rescans the range bins for the range corresponding to the half

power point, i.e. the mean elevation of the surface at that point. This algorithm fails to work effectively for echoes that have multiple leading edges. However, in these situations, the multiple leading edges refer to transitions between two or more surface types, and as a result the mean elevation is a lot more difficult to estimate. The elevation profiles shown in figure 4.5-1 through to figure 4.5-6 have all been regenerated using this simple algorithm.

Figure 4.5-1 illustrates the mean elevation and peak power profile for a scenario consisting of rolling hills and inland lakes, computed using the simple open loop tracking algorithm described above. The flat regions in the elevation profile (15 km to 30 km and 93 km to 102 km) represent lakes, corresponding to the high reflectivity in the same regions of the peak power profile. The 'glitch' on the ascent to the hill (at 51km) is an artefact of the tracking algorithm; at this point there are two leading edges giving rise to an erroneous value of mean elevation. The edges of the lakes are also badly defined because the algorithm may track the wrong surface at the transition. There are a few more smaller irregularities at the transitions between different surface types. However this represents a good picture of the surface elevation.

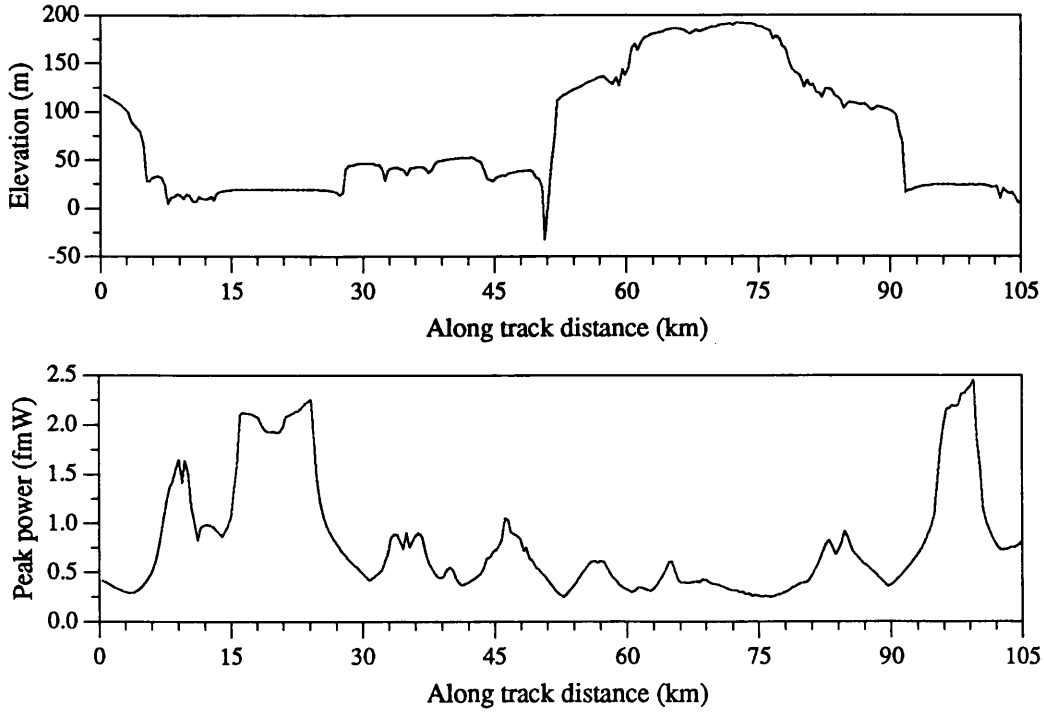

Figure 4.5-1. The elevation and peak power profile of the rolling hills and lakes scenario.

The along track axis of the scenarios is determined based on the assumption that the satellite speed is 7km/s and that the PRF is 1 kHz. Thus 70 km corresponds to 10s of simulation data or 200 'source packets' where a source packet represents the average of 50 individual echo waveforms.

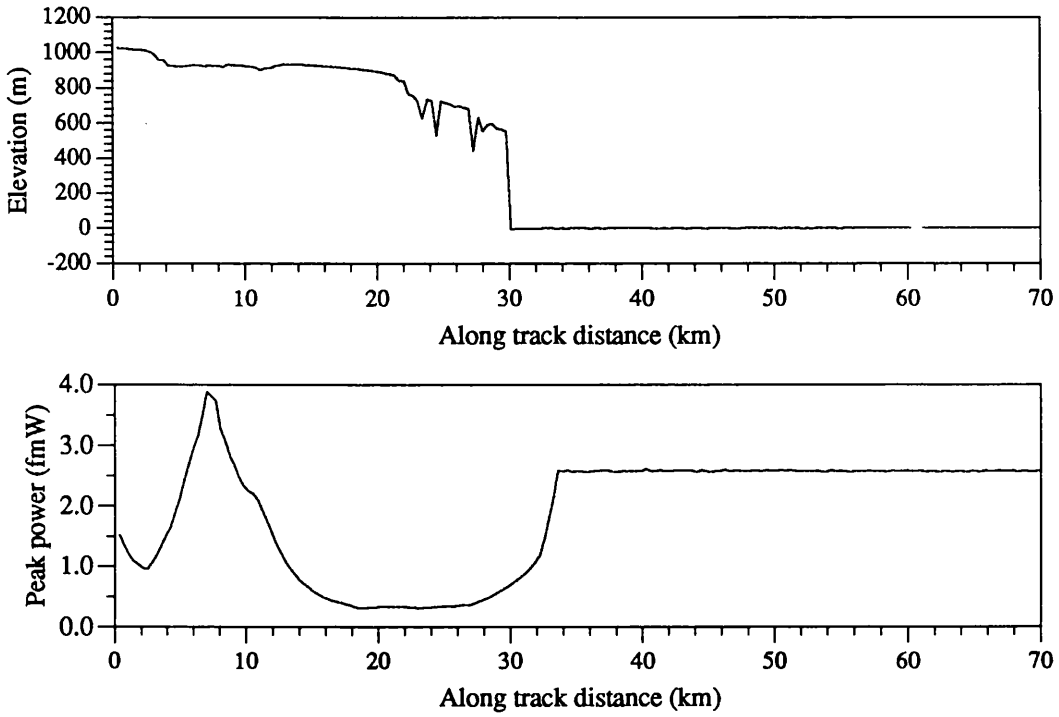

Figure 4.5-2. The along track profiles of elevation and peak power as the altimeter passes from an ice sheet to an ice shelf.

Figure 4.5-2 shows the elevation profile of a scenario comprising an ice sheet falling into an ice shelf. The transition between the two is marked by a change in elevation of 600 m and a change in power of 8 dB. Figure 4.5-3 illustrates a scenario comprising open ocean, clusters of sea ice and a tabular iceberg 50 m high. Fluctuations in the sea ice are clearly evident (at 32 km), representing rougher ice. Figure 4.5-4 is a typical profile encountered by an ocean-dedicated altimeter - an ocean to cliff transition. The cliff face is 200 m high, and the reflectivity changes by 6 dB. The power peaks artificially at 33 km, representing the incoherent addition of power from both surfaces as it passes over the transition. Figure 4.5-5 shows the mean elevation of the arid scenario which consists of almost 40 km of desert, followed by rougher terrain, and eventually a small mountain. The transition from desert to rough terrain is marked by a 20 to 25 dB change in reflectivity, which

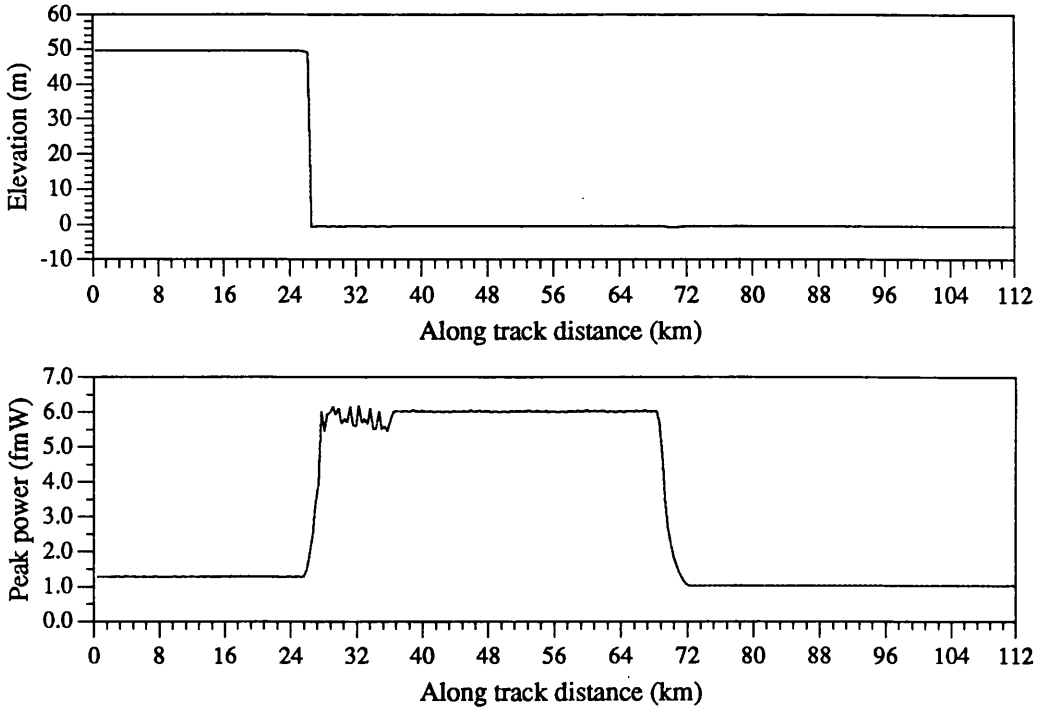

Figure 4.5-3. The along track profiles of elevation and power for the sea ice scenario.

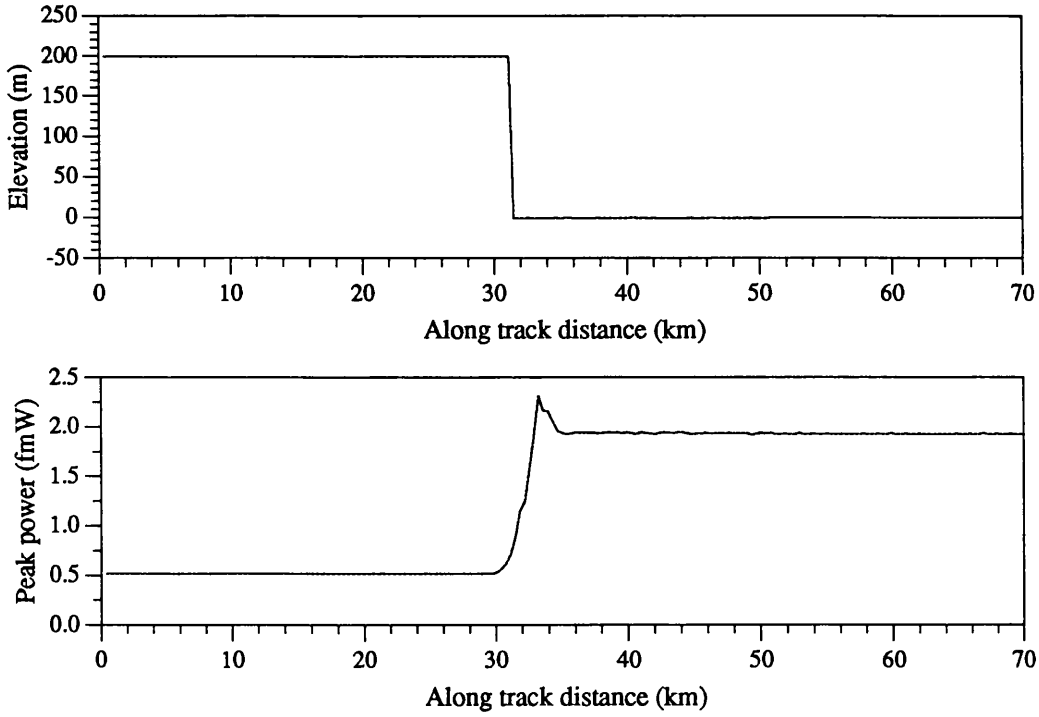

Figure 4.5-4. Along track profile of elevation and power for a cliff to ocean scenario.

corresponds to a change in backscatter coefficient from 13 dB (desert) to -10 dB (rough terrain). Figure 4.5-6 shows the mean elevation of a scenario that consists of a small mountain peak.

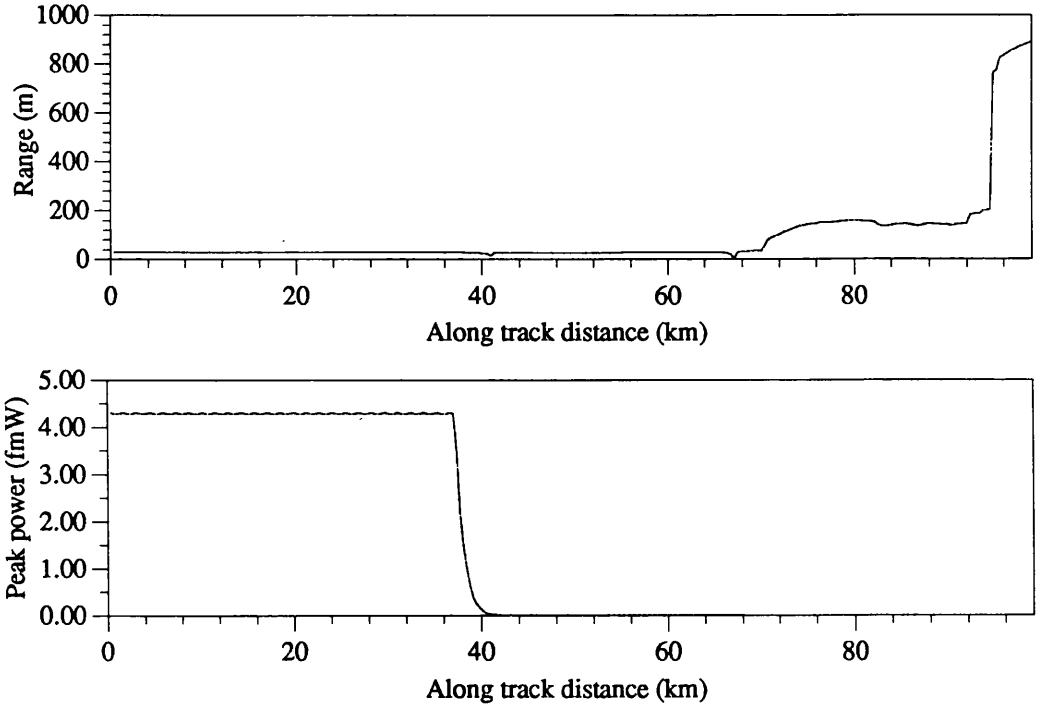

Figure 4.5-5. The along track profiles of elevation and peak power of the arid scenario.

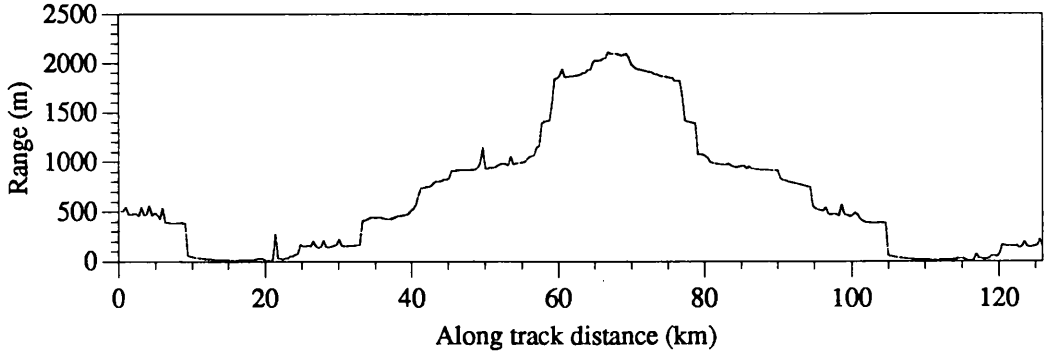

Figure 4.5-6. The along track elevation profile of the mountain scenario.

4.5.2 Authenticity of echo waveforms

Figure 4.5-7 illustrates a number of the echoes from the ice sheet-ice shelf scenario. The echoes are numbered to correspond to the positions of the along track axis of figure 4.5-2. The specular return from the 22nd source packet (i.e. 7.7km) is evident for more than 40 source packets. There is a diffuse component in most of these returns, arising from the local surface roughness. The specular component migrates through the return until it is attenuated by the antenna pattern (e.g. at the 42nd source packet or 14.7 km). After the 42nd source packet, the leading edge of the echo is broadened as a result of the sloping surface. A second return appears after 28.7 km, as a result of the step change in elevation from the ice sheet to the ice shelf. The two returns are separated by approximately 1000 range bins (each 0.45 m wide for the chirp bandwidth of 320 MHz), corresponding to 450 m which is equal to the step change in elevation. Thus the interpretation of the echo waveforms are clearly consistent with the along track profile shown in figure 4.5-2.

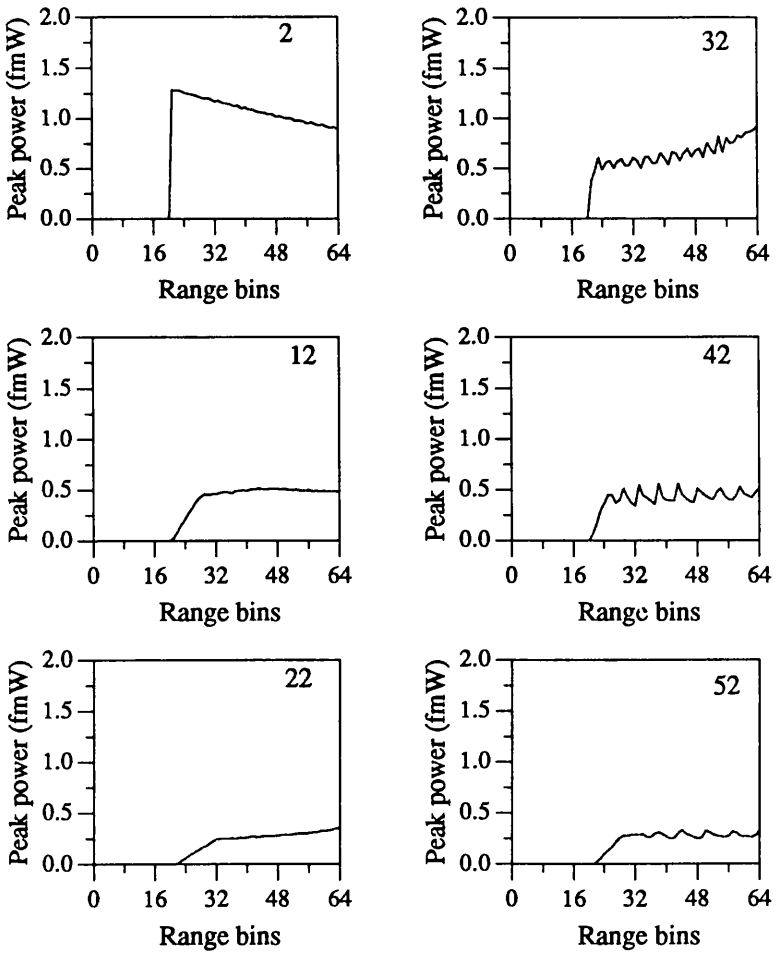

Figure 4.5-8 The leading edge of the echoes of figure 4.5-7 in a 64 bin range window.

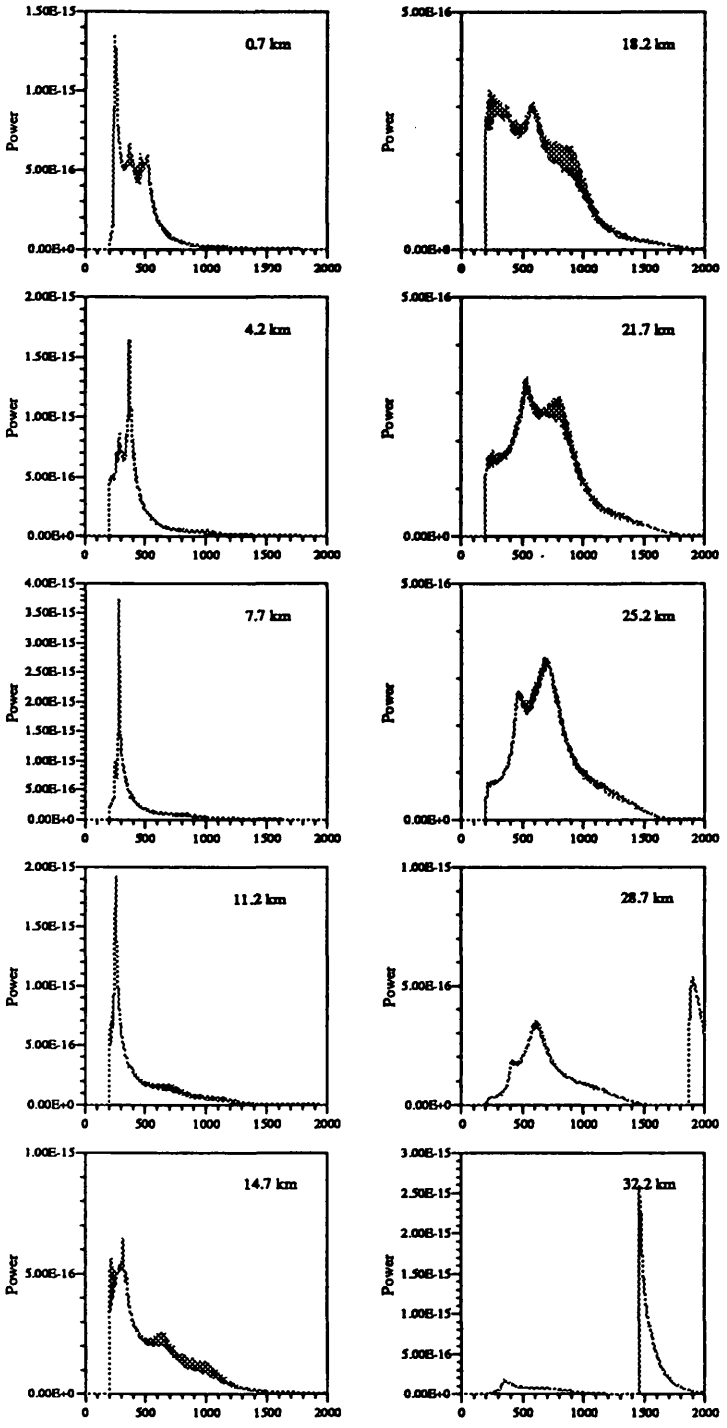

Figure 4.5-7 Echoes at different points in the ice sheet-ice shelf scenario. Each plot shows the echo power as a function of range (in units of range bins).

Figure 4.5-8 illustrates the leading edge of the echoes of figure 4.5-7 in a 64 bin range window. Figure 4.5-9 illustrates some SEASAT altimeter echoes as it passed over a sloping continental ice sheet surface (Thomas et al., 1983). The shape of the echoes are similar for the same type of terrain.

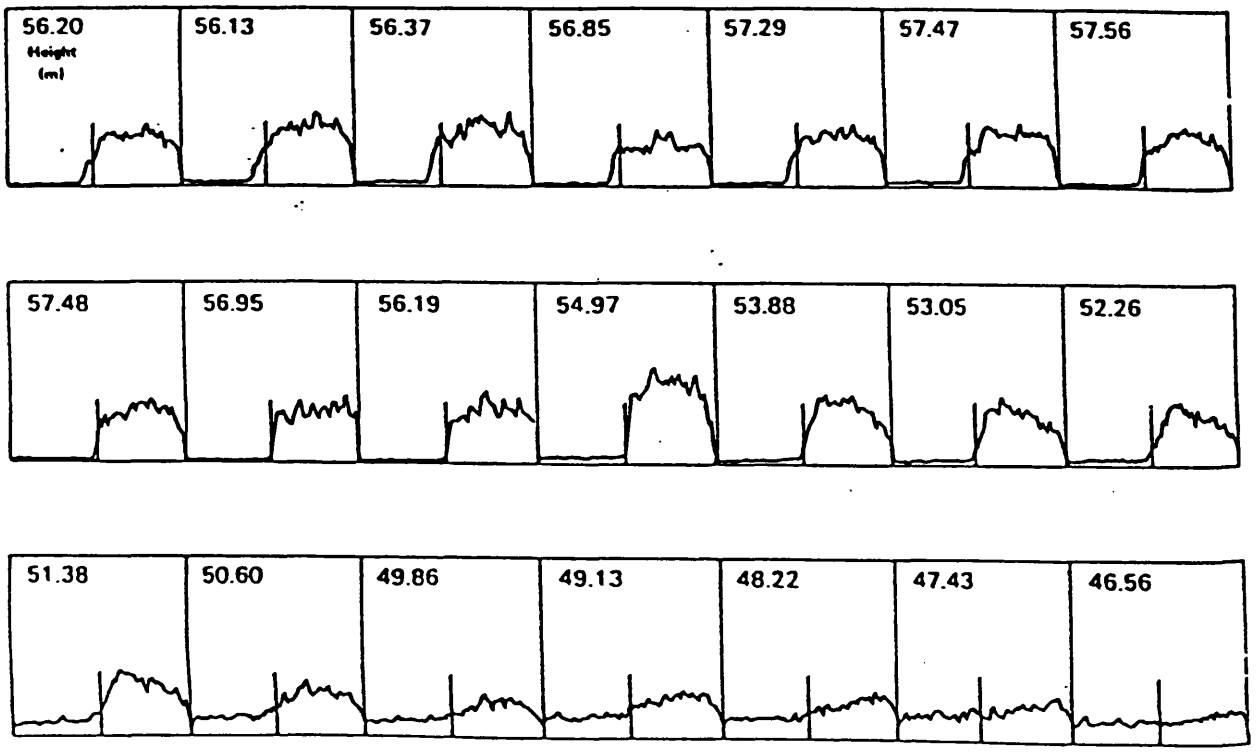

Figure 4.5-9 Some examples of echoes from the SEASAT altimeter as it tracked a sloping continental ice sheet surface (after Thomas, Martin and Zwally, 1983).

4.5.3 Dynamic range of echoes in a scenario

Table 4.5-1 shows the maximum signal strength for the scenarios shown in §4.5.1. The values of maximum signal correlate well with the the values computed from the radar equation. For example, the returned power is - 140 dBW for a backscatter coefficient of 10 dB, an antenna gain of 42 dB, a wavelength of 2.2 cm, and an altitude of 800 km. This is the echo power from the simulated surface, computed using (3.1-1). It is assumed that the resolution cell size is 3.125 ns. The simulated signal in the RSS differs in three

respects. Firstly, the echo is modelled in the frequency domain. Thus the compression gain must be included in the RSS since it will no longer occur at the deramping stage. Secondly, the antenna of the altimeter is disconnected for testing. This must also be compensated for in the RSS. Thirdly, the powers in table 4.5-1 are computed assuming that the transmit power is 1 W, whereas in the RSS, the value of the altimeter transmit power can be arbitrary. Thus the signal power levels shown in §4.5.1 must be corrected as follows:

$$P_o' \text{ (dBm)} = P_o\text{(dBW)} + 10\log_{10}G_o + 10\log_{10}BT + 10\log_{10}P_t + 30 \qquad (4.5\text{-}1)$$

Thus if the chirp bandwidth is 320 MHz, the chirp duration is 102.4 μs, and the modelled transmit power of the altimeter is 5 W, then the output power level of the RSS is - 30 dBm if the echo power from the Brown model is - 150 dBW.

Scenario	Maximum signal power (dBW)
Hills	- 146
Ice sheet/shelf	- 144
Sea ice	- 142
Ocean cliff	- 147
Arid	- 144
Mountain	- 178

Table 4.5-1 Dynamic range and maximum signal power of echoes for each scenario.

The dynamic range of the echoes for each scenario shown in §4.5.1 and the dynamic range of the RSS signal over five resolutions ise tabulated in table 4.5-2. The dynamic range of the RSS signal is defined as the strongest signal at the coarsest resolution divided by the weakest signal at the finest resolution. The maximum dynamic range of the RSS signal over all surfaces is 50 dB, and the maximum range of RSS attenuation required is 73 dB. Figure 4.5-10 shows the RSS signal in the output power window for each of the scenarios. As shown in figure 4.5-10, it is possible that the 60 dB RSS attenuator might not have a sufficient range to simulate the dynamic range of the RSS signal. From figure 4.5-10, four of the scenarios can accommodate all five resolutions; the other two can accommodate four resolutions. In practice, the altimeter will track a strong signal with a fine resolution, and a weak signal with a coarse resolution; thus it will be possible to apply

the gain change for the fifth resolution for the arid and mountain scenarios. The exception to this is during the acquisition phase when the altimeter will automatically open the range window with the coarsest resolution irrespective of the signal level (see appendix A.7 for a brief description of the acquisition sequence).

Scenario	Echo dynamic range (dB)	RSS signal dynamic range(dB)	Req'd attenuator Range (dB)
Hills	11	35	59
Ice sheet/shelf	12	36	60
Sea ice	7	31	55
Ocean cliff	6	30	54
Arid	25	49	73
Mountain	20	44	68

Table 4.5-2 The dynamic range of echoes and of the RSS signal and the required range of attenuation in the RSS for each scenario. The RSS signal dynamic range is defined over 5 resolutions, each by a factor of four.

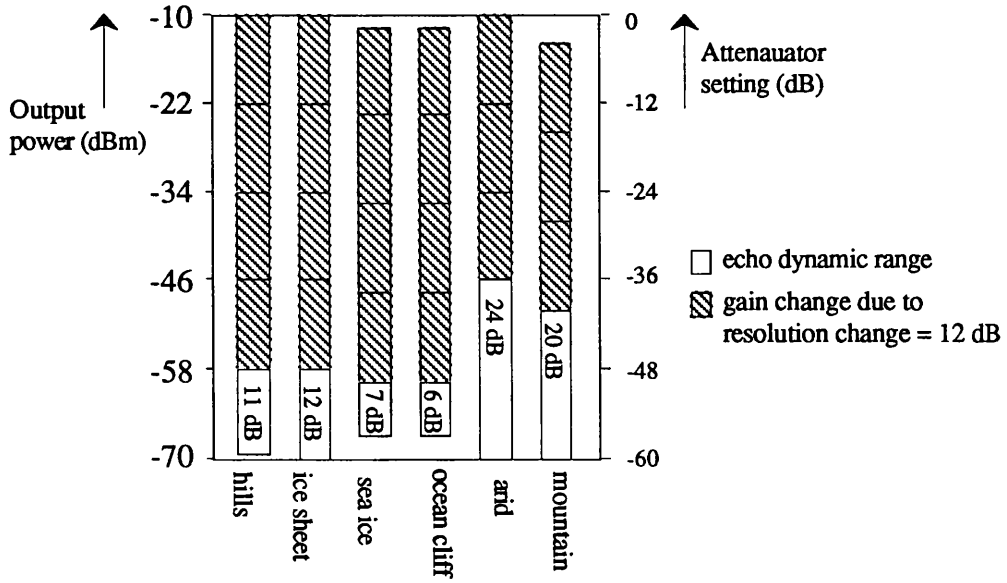

Figure 4.5-10 The dynamic range of the echo and the dynamic range of the RSS signal as a function of resolution. The white box shows the dynamic range of the individual scenarios. The striped boxes show the required gain change to effect a resolution change.

4.6 Summary

This chapter has presented a description of the prototype RSS to test the adaptive-resolution altimeter. The principal points of the chapter can be summarised by the following statements.

The timing of the simulated echo is critically dependent on the instant at which the chirp carrier is triggered, but is less dependent on the time origin of the baseband signal. This chapter has shown that a misalignment of the baseband signal with respect to the chirp can be tolerated. The principal effect is to raise the level of the noise floor in the range window. The implication is a degradation in the timing precision in the SMLE algorithm, and a small height error in the OCOG tracking algorithm. In the latter case it would be necessary to retrack the echoes afterwards to eliminate this small error.

The chirp duration for the RSS is a compromise between the maximum echo duration and minimum echo shape distortion due to group delay distortion in the anti-alias filters. A pulse length of 40 μs would allow 1024 resolution cells to be modelled, and would not significantly affect the echo shape.

The upconversion unit for the baseband chirp will track the input baseband chirp with no error; however the initial transients may be severe leading to chirp phase distortion. This arises from the fact that it is a second order loop.

Gain compensation parameters have been derived for all possible sources of error. A pre-distortion function is derived to compensate for the frequency response of the filter and the DAC. The effect of not pre-distorting the echo is analysed by observing the effect of the the filter distortion on the height error characteristic of the OCOG algorithm. From this analysis it became apparent that not only was pre-distortion essential, but that the OCOG is only useful for tracking rectangular waveforms.

The six scenarios to be used in the simulations have been reviewed. The actual scenario profiles are regenerated from the echo profiles using a simple tracking algorithm.

Chapter 5

Results obtained from the prototype RSS

Introduction

This chapter analyses the performance of the prototype RSS and interprets the main results in terms of their effect on the altimeter performance, particularly the time delay and power level measured by the altimeter. For most of the results presented, a detailed description of the measurement set up is available in the 'RSS Acceptance Procedures' (Sheehan[55], 1992).

Section 5.3 presents some results and analysis of the chirp generator used with the RSS. The latter part of the chapter discusses how the RSS will be used to test the altimeter. Although the altimeter was not ready for final testing at the time of writing this thesis, a test philosophy is presented that will be used to test the altimeter (Sheehan[56], 1992).

Thus the emphasis of this chapter is on analysing the performance of the RSS, and verifying that it is capable of exercising the altimeter breadboard.

5.1 RSS TIMING

The timing of the RSS echo is critically dependent on the stability of the reference clock, and on the stability of the altimeter transmit instant to which all the RSS operations are referenced. For return signal simulation, it is necessary to use the reference clock that was used in the altimeter, so that the timing of the RSS chirp is synchronised to and delayed with respect to the altimeter transmit instant. The tests on the RSS timing were all conducted with a 40 MHz stable clock generated from a HP8082A pulse generator, triggered by a HP8565A signal source running at 40 MHz. The altimeter transmit pulse at the pulse repetition frequency was generated from a low frequency signal generator whose output is synchronised to the 40 MHz clock through a D-type flip-flop. The measurement set up for the time delay measurements is shown in figure 5.1-1.

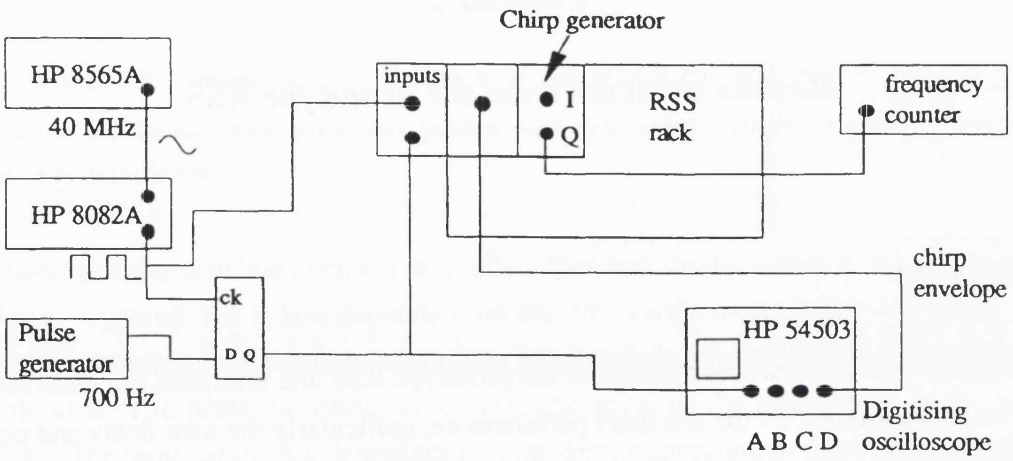

Figure 5.1-1 The measurement set up for the timing measurements of the RSS. The generation of the stable 40 MHz reference clock and the synchronised altimeter transmit instant are also shown.

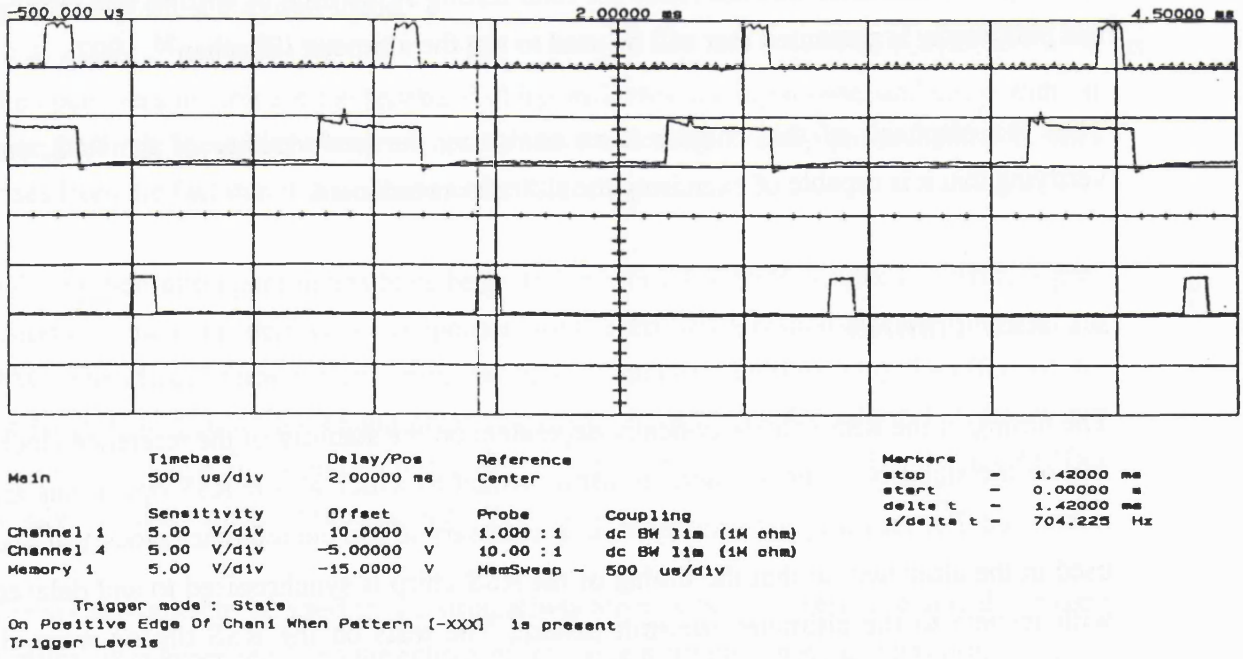

Figure 5.1-2 The operation of the RSS in real time for a PRF of 0.7 kHz, measured on the digitising oscilloscope. The top trace represents the altimeter transmit instant, the lower trace represents the envelope of the chirp, and the middle trace represents the transfer of data from the DRAMs to the FIFOs.

5.1.1 PRF timing

Figure 5.1-2 shows three of the timing signals that determine real time operation. The altimeter transmit instant (top trace) is used to reference the timing of the RSS chirp whose envelope is shown (lower trace). The middle trace indicates the transfer of data from the DRAMs to the FIFOs. The trailing edge of this signal determines when the echo data is in the FIFO and ready to be modulated onto the chirp. The altimeter transmit instant was increased until some of the RSS cycles began to slip, and the maximum PRF that the RSS will operate at was measured at just over 0.7 kHz.

5.1.2 Timing precision

The ultimate timing precision depends on the stability of the reference clock. The long term stability (e.g. 1 year) of the 40 MHz signal source is 0.2 ppm; thus this will produce a bias of ± 0.533 ns (±8 cm) over the 5.333 ms return time when operating for long periods of time. If the required timing precision of the altimeter is 670 ps (10 cm), then the RSS must be precise to approximately 67 ps. The altimeter clock precision is 0.02 ppm; thus when the RSS operates in conjunction with the altimeter, the available precision will be increased to 53.3 ps.

The short term timing stability (i.e. over 5 ms) depends on the phase noise spectrum of the signal generator (or altimeter clock if being used), and is considerably better than the long term stability (typically by a factor of 20 to 50 but can be as high as 100). Thus the timing precision (σ_t) measured over 5 ms is at least ± 25 ps. The residual timing of the RSS signal is achieved by offsetting the start frequency of the baseband chirp. If the error in the output frequency of the baseband unit is ± σ_f Hz, then the equivalent timing error after deramp in the altimeter is:

$$\frac{20\,\sigma_f}{b} \qquad (5.1\text{-}1)$$

Thus the error is more severe for slower ramp rates. The total timing jitter on the RSS chirp, after multiplication to Ku-band, is:

$$\sigma_t + \frac{20\,\sigma_f}{b} \qquad (5.1\text{-}2)$$

Frequency jitter of ± 1 Hz was measured on the output of the baseband unit. Then if σ_t =

25 ps and the chirp ramp rate b is 16 x 10^{12} Hz/s, then the total timing jitter on the RSS signal is ± 26.25 ps. Conversely if the ramp rate is 1 x 10^{12} Hz/s, the timing jitter is as high as ± 45 ps.

5.1.3 Timing jitter resulting from phase noise on the DAC clock

The phase noise on the synthesised DAC sampling frequency was measured on a spectrum analyser by measuring the noise at discrete frequencies, and integrating over frequency. The measurement were made for sampling frequencies at the finest resolution for the three pulse lengths shown in table 5.1-1.

Chirp duration (μs)	Sampling frequency (MHz)	rms jitter (◦)	Integrated over	Phase noise at 1 kHz (dB/Hz)	Phase noise at 10 kHz (dB/Hz)	Phase noise at 100 kHz (dB/Hz)
19.2	26.66	28	1kHz - 5MHz	-34	-69	-88
100	5.12	26	1kHz - 5MHz	-37	-70	-90
300	1.71	20	.2kHz - 1MHz	-54	-74	-94

Table 5.1-1 The measured phase jitter of the frequency synthesiser for uncompressed chirp pulse lengths of T = 19.2, 100, 300μs.

The following analysis investigates the effect of phase jitter on the echo in the altimeter range window. The timing jitter on the DAC sampling frequency will perturb the amplitude of the reconstructed signal in the RSS. The following first order approximation expresses the timing jitter in terms of an equivalent amplitude jitter (with a jitter-free clock):

$$\Delta a_i = \frac{a_{i+1} - a_i}{\tau} \Delta t_i \qquad \Delta t_i > 0$$
$$\Delta a_i = \frac{a_{i+1} - a_{i+2}}{\tau} \Delta t_i \qquad \Delta t_i < 0 \qquad (5.1\text{-}3)$$

where Δt_i is the timing jitter at the i^{th} sample point, τ is the sampling period, and a_i is the amplitude value of the i^{th} sample.

Since the timing jitter is now modelled as an equivalent amplitude jitter, the RSS signal can be considered to be regularly sampled, and thus the software model of the RSS-altimeter described in §3.3.1 can be used to model the effect. The test waveforms, shown in figure 5.1-3(a), were passed to the software model of the altimeter for a range of values of phase noise. The timing jitter is assumed to be a Gaussian random variable with variance given by:

$$\overline{\Delta t^2} = \left(\frac{\tau}{2\pi}\right)^2 \overline{\Delta\phi^2} \qquad (5.1\text{-}4)$$

where $\Delta\phi$ is the phase jitter on the synthesised clock signal feeding the digital-to-analogue converter.

Figure 5.1-3(b) is a plot of the noise variance in the range window computed for the test waveforms shown in figure 5.1-3(a). For the RSS phase jitter of 28° (0.5 rad) the variance of the power in the range window is about 2 % of the mean value when the phase spectrum of the RSS signal is deterministic. This variation is intolerable for power level calibration considering that the range bin flatness in an altimeter is typically 2.3% (0.1 dB) (Cudlip et al., 1992), Thus such a deterministic signal generated by the RSS would be unsuitable for AGC calibration.

The effect of 28° of phase jitter causes approximately 0.5% variance in the mean detected power in the altimeter range window when the phase in each of the simulated range bins is random and the amplitude spectrum is constant over all the range bins. Thus the power level of the simulated echo spectrum is flat to ± 0.01 dB for a phase jitter of 28°. Thus it could be used for AGC level calibration in the altimeter.

It is also clear from figure 5.1-3(b) that echo spectra with smaller bandwidth are less affected by the phase jitter on the synthesised clock. In normal operation of the altimeter, the signal is exponentially-distributed with S/N = 1. After 50 pulse averaging there is a residual 2% fading variation in the range window. In this case, an additional 0.5% variation resulting from the phase noise would be reduced to 0.07 % after 50 pulse averaging, and thus would be difficult to observe on the power spectrum, and has no effect on the timing on the echo.

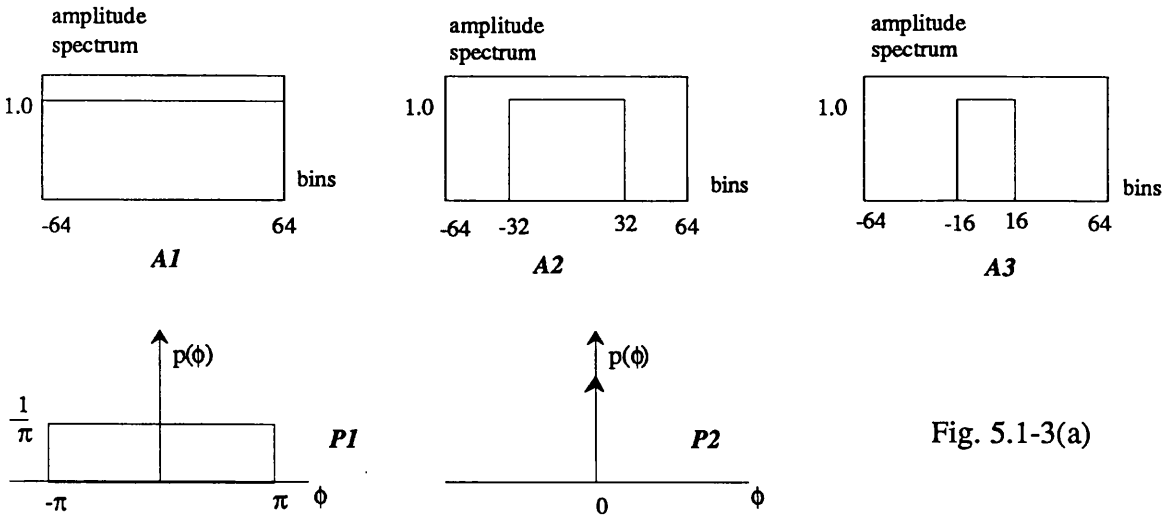

Fig. 5.1-3(a)

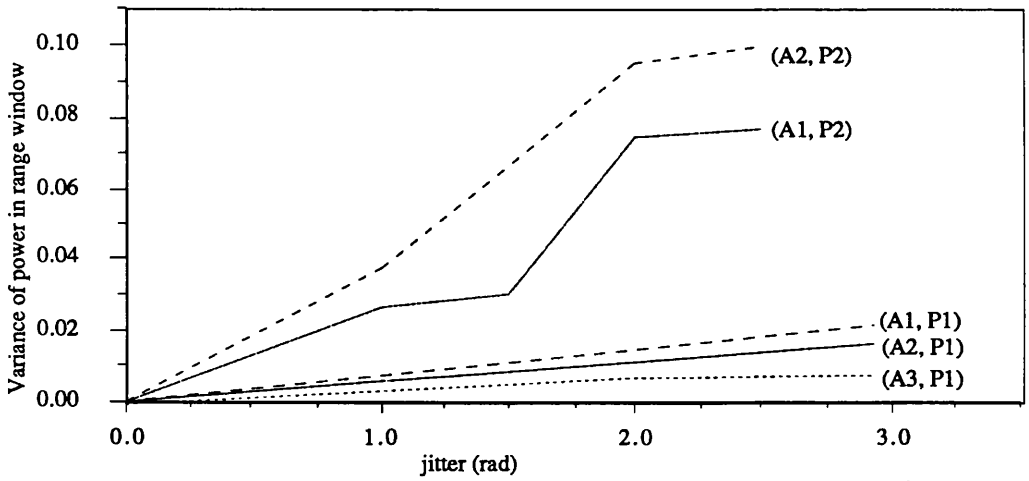

Fig. 5.1-3(b)

Figure 5.1-3(a) The amplitude and phase spectra that are used in the simulation of timing jitter.

Figure 5.1-3(b) Variance of the power in the range window with rms phase jitter on the sampling frequency of the digital to analogue converter for five separate examples.

5.1.4 Timing dispersion

The measured group delay and insertion loss characteristic of the the anti-alias filters for the four resolutions of the 19.2 μs pulse length are shown in figure 5.1-4. The group delay variation is less than ± 3.125 ns, ± 12.5 ns, ± 50 ns, and ± 200 ns for the 1st, 2nd, 3rd and 4th resolutions respectively. Thus the energy in the range bins of the simulated echo is shifted by at most a single range bin (i.e. adjacent range bin) for each of the resolutions. The greatest rate of variation does not occur at the passband in each case (shown by marker on plot); thus the energy at the leading edge is redistributed by an even smaller amount.

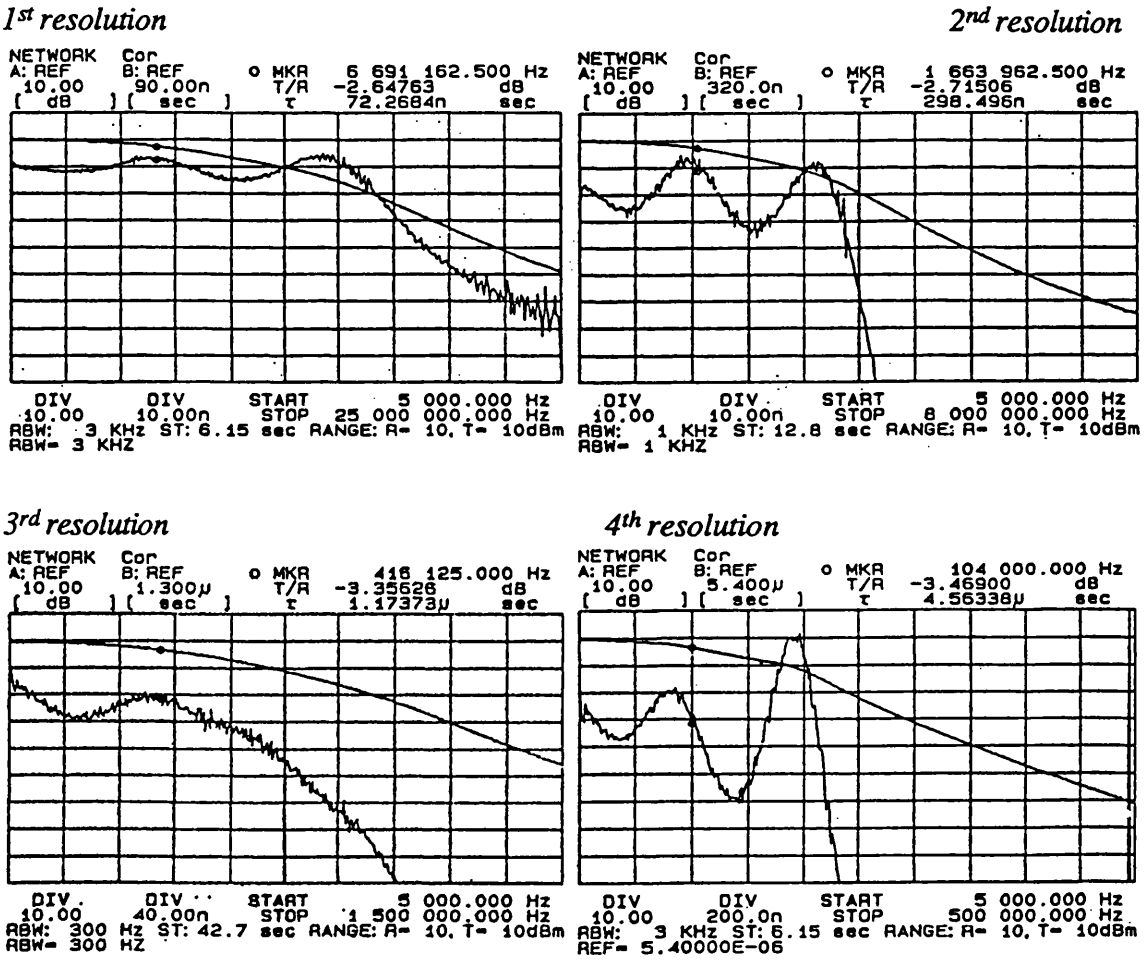

Figure 5.1-4 The measured insertion loss and group delay characteristics of the filters corresponding to the four resolutions for the 19.2 μs pulse length. The marker on each of the plots represents the cutoff frequency of the filter.

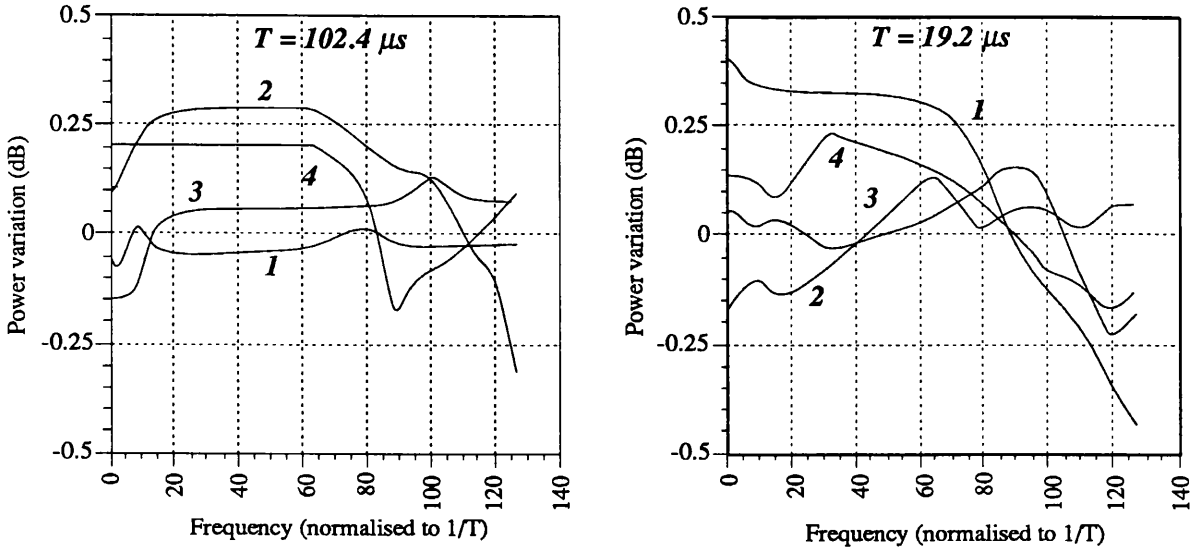

Figure 5.2-1 Measured power variation over the passband of the baseband channels for the 102.4 μs and 19.2 μs pulses after the echoes have been pre-distorted to compensate for the insertion loss of the filters and the frequency response of the DACs.

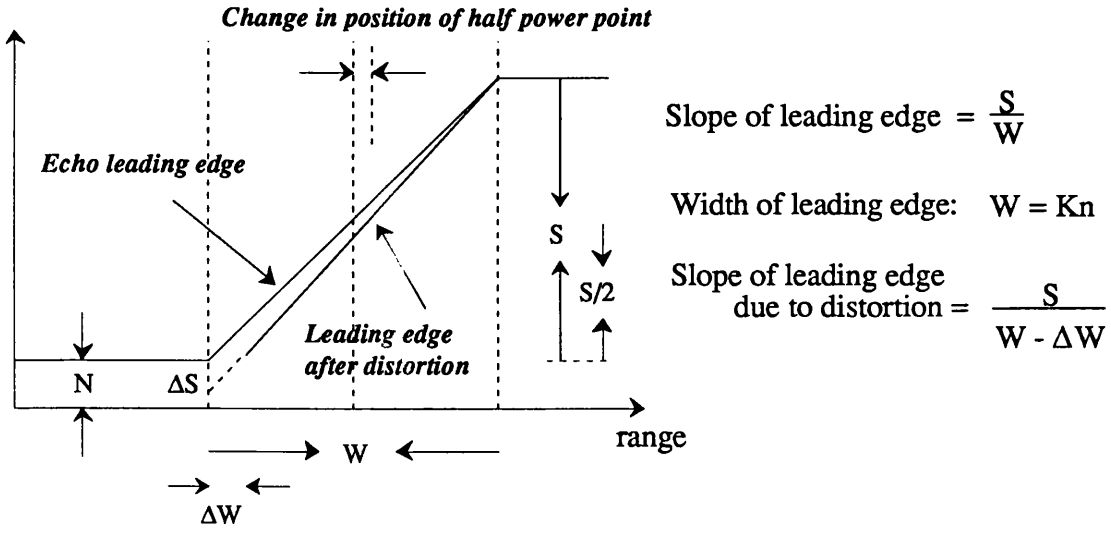

Figure 5.2-2 The shift in the position of the half power point of the leading edge of the echo as a result of increasing attenuation at the bandedge of the anti-alias filter. This example specifically refers to the finest resolution at the 19.2 μs pulse length (whose power variation over the channel bandwidth is shown in figure 5.2-1).

5.2 RSS ECHO SHAPE FIDELITY

5.2.1 Gain flatness

The measured insertion loss characteristic of the linear phase anti-alias filters is shown in figure 5.1-4. As discussed in §4 the echo will undergo severe leading edge attenuation unless the roll-off is compensated, causing the effective position of the leading edge to be shifted towards the later range bins. The pre-distortion function in (4.4-2) was computed by fitting a 4th order polynomial to the passband of the filter at the finest resolution for the 102.4 μs pulse length, and multiplying this polynomial by the frequency response of the DACs. The inverse of this product is used to weight the echo spectrum over the passband of the echo for each resolution and for all the pulse lengths investigated.

The frequency response of the pre-distorted echo emerging from the baseband channels was measured by generating single frequency tones that are weighted by the pre-distortion factor, as described in appendix A.8. Figure 5.2-1 shows the corrected frequency response of the baseband channels for the four resolutions of the 102.4 μs and 19.2 μs pulse lengths. The responses for the coarser resolutions are scaled successively in frequency by a factor of 4 so that they fit on the same frequency axis as the response for the finest resolution. The frequency of the tone in each case is n/T where T is the chirp pulse length.

The greatest deviation from gain flatness occurs at the finest resolution for the 19.2 μs pulse length (i.e. highest frequency filter). In this case, the response of the channel rolls off at almost 1 dB in 50 range bins (i.e n = 70 to n = 120). Consider the effect of this roll off on the leading edge of the echo shown in figure 5.2-2. In the analysis, k_t refers to the attenuation at the leading edge of the echo in dB/range bin. From figure 5.2-2, the slope of the leading edge of the distorted echo is:

$$\frac{S}{W - \Delta W} = \frac{S}{W} \cdot 10^{n\frac{k_t}{10}} \qquad (5.2\text{-}1)$$

where n is the number of range bins corresponding to the leading edge.

The change in position of the half power point is given as:

$$\frac{W}{2}\left(1 - 10^{-\frac{n}{2}\frac{k_t}{10}}\right) \qquad (5.2\text{-}2)$$

From (5.2-2) it is apparent that the magnitude of the shift is magnified for smaller leading edge slopes. Table 5.2-1 shows the magnitude of the shift in the leading edge and the percentage change in the slope of the leading edge for leading edges of various widths.

The response at the finest resolution for the 102.4 μs pulse length, on the other hand, does not roll off but is very flat up to the end of the passband. As a result, the leading edge is not shifted, and the slope of the leading edge is not affected.

Leading edge width (range bins)	Shift (range bins)	% change in slope
2	0.005	0.9
4	0.018	1.86
8	0.073	3.75
16	0.289	7.6
32	1.14	15.8

Table 5.2-1 The shift in the leading edge as a result of the distortion in the baseband channels of the RSS.

5.2.2 Dynamic range of a single echo

The dynamic range of the baseband signal is approximately 40 dB, but is reduced after modulation onto the chirp. The measurement of the dynamic range of the RF echo is not straightforward since the echo is pulsed, and may only last for 1.5 % of the PRI (i.e. for the 19.2 μs pulse, and a PRF of 700 Hz).

5.2.2.1 Measurement of carrier and sideband suppression

The following analysis shows how the suppression of the unwanted sideband and carrier can be inferred from the square law-detected output of the RSS. Figure 5.2-3(a) shows the signal components at the output of the SSB modulator, and figure 5.2-3(b) shows the vector summation of these signals. From figure 5.2-3(b), the square of the resultant voltage signal (i.e. detected output) is:

$$|V_{res}|^2 = (V_s + V_1\cos\theta_1 + V_2\cos\theta_2)^2 + (V_1\sin\theta_1 + V_2\sin\theta_2)^2 \qquad (5.2\text{-}3)$$

which can be expanded as:

$$|V_{res}|^2 = V_s^2 + V_1^2 + V_2^2 + 2V_s(V_1\cos\theta_1 + V_2\cos\theta_2) + 2V_1V_2\cos(\theta_1 - \theta_2) \quad (5.2\text{-}4)$$

Assuming that V_1 and $V_2 << V_s$, then the cross-product term $2V_1V_2\cos(\phi_1-\phi_2)$ may be ignored, and the mean level of the output is V_s^2. The two vectors V_1 and V_2 have phases:

$$\theta_1 = \Delta\omega t + \phi_1 \qquad \text{and} \qquad \theta_2 = 2\Delta\omega t + \phi_2 \quad (5.2\text{-}5)$$

The peak to peak amplitude of the θ_1 term in (5.2-4) is:

$$A_{\theta_1} = 4V_sV_1 \quad (5.2\text{-}6)$$

The peak to peak amplitude of the θ_2 term in (5.2-4) is:

$$A_{\theta_2} = 4V_sV_2 \quad (5.2\text{-}7)$$

The mean power level of the output is:

$$A_m = V_s^2 \quad (5.2\text{-}8)$$

Then from (5.2-6) and (5.2-8) the relative amplitude of the carrier are then given by:

$$\frac{V_1}{V_s} = \frac{A_{\theta_1}}{4A_m} \quad (5.2\text{-}9)$$

and from (5.2-7) and (5.2-8) the relative level of the unwanted sideband is:

$$\frac{V_2}{V_s} = \frac{A_{\theta_2}}{4A_m} \quad (5.2\text{-}10)$$

The above analysis is applicable when the baseband echo is a single tone, and is modulated onto a CW or chirp carrier. Figure 5.2-4 shows the detected output power for three different baseband frequencies. For each plot, there are two frequency components - one at the frequency of the wanted sideband, and the other at twice the frequency. The detector used in the measurement had a rise time of 10 ns and is negative going. In each case, the carrier suppression is in excess of -19.5 dBc and the sideband suppression is approximately - 28 dBc. Figure 5.2-5 shows the measured carrier and sideband suppression across the bandwidth of the baseband signal.

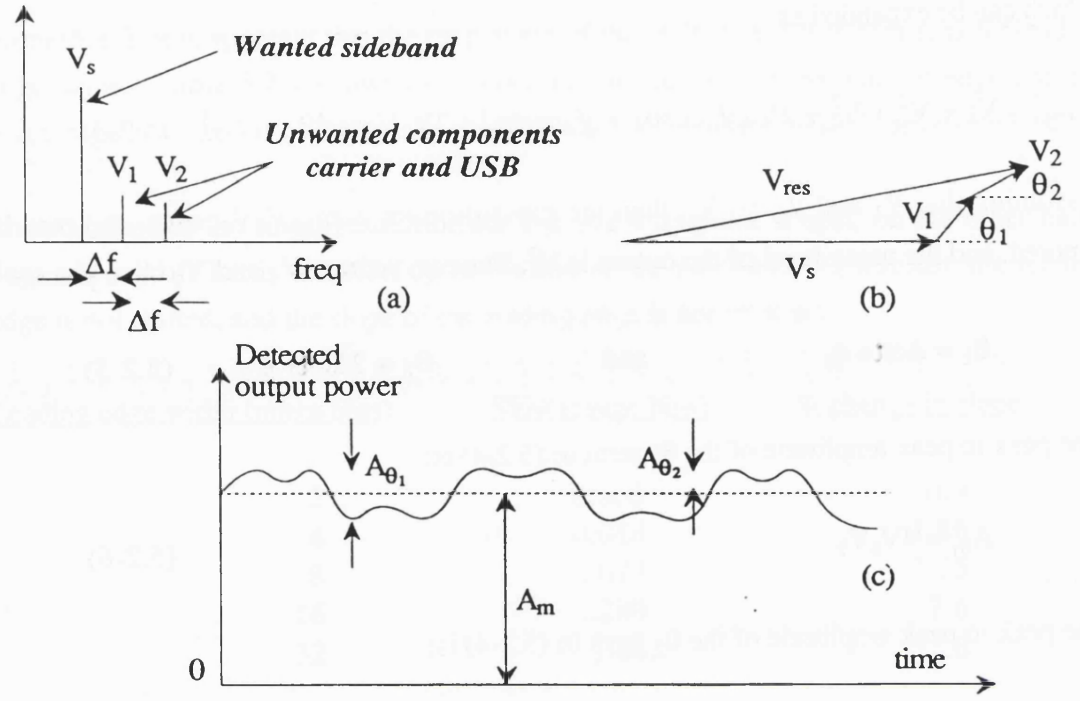

Figure 5.2-3 (a). The output of the SSB modulator.
(b) The vector summation of the signals at the RSS output.
(c) An example of the detected output power.

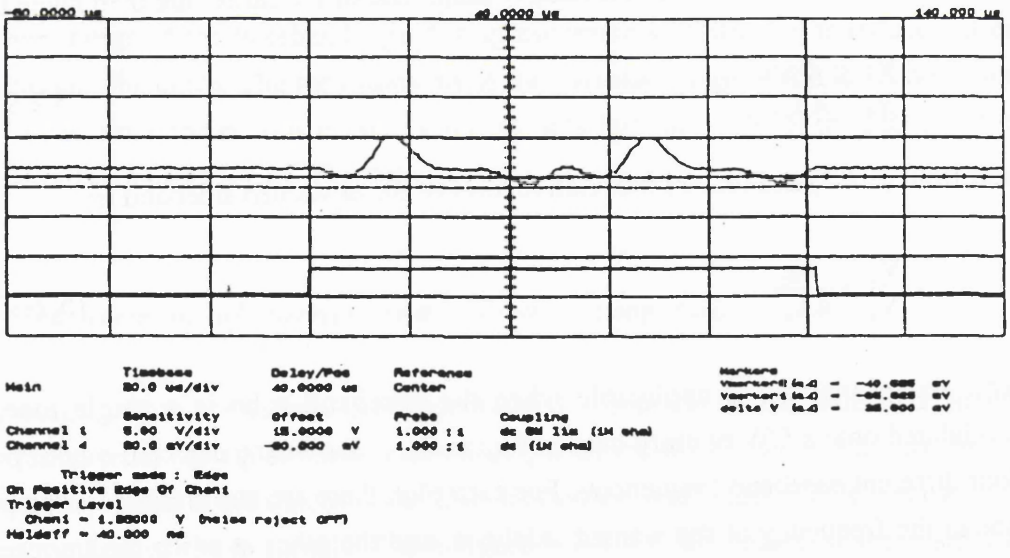

Figure 5.2-4(a) Measured detected power at the output of the RSS when a single tone with 2 cycles of variation is modulated onto the chirp of length 102.4 μs.

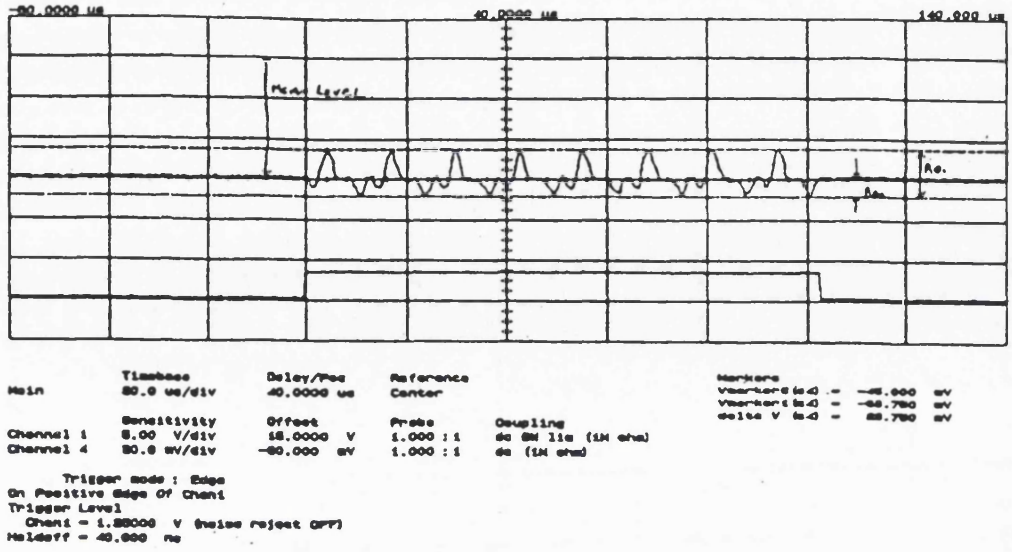

Figure 5.2-4(b) Measured detected power at the output of the RSS when a single tone with 8 cycles of variation is modulated onto the chirp of length 102.4 μs.

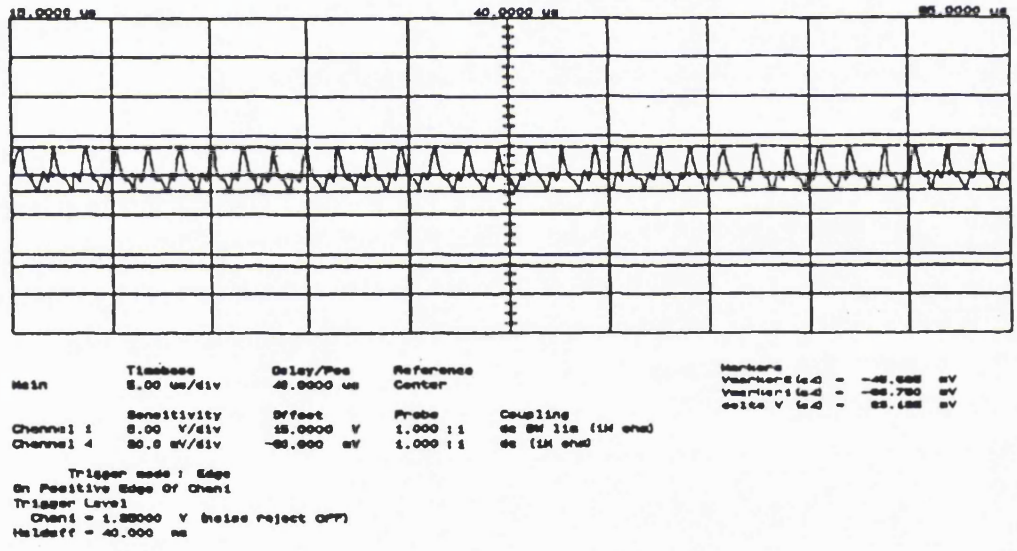

Figure 5.2-4(c) Measured detected power at the output of the RSS when a single tone with 64 cycles of variation is modulated onto the chirp of length 102.4 μs. The resolution time base of the time base was enhanced to show the high frequency detail. In each of the plots, there is a frequency component at the frequency of the baseband tone. There is also a double frequency component corresponding to the carrier breakthrough.

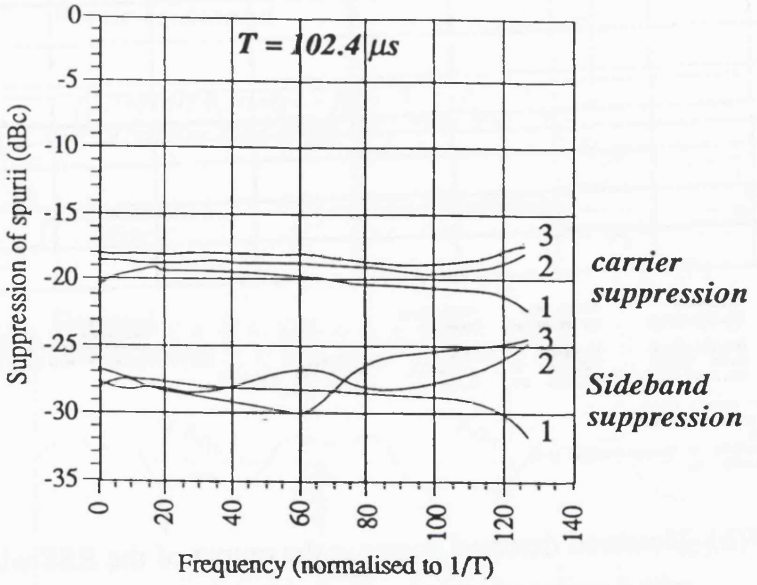

Figure 5.2-5 Measured carrier and sideband suppression over the baseband bandwidth. The carrier suppression is typically - 18 dB and the sideband suppression is greater than - 25 dB.

Figure 5.2-6 shows the amplitude and phase imbalance between the in-phase and quadrature channels of the RSS baseband signals for the first four resolutions and for the 102.4 µs pulse length. The amplitude difference is less than ± 0.1 dB and the phase difference is less than 3°. The image suppression for such an imbalance is theoretically - 44 dBc. However this calculation does not take into account imbalances on the RF input of the SSB modulator.

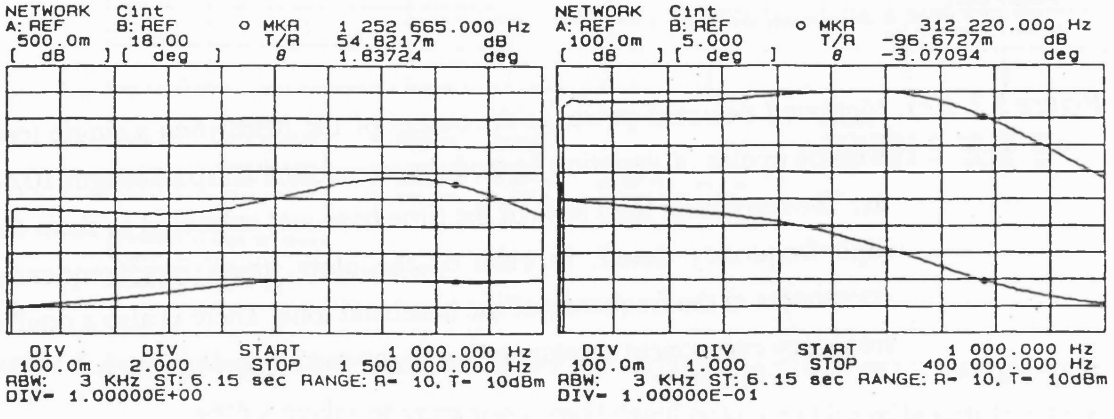

1st resolution *2nd resolution*

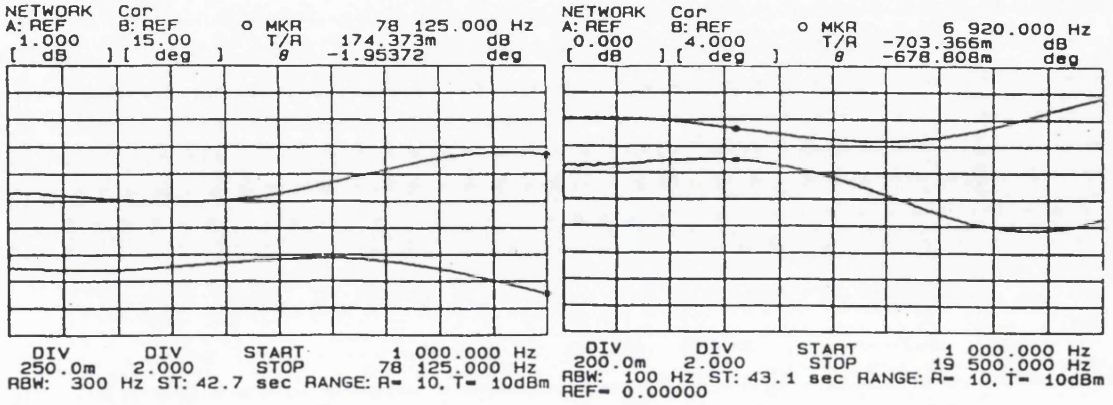

3rd resolution *4th resolution*

Figure 5.2-6 Measured amplitude and phase imbalance between the in-phase and quadrature baseband channels of the RSS for the first four resolutions and the 102.4 μs pulse length. The amplitude difference is typically less than 0.2 dB and the phase difference is typically less than 2°.

5.2.2.2 Effect of spurii on the echo shape

The effect of the spurii is to leak some of the echo energy into the earlier range bins of the altimeter after the simulated echo has been deramped. It is shown in appendix A.1 that the echo spectrum in the altimeter is given as:

$$P(\omega) = \begin{cases} \left(\frac{1+k}{2}\right)^2 \left|a(\omega+\delta)\right|^2 & \omega > -\delta \\ \left(\frac{1-k}{2}\right)^2 \left|a(-\omega+\delta)\right|^2 & \omega < -\delta \\ \left(\frac{1+k}{2}\right)^2 \left|a(\omega+\delta)\right|^2 + k_c & \omega = -\delta \end{cases} \qquad (5.2\text{-}11)$$

From (5.2-11), it is seen that the noise floor of the range window is effectively raised by the breakthrough of the image of the simulated echo spectrum which appears as a pre-cursor to the desired echo spectrum, in inverted form in the range window. The level of the noise floor, as shown in figure 5.2-2, is then limited by the suppression of the sideband. This unwanted component is multiplicative noise, and thus, unlike additive noise whose mean is zero, averaging will only reduce the level of the noise to the mean level of $|a(-\omega)|^2$.

The noise floor in the altimeter can be removed, but must be carefully estimated in the early range gates of the range window (i.e. where there is no signal), and is subtracted from the signal + noise in all other range bins. The additional contribution to the noise floor however is shape dependent, and thus will introduce a small error into shape of the echo spectrum. If the unwanted component is suppressed by -20 dBc, then the maximum error in the echo spectrum is 0.043 dB; however if the suppression is at least - 25 dBc, as it is in this case, the maximum error is only 0.013 dB.

The effect of the carrier breakthrough is to add a component of power to one of the range bins close to or on the leading edge of the echo (depending on how the return is tracked by the altimeter). Again if the suppression of the carrier is -20 dB, then the perturbation to the single range bin is approximately 0.04 dB.

In summary, the dynamic range of the simulated echo is limited primarily by the level of the image sideband resulting from the SSB modulator. The carrier breakthrough merely distorts a single range bin, and thus is not considered to affect the dynamic range of the echo.

5.2.3 Out of band spurii

Spurii of the chirp carrier in the RSS can give rise to a baseband component in the altimeter if a spurious component of the same ramp rate exists in the altimeter. The sub-harmonic in the RSS, shown in figure 5.2-8, was measured at 19 dB down on the desired component, shown in figure 5.2-7.

The out of band spurious signals are attenuated in the altimeter by the frequency response of the RF circuitry, particularly the deramp mixer, which has been designed to operate at Ku-band. We can reasonably expect the conversion loss of the mixer to be 5 dB worse at the frequency of the sub-harmonic. Thus the baseband component resulting from the sub-harmonic will be 24 dB below the level of the desired baseband component.

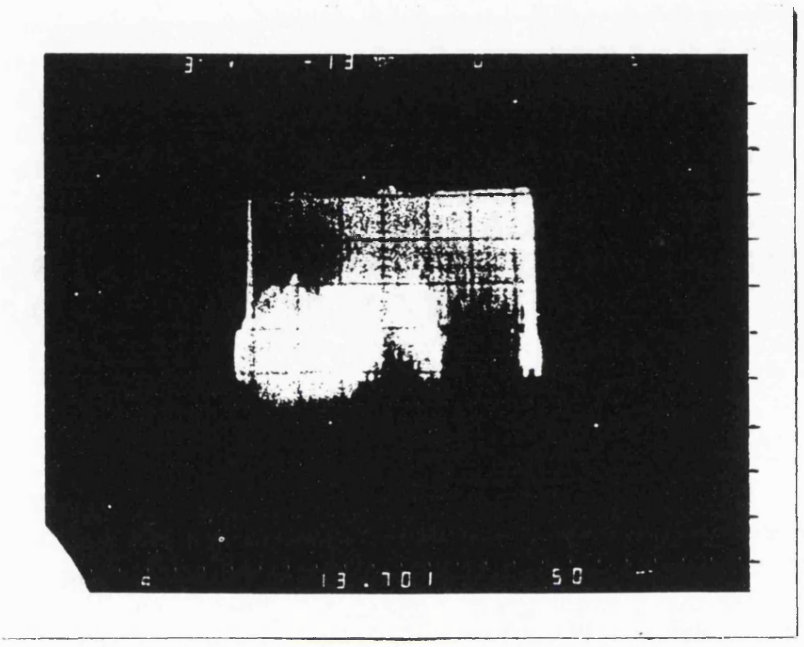

Span/div	50 MHz
Amp/div	5dB
Freq	13.7 GHz
Ref	- 13 dBm
Res. B/W	3 MHz

Figure 5.2-7 Measured output of the RSS corresponding to a point target response. The chirp bandwidth is 320 MHz, the the duration is 102.4 μs.

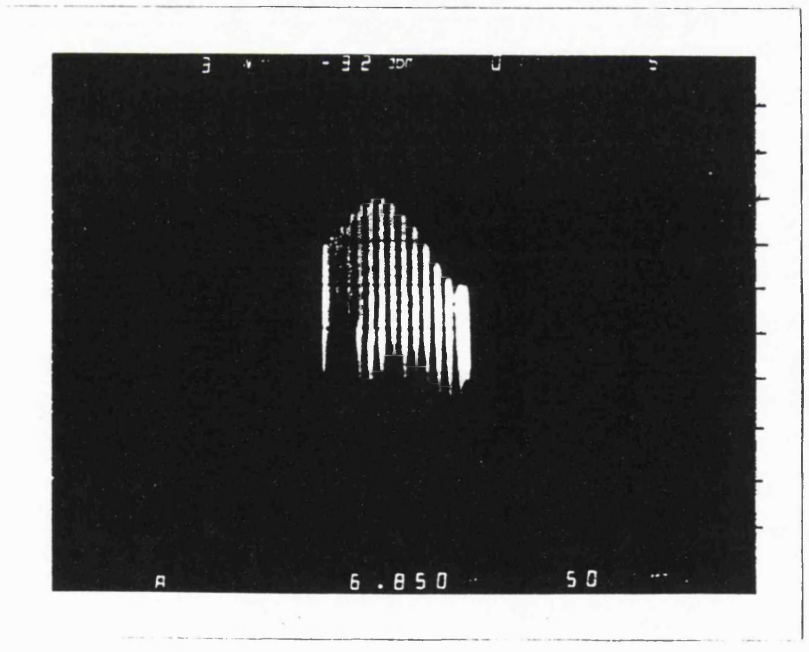

Span/div	50 MHz
Amp/div	5dB
Freq	13.7 GHz
Ref	- 32 dBm
Res. B/W	3 MHz

Figure 5.2-8 Measured sub-harmonic of the desired output signal of the RSS. It is 19 dB below the signal shown in figure 5.2-7.

5.3 THE CHIRP GENERATOR

The testing of the RSS chirp generator is important for two reasons: firstly, the performance of the chirp generator must be properly characterised in order to determine its effect on the simulation; secondly, the chirp generator is also one of the major RF components of the altimeter. The amplitude response of the chirp generator over the chirp bandwidth was measured in two ways.

Firstly, the amplitude response of the chirp generator was measured by chirping the unit to the desired measurement frequency, and measuring the amplitude on a spectrum analyser for a number of frequencies across the chirp bandwidth. Figure 5.3-1 shows the amplitude response of the chirp generator. The response rolls of at higher frequencies by approximately 1 dB. The dip in the middle of the response occurs at 20 times the natural frequency of the phase locked loop. At these frequencies, the sidebands are high, and extract power from the fundamental component.

Figure 5.3-2 shows the detected amplitude response of the chirp generator as it is chirps from 13.54 GHz to 13.86 GHz for three different ramping rates. The upper trace is the envelope of the chirp; the rising edge marks the lowest frequency of the chirp, and the falling edge the highest frequency of the chirp. The variation in power from the square law detector over the chirp bandwidth is:

$$10\log_{10}\frac{V_{max}}{V_{min}} \qquad (5.3\text{-}1)$$

which is approximately 0.6 dB for each of the pulse lengths. The dip in the response, observed in figure 5.3-1, is not seen in figure 5.3-2 because the detector responds to the total power (including the power in the sidebands). It will be shown in §6.2 that the amplitude distortion will result in a change in the sidelobe levels of the point target response in the altimeter, and will introduce a small bias into the estimated height made by the altimeter.

The rising edge of the lower trace in figure 5.3-2(a) represents the recovery chirp which ramps down to the start frequency (13.54 GHz) of the 300 μs RSS chirp whose envelope is shown on the upper trace. It is apparent that the detected chirp power at the high frequency (13.86 GHz) is proportional to 180 mV. The detected chirp power at the falling edge of the chirp envelope reduces as the ramp rate increases (i.e. duration decreases), as

shown in figure 5.3-2 (b) and (c). However it falls to 180 mV after approximately 50 μs in each case. It is evident that the final frequency is lagging for the faster ramp rates, i.e. the PLL is failing to respond quickly enough to the input sweep rate. The implication is a frequency error at the extremities of the chirp. If the trace for the slowest ramp rate can be assumed to have negligible frequency error, then the output frequency lags by approximately 16 MHz at the trailing edge for the 102.4 μs pulse, and lags by approximately 37 MHz for the 19.2 μs pulse.

It is shown in appendix A.9 that the implementation of a PLL in the multiplier unit using a high gain amplifier and passive filter rather than an active filter is causing problems for larger ramp rates. The maximum rate of change of the VCO output frequency is proportional to the difference between the input to the passive filter and the output ramp from the passive filter. Since the maximum input voltage to the passive filter is limited by the supply rail of the operational amplifier, the maximum rate of change of frequency is thus restricted for higher frequencies (where a higher voltage is required to drive the VCO). A mathematical analysis in appendix A.9 showed that the maximum rate of change of frequency in the steady state is actually 1.1 x 10^{13} Hz/s which is just above the required value of 0.833 x 10^{13} Hz/s (i.e. to sweep 160 MHz in 19.2 μs). Thus there is only a small factor in hand, which may not be sufficient to track the transients in the PLL as the input changes from CW to chirp and vice-versa.

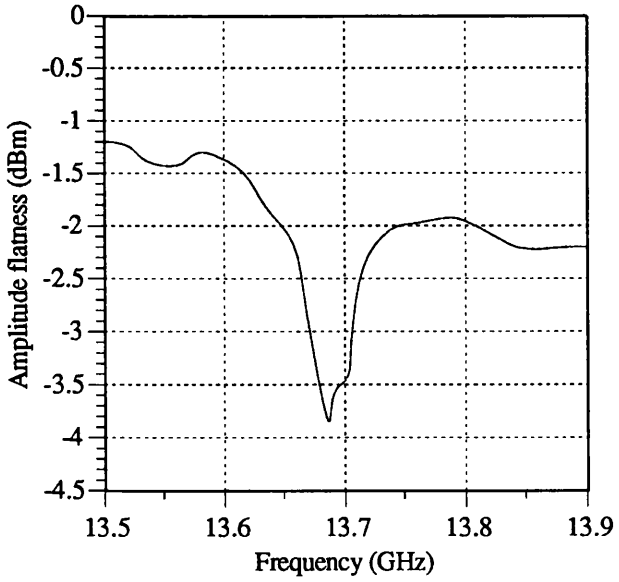

Figure 5.3-1 The static measurement of the amplitude flatness of the chirp.

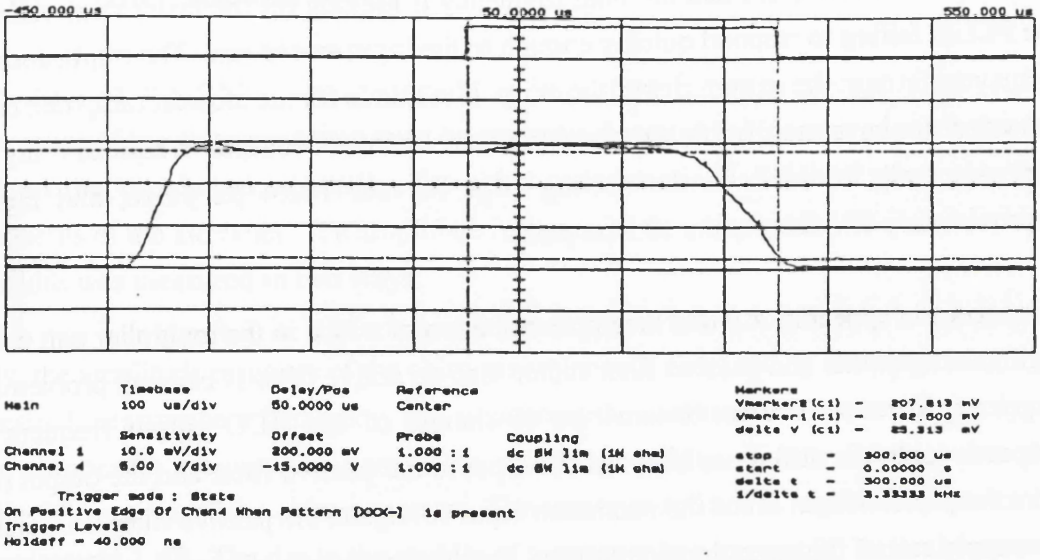

Figure 5.3-2(a) The detected amplitude response for the 300 µs pulse. The bandwidth of the chirp is 320 MHz. The upper trace is the envelope of the chirp, and the lower trace is the detected amplitude response.

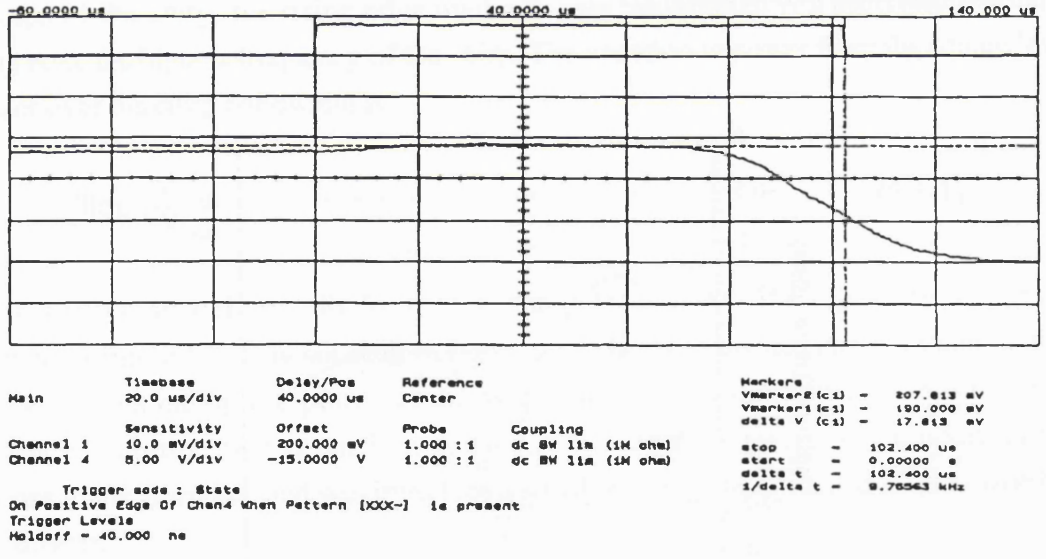

Figure 5.3-2(b) The detected amplitude response for the 102.4 µs pulse. There is a lag in the response of the chirp at the higher frequencies.

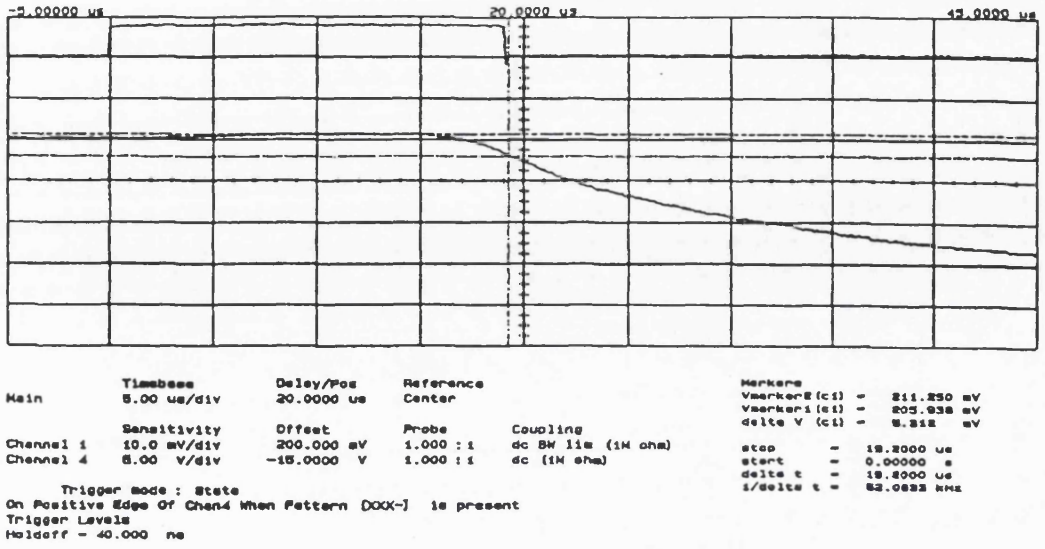

Figure 5.3-2(c) The detected amplitude response for the 19.2 μs pulse. There is an even greater lag in the response of the chirp at the higher frequencies.

5.4 TESTING THE ALTIMETER

The altimeter breadboard was not ready for testing at the time of writing this thesis. As a result this section will describe a philosophy for testing the altimeter rather than presenting results. There are multiple unknown quantities in the altimeter that need to be experimentally determined, and these will now be discussed.

A comparison of the different tracking algorithms is the most important test that will be done. The RSS-altimeter combination allows the dynamic performance of different tracking algorithms under real conditions to be determined. The echoes from the scenarios in §4.5 will be passed to the altimeter and will be tracked by both the MFT and OCOG tracking algorithms, described in appendix A.6. The yardstick for comparing the performance was given by the 9 parameters in (2.2-1) and (2.2-2). From these parameters it is possible to determine which of the algorithms is better at tracking at the finest resolution, tracking with no saturation, and tracking the leading edge of the return.

This test can be extended to compare the performance of the algorithms under different noise conditions. The signal to noise ratio of the received echo can be changed by altering the signal power of the RSS signal given by (4.5-1), with respect to the noise floor of the altimeter. The same yardstick can be used to compare the tracking algorithms with a

variety of signal to noise ratios.

The results of this test should confirm that the criteria for changing resolution and for switching from the ocean mode to non-ocean mode are optimal (Griffiths et al., 1987). However it will not be apparent unless the criteria are changed slightly from their optimum values. Indeed it may happen that the criteria are not optimum.

Since the performance of both algorithms depends on the noise level, the RSS can also be used to investigate methods of removing the noise floor from the altimeter echo prior to being tracked. The removal of the noise floor is not as easy as it is in the SMLE algorithm since it is quite probable that signal will occupy the early range bins where the estimate of the noise would be made.

In many of the above tests, it will be desirable to start the simulation with the surface in lock so that only the tracking performance is being investigated. Another useful test is to measure the length of time required to acquire the simulated surface without any *a priori* knowledge of the two way delay to the surface. The two way delay of all the echoes to the simulated surface can be offset in order to compute the acquisition for a number of different cases.

5.5 PERFORMANCE OF DIFFERENT TRACKING ALGORITHMS

The procedure for measuring the dynamic performance of the tracking algorithms is given in §5.4. The height error characteristic, which is another measure of the performance of the tracking algorithms and does not necessitate an altimeter for its measurement, is computed in this section for a number of different echoes. The OCOG and MFT tracking algorithms, defined in appendix A.6, are both analysed and compared.

The echoes in figure 5.5-1(a) and (b) are a representative set taken from the sea ice and rolling hills sequences of §4.5.1. The OCOG height error characteristic (right) is derived from the echo shown (left). From figure 5.5-1 the height error characteristic in most cases is a straight line with unity slope. The notable exception is the case when the leading edge of the echo is not well defined as illustrated by the first example of figure 5.5-1(b), which is the return from a sloping surface.

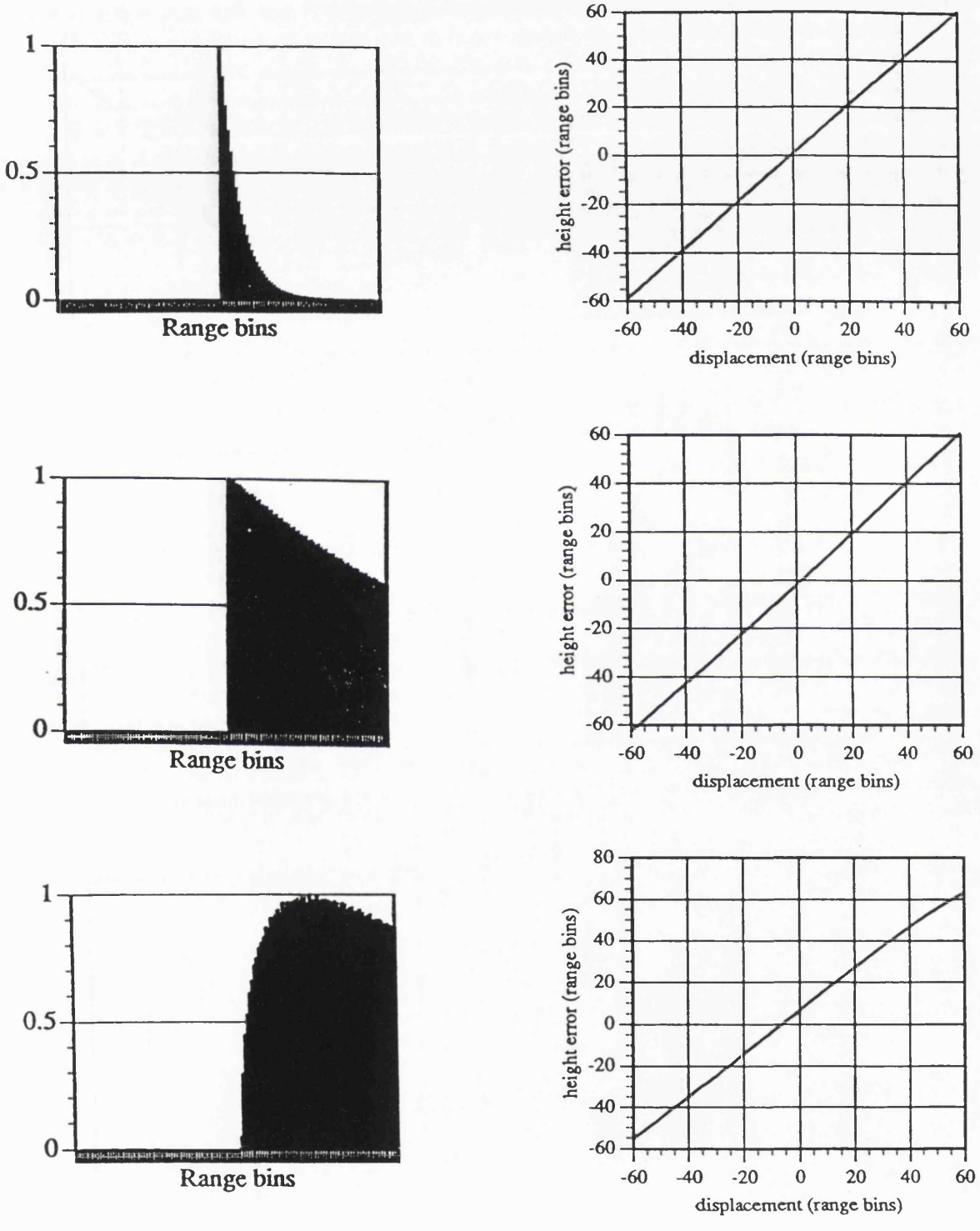

Figure 5.5-1(a) The height error characteristic (right) is shown for selected echo waveforms (left) from the sea ice scenario.

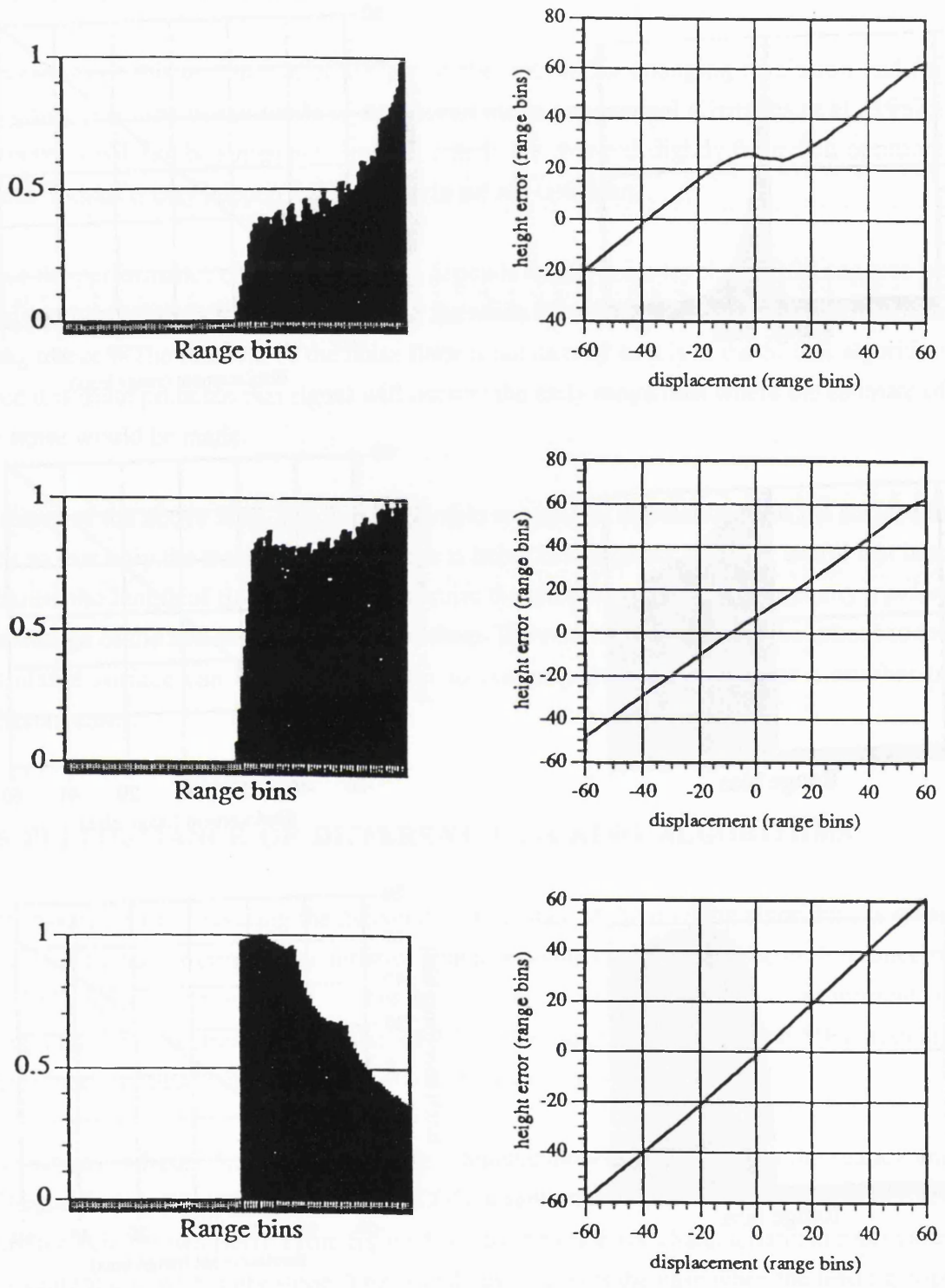

Figure 5.5-1(b) The height error characteristic (right) is shown for selected echo waveforms (left) from the rolling hills scenario.

In each case the height error characteristic of the MFT algorithm is a straight line with unity slope. It is not difficult to understand why this is so since the MFT algorithm fits a rectangular echo shape, which has a linear height error characteristic, to the recorded echo shape. The main drawback of the MFT algorithm is that the choice of threshold determines the position of the leading edge of the fitted rectangular waveform. Obviously if the threshold is too high, the height error characteristic will still have unity slope, but it will be offset from the ideal linear characteristic. Similarly, if the threshold is below the noise floor, the algorithm will interpret noise as signal, yielding an offset in the opposite direction.

The effect of different thresholds is illustrated in figure 5.2-2(b). In this case the noise floor is assumed to have a sloping shape shown in figure 5.2-2(a). The threshold positions are shown in both figures. The height error characteristic is increasingly offset as the threshold becomes immersed in the noise floor. The computed height error saturates for large displacements of the echo in the range window, and the amount of saturation increases as the threshold level is lowered into the noise floor. The MFT algorithm is sensitive to the level of the noise floor. However the threshold can be adaptively changed by estimating the noise in the early range bins, and placing the threshold above this.

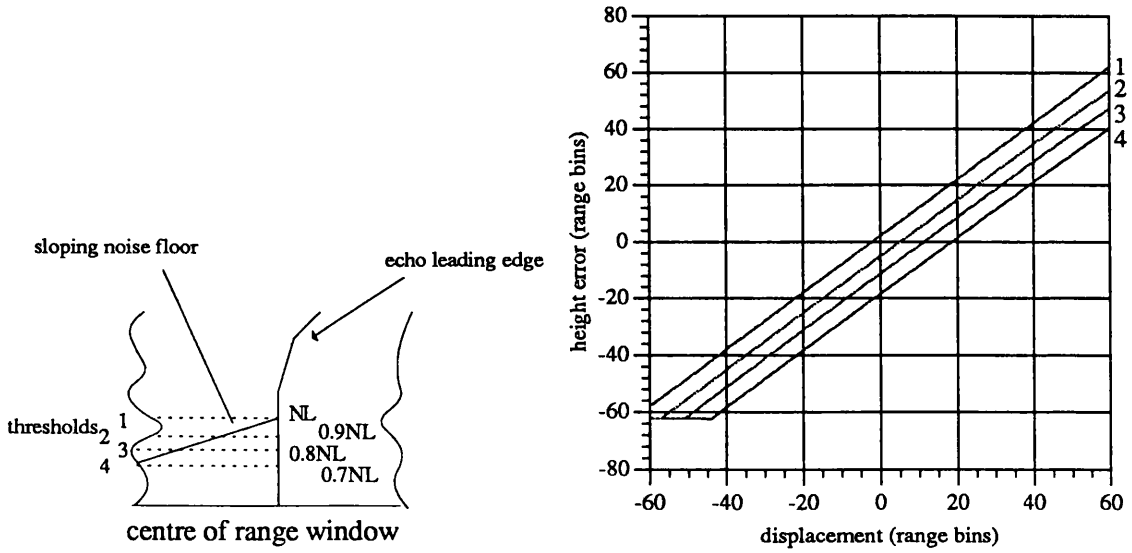

Figure 5.2-2 The height error characteristic (right) of the MFT algorithm for a sloping noise floor (left). The threshold positions are indicated by numbers 1 to 4 in both diagrams.

The OCOG, as illustrated in appendix A.6, is extremely sensitive to the noise floor. The performance of the algorithm is seriously impaired for modestly high noise levels since noise is treated as signal in the estimation of the position of the leading edge. Overall it appears that the MFT has more robust operation. It is also more conducive to adaptive processing, as illustrated in appendix A.6.2.

Chapter 6

Analysis of chirp errors

Introduction

It has been noted throughout this thesis that the distortion on the chirp is critical to the fidelity of the return signal simulation and to the operation of the altimeter. The analysis in chapter 3 assumed an ideal chirp. However, the chirp waveform is distorted by the frequency response of the components in both the transmit and receive chains of the altimeter. Typically this distortion is more severe in the transmit chain as a result of the high power TWT amplifier and the delay line (if in orbit calibration is to be included). A typical profile of the amplitude and phase distortion is shown in figure 6.1-1. These profiles are similar to those measured or inferred in §5.3.

Consider the nominally linear sweep used in (3.1-6), with an amplitude distortion $A_d(t)$ and a phase distortion $\Delta\phi(t)$:

$$A_d(t)\cos\left(\omega_o t + \pi b t^2 + \Delta\phi(t)\right) \qquad 0 \le t \le T \qquad (6.1\text{-}1)$$

When the transmit or RSS chirp is deramped with the deramp chirp, the resultant amplitude distortion is the product of the individual amplitude distortions, whereas the resultant phase distortion is the difference between the two phase distortions. It is quite possible that the resultant phase distortion can be zero, which will occur if the two chirps are aligned and have the same phase distortion. Since the deramp chirp is ideally aligned with the returned echo (i.e. alignment of chirps for correct tracking), it would seems that the effect of amplitude distortion is more severe than that of phase distortion. However this is generally not the case, as we will show in §6.3. A novel approach to the effect of phase errors is presented in §6.2 which precisely quantifies the error in the altimetric height measurement as a result of the phase errors. Another common approach to phase errors is critically assessed, and shown to be inappropriate for quantifying the errors on chirp waveforms.

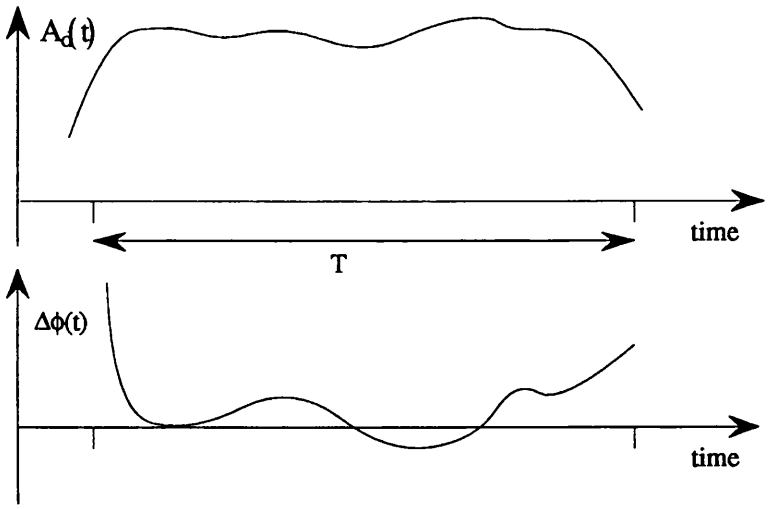

Figure 6.1-1. A typical profile of the amplitude and phase distortion of an FM chirp. The distortion is more severe at the bandedges. The amplitude distortion is typically 2 dB peak-to-peak (c.f. chapter 5) and the phase distortion is typically 2° peak to peak (Franchin, 1989).

6.1 ANALYSIS OF CHIRP ERRORS USING A FOURIER SERIES

6.1.1 Phase errors

Let $\Delta\phi(t)$ be the resultant phase distortion of the altimeter baseband signal. This is given by:

$$\Delta\phi(t) = \Delta\phi_t(t) - \Delta\phi_d(t - t_d + t_{pt}) \qquad (6.1\text{-}2)$$

where t_{pt} be the two-way propagation delay of the echo from a point target, and t_d be the instant of deramp measured with respect to the instant of transmission. The baseband signal in the altimeter after deramp is:

$$\cos\left[2\pi b t_\Delta t + \Delta\phi(t)\right] \qquad (6.1\text{-}3)$$

where $t_\Delta = t_{pt} - t_d$ is the time delay between the received chirp and the deramp chirp. Consider the resultant phase distortion shown in (6.1-2) as a Fourier series:

$$\Delta\phi(t) = \phi_o + \sum_{i=1}^{\infty} \phi_i \sin(i\omega_m t) \qquad (6.1\text{-}4)$$

where ω_m is the angular frequency of the fundamental frequency of the series and ϕ_i are the Fourier coefficients. If the distortion is assumed to be periodic with period T (i.e. chirp length) then the angular frequency of the fundamental component is defined as:

$$\omega_m = \frac{2\pi}{T} \tag{6.1-5}$$

The complex baseband signal is given as:

$$\exp[j2\pi bt_\Delta t]\exp[j\phi_o]\prod_{i=1}^{\infty}\exp[j\phi_i\sin(i\omega_m t)] \tag{6.1-6}$$

A typical component of the infinite product of terms from (6.1-5) can be expanded as a Fourier series:

$$\exp[j\phi_i\sin(\omega_m t)] = \sum_{-\infty}^{\infty} J_n(\phi_i)\exp[jni\omega_m t] \tag{6.1-7}$$

where J_n is a Bessel function of the 1st kind and n^{th} order (Gradshteyn and Ryzhik, 1980):

$$J_n(\phi_i) = \frac{1}{2\pi}\int_{-\pi}^{\pi}\exp[j(\phi_i\sin\theta - n\theta)]\,d\theta \tag{6.1-8}$$

Therefore the distorted signal in (6.1-5) can be rewritten as:

$$\exp[j2\pi bt_\Delta t]\exp[j\phi_o]\prod_{i=1}^{\infty}\left\{\sum_{n=-\infty}^{\infty} J_n(\phi_i)\exp[jni\omega_m t]\right\} \tag{6.1-9}$$

When the range window is formed by taking the Fourier Transform of (6.1-9) and squaring it, the Bessel functions corresponding to $\pm n$ give rise to a set of *paired echoes* as shown in figure 6.1-2. It should be clear that if there are k cycles of phase variation in the chirp (i.e. the k^{th} harmonic is the predominant signal) , then the first set of paired echoes will occur k range bins from the main lobe of the point target response.

The paired echoes around the true point target response affect the shape of the surface echoes processed in the range window. The paired echoes are simply weighted and shifted

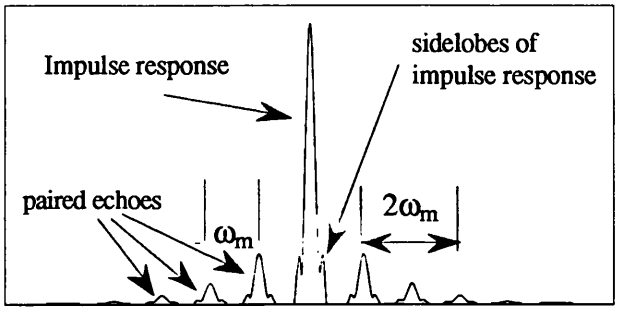

Figure 6.1-2. The phase distortion manifested as an equivalent modulation of the point target response by sets of paired echoes.

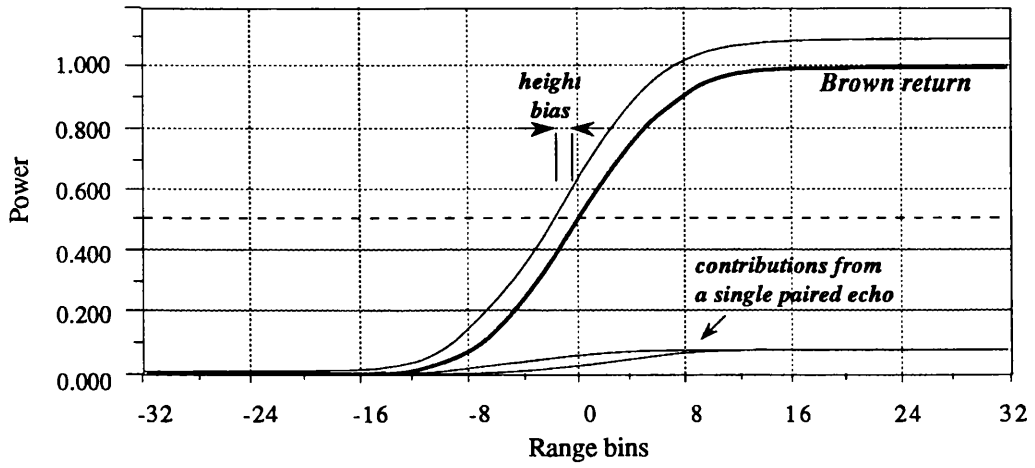

Figure 6.1-3 The effective shift in the power from the plateau region of the echo to the earlier range bins. In this case the echo was chosen to be a Brown echo.

versions of the true point target response, and as a result the echo in the presence of phase distortion is linear combination of shifted and weighted versions of the undistorted echo. This has the effect of moving power from the plateau region of the echo into the early range bins, thus causing an effective bias in the height estimate made by the altimeter (Brooks and Dooley, 1975). This height bias is illustrated in figure 6.1-3.

The model constructed so far is very successful in providing an intuitive understanding of how the height bias comes about. In order to quantify the height bias precisely, it is necessary to compute the Fourier Transform of (6.1-9), including as many terms as are required to model the distortion. However the model is ineffective because:

1) the positions and amplitudes of the paired echoes do not translate easily into an equivalent height bias;
2) many of the Bessel function terms of (6.1-8) determine the amplitude of a single set of paired echoes because of the large amount of intermodulation, and
3) it is difficult to quantify the error in the measurement using this model because of the large number of terms.

The model does work in the simple case of a sinusoidal phase distortion with small coefficient ϕ_i. In this case the Bessel functions corresponding to n=0, n=1 and n>1 can be approximated by 1, $\phi_1/2$ and 0 respectively. Thus the phase distortion is manifested by a single set of paired echoes about the point target response. Most analyses (Somma et al., 1980; Francis, 1982) approximate (6.1-6) by a single complex term, thus yielding a single set of paired echoes. In the case of the radar altimeter, it is necessary to specify a side lobe level that is sufficiently low such that it can be assumed not to affect the height estimate. It is not possible, without much difficulty, to quantify the error resulting from the distortion.

6.1.2 Amplitude errors

The amplitude distortion on the chirp can be treated in a similar fashion with the amplitude being described as:

$$A_d(t) = 1 + a_o + \sum_{i=1}^{\infty} a_i \sin(i\omega_m t) \qquad (6.1\text{-}10)$$

The angular frequency is defined by (6.1-5) if the distortion is assumed to be periodic

with a period equal to the chirp length. It is not too difficult to show that the baseband signal in the altimeter is given by:

$$s(t) = (1 + a_o)e^{j2\pi bt_\Delta t} + \sum_{i=1}^{\infty} a_i e^{j(2\pi bt_\Delta \pm i\omega_m)t} \qquad (6.1\text{-}11)$$

When the range window is formed in the altimeter, the Fourier components appear in each of the range bins of the range window, symmetrically disposed about the point target response. If the amplitude error is slowly varying, then the bulk of the spectral energy is in the low frequencies, i.e. in the first 3 or 4 range bins either side of the point target response. It must be obvious that the effect of amplitude distortion is to change the level of the main lobe and the sidelobes of the point target response of (6.1-11).

We will see in §6.3 that amplitude distortion is similar to amplitude weighting, and that if a weighting function is used in the processing, then the effect of amplitude distortion tends to be minimised.

6.2. ANALYSIS OF CHIRP PHASE ERRORS USING A POWER SERIES

6.2.1 The power series approach

The second approach is to model the phase distortion using a power series as in (2.3-10):

$$\Delta\phi(t) = \phi_o + \sum_{i=1}^{\infty} \phi_i \left(\frac{t}{T}\right)^i \text{ radians} \qquad 0 \le t \le T \qquad (6.2\text{-}1)$$

where ϕ_i are the polynomial coefficients. Consider the effect of the phase distortion on (3.1-6). This can be rewritten as:

$$g(t) = d(t) \otimes \cos\left(\omega_o t + \pi bt^2 + \Delta\phi(t)\right) \qquad (6.2\text{-}2)$$

So, g(t) is given by:

$$g(t) = \int_\tau d(t)\cos\left(\omega_o(t-\tau) + \pi b(t-\tau)^2 + \Delta\phi(t-\tau)\right)d\tau \qquad (6.2\text{-}3)$$

Consider the baseband signal after this signal has been deramped in the altimeter (see appendix A.1):

$$F_a(t) = \int_\tau d(t)\exp[-j(\omega_o\tau - \pi b\tau^2 + 2\pi bt\tau)].\exp(-j\Delta\phi(t-\tau)).\{U(t-\tau) - U(t-\tau-T)\}d\tau \tag{6.2-4}$$

Again neglecting the small temporal misalignment of the return and deramp chirp, (6.2-4) reduces to:

$$F_a(t) = \{U(t-\tau) - U(t-\tau-T)\}.\exp(-j\Delta\phi(t)) \int_\tau d(t)\exp[-j(\omega_o\tau - \pi b\tau^2 - \Delta\phi(\tau) + 2\pi bt\tau)]d\tau \tag{6.2-5}$$

This equation contains three terms, the first two of which are fully deterministic. The last is a function of the delay time variable. The spectrum of $F_a(t)$ is given by:

$$f_a(\omega) = S_r(\omega) \otimes \Phi(\omega) \otimes \int_\tau d(\tau)\exp[j(\omega_o\tau - \pi b\tau^2 + \Delta\phi(\tau))].S_r(\omega - b\tau)d\tau \tag{6.2-6}$$

where $S_r(\omega)$ is the point target response in the range window and $\Phi(\omega)$ is the spectrum of the phase distortion. Rearranging (6.2-6) gives:

$$f_a(\omega) = \int_\tau d(\tau)\exp[j(\omega_o\tau - \pi b\tau^2 + \Delta\phi(\tau))].S_1(\omega - b\tau)d\tau \tag{6.2-7}$$

with:

$$S_1(\omega) = S_r(\omega) \otimes \Phi(\omega) \tag{6.2-8}$$

The mean power in the range window is the expectation value of $f_a(\omega)f_a^*(\omega)$:

$$\langle f_a(\omega)f_a^*(\omega)\rangle = \int_{\tau 1}\int_{\tau 2} \langle d(\tau 1)d(\tau 2)\rangle\{\exp[j(\omega_o(\tau_2-\tau_1)+\pi b(\tau_2^2-\tau_1^2)+\Delta\phi(\tau_2)-\Delta\phi(\tau_1))]\}. S_1(\omega-2\pi b\tau_1)S_1^*(\omega-2\pi b\tau_2)d\tau_1 d\tau_2 \tag{6.2-9}$$

Recall that $d(\tau)$ is a Poisson process and its second order correlation function is defined as (Papoulis, 1965):

$$\langle d(\tau_1) \, . \, d(\tau_2) \rangle = \langle d(\tau_1) \rangle \, . \, \delta(\tau_1 - \tau_2) + \langle d(\tau_1) \rangle \, . \, \langle d(\tau_2) \rangle \qquad (6.2\text{-}10)$$

Assuming that the phase of the exponential function of (6.2-7) is random, i.e. Gaussian statistics, and thus that the mean value is zero except when $\tau_1 = \tau_2$ (when it is unity). Substituting (6.2-10) into (6.2-9) gives:

$$\langle | f_a(\omega) |^2 \rangle = \int_{\tau 1} \int_{\tau 2} \langle d(\tau_2) \rangle \, \delta(\tau_2 - \tau_1) \, S_1(\omega - 2\pi b \tau_2) S_1(\omega - 2\pi b \tau_1) \, d\tau_1 d\tau_2 \qquad (6.2\text{-}11)$$

Noting that:

$$\int_{-\infty}^{\infty} \delta(\tau_1 - \tau_2) d\tau_1 = \begin{matrix} 1 & \tau_1 = \tau_2 \\ 0 & \tau_1 \neq \tau_1 \end{matrix} \qquad (6.2\text{-}12)$$

Then:

$$\langle | f_a(\omega) |^2 \rangle = \left\langle d\left(\frac{\omega}{2\pi b}\right) \right\rangle \otimes \left| S_r(\omega) \otimes \Phi(\omega) \right|^2 \qquad (6.2\text{-}13)$$

and substituting (3.1-29) into (6.2-13) gives:

$$\langle | f_a(\omega) |^2 \rangle = \langle | f(\omega) |^2 \rangle \otimes \left| S_r(\omega) \otimes \Phi(\omega) \right|^2 \qquad (6.2\text{-}14)$$

Thus the distorted power spectrum can be computed from the multiple convolution of (6.2-14) involving the impulse response of the altimeter and the spectrum of the phase distortion. The spectrum of the phase distortion is given by:

$$\Phi(\omega) = \int_0^T \exp\left[j \left(\phi_o + \sum_{i=1}^{\infty} \phi_i \left(\frac{t}{T} \right)^i - \omega t \right) \right] dt \qquad (6.2\text{-}15)$$

Note that the integral limits could have been chosen to be [-T/2,T/2] but were taken to be

[0,T] as this considerably simplifies the analysis. The equivalence between the two cases is shown in appendix A.10. Let us define $\Phi_i(\omega)$ such that:

$$\Phi_i(\omega) = \int_0^T \exp\left[j\left(\phi_i\left(\frac{t}{T}\right)^i - \omega t\right)\right]dt \qquad (6.2\text{-}16)$$

The ϕ_0 term has no effect since it is a constant phase and will not affect the square law-detected output. The term involving ϕ_1 represents a frequency component and thus causes a shift in the effective impulse response by ϕ_1. Note that, from (6.2-1), ϕ_i is a normalised coefficient, and thus the actual frequency shift is ϕ_i/T. The term involving ϕ_2 represents a Fresnel function, which is similarly shifted by an amount proportional to ϕ_2. Since the higher order terms are narrow peaked functions centred on ϕ_i/T, we postulate that each of the higher order terms will shift the response by an amount proportional to ϕ_i.

In order to demonstrate that the higher-order ϕ_i terms do shift the impulse response by an amount proportional to ϕ_i, a simulation was undertaken. The software model described in §3.3.1 was used to model the phase distortion on the chirps. The echo used in the model is the Brown return shown in figure 6.1-3. The phase distortion is applied by multiplying the undistorted signal by the complex phase term (c.f. (6.2-4)), as follows:

$$F_a(t) = F(t) \,.\, e^{-j\Delta\phi(t)} \qquad (6.2\text{-}17)$$

where $F_a(t)$ is the baseband altimeter signal, F(t) is the baseband signal corresponding to the simulated spectrum. This signal is then processed to form the range window of the altimeter. The final part of the analysis uses two algorithms to compute the position of the half power point for both the undistorted and distorted echo spectra in the range window. The first is the SMLE algorithm (defined in appendix A.6) and the other is a simple algorithm that first searches the range bins for the peak power, and then locates the position of the range bin corresponding to the half power point. The resulting height bias can then be computed

The simulation was run for a range of values of ϕ_i when each of the other ϕ_j's ($j \neq i$) are set to zero. Figure 6.2-1 shows the height bias for the first four phase error coefficients and for the two estimation algorithms. The ideal curve shows the height bias for the simple algorithm, and the other four curves show the height bias for the SMLE algorithm. The results clearly demonstrate a linear relationship between height bias resulting from phase distortion and each of the normalised coefficients. This result is obvious for a linear phase

error on the chirp, i.e. a constant frequency shift will produce an equivalent bias. The deviation for high values of phase distortion, which does not occur for the simpler tracking algorithm, is attributed to the non-linearity in the height error vs. displacement characteristic of the SMLE algorithm.

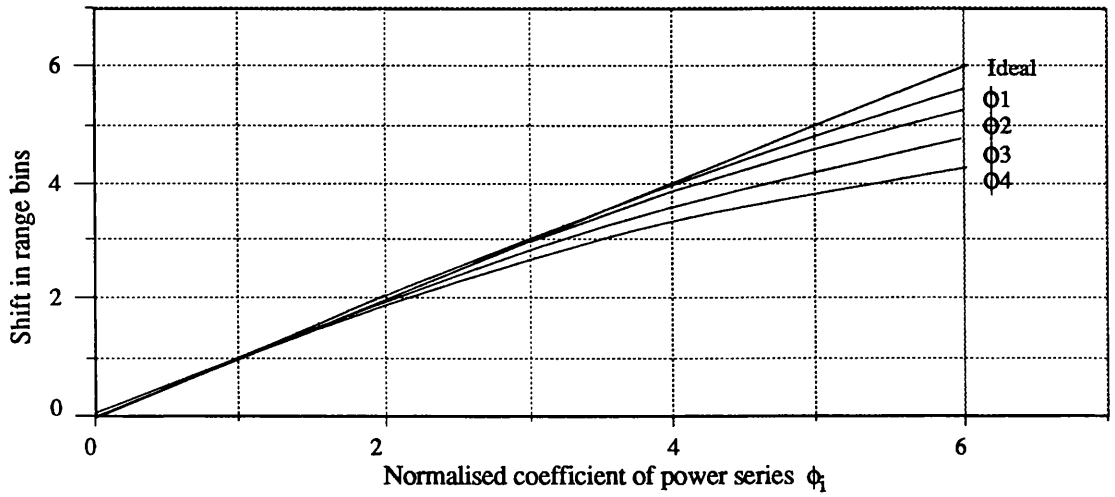

Figure 6.2-1. Results of a simulation showing the shifts in the response of each $\phi_i(\omega)$ as a function of ϕ_i.

Now consider the total height bias resulting from the total distortion. By substituting (6.2-16) into (6.2-15), $\Phi(\omega)$ is given by a multiple convolution:

$$\Phi(\omega) = \Phi_1(\omega) \otimes \Phi_2(\omega) \otimes \ldots\ldots \otimes \Phi_i(\omega) \otimes \ldots \qquad (6.2\text{-}18)$$

The normalised frequency shift from the convolution with $\Phi(\omega)$ is equal to ϕ_i.If this is applied to the multiple convolution, then the total shift in angular frequency resulting from the distortion is:

$$\Delta\omega = \frac{2\pi}{T} \cdot \sum_{i=1}^{\infty} \phi_i \qquad (6.2\text{-}19)$$

This is a simple but very important result. It specifies the shift in the echo resulting from the phase distortion on the chirp waveform. The bias in the height estimate is given by:

$$\Delta h = \frac{c}{2B} \cdot \sum_{i=1}^{\infty} \phi_i \qquad (6.2\text{-}20)$$

which is the mean instantaneous frequency averaged over the chirp duration (c.f. 2.3-11).

6.2.2 Limit of applicability of the power series approach

The resultant shift in (6.2-19) was determined on the premise that the echo shape remained undistorted, and was merely shifted in the range window. Let us now consider the amount of distortion that can be tolerated by the echo before the leading edge slope is significantly changed. The leading edge slope was computed from the SMLE algorithm using the model defined above. The percentage change in the slope of the leading edge of the echo as a function of the first three phase distortion coefficients is shown in figure 6.2-2.

It is seen that phase distortion coefficients as high as 2 (i.e will shift the echo by 2 range bins) will produce less than 2% change in the slope of the echo leading edge. Thus for such distortion parameters, the predominant effect on the echo is a shift in the range. For distortion coefficients greater than 2, the slope of the leading edge changes and the echo shape is distorted.

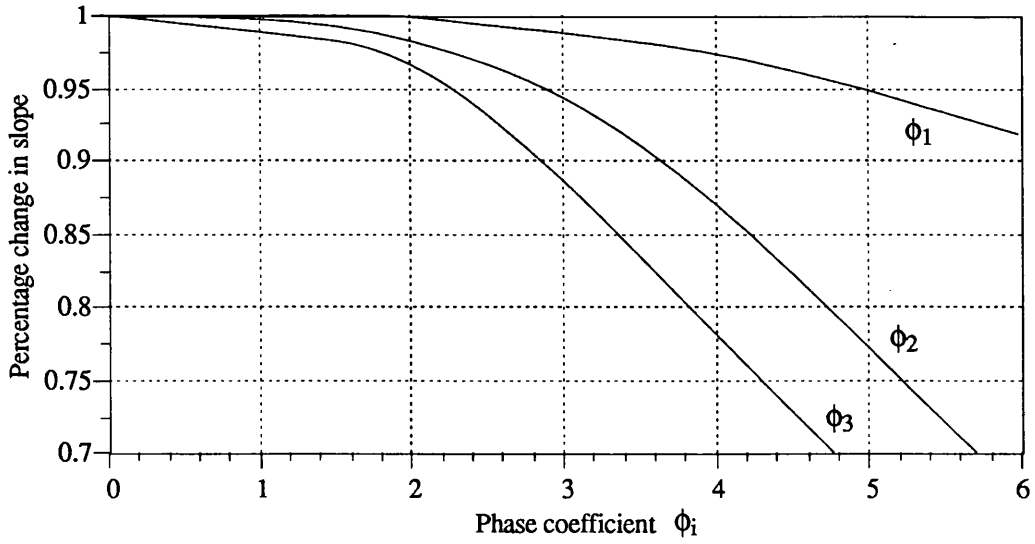

Figure 6.2-2 The percentage change in the slope of the leading edge as a function of the phase distortion coefficients.

When the phase distortion consists of a number of different order coefficients, it is more difficult to determine whether or not the approach is as precise. An empirically-derived conservative rule of thumb is that the resultant normalised bias:

$$\sum_{i=1}^{\infty} \phi_i < 2 \qquad (6.2\text{-}21)$$

This was found to work well in the simulation program, causing a change in the slope of the leading edge of less than 2 % for all the examples considered (see §6.2.3).

6.2.3 Examples of phase distortion

Two useful conclusions can be immediately drawn from the analysis in §6.2.1. Firstly, in the case of a phase error that is symmetric about the centre of the pulse, the series in (6.2-20) can be shown to be identically zero, i.e.

$$\sum_{i=1}^{\infty} \phi_i = 0, \qquad (6.2\text{-}22)$$

a result that indicates no bias in the height estimate. Secondly, an anti-symmetric phase error will give a maximum value of this series for a given root mean square phase error. Thus anti-symmetric phase errors are considerably more critical than symmetric phase errors. Consider a number of examples.

Example 1

Consider a sinusoidal phase error, shown in figure 6.2-3, with a peak error of ϕ_p. Five terms of a power series are required to curve fit this sinusoid (also shown on figure 6.2-3):

$$f(x) = \phi_p(-\ 55.3x^5 + 138x^4 - 99.5x^3 + 11.2x^2 + 5.44x) \qquad (6.2\text{-}23)$$

where ϕ_p is the normalising factor. Substituting the coefficients of (6.2-23) into (6.2-19), we get a bias of $0.16\phi_p$ range bins resulting from the sinusoidal phase distortion.

The Fourier series approach dictates that the level of the sidelobes are all changed by the paired echoes produced by the Bessel functions. If the phase error is small, then the

spectrum of paired echoes can be replaced by one set of echoes. For example, if the peak phase error is 0.2 rads (11.5°), the paired echoes from the Fourier approach are - 14.8 dB down. The resulting shift from the Power series approach is 0.03 range bins or 1.4 cm (if the chirp bandwidth is 320 MHz).

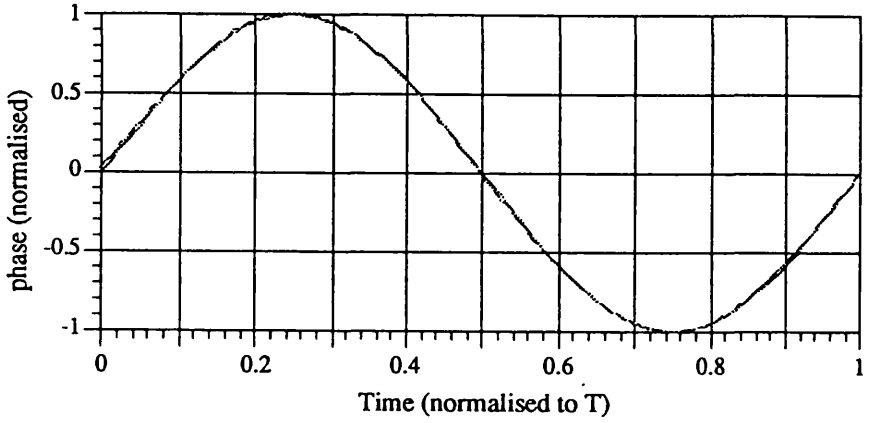

Figure 6.2-3. An example of sinusoidal phase distortion, with a superimposed curve fitted 5th order polynomial.

Example 2

Typically chirp phase errors will not be sinusoidal. There will be a ripple in the passband, but there will be an obvious departure at the bandedges of the chirp due to the poor phase response of the RF components or for the reasons cited in chapter 5.

Consider a typical phase error, as shown in figure 6.2-4. It is curve fitted by the following polynomial (also shown in figure 6.2-4):

$$f(x) = - 16.02x^5 + 40.0x^4 - 95.2x^3 + 102.8x^2 - 39.6x + 4.00 \qquad (6.2\text{-}24)$$

By substituting the coefficients from (6.2-24) into (6.2-19), we see that this type of phase distortion produces a bias corresponding to $4\phi_p$ range bins, where ϕ_p is the denormalising factor. In this case the peak variation of the midband sinusoidal component is ϕ_p. From eqn. 6.1-26, a value of $\phi_p = 11.5°$ will produce a bias of 20 cm (B = 600 MHz). This means that a peak-to-peak phase error of 45° can be tolerated if a range error of 10 cm is allowed.

The predominant frequency in the Fourier approach is close to the frequency of the

midband ripple. The amplitude of this tone is ϕ_p. Thus if only one set of paired echoes was chosen, the Fourier approach would produce almost the same set of paired echoes for a completely different and considerably more severe case. Obviously, the distortion on the bandedge of the chirp is more severe than distortion at the centre of the chirp.

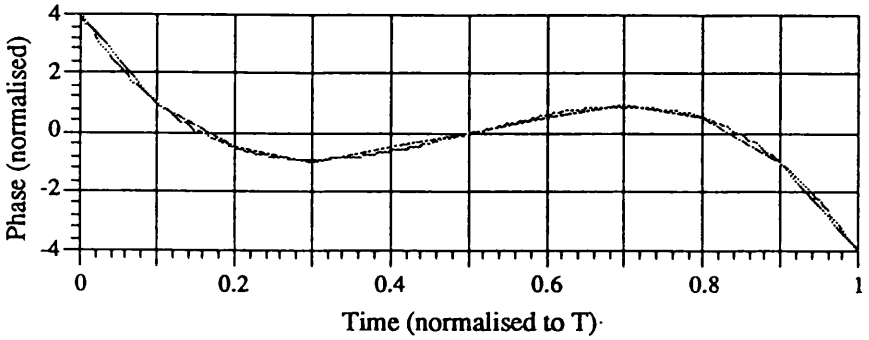

Figure 6.2-4. An example of an anti-symmetric phase error, and a curve fitted 5th order polynomial.

6.2.4 Summary of the power series approach to phase errors

There are four main points to be summarised.

1) The power series gives a precise estimate of the height bias resulting from the phase distortion on the chirped waveform.

2) The definition of the height bias assumes that the FFT length in the altimeter is [0,T]. The definition for an FFT length of [-T/2, T/2] is derived in appendix A.10. The height shift versus distortion coefficient characteristics are different. However, it is shown in the appendix that the resulting height bias from all the terms is independent of the definition of the FFT length.

3) Distortion at the bandedge is more severe than distortion at the centre of the chirp.

4) An example showed that if only one set of paired echoes was analysed in the Fourier approach, the results could be very misleading.

6.3 ANALYSIS OF AMPLITUDE ERRORS USING A POWER SERIES

6.3.1 Simulation of amplitude distortion

Consider a power series representation of amplitude distortion:

$$A_d(t) = 1 + a_o + \sum_{i=1}^{\infty} a_i\left(\frac{t}{T}\right)^i \qquad (6.3\text{-}1)$$

Thus the distorted point target response is given as:

$$S_1(\omega) = \int_{-T/2}^{T/2} \left(1 + a_o + a_1\left(\frac{t}{T}\right) + a_2\left(\frac{t}{T}\right)^2 + a_3\left(\frac{t}{T}\right)^3 + \cdots\right) e^{-j\omega t} dt \qquad (6.3\text{-}2)$$

So:

$$S_1(\omega) = (1+a_o)S(\omega) + ja_1\frac{dS(\omega)}{d\omega} - a_2\frac{d^2S(\omega)}{d\omega^2} - ja_3\frac{d^3S(\omega)}{d\omega^3} + \cdots \qquad (6.3\text{-}3)$$

where $S(\omega)$ is the undistorted sinc function. All the imaginary components are odd, and the real components are even. Thus the distorted point target response is necessarily even or symmetric. Since there is no asymmetry in the side lobes of the point target response, any bias that results from amplitude distortion must result from a relative change in the level of the side lobes. This has already been confirmed from §6.1.2. Figure 6.3-1 shows the relative change in the sidelobes for the amplitude distortion function:

$$A_d(t) = 1 - a_2t^2 \qquad -\frac{T}{2} \le t < \frac{T}{2} \qquad (6.3\text{-}4)$$

for the cases $a_2 = -2, 0, 2$. A change in the sidelobe level and a broadening of the main lobe occurs and the respective sidelobe levels are -25, -16.1 and -10 dB.

Since it was difficult to apply a model to quantify the height bias resulting from amplitude distortion, a computer simulation, similar to that in §6.2.1, was undertaken. A Brown model was again chosen as the echo waveform. The distortion was applied by multiplying the RSS baseband signal F(t) by the term in (6.3-1). Thus the baseband altimeter signal is:

$$F_a(t) = A_d(t)F(t) \qquad (6.3\text{-}5)$$

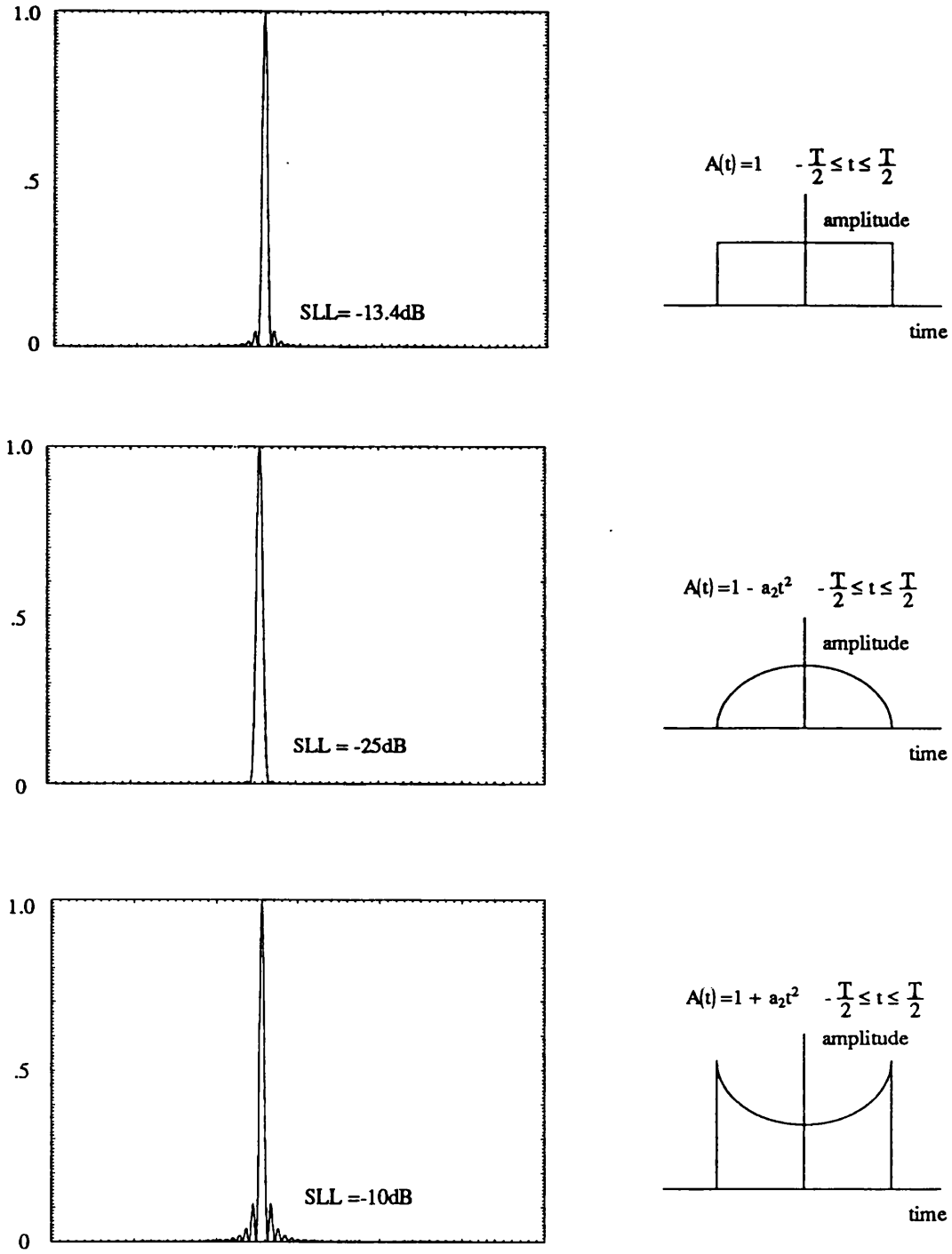

Figure 6.3-1. The impulse response of the altimeter when the amplitude distortion profile of the chirp is defined by $A_d(t) = 1 + a_2t^2$. The predominant effect is a relative change in the level of the sidelobes.

The height bias was computed as discussed in §6.2.1. Figure 6.3-2 shows the the height bias as a function of the distortion coefficient a_i as each of the coefficients are varied in turn. The results are initially disappointing in that there is no visible relationship between the height bias and the distortion coefficients. Figure 6.3-2 also shows the height bias when a Hanning weighting function is applied in conjunction with the amplitude distortion. A few interesting observations can be made.

1) The height bias for the distortion function with $a_2 = -2$ (all other $a_i = 0$) is equal to that when a Hanning function is applied separately. This is explained by the fact that the two functions are not too dissimilar.

2) The height bias is a fixed value when a Hanning function is applied in conjunction with the distortion profile, and this is equal to the value of the bias when a Hanning function only is applied to the signal. Thus, a fixed height bias will exist if a Hanning function is used to process the echo in the range window, but this height bias will be insensitive to any amplitude distortion on the pulse. The height bias corresponds to -0.0656 range bins, i.e. approximately 2 cm for B = 600 MHz.

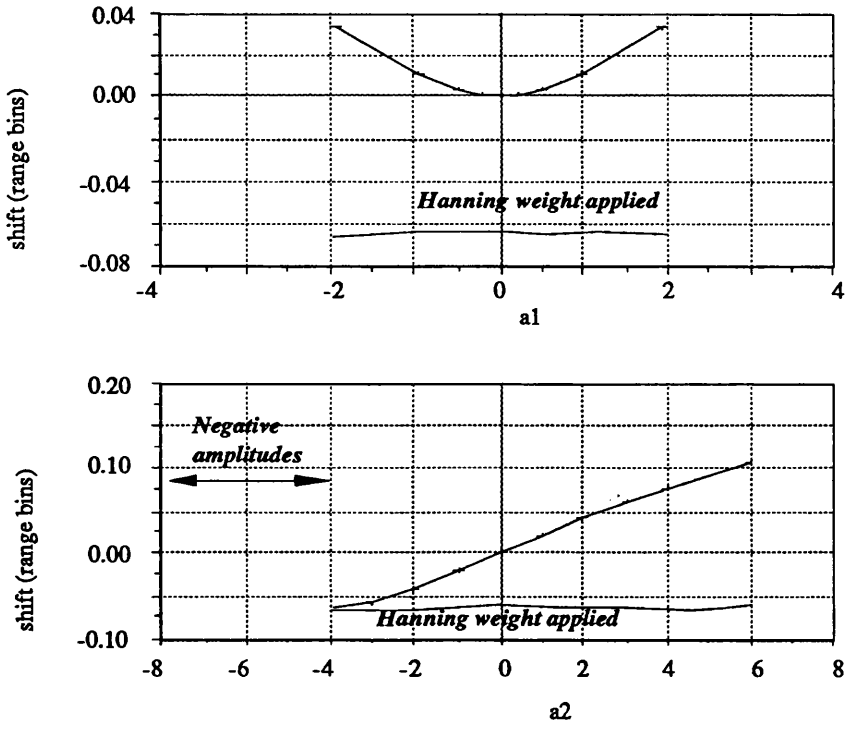

Figure 6.3-2 The shift of the echo in the range window as a function of the the first two amplitude distortion coefficients, and the shift due to a Hanning function.

Figure 6.3-3 illustrates how the slope of the leading edge of the echo in the range window is affected by the amplitude distortion of the chirp. The relationship between the slope of the leading edge and the distortion coefficient is obvious from the curves for each of the coefficients; however it is difficult to determine the change in slope for a distortion function that contains many different terms from these curves. The maximum change in slope over the full range of values is approximately 0.4 % which is not significant.

Thus it can be concluded that amplitude distortion does not significantly alter the leading edge slope of the echo or introduce any height bias (if a Hanning weighting function is used).

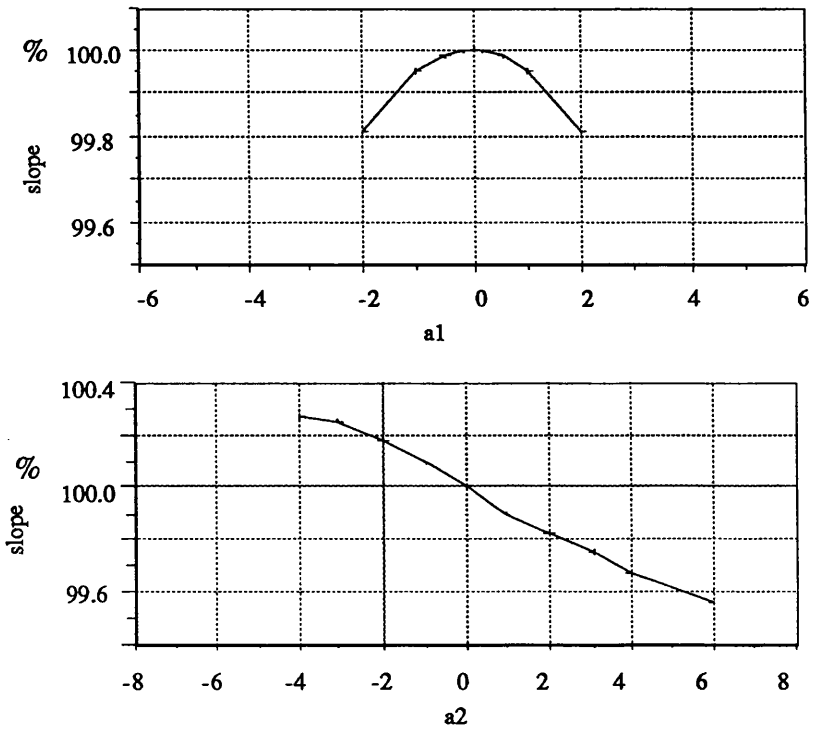

Figure 6.3-3. The results of a computer simulation showing the change in slope and the shift in the response as the coefficients a_1 and a_2 are varied in turn.

6.3.2 *The combined effect of phase and amplitude errors*

The amplitude and phase errors of a chirp are independent. Moreover, amplitude and phase errors affect the point target response in different ways: phase errors translate the position of the point target response and amplitude errors change the level of the sidelobes. Both effects are orthogonal, thus the combined height bias is the sum of the two individual effects. The point target response for combined amplitude and phase distortion can be shown to be given by:

$$S_1(\omega) \otimes \Phi(\omega) \qquad (6.3\text{-}6)$$

where $S_1(\omega)$ is the point target response for the amplitude distorted chirp, and $\Phi(\omega)$ is the spectrum of the phase distortion. By applying the convolution argument in §6.2.1, the height bias is the sum of the two individual height biases.

Figure 6.3-4 shows how a Hanning function changes the height bias vs distortion coefficient characteristic. Each of the curves are simply offset by -0.0656 range bins. A Welch function (triangular) produces a bias of -0.0256 range bins. Thus the height bias resulting from the amplitude distortion can be simply added to the height bias resulting from the phase distortion.

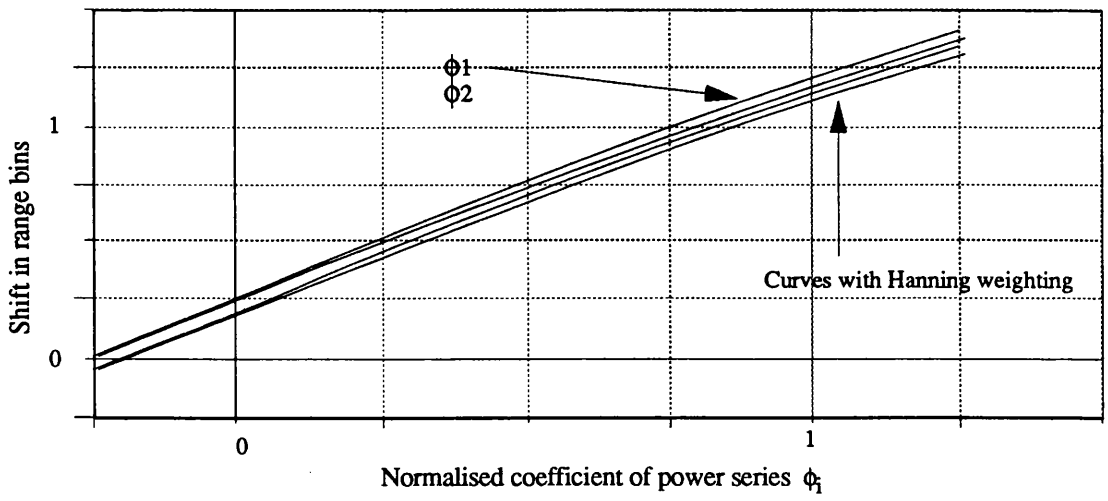

Figure 6.3-4. The effect of a Hanning weighting function on the height bias vs phase distortion characteristic. Note that the altimeter FFT was defined over [0,T] for both the Hanning function and the phase distortion.

6.4 SUMMARY

The two methods of analysing chirp errors presented in this chapter have their respective merits and drawbacks.

The Fourier series approach is useful for setting a specification for the design of chirp generators (Griffiths, 1989). The usefulness is immediately obvious because of the ease with which the sidelobe levels of the altimeter point target response can be experimentally measured. However, using this method, there is no clear idea of how the multiple sets of paired echoes and their intermodulation products affect the estimate of height made by the altimeter. This is an area that has not been fully investigated by most researchers, most of whom only have only considered a single set of paired echoes, thereby simplifying the analysis.

The power series approach is completely different. It does not make any approximations, and uses all the terms of the power series required to define the chirp phase errors. It is thus a substantially more accurate method of analysis.

For most types of chirp phase error, the greatest rate of change of the chirp error occurs at the bandedge of the chirp. Thus the power series approach is naturally suited to modelling these types of error.

The power series approach could not be applied successfully to model the effect of amplitude distortion. However,it was observed that the effect of amplitude distortion was minimised if a Hanning weighting function was applied to the signal in the range window. The magnitude of this bias error (2 cm) is consistent with the value of the ERS-1 altimeter bias measured by Francis and Duesmann (1987).

Chapter 7

Summary and conclusions

7.1 SUMMARY

The purpose of this thesis has been to investigate methods of pre-launch testing of advanced satellite radar altimeters. The conventional pulse-limited altimeter is prone to slope-induced error; nonetheless the concept has been adapted for use over rough terrain. The proposed Advanced Terrain-Tracking Altimeter has thus been the main focus of this study. The principal ideas generated in the research and expounded in this thesis can be summarised by the following statements:

1) The methods of testing a conventional ocean-dedicated, pulse-limited satellite altimeter prior to launch are well established. Parameter characterisation is performed using a return signal simulator, and internal calibration can be performed by coupling a sample of the transmitted signal to the receiver. The former gives an initial assessment of the dynamic performance of the altimeter, and allows the error from the altimeter hardware to be experimentally determined prior to launch, as discussed in chapter 2. The latter procedures have been successfully used with the ERS-1 altimeter, both pre-launch and in-orbit. Some of the problems associated with these techniques have been outlined.

2) A return signal simulator has been identified as the only tool which enables the analysis of the dynamic performance of the Adaptive Terrain-Tracking Altimeter prior to launch. It allows the resolution switching criteria, and the tracking algorithms of the altimeter to be tested over simulated terrain. Particular measures of performance have defined in chapter 2 which will form the foundations for the analysis of the tracking performance of the prototype altimeter being built by British Aerospace. These measures, I expect, will prove not to be comprehensive; but they do at least allow a direct comparison between different tracking algorithms over a particular simulated surface. In chapter 5, a test philosophy for the ATTA has been outlined.

3) A Poisson process has been used successfully to model the scattering from a surface. The process itself is obviously physically similar to the scattering from the surface. However the mathematical properties of the Poisson process allowed (i) the return signal

to be rigorously defined, and (ii) the effect of chirp phase distortion on the height estimate made by the altimeter to be precisely quantified.

4) A very useful and simple expression for the return signal results if the echo timing is defined in the spectral domain, and the approximations required to do this are shown to be negligible. This led to a simple design of an RSS based on the Fourier Transform. The big advantage of the design is that the echoes can be computed prior to simulation. Moreover it enables the echo resolution to be changed quickly and easily.

5) A number of different RSS designs were shown to originate from the model used to describe the scattering. A couple of the designs considered were shown to be extremely complex, sensitive to errors and/or required excessively high sampling rates.

6) The method by which the coarser resolutions were generated is one of the core areas of the research. It is shown that by truncating the stored echo data set, and expanding the time axis of the reduced data set so that its duration is equal to duration of the original data set, that the spectral width of the echo has been compressed, and the return has been naturally de-resolved. It is shown to be only applicable when the echo is statistically stationary.

7) A software implementation of the return signal simulator-altimeter configuration has been developed, modelling all aspects of both the altimeter and RSS. It is capable of generating a coarser resolution, modelling a misalignment of baseband echo with RSS chirp, modelling chirp distortion in the up/downconversion, and generating an altimeter range window with a user-defined FFT length. It is used in chapter 3 to confirm that the echo in the range window was spectrally compressed according to the change in resolution, that the timing accuracy of the echo was preserved after a resolution change, and to investigate the signal to noise ratio properties of the simulated echo. In chapter 6 it is used to quantify the effect of the phase distortion on the height measurement made by an altimeter.

8) In the realisation of the RSS, the Fourier Transform is implemented as an FFT. Gain compensation parameters were derived to account for the difference. The practical aspects of the return signal simulator were examined; notably the high data rates required in order to model a representative echo duration and compensation factors for the timing of the echo, the group delay and insertion loss of the anti-alias filter and the gain of the echoes. This led to the construction of a complete prototype system capable of testing the ATTA.

A novel design capable of simulating a 16 second sequence in real time was pursued, in which a memory and control unit was designed to regulate the modulation of echo data onto a chirp. The prototype system is capable of operating at a PRF of 700 Hz. The simulator design is considerably simpler than other return signal simulators. It can handle larger and more representative echoes, and offers considerably more flexibility. For example, the bandwidth, and/or pulse length can be changed independently.

9) The measured results of the RSS suggested that it could be used to accurately generate the simulated echoes, and reproduce the timing of the echoes. The timing of the RSS echo is stable to ± 45 ps (7 mm). The fidelity of the echo shape was maintained to ± 0.025 dB for the 102.4 μs pulse length by properly compensating for the insertion loss of the anti-alias filters. The fidelity of the echo shape for the 19.2 μs pulse (which used the compensation data for the 102.4 μs pulse) was maintained to ±0.4 dB worst case. The level of the spurii in the RSS signal which contaminate the echo in the range window was determined, in a rather novel way. These were found to contribute a noise component of less than 0.04 dB to an echo spectrum.

10) The sequences of echoes that were generated to test the altimeter were also used to compare the height error characteristic of the OCOG and MFT tracking algorithms for different echo shapes. The OCOG was found to be sensitive to the echo shape, and in particular to the level of the noise in the early range bins. The MFT produced an almost linear characteristic independent of the echo shape; however it was found to produce a height bias that depended on the level of the noise floor.

11) Central to the RSS was the chirp generator. It was shown that the novel multiplier unit used in the chirp generator was theoretically able to respond to the input sweep rate. However, it was also shown that since the practical implementation of the PLL consisted of a high gain amplifier and passive filter rather than an active filter, the PLL was not in fact able to respond to the chirp sweep rates for the faster sweep rates. This was confirmed by measurements of the amplitude response of the chirp.

12) In order to complete the study of methods of pre-launch testing, some means of simulating the effect of chirp phase and amplitude errors is desirable, particularly the distortion on the transmit chain of the altimeter. The current method of phase and amplitude error analysis was shown to be suitable for specifying a tolerable sidelobe level for design purposes. However it was shown not to be suitable for estimating the effect of such errors on the parameters estimated by the altimeter. An alternative, more suitable

expression for the phase distortion profile was adopted, and it was found that an analytical expression could be derived which expressed the height bias as a function of the phase distortion coefficients. From this, a correction can be made for the altimeter bias resulting form chirp phase distortion.

13) It was noted that the effect of amplitude distortion was insignificant in the presence of a Hanning amplitude weighting function, and since a weighting function is employed in the altimeter to reduce the sidelobes of the point target response, amplitude distortion is deemed to be not as significant as phase distortion.

7.2 FURTHER INVESTIGATIONS AND APPLICATIONS

7.2.1 Further investigations

7.2.1.1 Testing the prototype altimeter

Unfortunately, time did not permit exercising the altimeter. A set of tests were defined (Sheehan[56], 1992) that would allow the altimeter to be tested. The main areas of interest are the following:

Choice of tracking algorithm

The MFT is reputed to have better performance than the OCOG for most terrain types and for most signal to noise conditions. However, the former is nonetheless affected by the level of the threshold relative to the noise floor. It would be interesting to investigate other tracking algorithms that are not so sensitive to the level of the noise floor, and ways of removing the noise floor from the range window.

Adaptive threshold setting is one way of reducing the sensitivity of the MFT algorithm to the level of the noise floor. The optimum level of the threshold could be the focus of a further study. The noise level in the range window would be estimated predominantly in the early range bins, and a threshold level could be set just above this noise level. It would also be necessary to check that the estimate of the noise level did not include signal power in the early range bins resulting from mistracking of the echo.

If the noise level could be confidently estimated, then it would be possible to eliminate it in the same way as for the SMLE. This would then result in a tracker with a linear height error characteristic.

Tracking performance

The second area of interest is in the actual tracking of the scenarios, and how closely the elevation profile from the tracking algorithm relates to that of the scenario itself. This study will reveal whether the tracked echo data will have to be retracked in order to estimate the mean elevation of the tracked surface.

The transients of the tracking loop and the effect of more agile loop constants on the resulting 'fast-delivery' elevation profile can also be studied using the RSS. This latter point is discussed in section 7.2.2.2.

7.2.1.2 Recommended hardware design changes

The maximum pulse repetition frequency of this prototype RSS was not limited by the quantity of data describing the echo shape, but rather by the slow data rates of the computer interfaces. An alternative design that would yield considerably faster interface speeds would incorporate the baseband and digital part of the RSS hardware, described in chapter 4, into a number of customised cards that slot into the RSS computer itself. The interface speeds would then be comparable to the corresponding access times for normal memory addressing. Since a single slot has 8 data registers and 8 control registers, only two slots would be required to accommodate all the functions of the RSS.

If this design change is implemented, there would be a number of significant benefits: (i) the maximum pulse repetition frequency would be well in excess of 1 kHz; (ii) the physical size of the RSS would be considerably smaller since it would be predominantly housed in the RSS computer; and (iii) the amount of interfacing would be considerably reduced since each RSS function could be assigned a memory address, thus allowing the corresponding piece of hardware to interface directly to the computer data bus.

The applicability of the RSS would be more extensive if it could be used for AGC or gain calibration. The phase noise on the clock frequency used to modulate the baseband signal onto the chirp was the main reason the RSS could not generate a reliable calibration signal. As discussed in chapter 4, the effective phase noise suppression is a function of both the the loop bandwidth and the range of the VCO, both of which depend on the uncompressed pulse length. A synthesiser with lower phase noise would result it it was designed for a particular uncompressed pulse length. Thus for a range of uncompressed pulse lengths, it may be necessary to program the loop bandwidth, and have a selectable VCO range.

7.2.2 Application of the RSS to other altimeters

7.2.2.1 Spacecraft docking radar

The satellite radar altimeter is an unique FM radar for the following reasons. Firstly, since the approximate range to the target is known and the maximum range variation is small compared to the range, it is possible to select a pulse repetition frequency that avoids any range ambiguities. Secondly, the bandwidth of the radar is unusually high (typically 320 MHz for ERS-1 altimeter (compared with typically 200 kHz for a long range surveillance radar). Thirdly, the ATTA has the unusual feature in that it is capable of changing its resolution. The RSS described in this thesis has been optimised to simulate the operation of such an altimeter, and thus there are not many ranging systems to which it can be directly applied.

One of the few ranging systems to use an adaptive resolution is a spacecraft docking radar, e.g. the CASSINI radar altimeter (Picardi et al. 1988). The tracking requirements of this type of altimeter are less severe than that of the ATTA since the altimeter ranges to approximately the same point on the surface each time. Thus only rates of change of the surface parameters due to the altimeters descent are critical. The principal differences between this type of altimeter and the ATTA are the following: (i) the return becomes progressively more beam-limited as the altimeter descends, i.e. the peak power increases and the echo becomes narrower; (ii) range ambiguities exist periodically on the descent, e.g. every 100 km for a PRF of 200 Hz; (iii) the return will be doppler shifted, and the size of the shift may vary depending on the speed of descent. An RSS, similar to that used to test the ATTA, could simulate the operation of this type of operation if the speed of descent was fed back to the RSS. It would be difficult for the RSS to model the progressive beam-limiting effect if the speed of descent is controlled by the altimeter during the simulation. However, this effect is negligible over a short distance and thus could be approximated *a priori* based on the assumption of constant speed. Range ambiguities do not present a problem because the altimeter has to lose lock temporarily for a short time as it passes over an ambiguity; the RSS has to change the reference trigger for the echo at this point. Doppler range processing is also easily simulated since it is merely a frequency shift proportional to the radial velocity of the satellite. The RSS for the ATTA also has the capability to enhance the resolution of the altimeter (either incrementally or progressively) as it approaches.

7.2.2.2 A constellation of altimeters

The feasibility of the proposal for a constellation of altimeters would benefit enormously from pre-launch testing using an RSS. An RSS would be particularly advantageous:

(i) in providing a means of inter-calibration of the altimeters,

(ii) in investigating the performance of the altimeter as a function of angle of approach over the same surface area.

A precision RSS would act as a yardstick for characterising the relative performance of the altimeters prior to launch by providing simulated echo signals to each. The RSS does not therefore have to be a pseudo-standard, as was the case for the pre-launch internal calibration in chapter 2, thus relaxing the requirements for inter-calibration. Any measured difference in the performance could be tweaked or applied later during the post-launch processing.

The tracking performance of the altimeter over the same transect of terrain as a function of angle of approach is a subject of interest that could be investigated using an RSS. Over rough terrain, we would not expect the tracking loops to be in a steady state. Thus the resolution used to track a scenario, and the resultant elevation profile are expected to differ depending on the direction of approach over the scenario. It could therefore be concluded that the altimeter should be used to merely track the terrain, and the elevation profile would be estimated during subsequent ground processing of the echoes in the range window. The present RSS will provide a forward and backward run over the simulated scenario, allowing this to be investigated for two different directions. A more sophisticated scenario description, representative of terrain in all 3 dimensions, would be required to investigate this more fully.

7.3 CONCLUSIONS

In respect of the research carried out, the following conclusions can be drawn.

The form of return signal simulation described in this thesis is the most suitable for testing an altimeter with an adaptive-resolution. The method of generating the coarser resolutions is novel, and is only valid when the statistics of the simulated return signal are stationary.

The only other method that offers similar performance, stability and adaptive operation requires the storage of N data sets for N different resolutions. The immense amount of data associated with this alternative makes an implementation infeasible.

The Poisson process is the most useful process for describing the scattering from the surface for a pulse limited altimeter.

The prototype return signal simulator displayed timing precision of ± 45 ps (7 mm). The gain of the simulated echo can be controlled to within ± 0.075 dB. This level of control is sufficient to allow the RSS to be used for AGC level calibration. The timing accuracy of the RSS signal using the laboratory setup of chapter 5 corresponded to about 20 % of a range cell, which is sufficient for simulation purposes. However this RSS can not be used for delay time calibration.

The length of the uncompressed pulse length is a limiting factor in this method of return signal simulation for both short and long pulse lengths. For short pulse lengths, the access time of the FIFO memory limits the echo duration; for long pulse lengths, the group delay of the anti-alias filters (lower cutoff frequency) is more sensitive to component tolerances, and the effective timing jitter resulting from frequency jitter before deramp is more severe for longer pulse lengths.

The digital generation of the baseband chirp is very stable, and allows the frequency and timing of the chirp to be accurately controlled.

The multiplication of the baseband chirp bandwidth to the desired RF bandwidth presented a problem. The multiplier ratio in the PLL of the upconversion unit was too high, giving rise to chirp phase errors. In future designs where increased range resolution is a requirement, it would be sensible to restrict the PLL multiplication ratio to approximately 5, and concentrate on increasing the baseband chirp bandwidth or using a more conventional multiplier approach.

The analysis of chirp phase and amplitude errors in chapter 6 showed that amplitude errors are insignificant when a Hanning weighting function is applied to the altimeter signal before the FFT. More importantly, the effect of phase errors can be quickly and easily interpreted as an equivalent height bias when the phase distortion is modelled as a power series.

The existing approach to both amplitude and phase errors is shown to be only useful for setting a specification for the tolerable sidelobe level.

The MFT tracking algorithm was shown to have a more linear height error characteristic than the OCOG tracking algorithm. The slope of the characteristic in the MFT algorithm is always unity; however the characteristic is offset from the origin by an amount that is threshold-dependent. A method of eliminating the noise floor from the range window is therefore desirable.

The measures defined in chapter 2 are sufficient to allow a preliminary assessment of the altimeter performance. It is only after testing that we will be able to define other (possibly more appropriate) measures of performance.

References

1 Andrewartha, R., Durrant, R., Griffiths, H.D., Wingham, D.J., Cudlip, W., Guzkowska, M., Rapley, C.G., Ridley, J., Bradford, J., Powell, R.J., Sohtell, P., 1988, 'An Adaptive Terrain-Tracking Altimeter'; Proc. *IGARSS'88 Symposium* Edinburgh, 1988, ESA SP-284, September 1989 (ESA Technical and Publications Branch, ESTEC, Postbus 299, 2200 AG Noordwijk, Netherlands).

2 Barrick, D.E., 'Relationship between Slope Probability Density Function and the Physical Optics Integral in Rough Surface Scattering'; Proc. *IEEE*, pp. 1728, 1968.

3 Bean, B.R. and Dutton, E.J.; Radio Meteorology, National Bureau of Standards Monograph, 1966.

4 Beckmann, P. and Spizzichino, A., 'Scattering of Electromagnetic Waves from Rough Surfaces'; Pergamon Press, New York, 1964.

5 Berry, M.V., 'Statistical Properties of Echoes'; Philosophical Transactions of the Royal Society, 1973.

6 Brooks, L.W. and Dooley, P.R., 'Technical Guidance and Analytical Services in support of SEASAT-A.'; Final report No. TSC-W3-20. Technical Service Corporation, NASA CR-141399, April 1975.

7 Brown, G.S., 'The average impulse response of a rough surface and its applications'; *IEEE Trans. Antennas Propag.*, 25, pp. 67-74, 1977.

8 Brown, R.D., Kahn, W.D., McAdoo, D.C. and Himwich, W.E., 'Roughness of the Marine Geoid from SEASAT altimetry'; *J. Geophysical Research*, Vol. 88, No. C3, pp. 1531 - 1540, February 1983.

9 Challenor, P. and Srokosz, M., 'Wave Studies with the Radar Altimeter'; Int. J. of Remote Sensing, Vol. 12, No. 8, pp. 1671 - 1686, August 1990.

10 Chase, R. and Mundt, M., 'Optimised Orbits for the Constellation of Space Station Polar Platforms'; *Proceedings of the 12th annual American Astronautical Society Guidance and Control Conference*, AAS Publications, San Diego, 1989.

11 Cudlip, W., Mantripp, D., Wrench, C.L., Griffiths, H.D., Sheehan, D.V., Lester, M., Leigh, R.P. and Robinson, T.R., 'Corrections for Altimeter Low-Level Processing at the Earth Observation Data Centre'; *Int. J. Remote Sensing* In press, 1992.

12 Dallas, J.L., Czechanski, J.P., Coyle, D.B., Zukowski, B.J. and Seery, B.D., 'Geodynamic Laser Ranging System Laser Transmitter'; *Proc. IGARSS'91*, Helsinki, Finland, CH2971-0/91/0000-0571$01-00, 2-6 June, 1991.

13 Durrant, R.J. and Richards, B., 'Technology Issues for Advanced Radar Altimetry'; *ESA Imaging Altimeter Consultative meeting*, MSSL/UCL London, 1990.

14 Fante, R.L., 'Signal Analysis and Estimation: an introduction'; p. 183, Wiley, 1988.

15 Franchin, G., Marcelli, A. and Maranta, P., 'Design and Development of the Waveform Generator IF/RF subsystem, Phase 1 - Final report'; contract no FV50274, 1989.

16 Francis, C.R., 'Radar Altimeter Calibration'; *Proc. EARSel Radar Calibration Workshop*, Alpbach, Austria, ESA SP-193 pp. 69-79, 6-10 December 1982.

17 Francis, C.R. et al, 'Radar Altimeter Test and Calibration Study, final report'; ESA contract report ESS/SS 1077, 1982.

18 Francis, C.R., 'The ERS-1 radar altimeter - an overview'; *Proceedings of a Workshop on ERS-1 Radar Altimeter Data Products*, Frascati, Italy, ESA SP-221, pp. 9-16, 8-11 May, 1984.

19 Francis, C.R. and Duesmann, B., 'ERS-1 Altimeter Calibration - A European Plan'; ESTEC document number ER-TN-ESA-RA-0003, 1987.

20 Francis, C.R. and Duesmann, B., 'ERS-1 Altimeter Height Calibration'; *Proc. IGARSS '88 Symposium*, Edinburgh, Scotland ESA SP-284, pp. 877-880, 13-16 September, 1988.

21 Gardner, F.M., 'Phaselock techniques', 2nd edition, Wiley, 1979.

22 Goldhirsh, J. and Rowland, J.R., 'A Tutorial Assessment of Atmospheric Height Uncertainities for High-Precision Satellite Altimeter Missions to monitor Ocean Currents'; *IEEE Trans. on Geoscience and Remote Sensing*, vol. GE-20, no.4, pp. 418-433, 1982.

23 Gradshteyn, I.S. and Ryzhik, I.M., 'Table of Integrals, Series, and Products'; Academic Press, London, 1980.

24 Griffiths, H.D., Milne, K., Rapley, C.G. and Wingham, D.J., 'A Study of Antenna Signal Processing Techniques for Radar Altimeters'; *ESA Contract Report 6001/84/NL/GM*, 1985.

25 Griffiths, H.D., Wingham, D.J., Challenor, P.G., Guymer, T.H. and Srokosz, M.A. 'A study of mode switching and fast-delivery product algorithms for the ERS-1 altimeter', *ESA contract report 6375/85/NL/BI*, 1987.

26 Griffiths, H.D., 'Phase and Amplitude Errors in FM radars'; Colloque international sur le radar, Paris, pp103-106, April 1989.

27 Griffiths, H.D. and Bradford W.J., 'Digital Generation of High Time Bandwidth Product Linear FM waveforms for radar altimeters'; Proc. IEE, Part F, Vol. 139, No. 2, pp. 160 - 169, April 1992.

28 Hayne, G.S., 'Radar Altimeter Mean Return Waveforms from Near-Normal-Incidence Ocean Surface Scattering'; *IEEE Trans. Antennas and Propag.*, vol. 28 no. 5, pp. 687-692, September, 1980.

29 Kuala, W.M., 'The Terrestrial Environment: Solid Earth and Ocean Physics'; report of a study at Williamstown, Mass., NASA CR-1579, April, 1969.

30 Levrini, G., Rubertone, F.S. and Rühe, W., 'The ERS-1 radar altimeter instrument'; *Proc. of a workshop on ERS-1 Radar Altimeter Data Products*, Frascati, Italy, ESA SP-221, 8-11 May, 1984.

31 Levrini, G., 'A study of the Performance of various tracking algorithms for a space radar altimeter'; Final report, ALT/SES/FR/002/90, December, 1990.

32 Lorrell, J., Colquitt, E. and Anderle, R.J., 'Ionospheric Correction for SEASAT Altimeter Height Measurement'; *J. Geophys. Res.*, 87, C5, pp. 3207-3212, 1982.

33 Manabe, S. and Stouffer, R.J., 'Sensitivity of a Global Climate Model to an increase of CO_2 Concentration in the Atmosphere'; *J. Geophys. Res.*, 85, C10, pp. 5529-5554, October 20, 1980.

34 MacArthur, J.L., 'Design of the Seasat-A Radar Altimeter'; *Oceans'76 Conference*, pp. 10B-1 to 10B-8, 1976.

35 MacArthur, J.L., 'SEASAT-A Radar Altimeter Design Description'; The John Hopkins University, report no. SDO-5232, Nov. 1978.

36 McGoogan, J.T., Miller, L.S., Brown, G.S., Hayne, G.S., 'The S-193 Radar Altimeter Experiment'; *Proc. IEEE*, vol-62, no.6, June, 1974.

37 McGoogan, J.T., 'Satellite Altimetry Applications'; *IEEE Trans. MTT-23*, pp. 970-978, 1974.

38 Moore, R.K. and Williams, C.S, 'Radar Terrain Return at Near-Vertical Incidence'; *Proc. IRE.*, Feb., pp. 228-239, 1957.

39 Papoulis, A., 'Probability, Random variables and Stochastic processes'; McGraw-Hill, 1965.

40 Parkes, S., Durrant, R. and Perry, J., 'BAe Systolic Digital Chirp Generator User Guide'; BAE/TS/SMP/BATS-1, 1991.

41 Picardi, G., Dai, C., Seu, R. and Coradini, A., 'Multimode Radar Altimeter (MRA)'; *IGARSS'88*, ESA SP-284, Vol 2, pp. 993 - 994, September 1988.

42 Quate, C.F. and Thompson, R.B., 'Convolution and Correlation in Real Time with Non-Linear Acoustics'; *Appl. Phys. Letters*, Vol. 16, p. 494, 1970.

43 Rapley, C.G., Griffiths, H.D., Squire, V.A., Lefebvre, M., Birks, A.R., Brenner, A.C. and 17 co-authors, 'A Study of Satellite Radar Altimeter Operation over Ice Covered Surfaces'; ESA Contract Report 5182/82/F/CG(SC), 1983.

44 Rapley, C.G. et al., 'Applications and Scientific Uses of ERS-1 Radar Altimeter Data', ESA Contract Report 5684/83/NL/BI, 1985.

45 Rapley, C.G., Guzkowska, M.A.J., Cudlip, W. amd Mason, I.M., 'An exploratory study of inland water and land altimetry using Seasat data'; European Space Agency, ESTEC Contract Report: 6483/85/NL/BI, 1987.

46 Rapley, C.G., Griffiths, H.D. and Berry, P.A.M., 'Proceedings of the Consultative Meeting on Imaging Altimeter Requirements and Techniques'; ESA Reference MSSL/RSG/90.01, 1990.

47 Rapp, R.H., 'The Determination of the Geoid Undulations and Gravity Anomolies from SEASAT Altimeter Data'; *J. Geophysical Research*, Vol. 88, No. C3, pp. 1552 - 1562, February 1983.

48 Ridley, J.K., 'Topography and Altimeter Tracking'; *ESA Imaging Altimeter Consultative meeting*, MSSL/UCL London, 31 May 1990.

49 Robinson, I. S., 'Satellite Oceanography'; Wiley, Chichester, 1985.

50 Rodriguez, E., 'Altimetry for Non-Gaussian Oceans: Height Biases and Estimation of Parameters'; *J. Geophys. Res.*, 93C, pp. 14107-14119, 1988.

51 Sheehan, D.V., Griffiths, H.D. and Wingham, D.J., A Return Signal Simulator for the Adaptive Terrain-Tracking Altimeter'; *Proc. IGARSS'91*, Helsinki, Finland, CH2971-0/91/0000-0591$01-00, 2-6 June, 1991.

52 Sheehan, D.V. and Griffiths, H.D., 'The Effect of Pulse Distortion on the Height Estimation of a Radar Altimeter'; *Int. J. Remote Sensing*, Vol. 13, No. 17, pp. 3303-3310, 1992.

53 Sheehan, D.V., 'The RSS Hardware Documentation: version 6.0'; UCL document, December 1992.

54 Sheehan, D.V., 'The RSS Control Software Documentation: version 6.0'; UCL document, December 1992.

55 Sheehan, D.V., 'The RSS Acceptance Test Procedures: version 6.0'; UCL document, October 1992.

56 Sheehan, D.V., 'The System Tests for the Altimeter: version 6.0'; UCL document, October 1992.

57 Somma, R. et al,. 'Radar Altimeter Phase A Study: Final Report', ESA Contract Report 4428/80/F/DD/SC, April 1981.

58 Somma, R. et al,. 'Radar Altimeter Technical Description', *Selenia Spazio Report no. ER-TN-SEL-RA-0018*, 1982.

59 Srokosz, M.A., 'On the Joint Distribution of Surface and Slopes for a Non-Linear Random Sea, with Applications to Radar Altimetry'; *J. Geophys. Res.*, Vol. 91C, pp. 995-1006, 1986.

60 Stanley, H.R., 'The GEOS-3 Project'; *J. Geophys. Res.*, Vol. 84, No. B8, pp. 3779-3783, July 1979.

61 Thomas, R.H., Martin, T.V. and Zwally, J.H., Annals of Glaciology, 4, 1983.

62 Townsend, W.T., 'An Initial Assessment of the Performane Achieved by the SEASAT-1 Radar Altimeter'; *IEEE J. Oceanic Engineering*, vol. OE-5, no. 2, pp. 80 - 92, April 1980.

63 Ulaby, F.T., Moore, R.K. and Fung, A.K., 'Microwave Remote Sensing'; vol.2, Addison-Wesley, 1982.

64 Ulaby, F.T., Moore, R.K. and Fung, A.K., 'Microwave Remote Sensing'; vol.3, Addison-Wesley, 1982.

65 Vass, P. and Handoll, M., 'UK ERS-1 Reference Manual', Document no. *DC-MA-EOS-ED-0001*, Printing department, Royal Aerospace Establishment, Farnborough, January, 1991,

66 Walsh, E.J., 'Analysis of NRL radar altimeter data'; *Radio Science,* vol. 9, no. 8, 9 pp. 711-722, August - September 1974.

67 Walsh, E.J., 'Pulse-to-Pulse Correlation in Ssatellite Radar Altimeters'; *Radio Science,* vol. 17, no. 4, pp. 786-800, July - August 1982.

68 Wingham, D.J., 'An Automatic Tracking Mode Switching Algorithm for the ERS-1 Altimeter'; *Proc. IGARSS'86*, Zurich, Ref. ESA SP-254, 8-11 September 1986.

69 Wingham, D.J. et al., 'Proposal for Advanced Altimeter Breadboard and Testing'; A0/1-1947/NL/JG, 1987

70 Wingham D.J., 1990, 'Acquisition and Tracking Study', Work Package 2230 report. Doc. no. UCLEE/RA-PHASE A/002

71 Wingham, D.J. and Laxon, S.W., 'WP100: Scenario definition'; part of Levrini et al.,'A Study of the Performance of Various Tracking Algorithms for a Space Radar Altimeter'; ALT/SES/FR/002/90, Dec. 1990.

72 Wingham, D.J. and Rapley, C.G., 'Saturation Effects in the SEASAT Altimeter Receiver'; *Int. J. Remote Sensing*, Vol. 8, no. 8, pp. 1163-1173, 1987.

73 Wingham, D.J. and Rapley, C.G., 'A new approach to topographic altimetry'; *Proc. IGARSS'88 Symposium*, Edinburgh, ESA SP-284, Sept. 13-16, 1988.

74 Wrench, C.L., 'Altimeter Tropospheric Refraction Corrections'; *UK-ERS Data Centre Product Support Team Report*, DC-RP-PST-PC-0001, 1986.

75 Yaplee, B.S., Shapiro, A., Uliano, E.A., Hammond, D.L., and Craig, K.L., 'Experiment Verification of the Proposed SKYLAB Alitmeter Measurement'; paper presented at the 15th Plenary Meeting of COSPOR, Madrid, May 1972.

76 Zwally, H.J., Bindschadler, R.A., Brenner, A.C., Martin, T.V. and Thomas, R.H., 'Surface elevation contours of Greenland and Antartic ice sheets'; *J. Geophys. Res.*, 88C, pp. 1589-1596, 1983.

Appendix 1

Mathematical description of the altimeter

A.1.1 Timing of the echo and formation of the range window

The transmit chirp is defined by a linear frequency modulation and is given by:

$$\cos\left(\omega_o t + \pi b\, t^2\right) \qquad \text{(A.1-1)}$$

The return from a point target at a time t_i is:

$$\cos\left(\omega_o(t - t_i) + \pi b\,(t - t_i)^2\right) \qquad \text{(A.1-2)}$$

The altimeter triggers a deramp chirp at a time t_h, where t_h has been extracted from the tracking loop:

$$\cos\left(\omega_o(t - t_h) + \pi b\,(t - t_h)^2\right) \qquad \text{(A.1-3)}$$

The signals defined by (A.1-2) and (A.1-3) form the two inputs of a single sideband mixer. The lower sideband of the mixed signal is selected and given as:

$$\frac{1}{2}\cos\left(\omega_o(t_h - t_i) + \pi b\left(t_i^2 - t_h^2\right) + 2\pi b t(t_h - t_i)\right) \qquad \text{(A.1-4)}$$

This represents a tone whose frequency is proportional to the time difference between the reflected chirp and the deramp chirp. This frequency is therefore a measure of the extent to which the return is mis-tracked. The quadrature component of this baseband signal is:

$$\frac{1}{2}\sin\left(\omega_o(t_h - t_i) + \pi b\left(t_i^2 - t_h^2\right) + 2\pi b t(t_h - t_i)\right) \qquad \text{(A.1-5)}$$

These baseband signals are digitised and processed in a Fast Fourier Transform. Rather than using the FFT at this stage, it is more convenient to use the FT of the complex signal defined by eqn.'s A.1-4 and A.1-5. Let the constant phase term be:

$$\phi_o = \omega_o(t_h - t_i) + \pi b\left(t_i^2 - t_h^2\right). \qquad \text{(A.1-6)}$$

The output of the FT is given by:

$$\frac{1}{2}\int_{o}^{T} \exp\left[j\left(2\pi b\, t\,(t_h - t_i) - \omega t + \phi_o\right)\right] dt \qquad \text{(A.1-7)}$$

Evaluating (A.1-7) gives:

$$\exp\left[j\left(\phi_o + (2\pi b(t_h - t_i) - \omega)\frac{T}{2}\right)\right] T \frac{\sin\left((2\pi b(t_h - t_i) - \omega)\frac{T}{2}\right)}{(2\pi b(t_h - t_i) - \omega)\frac{T}{2}} \qquad \text{(A.1-8)}$$

The power spectrum is the squared modulus of eqn. A.1-8 and is given by:

$$P(\omega) = \left[T \frac{\sin\left((2\pi b(t_h - t_i) - \omega)\frac{T}{2}\right)}{(2\pi b(t_h - t_i) - \omega)\frac{T}{2}} \right]^2 \qquad \text{(A.1-9)}$$

This is the response of the altimeter to a point target response, and thus is known as the impulse response of the altimeter. It can be rewritten as

$$P(\omega) = \left[T \frac{\sin\left(\omega\frac{T}{2}\right)}{\omega\frac{T}{2}} \right]^2 \otimes d(\omega) \qquad \text{(A.1-10)}$$

where:

$$d(\omega) = \delta(\omega - 2\pi b(t_h - t_h)) \qquad \text{(A.1-11)}$$

is the impulse response of the target defined in (3.1-3), mapped into the frequency space of the altimeter. The width of this function defines the frequency resolution of the altimeter.

A.1.2 Processing the simulated echo in the altimeter

The simulated echo for a given resolution is given by (3.1-19):

$$g(t) = \left[I(t)\cos\left(\omega_o(t - t_r) + \pi b(t - t_r)^2\right) + Q(t)\sin\left(\omega_o(t - t_r) + \pi b(t - t_r)^2\right)\right] \qquad \text{(A.1-12)}$$

where t_r be the time of the RSS chirp with respect to the transmit chirp. If this is mixed with the deramp chirp given by (A.1-3), the baseband signals in the altimeter are given by:

$$I_a(t) = \frac{1}{2}\left\{I(t)\cos\left(\phi_o + 2\pi bt(t_h - t_r)\right) + Q(t)\sin\left(\phi_o + 2\pi bt(t_h - t_r)\right)\right\} \quad \text{(A.1-13a)}$$

$$Q_a(t) = \frac{1}{2}\left\{-I(t)\sin\left(\phi_o + 2\pi bt(t_h - t_r)\right) + Q(t)\cos\left(\phi_o + 2\pi bt(t_h - t_r)\right)\right\} \quad \text{(A.1-13b)}$$

where $\phi_o = \omega_o(t_h - t_r) + \pi b\left(t_r^2 - t_h^2\right)$ (A.1-14)

The Fourier Transform of the altimeter baseband signal is given as:

$$\int_o^T [I_a(t) + jQ_a(t)]\, e^{-j\omega t}\, dt \quad \text{(A.1-15)}$$

Substituting (A.1-13a) and (A.1-13b) into (A.1-15) gives:

$$\frac{1}{2}\int_o^T [I(t) + jQ(t)]\,[U(t) - U(t - T)]\, e^{-j\left(\phi_o + 2\pi b(t_h - t_r)\right)}\, e^{-j\omega t}\, dt \quad \text{(A.1-16)}$$

Note that $F(t) = I(t) + jQ(t)$; thus (A.1-16) represents a frequency shifted version of the simulated echo spectrum. The detected power spectrum is then given by:

$$P(\omega) = \left| f(\omega - 2\pi b(t_h - t_r)) \otimes T\,\frac{\sin(\omega T/2)}{\omega T/2} \right|^2 \quad \text{(A.1-17)}$$

This illustrates that the echo spectrum in the altimeter is merely shifted in frequency by an amount proportional to the time difference between the RSS chirp and the deramp chirp. Figure 3.1-7 shows how the simulated echo spectrum is shifted in frequency as it is tracked in the altimeter. It should be apparent in the derivation of (A.1-17) that the timing t_r of the RSS chirp was critical in providing the timing. However, the spectrum f(w) of the echo is equally critical in defining the timing since the tracking point is made to the half power point of the leading edge of the power spectrum. If $t_r = t_h$:

$$P(\omega) = \left| f(\omega) \otimes T\,\frac{\sin(\omega T/2)}{\omega T/2} \right|^2 \quad \text{(A.1-18)}$$

This expression is used in (3.2-3).

A.1.3 The power spectrum of an echo at a coarser resolution

For a coarser resolution, i.e. $\eta < 1$, the baseband signal in the altimeter is a truncated form of the simulated baseband signal for the finest resolution. Consider the case of no tracking error. Thus:

$$I_a(t) + jQ_a(t) = [I(\eta t) + jQ(\eta t)]\,[U(t)U(T - t)] \qquad \text{(A.1-19)}$$

The power spectrum is formed by first Fourier Transforming, and then squaring:

$$P(\omega) = \left| b(\omega) \otimes T\,\frac{\sin(\omega T/2)}{\omega T/2} \right|^2 \qquad \text{(A.1-20)}$$

where

$$b(\omega) = \int_0^T [I(\eta t) + jQ(\eta t)][U(t)U(T - t)]\, e^{-j\omega t}\, dt \qquad \text{(A.1-21)}$$

The power spectra of (A.1-19) and (A.1-20) are both filtered by the anti-alias filters of the altimeter, which has a fixed bandwidth.

A.1.4 Model of the Software Simulator

The following equations have been used in the software model of the echo simulator. The mathematical model of the altimeter is the same as that described in §A.1.1.

Echo characteristics

The Rayleigh amplitude distribution is defined as:

$$P(x) = \frac{1}{\sqrt{2\pi}\sigma_x}\, e^{\left(-\frac{x^2}{2\sigma_x^2}\right)} \qquad \text{(A.1-22)}$$

Thus if σ_x is the mean amplitude, then x is a random variable drawn from this distribution. The uniform phase distribution is defined as:

$$P(\phi) = 1 \qquad \text{(A.1-23)}$$

Upconversion/downconversion

The upconversion/downconversion is modelled by (A.1-13a) and (A.1-13b) which relate the baseband signals in the altimeter to the simulated baseband signals. These can be rewritten as:

$$\begin{pmatrix} I_a(t) \\ Q_a(t) \end{pmatrix} = \frac{1}{2} \begin{pmatrix} \cos(\phi_o + 2\pi b(t_h - t_r)) & \cos(\phi_o + 2\pi b(t_h - t_r)) \\ -\sin(\phi_o + 2\pi b(t_h - t_r)) & \sin(\phi_o + 2\pi b(t_h - t_r)) \end{pmatrix} \begin{pmatrix} I(t) \\ Q(t) \end{pmatrix} \quad \text{(A.1-24)}$$

This can be more simply written as:

$$I_a(t) + jQ_a(t) = \frac{1}{2}\{I(t) + jQ(t)\}\, e^{-j(\phi_o + 2\pi b(t_h - t_r))} \quad \text{(A.1-25)}$$

where $t_h - t_r$ is the time difference between the RSS chirp and the deramp chirp. Any distortion introduced by the chirp will modify the signal in the altimeter as follows:

$$I_a(t) + jQ_a(t) = \frac{A_d(t)}{2}\{I(t) + jQ(t)\}\, e^{-j\phi((t))} \quad \text{(A.1-26)}$$

where $A_d(t)$ is the distorted amplitude profile of the chirp, and $\phi(t)$ is the phase distortion profile of the chirp. This equation is used extensively in the simulations in chapter 6.

A.1.5 Model for imperfect single side band modulation

Consider a single sideband modulator with an amplitude imbalance k between the two arms of the modulator, and a carrier leakage of k_c. The resultant signal is given as:

$$g(t) = \cos(\omega_o t + \pi bt^2)\cos(\omega_1 t) + k\sin(\omega_o t + \pi bt^2)\sin(\omega_1 t) + k_c \cos(\omega_o t + \pi bt^2 + \phi_o) \quad \text{(A.1-27)}$$

This can be expanded as:

$$\begin{aligned} g(t) = {} & \frac{1}{2}\{\cos((\omega_o - \omega_1)t + \pi bt^2) + \cos((\omega_o + \omega_1)t + \pi bt^2)\} \\ & + \frac{k}{2}\{\cos((\omega_o - \omega_1)t + \pi bt^2) - \cos((\omega_o + \omega_1)t + \pi bt^2)\} \\ & + k_c \cos(\omega_o t + \pi bt^2 + \phi_o) \end{aligned} \quad \text{(A.1-28)}$$

The lower sideband has amplitude (1 + k)/2; the upper sideband has amplitude (1 - k)/2, and the carrier breakthrough is k_c. Thus the unwanted (upper) sideband suppression is:

$$S_u = \left(\frac{1-k}{1+k}\right)^2 \qquad \text{(A.1-29)}$$

The carrier suppression is:

$$S_c = \left(\frac{2k_c}{1+k}\right)^2 \qquad \text{(A.1-30)}$$

Consider the simulated echo:

$$\begin{aligned} g(t) = {} & \cos\left(\omega_o(t-t_r) + \pi b(t-t_r)^2\right)I(t) + k\,\sin\left(\omega_o(t-t_r) + \pi b(t-t_r)^2\right)Q(t) \\ & + k_c \cos\left(\omega_o(t-t_r) + \pi b(t-t_r)^2 + \phi_o\right) \end{aligned} \qquad \text{(A.1-31)}$$

Consider initially the sideband components. The effect of the carrier component will be analysed later. Eqn. (A.1-31) can then be rewritten as:

$$\begin{aligned} g(t) = {} & k\left\{\cos\left(\omega_o(t-t_r) + \pi b(t-t_r)^2\right)I(t) + \sin\left(\omega_o(t-t_r) + \pi b(t-t_r)^2\right)Q(t)\right\} \\ & +(1-k)\cos\left(\omega_o(t-t_r) + \pi b(t-t_r)^2\right)I(t) \end{aligned} \qquad \text{(A.1-32)}$$

The first term in (A.1-32), after being deramped in the altimeter, turns out to be the same as (A.1-6) but weighted by a factor k. That is:

$$\frac{k}{2}\int_o^T [I(t) + jQ(t)]\,[U(t) - U(t-T)]\,e^{-j\left(\phi_o + 2\pi b(t_h - t_r)\right)}\,e^{-j\omega t}\,dt \qquad \text{(A.1-33)}$$

Consider the second term. Using the definitions for I(t) from (3.1-12), this error term can be evaluated as:

$$e(t) = (1-k)\cos\left(\omega_o(t-t_r) + \pi b(t-t_r)^2\right)\int_{t_1-t_r}^{t_N-t_r} d(s+t_r)\cos B(t,s) \qquad \text{(A.1-34)}$$

which is equal to:

$$e(t) = \frac{(1-k)}{2}\int_{t_1-t_r}^{t_N-t_r} d(s+t_r)\left\{\begin{array}{l}\cos\left[\omega_o(t-t_r) + \pi b(t-t_r)^2 - B(t,s)\right] \\ +\cos\left[\omega_o(t-t_r) + \pi b(t-t_r)^2 + B(t,s)\right]\end{array}\right\}ds \qquad \text{(A.1-35)}$$

When this is deramped by the chirp given by (A.1-3) and the double frequency terms are

neglected (since in practice they are filtered out), the in-phase term of the error in the altimeter is given by:

$$e_I(t) = \frac{(1-k)}{4}\int_{t_1-t_r}^{t_N-t_r} d(s+t_r)\left\{\begin{array}{l}\cos\left[\phi_o + 2\pi b(t_h-t_r)t - B(t,s)\right] \\ +\cos\left[\phi_o + 2\pi b(t_h-t_r)t + B(t,s)\right]\end{array}\right\}ds \qquad \text{(A.1-36)}$$

where ϕ_o is defined in (A.1-14). The quadrature term of the error is therefore given as:

$$e_Q(t) = -\frac{(1-k)}{4}\int_{t_1-t_r}^{t_N-t_r} d(s+t_r)\left\{\begin{array}{l}\sin\left[\phi_o + 2\pi b(t_h-t_r)t - B(t,s)\right] \\ +\sin\left[\phi_o + 2\pi b(t_h-t_r)t + B(t,s)\right]\end{array}\right\}ds \qquad \text{(A.1-37)}$$

Thus:

$$e(t) = \frac{(1-k)}{4}\int_{t_1-t_r}^{t_N-t_r} d(s+t_r)\left\{\begin{array}{l}e^{jB(t,s)}e^{-j(\phi_o + 2\pi b(t_h-t_r))} \\ +e^{-jB(t,s)}e^{-j(\phi_o + 2\pi b(t_h-t_r))}\end{array}\right\}ds \qquad \text{(A.1-38)}$$

From (3.1-12) and (3.1-13), this error term can be expressed in terms of the RSS baseband signals, as follows:

$$e(t) = \frac{(1-k)}{2}\frac{1}{2}\left\{[I(t)+jQ(t)]e^{-j(\phi_o + 2\pi b(t_h-t_r))} + [I(t)-jQ(t)]e^{-j(\phi_o + 2\pi b(t_h-t_r))}\right\} \text{(A.1-39)}$$

When this signal is added to the first term given in (A.1-33), the signal plus unwanted sideband is given by:

$$F_a(t) = \frac{(1+k)}{2}\frac{1}{2}\left\{[I(t)+jQ(t)]e^{-j(\phi_o + 2\pi b(t_h-t_r))}\right\} + \frac{(1-k)}{2}\frac{1}{2}\left\{[I(t)-jQ(t)]e^{-j(\phi_o + 2\pi b(t_h-t_r))}\right\} \qquad \text{(A.1-40)}$$

Eqn. (A.1-7) allows the first term of (A.1-40), i.e. the power of the wanted component, to be expressed as:

$$\left(\frac{1+k}{2}\right)^2 P(\omega) = \left(\frac{1+k}{2}\right)^2 \left| f(\omega - 2\pi b(t_h - t_r)) \otimes T\frac{\sin(\omega T/2)}{\omega T/2}\right|^2 \qquad \text{(A.1-41)}$$

The power of the unwanted sideband is therefore:

$$\left(\frac{1-k}{2}\right)^2 P(-\omega) = \left(\frac{1-k}{2}\right)^2 \left| f(-\omega - 2\pi b(t_h - t_r)) \otimes T\frac{\sin(\omega T/2)}{\omega T/2}\right|^2 \qquad \text{(A.1-42)}$$

The unwanted component is manifested as an inversion of the echo spectrum in the range window. The suppression of the unwanted component is defined as:

$$S_u = \left(\frac{1+k}{1-k}\right)^2 \frac{P(\omega)}{P(-\omega)} \qquad \text{(A.1-43)}$$

The effect of carrier breakthrough is easier to analyse. After the carrier component has been deramped in the altimeter, as in section A.1.1, the effect is to add power to a single range bin. The proportion of power added is given by the carrier suppression S_c in (A.1-30).

Appendix 2

Effect of windowing a sampled data set

This appendix derives the relation between the continuous signal and the discrete signal used in the FFT. A similar proof is available in most digital signal processing text books.

The sampled version of the echo spectrum f(ω) is:

$$\tilde{f}(\omega) = f(\omega) \sum_{m=-\infty}^{\infty} \delta\left(\omega - \frac{2\pi m}{T}\right) \qquad \text{(A.2-1)}$$

where T is the chirp length, δ is the Dirac function. The function f(ω) is given by:

$$f(\omega) = \sum_{n=0}^{N-1} F(nT_s)\, e^{-j2\pi f T_s n} \qquad \text{(A.2-2)}$$

Take the inverse Fourier Transform by multiplying both sides of (A.2-1) by $e^{(j2\pi ft)}$ and integrating on f from -∞ to ∞. So:

$$\tilde{F}(t) = \sum_{n=0}^{N-1} F(nT_s) \quad \times \quad \sum_{m=-\infty}^{\infty} \int_{-\infty}^{\infty} df \delta\left(f - \frac{2\pi m}{T}\right) e^{j2\pi f(t - nT_s)} \qquad \text{(A.2-3)}$$

This can be rewritten as:

$$\tilde{F}(t) = \sum_{n=0}^{N-1} F(nT_s) \quad \times \quad \sum_{m=-\infty}^{\infty} e^{j2\pi m(t - nT_s)/T} \qquad \text{(A.2-4)}$$

Using the following expression (Fante, 1988):

$$\sum_{n=-\infty}^{\infty} \delta\left(f - \frac{n}{T}\right) = T \sum_{n=-\infty}^{\infty} e^{j2\pi nfT} \qquad \text{(A.2-5)}$$

enables us to express (A.2-4) as:

$$\tilde{F}(t) = T \sum_{p=-\infty}^{\infty} \left[\sum_{n=0}^{N-1} F(nT_s)\, \delta(t - nT_s - pT) \right] \qquad \text{(A.2-6)}$$

This represents a function that samples F(t) at samples t = 0, T_s, $2T_s$, ... $(N-1)T_s$, and then repeats periodically outside this interval. This equation is particularly useful for analysing the effect of different windowing intervals T. For example if F(t) contains a periodic component of period T_o, then erroneous results will be obtained unless the windowing function is an integral multiple of the signal period T_o.

Appendix 3

Operation of the chirp generator in the RSS

This appendix describes the programming and operation of the digital chirp generator when used in conjunction with the RSS. §A.3.1 defines all the modes of operation and defines how the timing and resolution programming of the chirp is carried out. §A.3.2 describes a modification to the program that accounts for the different group delay of the anti-alias filter with resolution.

A.3.1 No compensation for the group delay variation of the filter

The chirp generator operates in either a ramp/timer mode or a timer mode. In the ramp/timer mode, the chirp generator is programmed to ramp towards a specified final frequency with a specified ramp rate. The duration of the chirp is then indirectly determined by the frequency sweep and the ramp rate. In the ramp/timer mode, a counter is also pre-loaded to correspond to a particular time delay. After the counter has decremented to zero, the next command is executed. The timer mode is the same as the timer part of the ramp/timer mode. Both modes can be synchronised to an external trigger pulse or can be set to free run, i.e. the instruction can be delayed to commence only on detection of the trigger, or it can take place as soon as the timer from the previous instruction has decremented to zero.

The digital chirp generator is programmed by 10 bytes of data. Three bytes define the ramp rate to 24 bit precision. Another three bytes define the final frequency to 24 bit precision. Three more bytes define the 24-bit time word, and the last byte define the command, i.e. whether it is ramp/timer or timer, and whether it is synchronised or not.

The ramp/timer mode is the only mode used in the RSS. Figure A.3-1 shows the sequence of ramp/timer (sync) and ramp/timer commands required to generate all the timing and resolution information of the RSS chirp. The first command is synchronised to the trigger pulse used to mark the start of a pulse repetition interval. The final frequency of the first ramp/timer command defines the start frequency for the second chirp, i.e the RSS chirp.

The timing information of the first command defines the instant at which the second chirp is generated. Thus all the timing information for the RSS chirp is contained in the command for the first chirp. This is known as the recovery chirp since the start frequency of the RSS chirp is recovered in this way. The final frequency of the second ramp/timer command defines the bandwidth of the RSS chirp. The ramp rate determines the resolution used. The only requirement on the timing information of the second command is that it is greater than the chirp duration. The whole sequence is repeated for the next PRI.

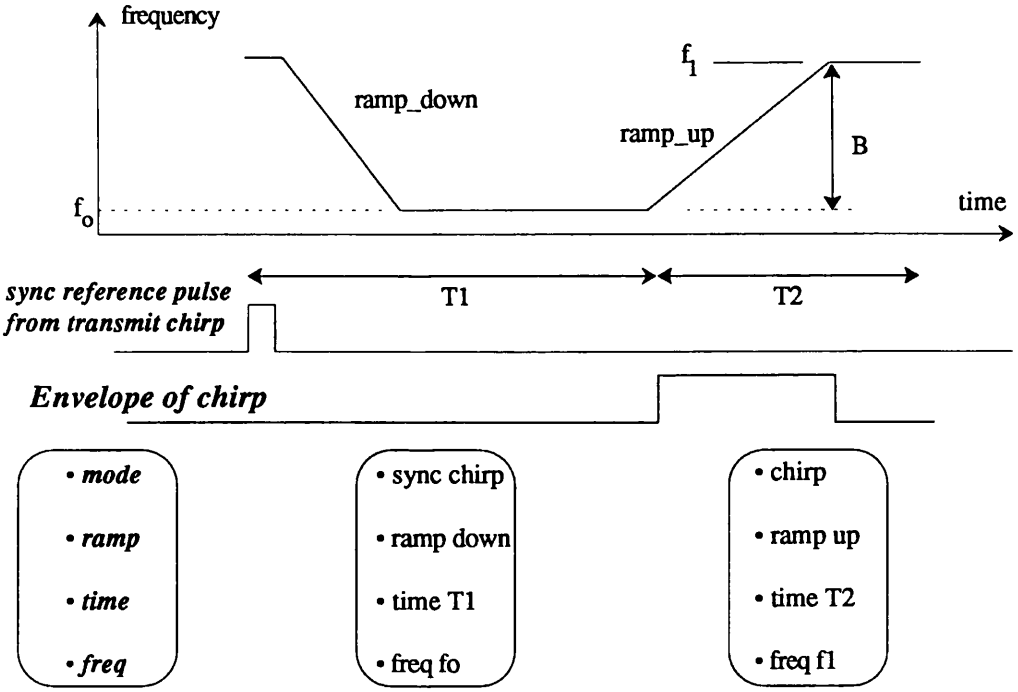

Figure A.3-1. The programming of the chirp generator.

The timing and frequency precision is referred to the reference 40 MHz altimeter clock f_{clk}, which is fed to the chirp generator. The frequency precision (24-bit) of the chirp generator is defined as:

$$\Delta f_{res} = \frac{f_{clk}}{2^{24}} \qquad \text{(A.3-1)}$$

which equals 2.384186 Hz at baseband. The ramp rate precision is defined as:

$$\Delta f_{res} = \frac{f_{clk} f_{clk}}{2^{24}}. \qquad \text{(A.3-2)}$$

which works out to be 95.367431 MHz/s. The 24 bit time word can produce a delay of 0.42 sec, which is more than adequate for the RSS.

There is a buffer in the digital chirp generator which will accept the next command while the current command is being processed. Thus the next instruction is immediately available to be processed on completion of the current command. This facility allows precise timing to be obtained in real time.

The interface to the chirp generator allows data to pass from the RSS computer in order to program the chirp generator. This data must be passed to the digital chirp generator during the processing period for the previous command so that the programmed chirp delay is correct. The data required is clocked into 10 addressable registers in the chirp generator The data is buffered via a FIFO and the addresses are generated by a PROM. The handshaking protocol is also generated by the PROM at the end of the data transfer.

A.3.2 Compensation for the filter group delay variation

Figure A.3-2 shows a modification to the chirp programming that accounts for the resolution-dependent group delay of the anti-alias filter. In this scheme the chirp is still triggered at the same time. However, a trigger pulse is generated after a time T3 before the chirp is generated where T3 is the group delay of the anti-alias filter at a particular resolution. Thus this trigger can be used to initiate the initiate the modulation so that the signals at the input to the SSB modulator are time-coincident. Thus the time for the recovery chirp is defined as:

$$T4 = T1 - T3 \qquad \text{(A.3-3)}$$

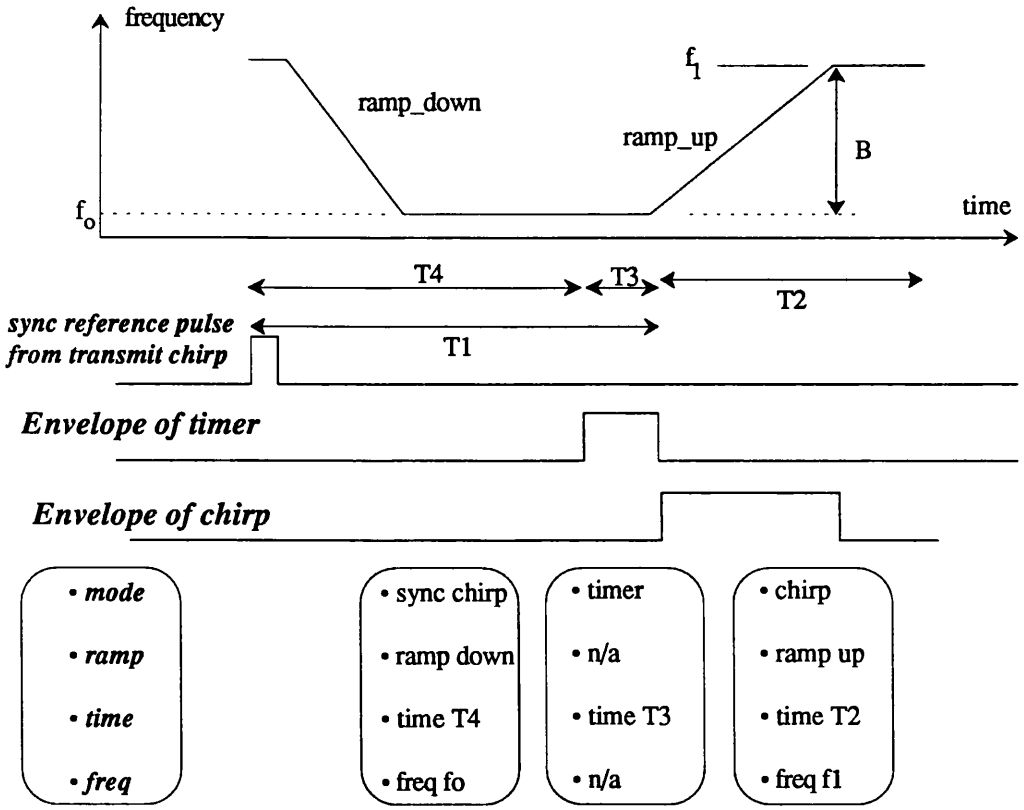

Figure A.3-2 Modification of the chirp generator programming to include compensation for the group delay variation.

Appendix 4

Circuit diagrams of the prototype RSS

This appendix contains a list of the circuit diagrams used in the RSS. A number of timing diagrams are included in sections when required to enhance the understanding of the circuit diagram.

A.4.1 DRAMs and DRAM controller

The purpose of the DRAM is to provide rapid transfer of the echo data to the FIFOs during a simulation. The FIFOs contain the data for a single echo, and must receive this data before the instant at which it is to be modulated onto the chirp. A block diagram of the configuration of the DRAMs, DACs, FIFOs and computer bus is shown in figure 4.3-3.

The control signal for the DRAMs and FIFOs are generated from two PROMs which contain the timing patterns for the refresh and read/write accesses respectively for the four DRAMs. These two PROMs are enabled and disabled by a third PROM which arbitrates and gives a priority to a read/write access when required. The PROM controlling the refresh is enabled periodically in order to refresh the DRAM data. A block diagram of the PROM configuration is shown in figure A.4-2.

When an instruction to transfer data is received, the control PROM (mother board, shown in figure A.4-1) is reset. It then enables the counters driving the read/write PROM (resident on the daughter board, shown in figure A.4-3), which generates the timing pattern for the strobes and control lines needed to transfer data between the FIFO and DRAM. The read/write PROM also increments another counter, the echo address counter, to point to the correct memory address of a particular sample of an echo in the DRAMs. The direction of transfer is controlled by one of the input lines (Addr 11, shown on the circuit diagram) from the RSS computer. A total of 512 bytes, corresponding to a single echo are transferred to the FIFOs in a single burst. The structure of the echo data in the DRAM memory is illustrated in figure A.4-4.

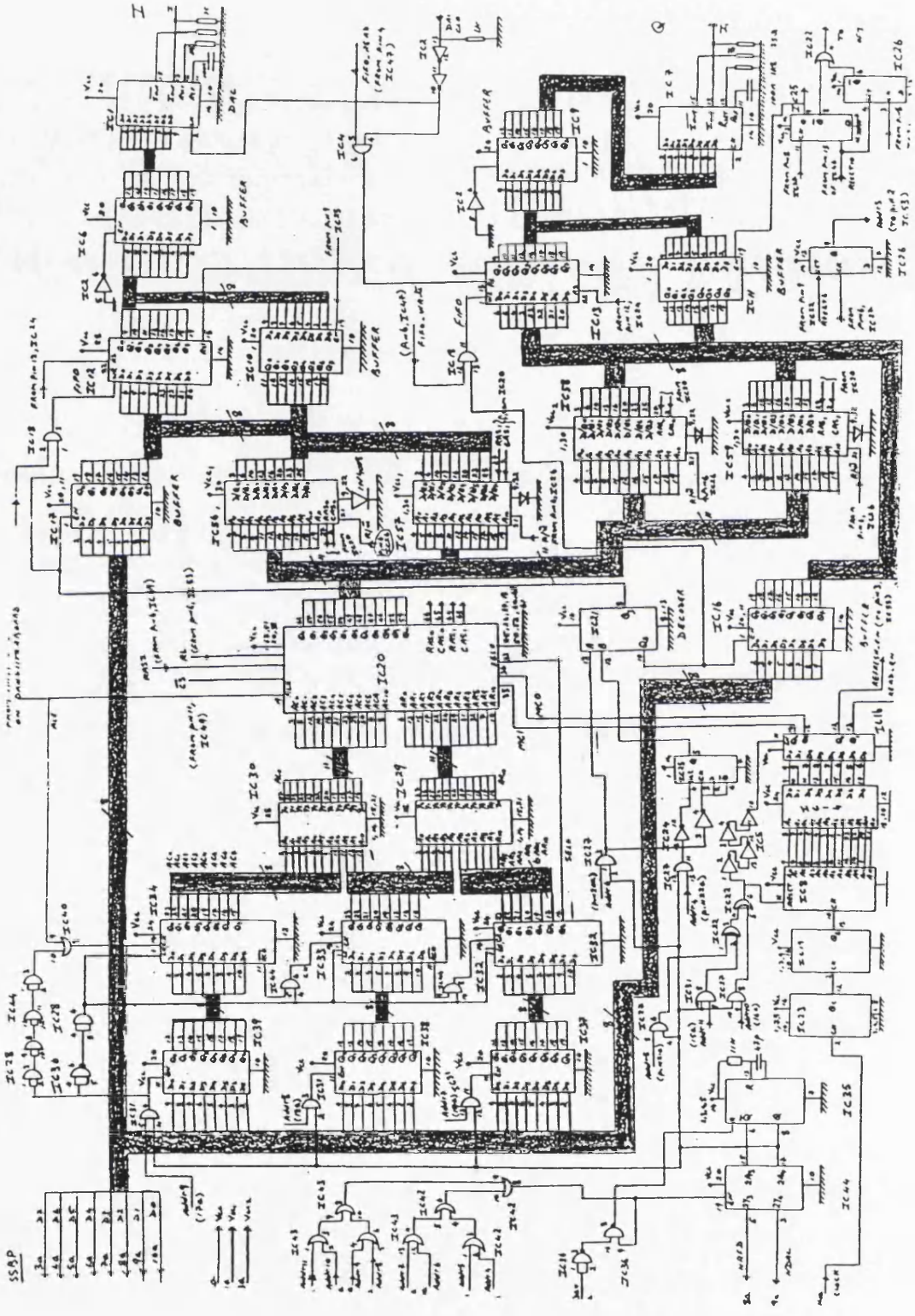

Figure A.4-1. A circuit diagram of the mother board of the memory and control unit

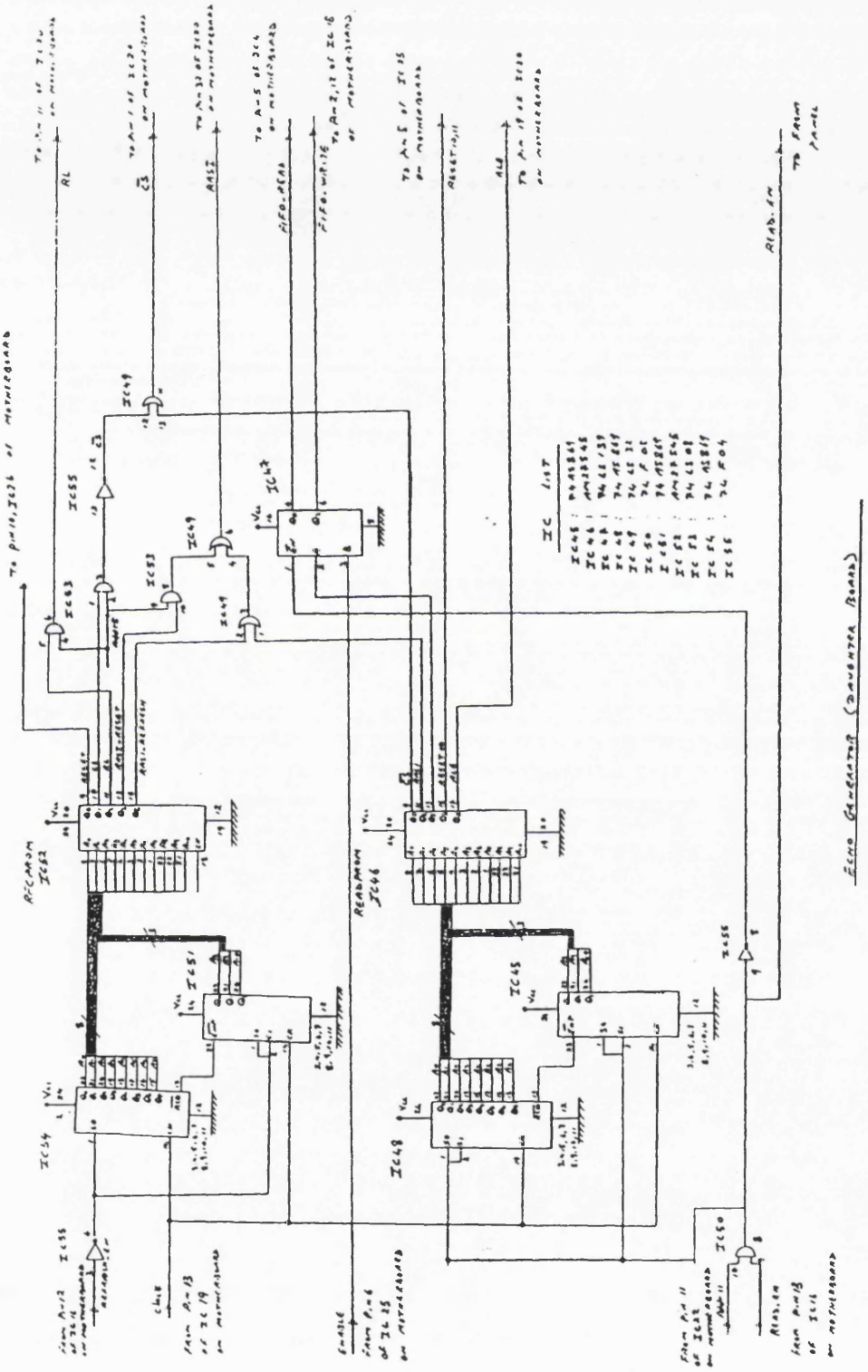

Figure A.4-2 A circuit diagram of the daughter board of the memory and control unit.

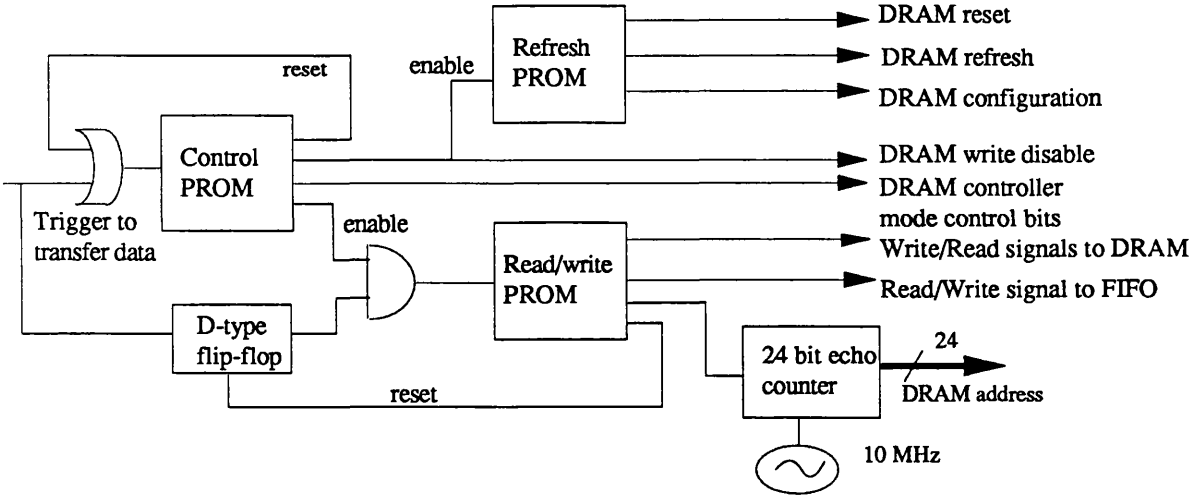

Figure A.4-3 The block diagram of the logic and timing circuitry for the DRAM. It consists of three PROMs containing the timing sequences for the control signals.

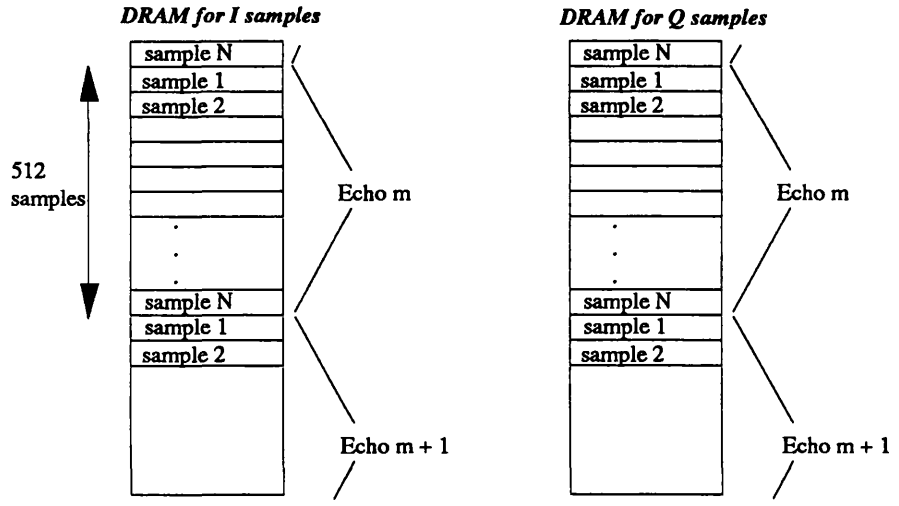

Figure A.4-4 The structure of the DRAMs for both I and Q channels. The samples of a single echo are stored consecutively, and the echoes in a sequence are stored consecutively. The DRAMs have a capacity for 16000 echoes each with 512 samples.

The DRAMs need to be refreshed every 4 ms; this can be done by strobing each of the 2048 rows of the DRAM. The switch between refresh and read/write is controlled by the logic shown in figure A.4-2, which assesses the priority of the read/write and refresh functions. The refresh must occur every 4 ms, but is also programmed to occur after a read/write operation. Thus if a read/write is requested, the refresh must terminate and resume after the read/write. Since the pulse repetition interval is approximately 1 ms, and the transfer of data is accomplished in 0.5 ms, there is always sufficient time to finish the refresh in each PRI. The effective refresh rate is 4 times the required rate. The refresh PROM contains the bit pattern to refresh the DRAM and configure the DRAM with the correct data.

The timing diagram for the data transfer is shown in figure A.4-5. The timing pattern in the PROM is clocked out at 10 MHz. The transfer of one byte of data requires 8 clock pulses. Thus the transfer of data takes place at 1.25 Mbytes/s. The address latch enable signal ALE increments the echo address counter, and clocks the new address into the DRAM controller on the falling edge of the pulse. The RASI pulse is the row address strobe pulse for the DRAM controller, and it signifies the instant when the row of the memory matrix is to be accessed. The CASI (column address strobe) is internally referenced to the RASI. The FIFO signal writes the data into the FIFO or reads from it depending on whether it is a read or write instruction. The CS is a chip select pulse.

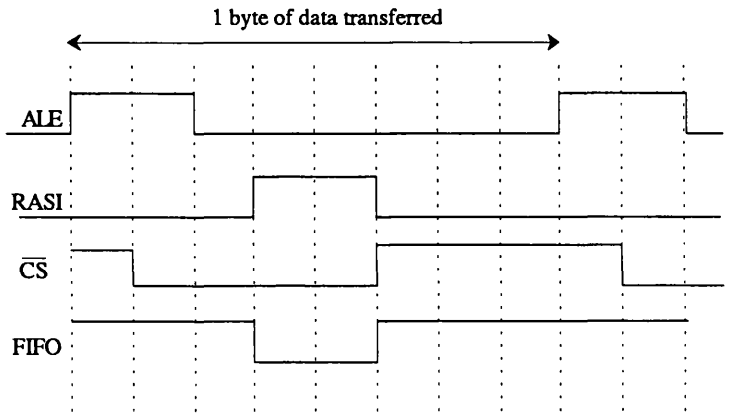

Figure A.4-5. The timing diagram for the transfer of data to and from the DRAM's.

A.4.2 RF front end

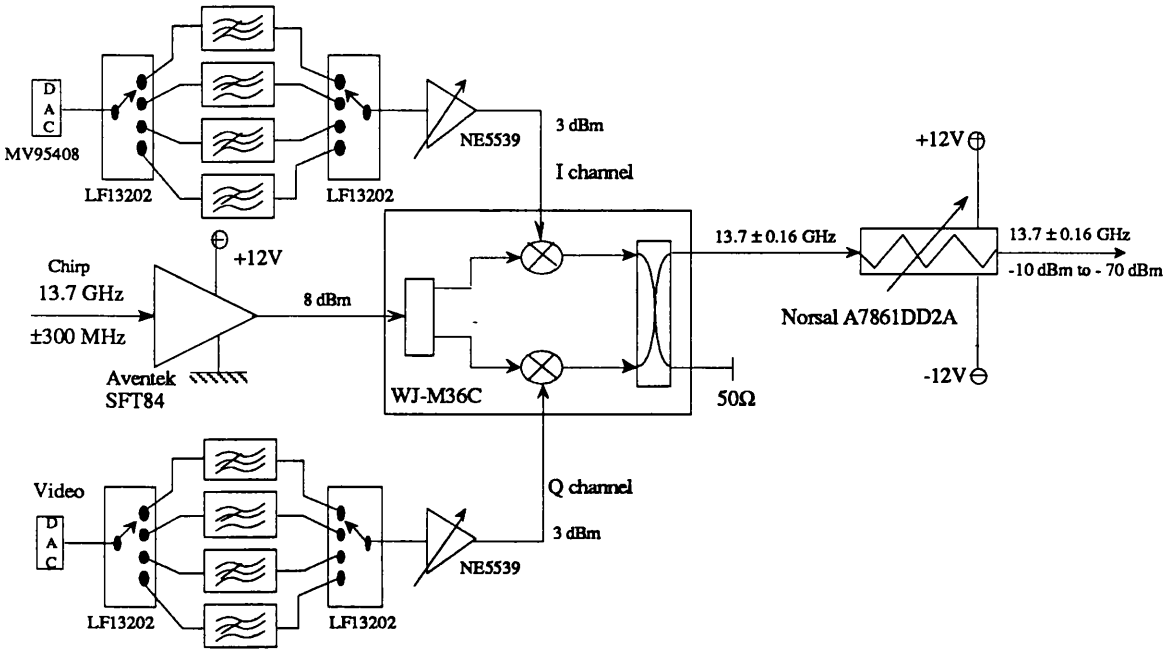

Figure A.4-6 A block diagram of the RF front end.

The RF amplifier shown in figure A.4-6 amplifies the output power of the chirp generator to 7 dBm, defining the quiescent point of the mixer in its linear region. The WJ-M36C single sideband modulator is specified to operate from 6 to 18 GHz with baseband operation from DC to 500 MHz. The Norsal attenuator is programmable and it defines the dynamic range of the echoes from the simulated surface.

The buffer amplifiers on the I and Q channels are NE5539 ultra high speed operational amplifiers, and are used to provide amplitude balance between the I and Q channels, and to compensate for the DC offset resulting from the unipolar operation of the DACs. The high speed operational amplifier requires compensation for gains less than 7. A block diagram of the buffer amplifier and the switch is shown in figure A.4-7. The LF13202 switch operates up to 50 MHz, offers an isolation of 50 dB and a switching time less than 1 μs. The switch is controlled from a 2 bit binary word. The filters are passive LC linear phase filters. They have been designed as connectorised modules so that they can be replaced with the filters corresponding to a different pulse length.

The output power of the baseband channel is approximately 3 dBm. The maximum baseband frequency is +6.666 MHz corresponding to the shortest pulse length of 19.2 μs.

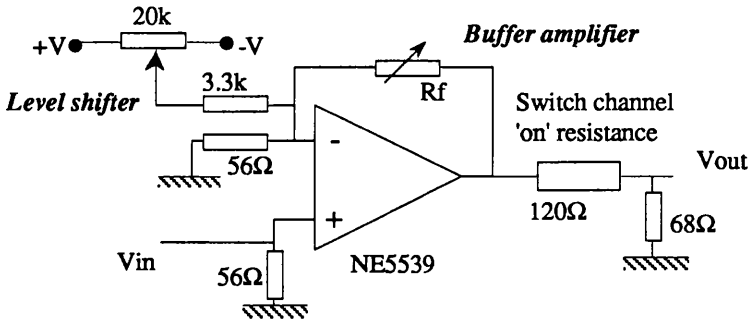

Figure A.4-7. A diagram of the level shifter and gain control for the baseband channels.

A.4.3 PLL synthesiser

A block diagram of the PLL synthesiser is shown in figure A.4-8 and the circuit diagram is shown in figure A.4-9. The difficulty in designing this circuit was producing a reference frequency into the PLL equal to 1/T where T is the chirp length. The two dividers divide the input clock down to a frequency close to or equal to 1/T. The input frequency to the phase detector of the MC145152 is multiplied by N to produce an output frequency of N/T. The divider in the MC145152 is programmed to divide by N/4, and two flip flop provide the additional division by 4. The loop bandwidth of the PLL is 40 Hz, thus giving a rather long loop settling time. The output frequency of the PLL remains fixed during the simulation, and is divided down according to the resolution chosen by the altimeter tracking loop.

The 74LS625 VCO chip does not cover the range of frequencies required by the PLL for all three pulse lengths used in the simulator. The overall frequency range is sub-divided into two more manageable ranges, thus requiring two VCOs with different tuning capacitors (as shown in figure A.4-9).

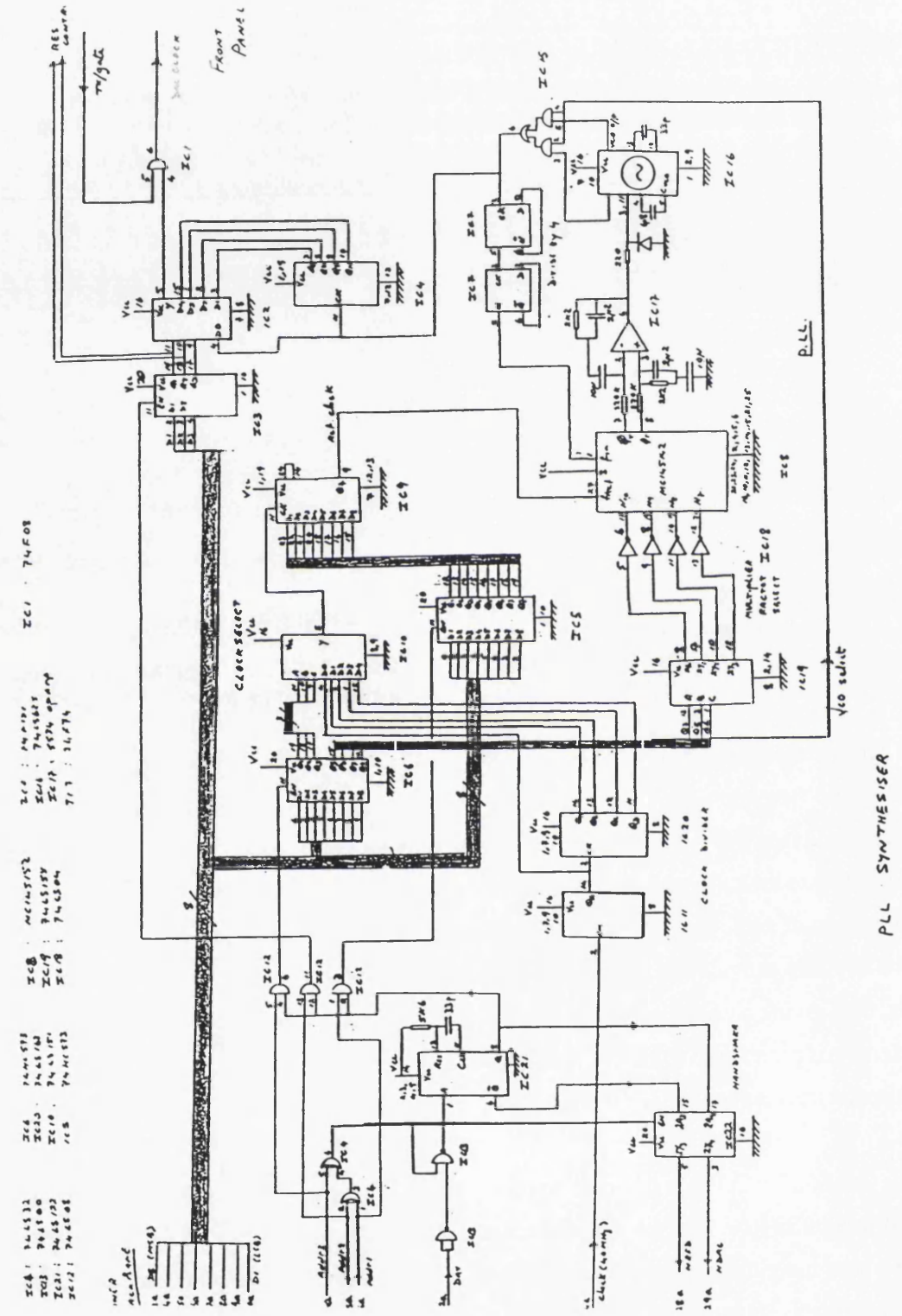

Figure A.4-9 The circuit diagram of the PLL synthesiser.

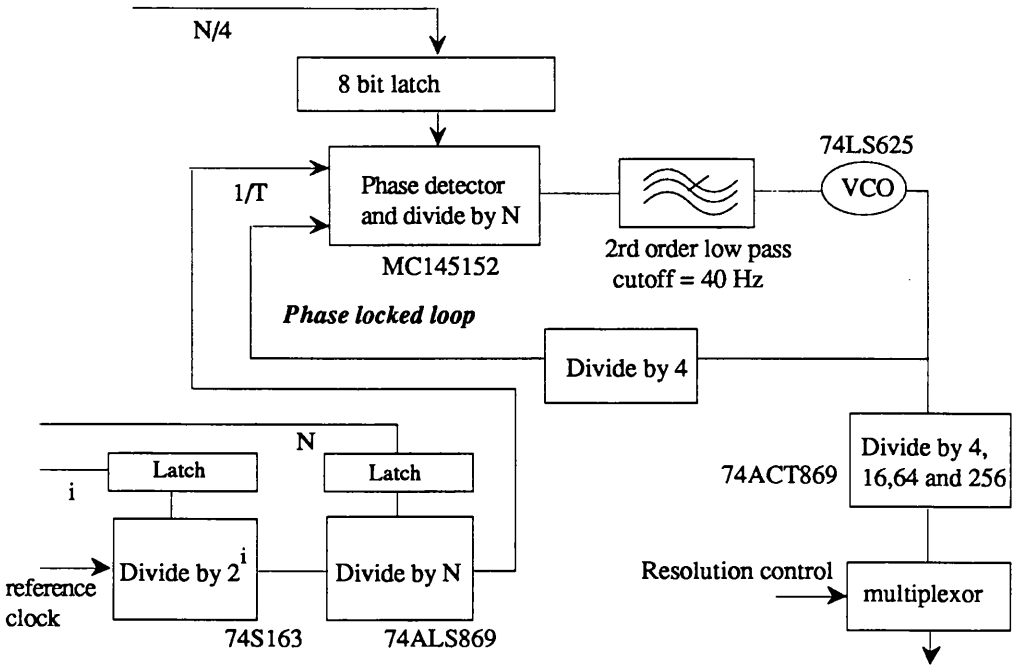

Figure A.4-8. The block diagram of the PLL synthesiser. The input reference frequency to the PLL is 1/T. The MC145152 chip contains a phase detector and a divide by N facility. This is therefore useful in generating the multiplier factor.

A.4.4 Other supporting circuit diagrams

Figure A.4-10 shows the circuit diagram of the interface to the chirp generator, and to the transmit chirp data registers. Figure A.4-11 show the GPIB interface between the RSS rack system and the computer.

A full description of the interfaces, the pin outs and the wiring schedules in the RSS is available in the 'RSS hardware documentation' (Sheehan[53], 1992).

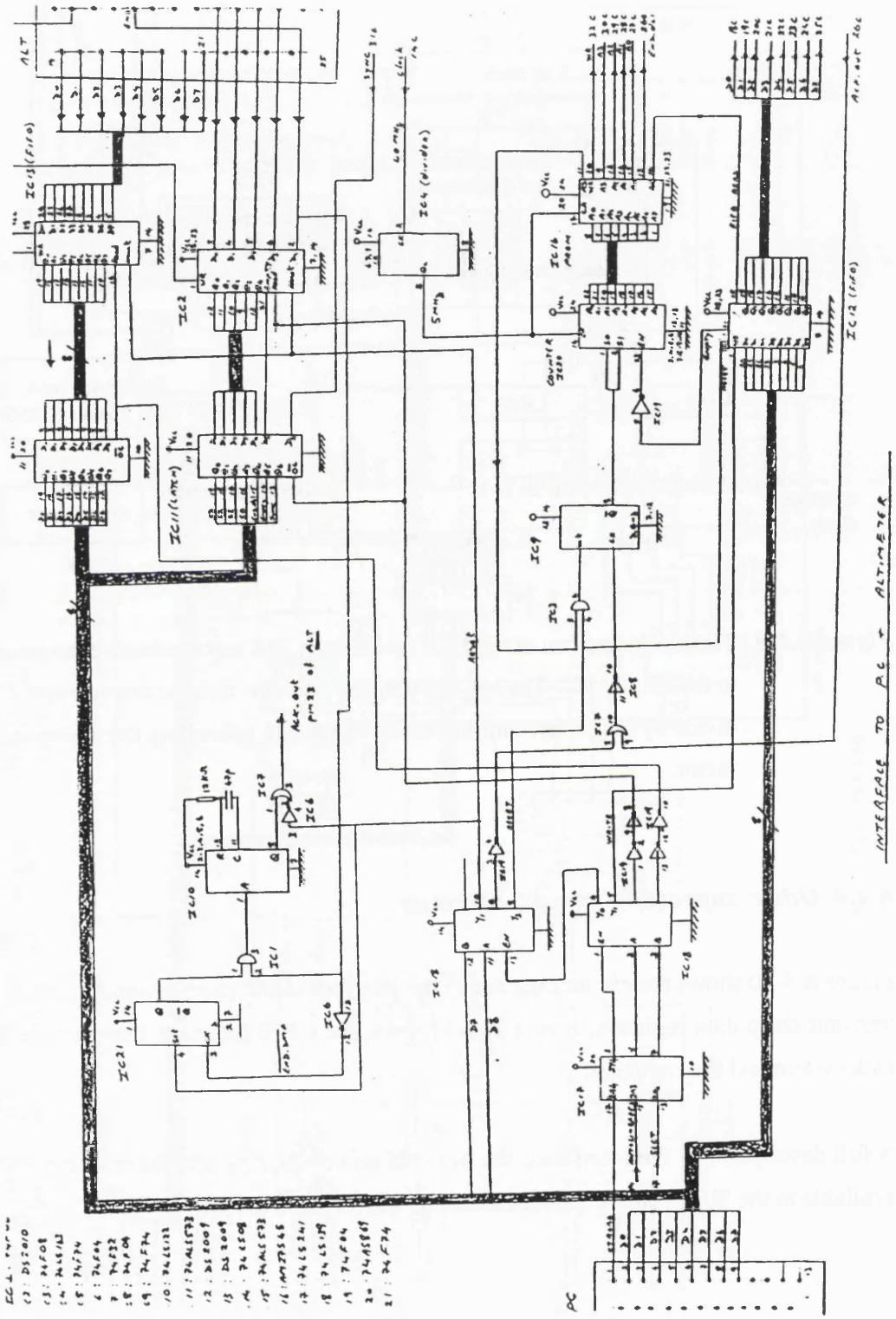

Figure A.4-10 The circuit diagram of the interface to the digital chirp generator.

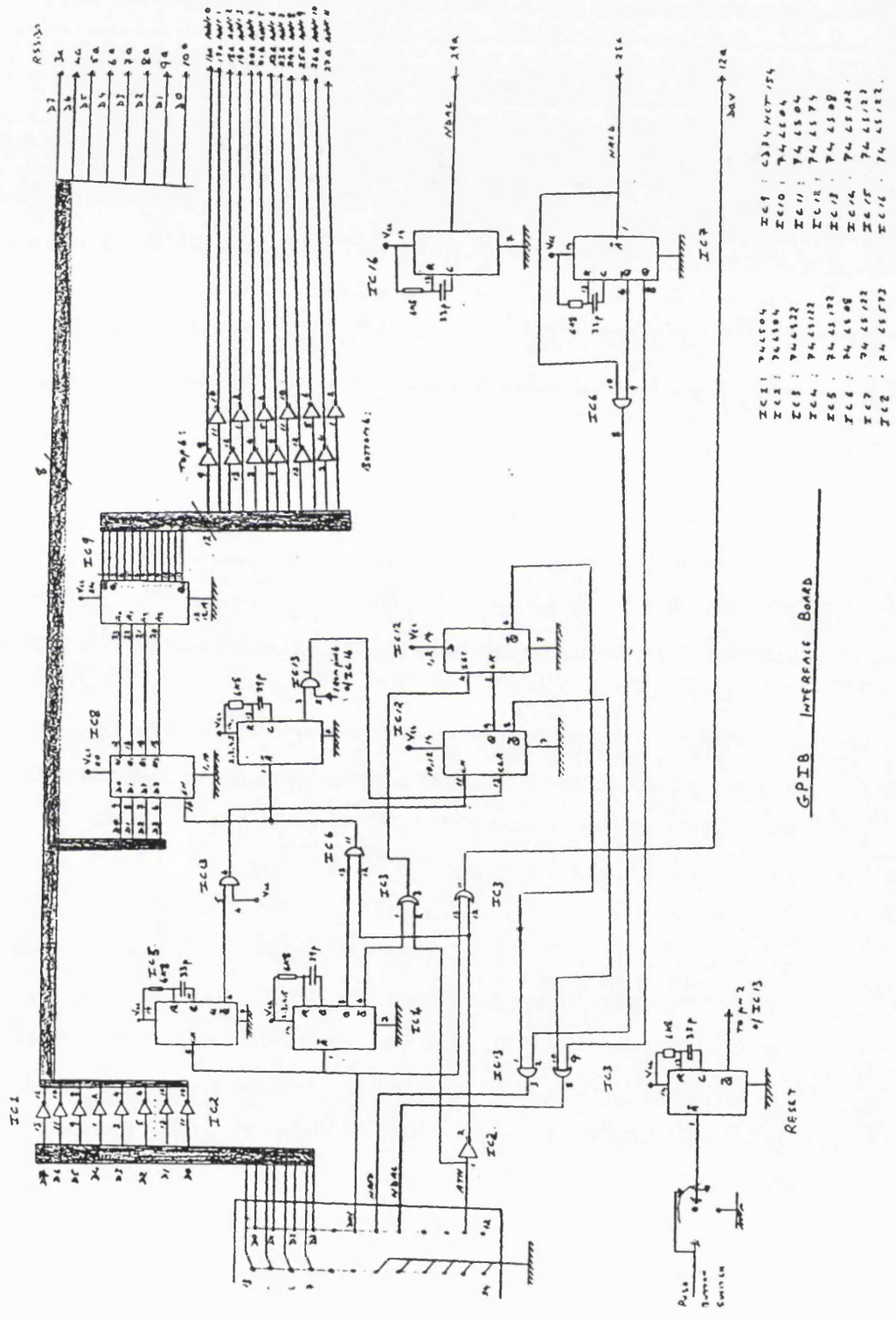

Figure A.4-11 The circuit diagram of the GPIB interface to the RSS rack system.

Appendix 5

A description of the control software

A diagram showing the data arrays and the processing delay for the time words, gain words, resolution and echo samples is given in figure A.5-1.The array containing the echo samples is implemented in hardware using the DRAMs as described in appendix A.4, and the other are implemented in software. Each array is 16000 elements long. There is a 5 pulse processing delay corresponding to an operational height of 800 km and a PRF of 1 kHz.

The software is programmed to start the simulation when it detects altimeter transmit chirp trigger instant present at the parallel port of the computer. This is a rough timing reference, that is used for data preparation. The precise timing of the echo is achieved if all the timing information has been transmitted to the chirp generator before the next transmit instant. The echo corresponding to the N^{th} PRI is thus prepared during the $(N-1)^{th}$ PRI. The first simulated pulse is generated after the processing delay. Every subsequent echo is routinely delayed by the same delay. The ramp rate information is read every 50 PRIs, but is only updated after the processing delay with respect to the time it is read.

The echo samples are passed from the DRAMs to the FIFOs every PRI. Before the operation takes place, a second command empties the FIFO so that the new echo data occupies the first 512 elements of the FIFO. If a coarser resolution has been used in the previous PRI, then the FIFO will not have been emptied. The DRAM counter will be pointing at the correct echo location unless it is necessary to jump to a different location in the DRAMs. The transfer of echo samples is initiated by a single command from the RSS computer. A flow chart of the real time simulation is shown in figure A.5-2.

The resolution of the echo is set once every 50 PRIs, i.e the rate at which the resolution is changes by the altimeter, and is delayed by the processing delay. The resolution datum is used to divide the PLL output frequency by the correct factor of 4, and to select the corresponding anti-alias filter. The power of the echo also depends on the resolution being

used to track it. The gain of the echo is increased by 6 dB every time the resolution is degraded by a factor of 4. The 6 dB change is implemented only every 50 PRIs, but the gain is none the less varying on a PRI basis. This is updated by setting the level of the attenuator every PRI.

The timing of the echo is achieved by programming the chirp generator with 20 bytes of data, as defined in appendix A.3. The sub-program synthesise_echo is shown in figure A.5-3.

Prior to performing a simulation, the simulator must be set up and the DRAMs must be loaded with the echo samples. The main program of the altimeter control software is shown in figure A.5-4. Instructions passed via the serial port are decoded, and the computer resets the hardware, identifies the simulation to be performed and passes the echo data to the DRAMs. When it is ready to start the simulation it signals this status to the altimeter computer via the serial port and waits for the 'start_simulation' instruction.

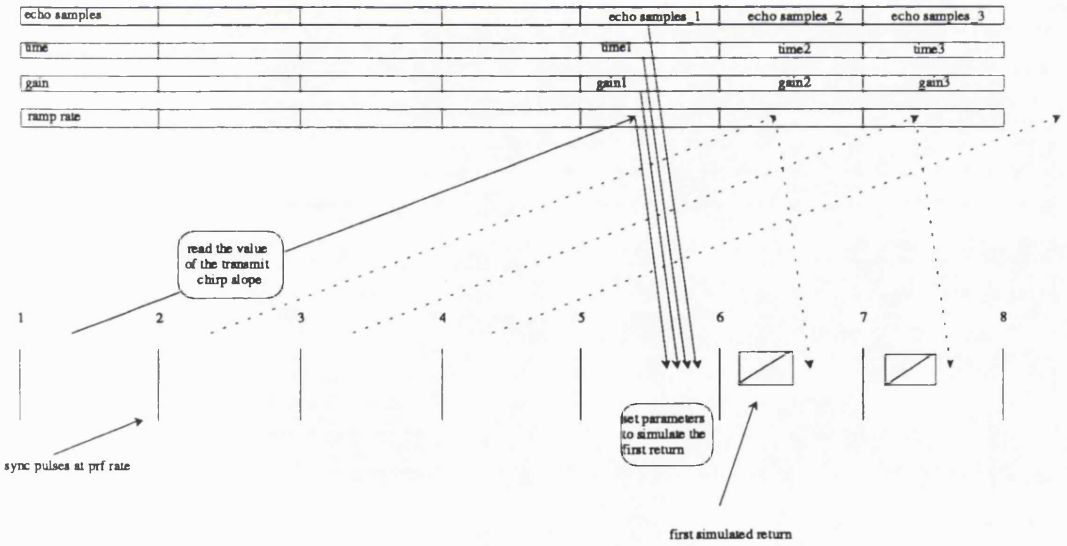

Figure A.5-1. The processing scheme for the control software as a function of the pulse repetition interval. The processing delay is shown for a PRF of 1 kHz.

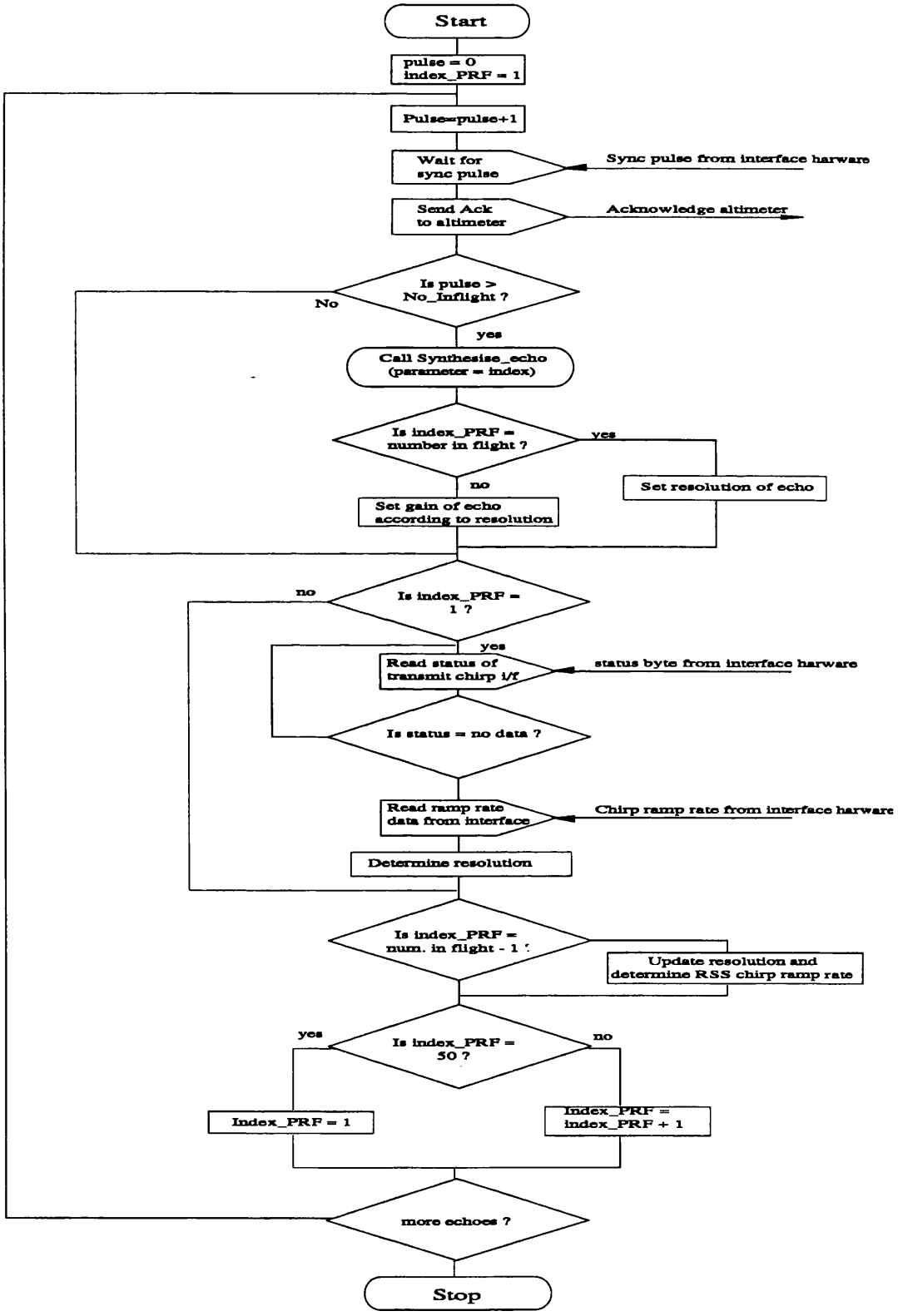

Figure A.5-2. A flow chart of the real time simulation routine.

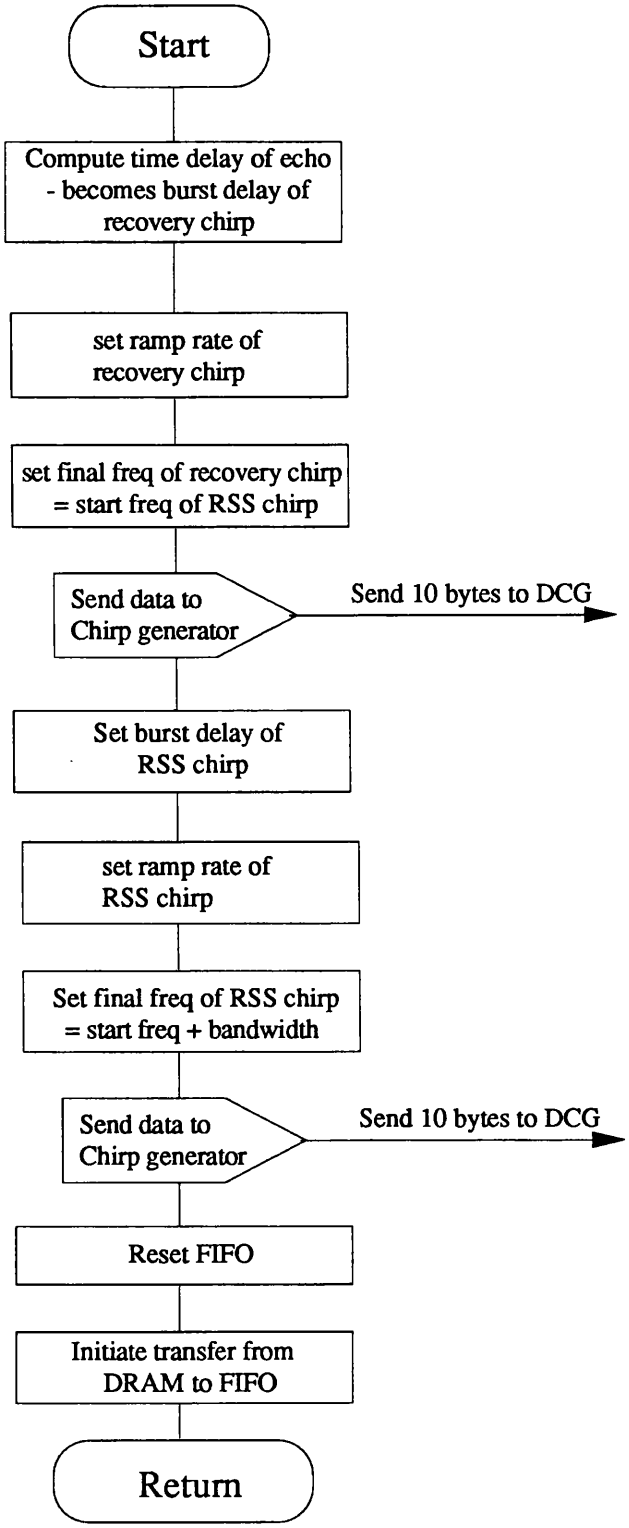

Figure A.5-3. A flow chart of the sub-program synthesise_echo.

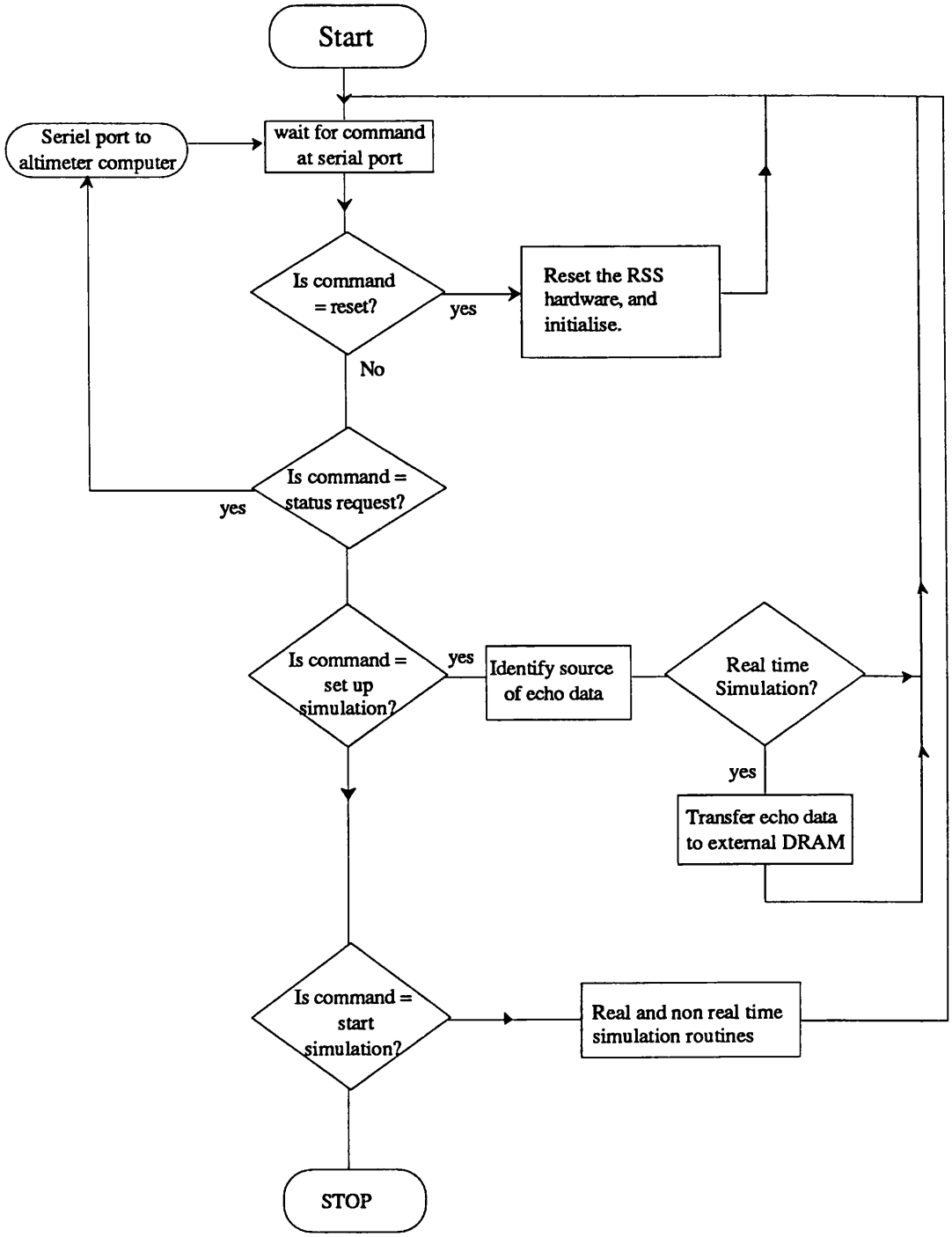

Figure A.5-4. A flow chart of the main program.

Appendix 6

The OCOG and MFT tracking algorithms

A.6.1 OCOG

The Offset Centre Of Gravity tracking algorithm was developed by Wingham. It is based on fitting a rectangular box waveform to the instantaneous energy of the received echo. The amplitude of the box waveform is estimated as twice the centre of gravity A where A is:

$$A = \frac{\sum_{i=-N_F/2}^{N_F/2} P_i^2}{2\sum_{i=-N_F/2}^{N_F/2} P_i} \qquad \text{(A.6-1)}$$

The width of the echo is defined by the requirement that the energy of the box waveform equals the energy of the instantaneous echo. Thus:

$$W = \frac{\sum_{i=-N_F/2}^{N_F/2} P_i}{2A} = \frac{\left(\sum_{i=-N_F/2}^{N_F/2} P_i\right)^2}{\sum_{i=-N_F/2}^{N_F/2} P_i^2} \qquad \text{(A.6-2)}$$

It is not known where the echo starts or stops in the range window. The only information available is the duration of the echo. The algorithm thus assumes that the echo is positioned symmetrically with respect to the centre of gravity. It estimates the leading edge by locating the centre of gravity of the echo, and offsetting the centre of gravity by half the echo width in order to find the position of the leading edge of the echo. The position estimate is:

$$P = \frac{\sum_{i=-N_F/2}^{N_F/2} iP_i}{\sum_{i=-N_F/2}^{N_F/2} P_i} - \frac{W}{2} \qquad \text{(A.6-3)}$$

The sensitivity of the position estimator to the average noise power is quite bad because of the linear weighting with distance in (A.6-3). Figure A.6-1 shows how the height error characteristic is distorted for low signal to noise ratios.

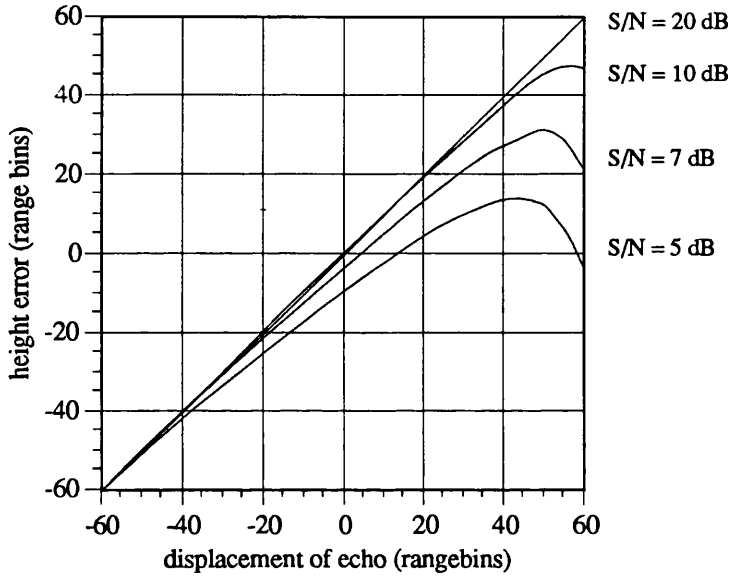

Figure A.6-1 The height error characteristic of the OCOG algorithm for different S/N.

To reduce this effect, the dynamic range of the dynamic range of the samples is artificially increased by squaring the samples prior to the computation of P, W, A. Thus the OCOG algorithm is defined by:

$$A = \frac{1}{2}\sqrt{\frac{\sum_{i=-N_F/2}^{N_F/2} P_i^4}{\sum_{i=-N_F/2}^{N_F/2} P_i^2}} \qquad \text{(A.6-4)}$$

$$W = \frac{\sum_{i=-N_F/2}^{N_F/2} P_i^2}{4A^2} = \frac{\left(\sum_{i=-N_F/2}^{N_F/2} P_i^2\right)^2}{\sum_{i=-N_F/2}^{N_F/2} P_i^4} \qquad \text{(A.6-5)}$$

$$P = \frac{\sum_{i=-N_F/2}^{N_F/2} iP_i^2}{\sum_{i=-N_F/2}^{N_F/2} P_i^2} - \frac{W}{2} \qquad \text{(A.6-6)}$$

The height error characteristic of the OCOG algorithm for different S/N ratios is shown in figure A.6-1. The model waveform in each case is taken to be a rectangular spectrum. The noise refers to the noise pedestal in the early range bins.

A.6.2 MFT

The first stage of the MFT algorithm is a threshold comparison in each of the range bins. A parameter T_i is set according to:

$$\begin{aligned} Ti &= 1 \qquad P_i > T_s \\ Ti &= 0 \qquad P_i < T_s \end{aligned} \qquad \text{(A.6-7)}$$

This algorithm is also based on the centre of gravity principle. The estimate of the width of the echo is:

$$W = \frac{\left(\sum_{i=-N_F/2}^{N_F/2} T_i\right)^2}{\sum_{i=-N_F/2}^{N_F/2} T_i} \qquad \text{(A.6-8)}$$

The position of the centre of gravity is given as:

$$B = \frac{\sum_{i=-N_F/2}^{N_F/2} iT_i}{\sum_{i=-N_F/2}^{N_F/2} T_i} \qquad \text{(A.6-9)}$$

The position of the leading edge of the echo is therefore given as:

$$P = \frac{\sum_{i=-N_F/2}^{N_F/2} iT_i}{\sum_{i=-N_F/2}^{N_F/2} T_i} - \frac{W}{2} \qquad \text{(A.6-10)}$$

The estimate of the centre of gravity of the echo is given as:

$$A = \frac{\sum_{i=-N_F/2}^{N_F/2} P_i^2}{2\sum_{i=-N_F/2}^{N_F/2} P_i} \qquad \text{(A.6-11)}$$

Appendix 7

The Acquisition phase for the ATTA

The proposed acquisition sequence for the adaptive terrain-tracking altimeter has three separate phases: - noise power estimation, detection of the surface, and AGC level setting. The method proposed by Levrini et al (1990) requires additional hardware at the front end of the altimeter receiver. For this reason, it is not compatible with the RA-2 design.

The acquisition is performed by transmitting a chirp with the lowest chirp rate at a PRF of 1 kHz. The first phase is the estimation of the noise level in the range window of the altimeter. During the first 5 pulse repetition intervals, no echo is received. This period is used to determine the background noise level in the range window. Thus 128 samples are available per range window, for 5 different range windows; thus the accuracy of the estimated noise level is:

$$\varepsilon_a = 10\log_{10}\left(1 + \frac{1}{\sqrt{740}}\right) = 0.16 \text{ dB} \qquad \text{(A.7-1)}$$

The mean level is defined as:

$$\langle N_o \rangle = \frac{\sum_{i=1}^{740} N_i}{740} \qquad \text{(A.7-2)}$$

The detection phase is required to detect the surface. The narrowest bandwidth chirp is used to initially acquire the surface at the coarsest resolution. The *a priori* range to the surface is 785 km to 815 km. The range window is initially placed at one extreme and moved progressively to the other extreme until lock is detected. At the coarsest resolution, the return is beam-limited, thus occupying only a single range bin. The signal to noise ratio is defined by the radar equation for the beam-limited case:

$$\left(\frac{S}{N}\right)_{BL} = \frac{P_t \lambda^2 G^2 \sigma^o \theta^2}{64\pi^2 h^2 k T_o B F} \qquad \text{(A.7-3)}$$

Thus:

$$\left(\frac{S}{N}\right)_{BL} = 42 \text{ dB} \qquad \sigma^o = 13\text{dB (ocean)} \qquad \text{(A.7-4a)}$$

$$\left(\frac{S}{N}\right)_{BL} = 19 \text{ dB} \qquad \sigma^o = -10\text{dB (worst case)} \qquad \text{(A.7-4b)}$$

The signal to noise ratio is sufficient Wingham (1990) to allow the detection of the surface even under the worst case conditions. The efficiency of the acquisition sequence depends on the length of the uncompressed pulse length. The maximum uncertainty in the position of the surface is 200 μs (30 km). Thus for a chirp length of 20 μs, at least 10 separate positions of the deramp chirp are required to cover the entire range. This is because an overlap between the deramp chirp and the received chirp is required in order to perceive an echo in the range window. Practically speaking, these two chirps should overlap by at least half the pulse length to prevent blurring the image in the range window and reducing its signal to noise ratio, and to track the dynamics of the surface. Thus the deramp chirp position is moved incrementally by half the chirp length until the surface is located. The maximum number (N) of such positions is

$$(N/2 + 1)T = 200\ \mu s \qquad \text{(A.7-5)}$$

For T = 20μs, N = 18, and for T=300μs, N =1.The worst case scenario is defined for a chirp length of 20μs and the full 18 positions of the deramp chirp to be interrogated.

Consider the return in the range window, which is exponentially faded with mean P_o. The probability distribution for M echoes summed prior to detection is

$$f(P) = \frac{P^{M-1}\exp[-P/P_o]}{P_o^M \Gamma(M)} \qquad \text{(A.7-6)}$$

The probability of failure is given by Wingham for a few typical examples (Wingham, 1990). For a threshold set 4.5 dB above mean noise with M=10, the probability of a false detection is 6.10^{-4} and if this threshold is set 10 dB below the mean signal level, the probability of a failed detection is less than 10^{-5}. This assumes a signal to noise ratio of 14.5 dB, and this is generally a lower limit. Thus the probabilities of false and failed detection are considerably lower. The probability of failed detection is reduced even more

when we consider that the range window is to be moved by half its width whenever a failed detection takes place, so that each range to the surface can be interrogated by two separate successive positions of the deramp chirp.

A false detection will allow the processing to proceed to the gain acquisition phase.

The gain acquisition is necessary to prevent the instrument from saturating. The dynamic range of σ^o is possibly in the region of 85 dB (although we have only considered a range of 55 dB for the RSS). The main constriction is the limited dynamic range of the ADC'c, which is 48 dB for an 8 bit number. The following method of gain acquisition is based on post-ADC observation of the signal and its saturation.

Allowing a limit of 10 dB at the lower end of the ADC dynamic range for targets with an unexpectedly low value of σ^o or unexpected atmospheric attenuation, and setting a threshold -10.9 dB fullscale on the upper end (Wingham, 1990), gives us an effective dynamic range of 27.1 dB. Thus 3 or 4 estimates of the gain are required to set the AGC of the altimeter during the acquisition phase (see figure A.7-1). It is not known how much signal power is lost due to saturation at the ADC's and as a result, the gain must be changed until the signal fits inside the effective dynamic range of the ADC. The gain acquisition also uses 10 pulse averaging in order to estimate the gain of the signal. The condition is as follows:

> *if the signal exceeds the threshold, then change AGC gain by 27.1 dB, and*
>
> *if the signal fits inside the threshold, scale the AGC so that the mean signal is normalised to-20 dB full scale.*

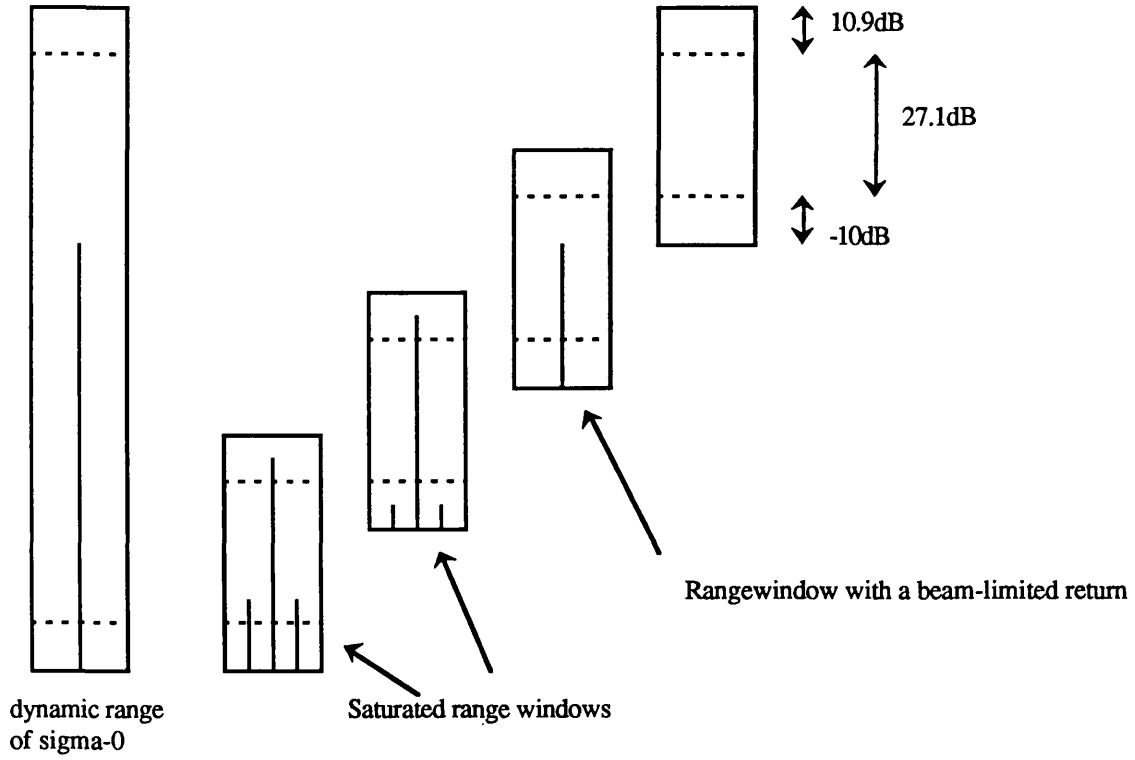

Figure A.7-1 The proposed gain acquisition phase for the ATTA.

Appendix 8

Analysis of gain flatness in the altimeter

The filter insertion loss responses shown in figure 5.1-5 can be curve-fitted in the passband of the response by:

$$IL(f) = 1 - 0.0975\left(\frac{f}{f_c}\right) - 0.7656\left(\frac{f}{f_c}\right)^2 + 0.533\left(\frac{f}{f_c}\right)^3 - 0.15\left(\frac{f}{f_c}\right)^4 \qquad \text{(A.8-1)}$$

where f_c is the filter cutoff frequency. The DAC frequency response is given by (4.4-1):

$$IL_{dac}(f/f_s) = \left[\frac{\sin\left(\pi\frac{f}{f_s}\right)}{\pi\frac{f}{f_s}}\right]^2 \qquad \text{(A.8-2)}$$

The pre-distortion function is therefore given as:

$$P_d(f/f_c) = \frac{1}{IL_{dac}(f/f_s)\, IL_{fil}(f/f_c)} \qquad \text{(A.8-3)}$$

The amplitudes of the tones used to verify that the baseband channels are weighted by the square root of the function in (A.8-3), and are also normalised so that the bandedge frequencies occupy the full dynamic range of the DACs.Thus the amplitude of the tones are given as:

$$A_d(f/f_c) = V_{fr}\sqrt{\frac{IL_{dac}(f_c/f_s)\, IL_{fil}(f_c/f_c)}{IL_{dac}(f/f_s)\, IL_{fil}(f/f_c)}} \qquad \text{(A.8-4)}$$

where V_{fr} is the full range voltage of the DACs. The frequency of the tones is defined as:

$$f = \frac{n}{T} \qquad \text{(A.8-5)}$$

where n is the parameter shown in the plot of figure 5.2-1.

The flatness of the baseband channels was measured by generating a tone that has been pre-distorted, and capturing the tone on a digital oscilloscope.

Appendix 9

Limitations in the method of chirp generation

The sampling phase locked loop in the chirp upconversion unit is implemented in a very unorthodox manner. Figure A.9-1(a) shows the PLL used in the upconversion unit, and figure A.9-1(b) illustrates a conventional PLL. The high gain amplifier and passive filter replaces the active filter of a conventional PLL. The gain of the amplifier must be high in order to approximate the infinite open loop gain of the integrator in the active filter.

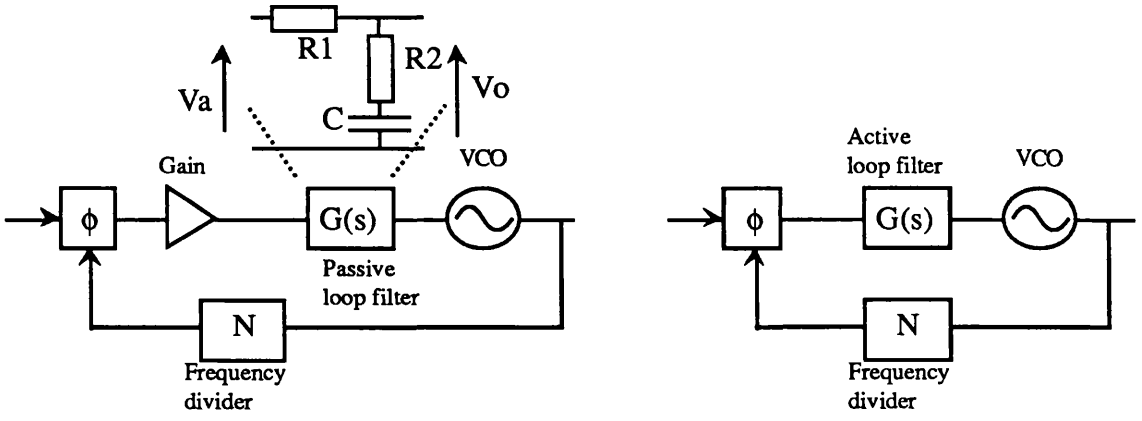

Figure A.9-1 The phase locked loop used in the upconversion unit, and a conventional PLL.

The active filter in a conventional PLL operates by producing a ramped output for a constant input as a result of the integrator, thus driving the VCO with a ramping voltage. The PLL shown in figure A.9-1(a) operates in a slightly different manner. In order to drive the VCO with a ramp, the input to the passive filter must also be a ramp.

The current in the capacitor is given by:

$$i_c = C\frac{dV_c}{dt} = \frac{V_a - V_c}{R_1 + R_2} \qquad \text{(A.9-1)}$$

where V_c is the capacitor voltage. Thus:

$$\frac{dV_c}{dt} = \frac{1}{\tau_1}(V_a - V_c) \qquad \text{(A.9-2)}$$

Since R2 << R1, and the capacitor current is very small, the VCO voltage V_o is can be approximated closely by the capacitor voltage. Thus the rate of change of the VCO output frequency sweep is given as:

$$\frac{d\omega_o}{dt} = \frac{K_v}{\tau_1}(V_a - V_c) \qquad \text{(A.9-3)}$$

The capacitor voltage charges up in order to produce a ramping input voltage. However from (A.9-3) it should be obvious that as the capacitor voltage charges up, the quantity $V_a - V_c$ decreases, thereby limiting the rate of change of frequency at higher frequencies. In order to obtain an estimate of the maximum rate of change of frequency, let us input the values of K_v, τ_1, V_a and the maximum VCO varactor voltage into (A.9-3). For a varactor range of 9.35 V to 11.35 V, $\tau_1 = 3.17 \times 10^{-5}$, $K_v = 230$ MHz/V (Franchin, 1989), and a maximum filter input voltage of 15 V, then the maximum rate of change of frequency at the output of the VCO is 2.5×10^{13} Hz/s. Thus it should be possible to sweep 480 MHz in 19.2 μs.

This is an over-optimistic result. In reality, the maximum output voltage of the operational amplifier will be closer to 13 V; thus the maximum rate of change of VCO output frequency is proportional to the difference between 13 V and the varactor voltage. At the highest frequency, this difference is 1.65 V rather than the ideal value of 3.65 V. Thus the maximum rate of change of frequency is in fact 1.1×10^{13} Hz/s. In order to sweep a bandwidth of 160 MHz in 19.2 μs, the rate of change of frequency is 0.833×10^{13} Hz/s. Thus the PLL has only got a margin of 30 % in hand for the maximum sweep rate at the highest frequency. In a steady state situation this may be sufficient; however since the input to the PLL is continually changing from CW to chirp and back to CW, this margin will most likely not be sufficient to track the transients. At the lower frequencies, the margin is considerably greater since the varactor voltage is smaller, and no problem was observed at these frequencies.

A higher op amp voltage supply rail may be the solution.

Appendix 10

Equivalence between the two phase distortion definitions:

$$\sum_{i=0}^{N} a_i x^i \quad \textbf{and} \quad \sum_{i=0}^{N} b_i (x - 0.5)^i$$

The phase distortion of chapter 6 analysis began by defining the the phase distortion over the interval [0,T]. This appendix defines the distortion using the interval [-T/2, T/2]. The normalised distortion over the latter interval is defined as:

$$\sum_{i=0}^{N} b_i (x - 0.5)^i \qquad \text{(A.10-1)}$$

This can be expanded as:

$$b_N \sum_{i=0}^{N} \binom{N}{i} (-0.5)^i x^{N-i} + b_{N-1} \sum_{i=0}^{N-1} \binom{N-1}{i} (-0.5)^i x^{N-1-i} + \ldots + b_1 (x - 0.5) + b_0. \qquad \text{(A.10-2)}$$

Expanding (A.10-2) to give:

$$a_N x^N + a_{N-1} x^{N-1} + \ldots + a_1 x + a_0, \qquad \text{(A.10-3)}$$

Then the coefficients b_i can be expressed in terms of a_i as follows:

$$b_N = a_N, \qquad \text{(A.10-4)}$$

$$b_{N-1} = a_{N-1} - \binom{N}{1} (-0.5)\, a_N, \qquad \text{(A.10-5)}$$

and, in general:

$$b_i = \sum_{k=0}^{N-i} \binom{i+k}{k} (0.5)^k a_{i+k} \qquad \text{(A.10-6)}$$

Figure A.10-1 shows the shift in the echo as a result of distortion defined by a single coefficient b_i. Note that the shift for the even coefficients is 0.

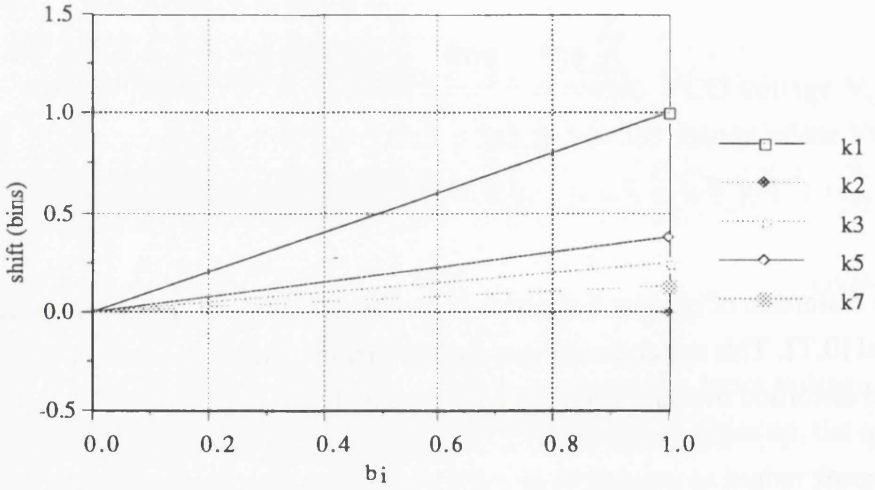

*Figure A.10-1.*The height bias as a function of the parameters b_i.

i	k_i
1	1.000
2	0.000
3	0.250
4	0.000
5	0.375
6	0.000
7	0.125
8	0.000

*Table A.10-1.*Slopes of the characteristics of the first 8 distortion coefficients.

The slopes of the curves differ from unity except for i=1. The slopes k_i of the first 8 curves are shown in Table A.10-1. Let the shift in the response corresponding to the coefficient b_i be $\Delta h(b_i)$. Consider a simple fourth order polynomial as an example to demonstrate the equivalence. The height bias is given by:

$$\Delta h = \sum_{i=1}^{4} k_i \Delta h(b_i) \qquad \text{(A.10-7)}$$

i.e. $\Delta h = k_1 \Delta h(b_1) + 0 + k_3 \Delta h(b_3) + 0$

$$a_1 + 0.5\binom{2}{1}a_2 + (0.5)^2\binom{3}{2}a_3 + (0.5)^3\binom{4}{3}a_4 + k_3 a_3 + k_3 0.5\binom{4}{3}a_4 \qquad \text{(A.10-8)}$$

Thus, given that $k_3 = 0.25$

$$\Delta h = \sum_{i=1}^{4} a_i \qquad \text{(A.10-9)}$$

Thus the resultant height error is the same irrespective of the definition of the phase distortion. Both definitions however give different characteristics for the height error vs distortion coefficient.

Appendix A.11

The Echo Generation Procedure

The echo profiles used in the thesis are generated in the following way:

1 A scenario is defined as a matrix of facets in the form given by figure 3.1-1. These scenarios have generally been artificially generated by Wingham; however the mountain scenario has been constructed from a Digital Elevation Map of the European Alps.

2 A numerical computation of the power using eqn. (3.1-1) is performed over all the facets that lie within the footprint of the altimeter for all the satellite positions. This yields a sequence of power profiles as a function of delay time. The echoes from real terrain (i.e. mapped by altimeters from previous missions are used to verify the echoes from similar sections of this artificially generated terrain.

   This is the extent of Winghams work, and this provides a large database of echo waveforms from a number of different scenarios. The elevation profiles of the scenarios are shown in §4.5.

3 The axis of the power profile is scaled by multiplying it by the chirp ramp rate (b=df/dt). At this stage of the generation procedure, we assume that we have *a priori* knowledge of the ramp rate corresponding to the finest resolution. Thus we are defining the echo in the frequency domain of the altimeter.

   This is the echo spectrum mentioned in figure 3.3-1. For much of the analysis in chapter 3, an echo spectrum of the form in figure 3.2-2 is assumed. This has only been chosen for its simplicity. Alternatively, any of the echo waveforms from Winghams database could have been chosen.